Deceleration of antiprotons from CERN's ELENA synchrotron and transport of antimatter beams through the GBAR experiment

Audric Husson

NNT : 2018SACLS255

Thèse de doctorat

Deceleration of antiprotons from CERN's ELENA synchrotron and transport of antimatter beams through the GBAR experiment

Thèse de doctorat de l'Université Paris-Saclay
préparée à Université Paris-Sud,
au CSNSM

Ecole doctorale n°576 Particules, Hadrons, Energie, Noyau, Instrumentation, Imagerie, Cosmos et Simulation (PHENIICS)
Spécialité de doctorat : Physique des Accélérateurs

Thèse présentée et soutenue à Orsay, le 17/12/2018, par

AUDRIC HUSSON

Composition du Jury :

Mme Amel KORICHI Directrice de recherche, CNRS (CSNSM)	Présidente
M. Patrick NEDELEC Professeur, Université Lyon 1 (IPNL)	Rapporteur
M. Christian CARLI Docteur, CERN (BE/ABP)	Rapporteur
M. David LUNNEY Directeur de recherche, CNRS (CSNSM)	Directeur de thèse

Á Mayette et Dédé ...

Contents

List of Figures

List of Tables

Chapter 1

Introduction

Einstein's theory of General Relativity (GR) is arguably one of the greatest scientific achievements ever. This elegant theory still awaits expression in the language of quantum physics - somehow now achieved for all of the other fundamental interactions of nature. The cornerstone of GR is the *Weak Equivalence Principle* (*WEP*) which expresses the equivalence of inertial and gravitational mass.

Numerous theoretical and experimental investigations proved that the gravitational mass and the inertial mass of ordinary matter are equivalent to one part per 10^{12}. Pointing out the lack of evidence considering the gravitational behavior of antimatter systems, theorists have built new models that in some cases violate CPT or Lorentz invariance as an explanation for baryogenesis or cosmological problems.

With advances in antimatter synthesis, tests of the WEP with antimatter are now achievable. Considering the weakness of gravity compared to any residual electrical or magnetic force, direct free-fall experiments with charged antimatter appear unrealistic. Antihydrogen is the best candidate because of its electrical neutrality and its lifetime compared to other neutral anti-systems like *positronium* atoms (Ps). But this apparent advantage implies the use of complicated systems to trap neutral atoms. Such trapping techniques have already been performed by antimatter experiments such as $ATRAP$ [1, 2, 3], $ASACUSA$ [4, 5, 6] and $ALPHA$ [7, 8, 9].

Even if these collaborations have already managed to synthesize antihydrogen atoms, the measurements of $F = M_g/M_I$, defined as the ratio of the gravitational mass M_g to the inertial mass M_I of antihydrogen, remains quite difficult.

In this chapter, a retrospective of the discoveries around antimatter is made as well as a summary of the great theories in particle physics and relativity. Finally, a panorama of attempts to measure the gravitational behavior of antimatter is presented.

1.1 Antimatter discovery

1.1.1 Dirac equation and the negative solution problem

In 1928, Paul A. M. Dirac by means of an innovative theoretical concept, obtained a relativistic theory of the electron. While major physicists of the time, like Oskar Klein or Walter Gordon, were already working on a relativistic equation, referred to as the Klein-Gordon equation, Dirac solved the problem of negative probability density functions by introducing a solution not based on a one dimensional wave function but on a four-dimensional wave function, called a spinor. Equivalent to four parallel Schrödinger equations with mixing terms[1], the equation can be formulated as:

$$i\frac{h}{2\pi}\frac{\partial\Psi}{\partial t} = -i\frac{h}{2\pi}\vec{\alpha}.\vec{\nabla}\Psi + \beta mc^2\Psi \tag{1.1}$$

where Ψ is a four-dimensional wave function; m, the mass of the particle, c the speed of light; h, Planck's constant and $\vec{\alpha}$,β are the 4x4 matrices acting on spinors, also known as *Dirac's matrices*.

This equation addresses the problem of the negative probability density while rigorously describing the spin, the magnetic moment and the spin-orbit interaction of the electron [10, 11]. However this equation raises a new problem; when a simple two-dimensional wave function may describe the electron spin states what happens to the other two dimensions ? Moreover, if the positive solutions of this equation describe the electron, what about the negative solutions ?

> "The relativity quantum theory of an electron moving in a given electromagnetic field, although successful in predicting the spin properties of the electron, yet involves one serious difficulty [...] connected with the fact that the wave equation [...] has, in addition to the wanted solution for which the kinetic energy of the electron is positive, an equal number of unwanted solutions with negative kinetic energy for the electron, which appear to have no physical meaning."
>
> Paul Dirac, 1930

In 1929, Hermann Weyl suggested that the negative energy solutions (and positive charge) stand for protons [12]. Dirac demonstrated that such a hypothesis leads to a violation of the electric charge conservation and postulated that vacuum is made of an infinite number of negative energy levels (later referred as the Dirac sea). Following this idea, if enough energy is transferred to a negative energy electron, it becomes a real electron (with positive energy) leaving a hole in the 'sea'.

> "A hole, if there were one, would be a new kind of particle, unknown to experimental physics, having the same mass and opposite charge of the electron."
>
> Paul Dirac, 1931 [13]

In 1931, Dirac put forward the controversial[2], but equally ingenious hypothesis that holes could be interpreted as new particles.

---

[1] In the low velocity approximation, one can find the Schrödinger equation : $i\frac{h}{2\pi}\frac{\partial\Psi}{\partial t} = -\frac{1}{2m}(\frac{h}{2\pi})^2\nabla^2\Psi$

[2] Robert Openheimer [14] opposed this idea arguing that it implies an unstable nature of the atom.

1.1.2 From theory to experiment : antimatter under the spotlight

In 1932, Carl Anderson discovered that, high energy photons from cosmic rays interacting with a lead screen, produce electrons as well as particles with almost the same mass but with opposite charge [15] as shown in Figure-1.1. Furthermore, these new particles can be converted back into two photons. The discovery was confirmed at the Cavendish Laboratory (Cambridge) by Patrick Blackett and Giuseppe Occhialini in 1933 [16].

The same year C.D. Anderson named this new particle, today interpreted as an anti-electron, *positron* [17]. Subsequently, as a confirmation, Irène and Frédéric Joliot-Curie identified positrons in the β^+ decay process of a phosphorus isotope [18] following:

$$^{30}P \rightarrow ^{30} Si + e^+ + \nu$$

Nevertheless, the Dirac equation in (1.1) is not only valid for electrons but for any spin-$\frac{1}{2}$ particles. Indeed, following this idea, the proton and the newly discovered neutron [19] should also present a corresponding anti-partner with the same mass but with opposite spin.

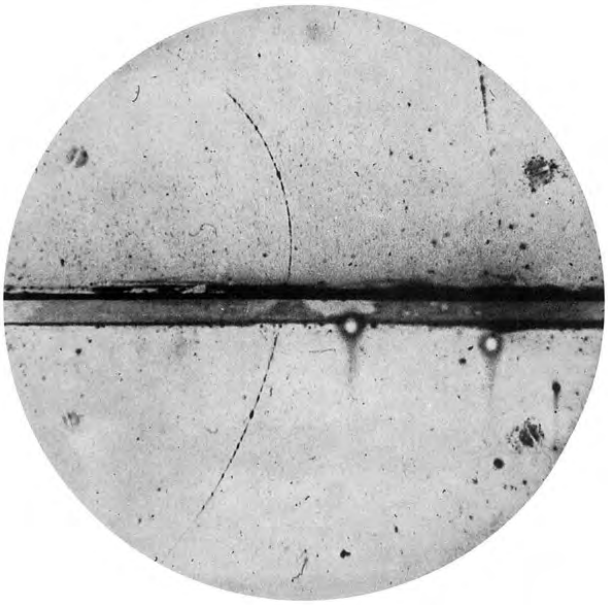

Figure 1.1 Cloud chamber photograph by C.D. Anderson [17]. A 63 MeV positron passed through a 6 mm lead plate and emerged at 23 MeV. The length of this path is at least 10 times greater than the possible trajectory of a proton with the same curvature.

Antiproton Discovery In 1955, after some minor unconfirmed cosmic-rays events [20, 21, 22], Emilio Segrè and Owen Chamberlain discovered the proton antimatter counterpart, named *antiproton* ($\bar{p}$ or pbar) [23]. They used the novel proton accelerator, called the *Bevatron*, at the Lawrence Berkeley National Laboratory designed to achieve a 6.5 MeV energy, which corresponds to the threshold that produces proton-antiproton pairs impinging an initial proton beam on a copper target. The detection of the antiprotons was performed via a momentum and time-of-flight identification, since the main contaminant particles were negative mesons produced in the reaction with a higher momentum.

Additional antimatter discoveries One year later, in 1956, following the same TOF discrimination principle in the same laboratory, the team of Oreste Piccioni and Bruce Cork discovered the neutron counterpart, the *antineutron* ($\bar{n}$) [24].

After single antiparticles, the production of antimatter turned to antinuclei, such as: *anti-deuterons* ($\bar{d}$) at Brookhaven first [25] and few months later in Europe at CERN in 1965 [26], *antihelium-3* nuclei ($^3\bar{H}e$) in 1971 [27] and *antitritons* ($^3\bar{H}^{(+)}$) in 1974 [28].

In 1995, a new step was taken by the *LEAR* (Low Energy Antiproton Ring) experiment at CERN. Colliding an antiproton beam circulating in a ring with a Xenon gas jet, the first (and simplest) atomic structures made of antimatter, *antihydrogen* atoms ($\bar{H}$), were synthesized. 11 events were recorded (with an hypothetical background of 2 ± 1 events) [29].

Furthermore, in 2010, the STAR experiment at RHIC, Brookhaven National Laboratory, announced the discovery of the first anti-hypernucleus, the *antihypertriton* ($^3_{\bar{\Lambda}}\bar{H}$) [30]. All these discoveries have been recently confirmed at high energy by the ALICE experiment, CERN-LHC [31, 32] as summarized in Figure-1.2. They also reported the discovery of *antihelium-4* nuclei ($^4\bar{H}e$).

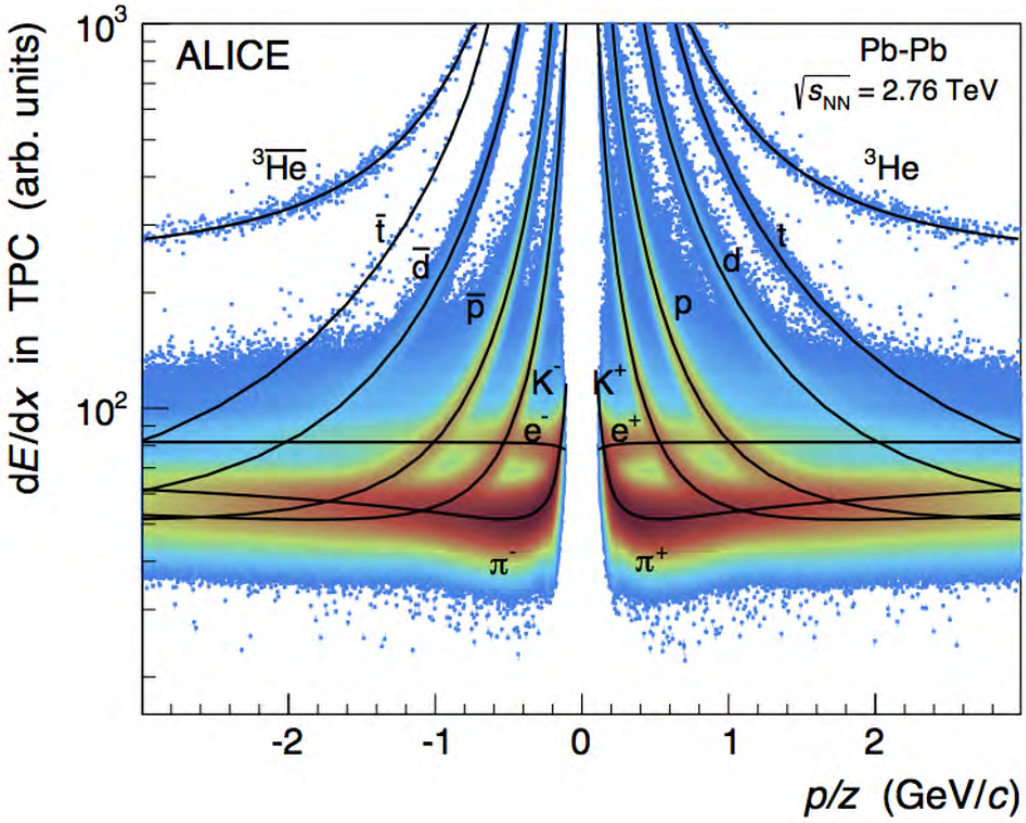

Figure 1.2 Energy-loss as measured in the Time Projection Chamber (TPC) of the ALICE experiment. The black lines correspond to the expected energy loss for different particles-antiparticles and nuclei-antinuclei. Data taken in lead–lead collisions at 2.76 TeV [33].

1.2 (anti-)atoms in an (anti-)Universe

The relativistic interpretation of the quantum theory gave birth to a new family of particles. As proof of his genius, Dirac is also at the origin of a theory today considered as the very first step of the quantum field theory[34][3]. This latter is undeniably one of the greatest achievements in modern physics describing three of the four known interactions (electromagnetism, weak and strong interactions).

The quantum field theory formalism implies that physical laws stay unchanged under the successive combined transformations:

- **C-symmetry**: charge conjugation, switching all particle properties with those of their corresponding antipartners.
- **P-symmetry**: parity transformation, opposing the spatial coordinates
- **T-symmetry**: time reversal

If there is no more doubt on the C-symmetry and P-symmetry violation in the weak sector [35, 36] and moreover on the combination of both CP-symmetry [37, 38, 39, 40], there is no hint yet of the violation of the CPT-symmetry[4].

Today, the invariance of the physical laws under the above CPT combination is widely recognized as an indisputable truth. The CPT-invariance implies that the inertial mass, charge magnitude, mean life and magnetic moment are identical for any particle and its corresponding antiparticle. One of the main goals of the current low-energy antimatter experiments is to confirm this statement. A non-exhaustive list of the last results can be found in Refs.-[7, 41, 42, 43, 44, 45, 46, 47, 48].

According to the invariance of the physics laws with respect to the CPT-symmetry, a major question remains partly unanswered : why are we made of matter and not antimatter ?

Astronomical observations show that in the observable Universe, antimatter particles are sporadically present. It means that no matter and antimatter macroscopic structures coexist in our close neighborhood. Indeed, such coexistence would lead to the emission of radiation coming from a large number of annihilations at the frontier between matter and antimatter.

The Standard Model of particle physics associated with the ΛCDM-model (or *Standard Cosmological Model*) explains at best the composition of our visible Universe. Shortly after the Big Bang, matter and antimatter are produced with *almost*[5] the same abundance. The coexistence of particles and antiparticles lead to annihilation processes producing the current observed photons. At the end of this phase, all particle-antiparticle couples disappeared. The exceeding particles remain forming the Universe as we know it.

Hints of this original event are still detectable by estimating the baryon-to-photon ratio in our visible Universe, also referred as baryon abundance $\eta = n_b/n_\gamma$, with n_b the number density of baryon and n_γ the number density of relic blackbody photons. According to [49], recent cosmological evaluations[6]: $5.8 \times 10^{-10} \leq \eta \leq 6.6 \times 10^{-10}$. It means

[3]The new quantum electrodynamic (QED) theory is the fruitful work of successive ingenius physicists whose apotheosis is reached in 1949 with the work of Julian Schwinger, Sin-Itiro Tomonaga and Richard Feynman.

[4]Considering the CPT symmetry, one should note that a violation of the CP-symmetry induces a violation of the T symmetry.

[5]The quasi-equality is here of crucial importance.

[6]The number density of relic blackbody photons is fixed by the Cosmic Microwave Background temperature $T = 2.7255(6)\ K$ to $n_\gamma = 410.7(3)\ cm^{-3}$. The baryon density n_b in the standard Big Bang Nucleosynthesis scenario (BBN) depends only upon $\Omega_b h^2$, the average baryon mass at the present epoch,

that almost one particle over 10^9 survived to the primordial annihilation.

Following this estimation, particle physicists and cosmologists have tried to explain this asymmetry. In 1966, Andrei Sakharov proposed an explanation [50] based on three conditions (referred as the *Sakharov conditions*):

1. The *C- and CP-symmetry violation* allows matter and antimatter to interact differently.
2. The *violation of the baryon conservation law* that explains the excess of baryons over antibaryons.
3. Interactions must be *out of thermal equilibrium.*

As described in the previous subsections, several experiments already established the violation of the C- and CP-symmetry. Moreover, the expansion phase during the early age of the Universe (when the annihilation process occurred) can be seen as an out-of-equilibrium system where particles and antiparticles do not achieve a thermal equilibrium. Unfortunately, no evidence of a broken baryon conservation law has yet been brought to light and still need to be found[7].

In parallel with the Sakharov conditions, another exotic hypothesis suggests the coexistence of matter and antimatter in equal quantities in the Universe. The absence of irradiating interface could be explained by an asymmetry in the gravitational behavior of antimatter with respect to matter [51, 52]. This Kant-like perspective of an 'antimatter island Universe' is unlikely at our scale and is not supported by recent cosmological observations on the Cosmic Microwave Background.

1.3 "Defying gravity"

Before drawing hasty conclusions about the disappearance of antimatter beyond the visible horizon, one should understand how gravity applies and what could differ from the behavior of matter.

1.3.1 The (not so) Weak Equivalence Principle

When physicists have to deal with macroscopic low energy experiments, they inevitably deal with Einstein's theory of General Relativity. This theory relies on postulates confronted by nearly one century of experimental tests without fault, among them the Equivalence Principle.

In its *weak* form or Weak Equivalence Principle (*WEP*), it asserts that in a gravitational field the acceleration of a "test particle" is independent of its mass and its composition but only depends on its initial position and velocity [53]. This principle is also called the Universality of Free-Fall (*UFF*). In the framework where the gravitational acceleration is indistinguishable from a mechanical acceleration, it is equivalent to say that gravitational mass is identical to inertial mass. When associated with the Local Lorentz Invariance (*LLI*) and the Local Position Invariance (*LPI*), this principle is known as the Einstein Equivalence Principle (*EEP*) and is at the foundation of the Einstein's Special and General Relativity theory.

---

and the Newtonian constant of gravitation G_N. It is now fixed to $n_b = 2.503 \times 10^{-7}\ cm^{-3}$. Larger references in [49].

[7] The baryon (and/or lepton) number violation can be accommodated in the Standard Model of particle physics via the existence of the *sphaleron*.

This Equivalence Principle is qualified as *weak* as opposed to the *Strong Equivalence Principle* whose demonstration is based on a pure geometrical approach of space-time and requires a more detailed but also constraining definition. This latter aims to generalize the WEP to any place in the Universe even in regions where the gravitational field suffers from important distortions[8]. The violation of such SEP would rest on the variation of fundamental constants, like the (Newton's) Gravitational Constant over time like for instance at the early age of the Universe or close to massive cosmological structures.

1.3.2 From theory to experiment

The EP has been the cornerstone of all gravity theories since Galileo's work 400 years ago. By investigating the motion of objects on inclined planes and pendulums[9], he understood that objects of different mass and composition accelerate similarly in the same gravitational field and formulated the first empirical law of free-falling bodies.

The first mathematical description of gravity was published by Sir Isaac Newton in 1687 in the famous *Pincipia*. By applying his second law, Newton considered the fundamental difference between the inertial and gravitational mass [54]. Let's consider Newton's law of motion for a free-falling body:

$$\vec{F} = m_{inertial}\ \vec{a}\ ;\ \text{with}\ \vec{F} = m_{gravitational}\ \vec{g}\ \ \text{then,}\ \vec{a} = \frac{m_{gravitational}}{m_{inertial}}\ \vec{g}$$

After testing his theory via the use of pendulums with different mass and composition, he found no deviation from $m_{gravitational}/m_{inertial} = 1$ with 10^{-3} accuracy. Using pendulums as well, Bessel improved this limit to 1 part per 10^5 in 1832. In 1889, Loránd Eötvös used an innovative system composed of a torsion balance. He demonstrated experimentally the equality with an accuracy of 1 part per 10^9[55, 56].

More than a century later, the mass identity is still of interest for various theoretical and experimental investigations. Most of the experiments challenging the EP are based on the comparison of the acceleration of test bodies made of different compositions. Paying tribute to the Baron von Eötvös, a new dimensionless parameter has been defined to quantify the equivalence between the inertial and gravitational mass. For two test bodies defined as A and B, the Eötvös parameter η is:

$$\eta(A,B) = \frac{\Delta a}{a_S} = 2.0\ \frac{(a_A - a_B)}{(a_A + a_B)} = 2.0\ \frac{(\frac{m_g}{m_i})_A - (\frac{m_g}{m_i})_B}{(\frac{m_g}{m_i})_A + (\frac{m_g}{m_i})_B} \tag{1.2}$$

with m_g and m_i, respectively the gravitational and inertial mass, Δa the hypothetical difference in acceleration and a_S the average acceleration.

In recent decades, the η parameter has continued to be lowered (cf Table-1.1). Its measurement and the test of the UFF is still necessary to test Einstein's theories at the highest level.

An important element one should notice, is the apparent simplicity of the experiments in Table-1.1. The use of a torsion balance or a test mas in a satellite orbiting around the Earth offer the possibility to confirm the WEP with a maximum accuracy of 10^{-15}. Is such a precision achievable for testing antimatter ? Could a deviation explain its disappearance ?

[8] The EEP require to work in local constant gravitational potential and then do not take into account for instance tidal effects induced by the rotation of the Earth or the revolution of the Moon.

[9] The free-falling object experiments from the Pisa tower is more a myth than reality.

Year	Authors & Reference	Limit on $\eta = \lvert\Delta a/a\rvert$ parameter	Method
1590	Galileo	2.10^{-2}	Pendulum
1687	Newton [54]	10^{-3}	Pendulum
1832	Bessel	2.10^{-5}	Pendulum
1908 (1922)	Eötvös [55, 56]	2.10^{-9}	Torsion Balance
1918	Zeeman	3.10^{-8}	Torsion Balance
1935	Renner	2.10^{-9}	Torsion Balance
1964	Dicke, Roll, Krotkov [57]	3.10^{-11}	Torsion Balance
1972	Braginsky, Panov	10^{-12}	Torsion Balance
1976	Shapiro, et al. [58]	10^{-12}	Lunar Laser Ranging
1987	Niebauer, et al. [59]	10^{-10}	Drop Tower
1989	Stubbs, et al. [60]	10^{-11}	Torsion Balance
1990	Adelberger, Eric G.; et al. [61]	10^{-12}	Torsion Balance
1999	Baeßler, et al. [62]	5.10^{-14}	Torsion Balance
2003	V. Nevizhevsky, et al. [63]	0.2 %	Neutron free-fall
2016	MICROSCOPE [64]	10^{-15}	Earth Orbit

Table 1.1 Progress in the evaluation of the Eötvös parameter η_E

1.4 What about antigravity ?

A gravitational asymmetry seems impossible holding as exact the GR theory with the EEP principle. But regarding the expansion mechanism and the composition of our Universe, theorists have developed new models including matter-antimatter gravitational asymmetry. For instance, Nieto and Goldman supported this point of view (cf. Ref.[65], Section 8) conjecturing a possible "fifth force" among the current gauge forces of the Standard Model (*SM*) without any contradiction with GR.

> "... the more precisely anomalous gravitational effects are ruled out in earth-based matter-matter experiments, the more unrestricted is the possibility that there can be a significant anomalous gravitational acceleration of antimatter"
>
> Nieto & Goldman, 1991, [65]

There is also no obvious evidence concerning CPT-symmetry. While many experiments rigorously proved the correctness of CPT for asymptotically flat-space relativistic local field theories, some Standard-Model Extensions (*SME*) assume a possible violation. Indeed, CPT-symmetry does not impose constraints on how antimatter interacts with a gravitational field induced by a matter structure. If one considers a simple gravitational experiment of a falling apple on Earth, the strict application of the CPT-symmetry means therefore to drop an "anti-apple" on an "anti-Earth".

1.4.1 Indirect estimation

A consequence of the WEP is a gravitational redshift [66]. For oscillatory systems, this latter is characterized by a shift in the observed frequencies compared to expectations with respect to the position of the studied system in the gravitational field.

We can here define a new parameter, the *matter-antimatter gravitational coupling* α as:

$$\bar{g} = \alpha g \tag{1.3}$$

with g and $\bar{g}$, the gravitational accelerations of matter and antimatter respectively. One can easily derive from (1.3) in the framework of a free-fall that :

$$\alpha = \frac{M_{\bar{A}}}{M_A} \quad \Longleftrightarrow \quad |1-\alpha| = \frac{\Delta M_{\bar{A}-A}}{M_{\bar{A}}} \tag{1.4}$$

where A represents a test mass and $\bar{A}$ its antimatter counterpart, M the gravitational mass of $A/\bar{A}$.

Attempts to establish a limit on the WEP with antimatter have already been performed. By measuring, the $K^0 - \bar{K^0}$ oscillation rate [37, 67, 68] or the proton/antiproton cyclotron frequency [69, 70, 71], one can extract an indirect limit on the gravitational asymmetry between matter and antimatter.

$$\Delta M_g.\phi_g \propto \Delta\omega \qquad with \quad \phi = \frac{GM}{Rc^2} \tag{1.5}$$

ΔM_g is the equivalent mass difference between matter and antimatter, GM the standard gravitational parameter, R the orbital radius, c the speed of light and $\Delta\omega$ the gravitational redshift[10]

The limits found are :

$\|1-\alpha\| \leq 2.0 \times 10^{-13}$	from neutral kaon mixing [68]
$\|\alpha - 1\| < 5 \times 10^{-4}$	from cyclotron frequency measurement [71]

If such results seems indisputable, a controversial argument emerges from their analysis. Indeed, the above values are established using the supergalactic cluster (the "great attractor") as the dominated excess mass. But the definition of the excess mass reference (the Earth, the Sun, the galactic nucleus or the supergalactic cluster) leads to different values of $|1-\alpha|$ with several orders of magnitude difference. As emphasized in reference-[72, 65] and in Ref.[66]-Section 5.4, the evaluation of the $|1-\alpha| = \Delta M/M_A$ value is still subject to a debatable definition and does not constitute an irrefutable proof.

1.4.2 Astronomical observations

On 23^{rd} February 1987[11], a type-II supernova exploding in the Large Magellanic Cloud [73] offered the opportunity to highlight a possible gravitational asymmetry. Three hours before the supernova appeared in the sky, a neutrino burst was detected in two different neutrino experiments: 11 events reported at *Kamiokande II* (Japan) [74, 75] and 8 events in IMB (USA) [76].
According to Ref.[77] and [78], these 19 events revealed statistically no difference in the arrival time of neutrinos, antineutrinos and photons. Demonstrating that (anti-)neutrinos and photons follow the same trajectories in the gravitational field of the galaxy, Krauss and Tremaine [78] estimated the WEP to be true with an accuracy of at least 0.5%. Considering at least one ν_e event, the autors of Ref.[79] derived the WEP to be validated to an accuracy of one part per 10^6.

[10] In the case of Ref.[71], the redshift is defined as a difference in the measured antiproton cyclotron frequency compared to proton one. In the case of the $K^0 - \bar{K^0}$ oscillation, it corresponds to the difference between their de Broglie frequencies define according to Ref.[68].

[11] IAUC 4316: 1987A; N Cen 1986

But again, the hypothesis used for the gravitational potential and the excess mass reference[12] is questionable. Furthermore, the difficulty to differentiate between neutrinos and antineutrinos and to clearly establish the flavor of the detected events raised the problem of their origin.

Despite other theoretical attempts to glimpse an asymmetry in the gravitational coupling for instance in (anti-)neutrino mixing between flavor eigenstates [80] or even in the solar neutrino "deficit" [81], no evidence has supported these theories so far.

1.4.3 Direct attempts

Seeing the limits of the indirect measurements, only direct tests seem to offer a level of confidence high enough to test the WEP. Considering the difficulty to synthesize antimatter and the incompatibility of mixing matter and antimatter, torsion-balance or pendulum experiments are obviously unfeasible with antimatter.

However, the neutron free-fall experiment[13] performed in 2003 [63] presents an interesting perspective for direct observation. Valery Nesvizhevsky and his team used Ultra-Cold Neutrons (UCN) to realize a single particle free-fall experiment. Such a free-fall test with antineutrons is unrealistic because the cooling and guiding processes that involve scattering and bouncing off of matter [82]. Nevertheless, improvements in antimatter trapping and cooling techniques for non neutral antimatter systems offer the possibility to reach energies low enough to observe gravitational effects.

In 1968, Witteborn and Fairbank proposed a direct measurement using cold electrons and positrons [83, 84, 85]. As shown in Figure-1.3, this experiment is based on the analysis of the time-of-flight distribution of electrons (resp.: positrons) falling freely within a shielded vacuum chamber. A cryogenic source at the bottom of the cavity emits cold electrons upwards in a fountain-like mode. A Multi-Channel Plate faces the source on the top of the cavity. The electrons are constrained to move along the axis of the vacuum cavity by a magnetic field of a coaxial superconducting solenoid. Residual fields mainly result from induced image and are reduced by surrounding the free-fall region with copper drift tubes (cf Figure-1.3).The charged particles experience an effective gravitational acceleration:

$$g_{eff} = g(1 - Qm_e/eM)$$

where Q and M are the charge and mass of the particle.

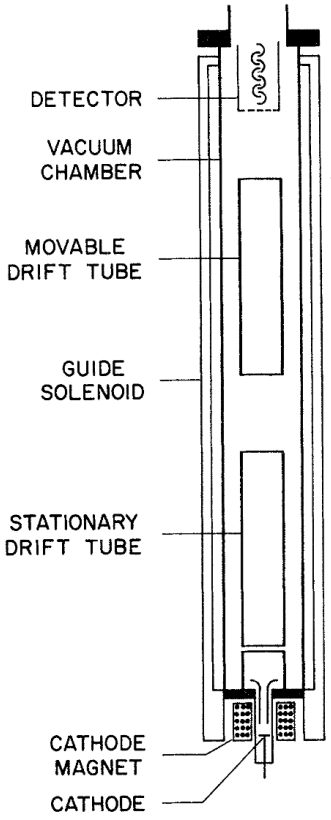

Figure 1.3 Schematic diagram of the helium-immersed portion of the Witteborn-Fairbank apparatus.

[12] The references [77] and [78] used the galaxy and the galactic nucleus as excess mass reference.
[13] Mentioned in Table-1.1

If all the residual forces are suppressed, the distribution of the electrons or positrons time of flight should display a cut off at $t_{cutoff} = \sqrt{2mh/mg} = \sqrt{2L/g}$ with the drift tube length L. F.C. Witteborn and W.M. Fairbank found that for the electron, g_{eff} was less than $0.09g$. A simple calculation gives an estimation of $g_{eff} = 2g$ in the positron case.

Considering the gravitational potential gradient of an electron or a positron at the Earth's surface equivalent to $mg = 5.6\ 10^{-11} eV.m^{-1}$, all vertical electric and magnetic gradients must be reduced below the $10^{-11}\ eV/m$ scale[14]. But even working in an insulating box with at least one trapped charge inside would lead to a force greater than mg. Systematic errors overwhelm all measurements. After several attempts and thorough research of noise sources, the result of $g_{eff} = 0.02g$ for electrons has not convinced the antimatter community [86] and no attempt has been made for positrons.

Following a similar method but with antiprotons, the PS200 experiment [87] (Fig.-1.4) accepted by CERN based on the capture and cooling of antiprotons into a Penning trap to make the same free-fall test as in the Witteborn-Fairbank's experiment. This experiment was installed at the LEAR facility, unfortunately this antiproton investigation stopped without any evidence. It seems realistic to suppose that such an experiment would suffer from the same systematics problems.

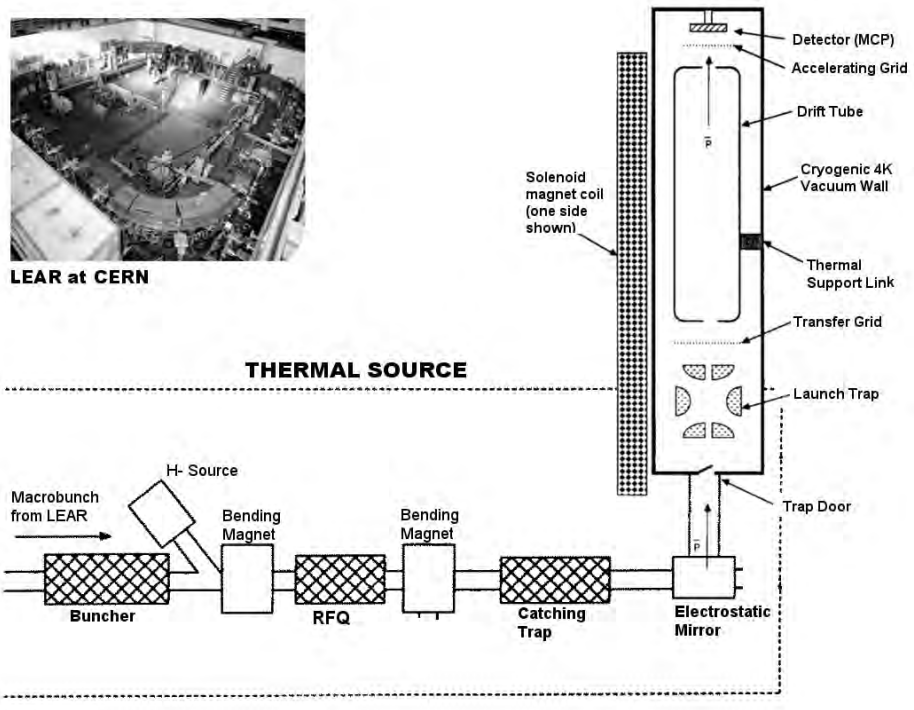

Figure 1.4 Schematic diagram of the apparatus for the proposed experiment PS200, based on Ref.-[88]

The previous attempts to test the WEP with single free-falling charged particles exhibit the most important problem in such gravity experiment: the lightness of particles. For instance, the ratio of the electrostatic and gravitational forces between two protons at $1m$ distance is tremendous:

[14]The corresponding electric field is 10 $fV/m = 10^{-11}\ V/m$

$$\left.\begin{array}{rrcl} \text{Electrostatic Force}: & F_E = k_C \frac{q_1.q_2}{d^2} & \rightarrow F = 2.3 \times 10^{-28}\ N \\ \text{Gravitational Force}: & F_G = G \frac{m_1.m_2}{d^2} & \rightarrow F = 1.87 \times 10^{-64}\ N \end{array}\right\} \frac{F_E}{F_G} \approx 10^{36}$$

Even if the associated technology has been improved, reaching a level of residual field lower than 10 $fV/m = 10^{-11}\ V/m$ appears quite challenging. The obvious conclusion is to perform such a free-fall test with neutral antimatter systems. Such experiments are now being pursued using laser cooling and velocity techniques to measure the time of flight or to measure the position in a magnetic antihydrogen trap. These experiments will be performed more precisely than either the antiproton or positron experiments.

1.5 Toward current experiments

As seen in this historical summary, antimatter has always attracted the interest of the scientific community. After a controversial theoretical discovery and unexpected experimental discovery, its apparent disappearance after the Big Bang remains an open question both in particle physics and cosmology.

Numerous speculations have been put forward regarding the dominance of matter in the very first moments of the Universe. Some of them find their origin in the gravitational behavior of antimatter. Thus, examples of repulsive gravity [89] or supersymmetric models (integrating 'supergravity') are flourishing. These theoretical concepts of gravitational asymmetry are clearly born from a scientific void for which neither the CPT symmetry (describing the non-gravitational interactions at the scale of the particles) nor relativity (describing the interaction of the gravity on large scales) are predictive. Nevertheless, in physics "the absence of proof is not a proof of absence" !

Nowadays, gravity theories like the Special or General Relativity, or any other cosmological models rely on pillars such as the WEP. This latter is verified through different measurements with very high accuracy. Unfortunately, all these experimental verifications only concern matter environments.

If attempts of indirect measurements have not been conclusive, new techniques in trapping, cooling and in detection systems make it possible to reach energies low enough, to explore the gravitational interaction. The use of neutral antimatter systems, like antihydrogen atoms, appears as the only way to test the WEP with antimatter[15].

In fact, three experiments are currently under development at CERN to determine the gravitational acceleration of antimatter: $AEgIS$ [92], $ALPHA-g$ [93] and $GBAR$ [94]. These experiments (in addition to $ATRAP$ and $BASE$) are located in CERN's AD hall, which is presently the worlds unique source of antiproton beams for experiments. The layout of the AD hall is shown in Figure-1.5.

The AD ring was used as an antiproton accumulator during CERN's illustrious period of proton-antiproton collisions with the SPS ring that produced the W and Z particles in UA1. The AD now stores antiprotons created from 26 GeV protons (from the PS) hitting an iridium target and decelerates them over a 110-second cycle during which magnetic ramping combined with stochastic and electron cooling reduces their energy to 5.3 MeV.

[15]The use of positronium atoms (Ps), bound states of an electron and a positron, has been investigated. The Ps lifetime in its ground state n=1, $t \approx 140ps$, is too short to see anything but a ballistic experiment seems realistic if excited to Rydberg states. Ref.[90, 91].

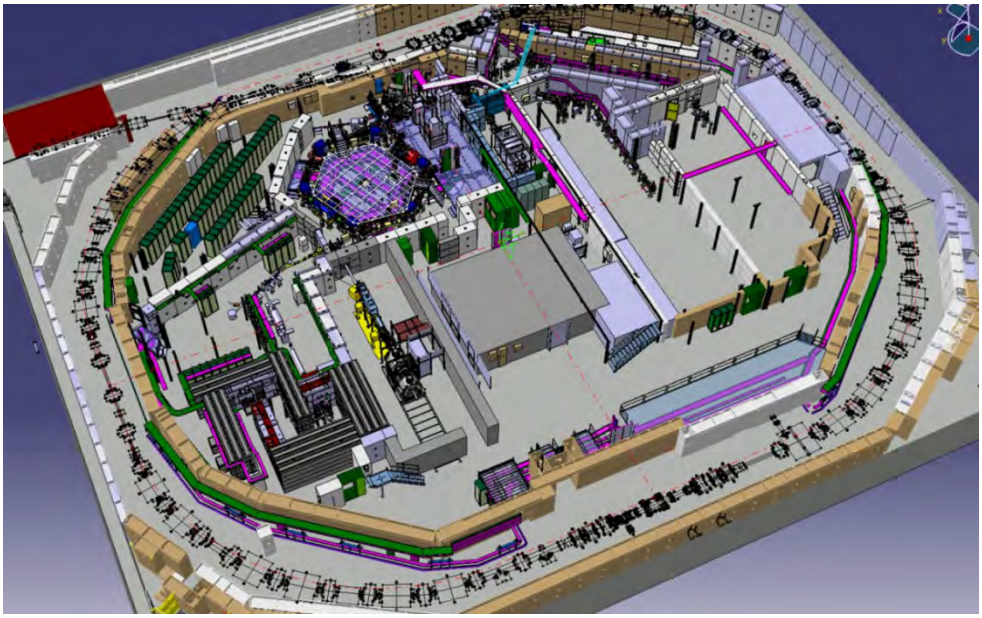

Figure 1.5 Antiproton Decelerator hall showing the AD ring plus experiments. The AD is the large exterior ring and the experiments are located in the hall on the right. The new ELENA ring is also visible (upper left). Figure from [95].

1.6 How to decelerate a beam (further)?

As mentioned in the previous section, the AD ring provides to most of the experiments using traps antiproton at 5.3 MeV when they require antiprotons of $1-5$ keV kinetic energy. Different beam deceleration techniques have been used to slow down the antiprotons by a factor 1000. All these techniques, however, have a price, that of a poor efficiency.

The experiments like BASE [96],ALPHA [7], ATRAP [1] and AEgIS [92] use degrader foils to slow AD beams. The beam passing through a thin metallic film, loses energy by interacting with the nuclei in presence. Such technique suffers from a low efficiency due to scattering in the degrader material and to adiabatic blow up of the beam emittance. Indeed, most of the antiprotons do not interact (enough) with or annihilate in the thick film and are lost. Less than 0.1% of the beam can be used and trapped.

The ASACUSA experiment benefits from a different deceleration via the use of a Radio-Frequency Quadrupole Decelerator ($RFQD$) [97]. It operates as an inverse linac, which decelerates the 5.3 MeV antiprotons extracted from the AD down to 100 keV with a deceleration efficiency of 30%. This post deceleration increases the trapping fraction of antiprotons into the "MUSASHI" catching trap by about two orders of magnitude, as compared to the conventional degrader method. However, the deceleration in the RFQD is accompanied by an adiabatic blow up which causes significant reduction of the trapping efficiency. The RFQD is also very sensitive to the upstream trajectory of the beam and optics mismatch errors through the connexion line with the AD ring. About 70% of the beam is lost when passing through the RFQD, the transverse beam size is big (160 mm) and the transport downstream has to be shortened. A degrader must be used anyway leading to a capture efficiency in the MUSASHI trap of $3-5$% of the antiprotons [98, 99].

Also located in the AD hall (see Figure-1.5) is the synchrotron ELENA [95], which will further transform the antiproton beam energies from 5 MeV to 100 keV. Such low energies open up beam-transport possibilities based on electrostatic optics. At CERN's

sister facility, ISOLDE beams are transported at 60 keV. Experiments at ISOLDE using Penning traps rely on electrostatic deceleration, which was adopted by the GBAR experiment to avoid the losses using foils. The implementation of this decelerator stage is the main subject of this thesis.

1.7 This thesis

In the course of this thesis, the dynamic, electrostatic-elevator decelerator was introduced and brought from conception to apparatus.

The decelerator system was simulated in its entirety, mostly using the ion optics program SIMION. But as the device is comprised of six electrodes, finding optimum voltage configurations proved practically impossible. The simulation process was therefore coded using a genetic algorithm that has been proven to provide more generalized solutions to many-variable problems. This is one of the first such studies using low-energy electrostatic beam optics.

In the course of this work, the decelerator instrument was constructed from scratch. A complete 50 keV proton beam line was also constructed and characterized as a test bench. After testing the different components individually, a first prototype demonstrated the deceleration of the 50 keV proton beam in Orsay. The system was then installed in an ultra-high-vacuum-compatible chamber, mounted on an adjustable chassis inside an IP3X-standard high-voltage protection cage and moved to CERN, where it was installed on the ELENA LNE50 extraction beam line.

The ELENA ring operates at pressures lower than 10^{-12} $mbar$. Due to an unfortunate vacuum leak in the helicoil-type seals that appeared during the high-temperature baking of the decelerator system, it was impossible to open the valve between ELENA and GBAR before the 2017 year-end technical stop. During the shutdown in early 2018 the decelerator electrodes were removed and remounted inside of standard CF UHV chambers that were designed and ordered. During this time, additional simulations and design was performed for the integration three additional components for GBAR: a proton source upstream of the decelerator, injection optics into the future antiproton Penning-trap and the switchyard to separate the unreacted antimatter beam components. The decelerator provided low-energy antiprotons from ELENA in late 2018.

The thesis is organized as follows. Chapter 2 describes the GBAR experiment in general and the antiproton decelerator concept in particular. Chapter 3 recalls some of the basics of electrostatics and the tools required to simulate the decelerator. The extension of the simulation to the genetic algorithm is presented in Chapter 4. Chapter 5 describes the mechanical design and the implementation and testing of the decelerator. Chapter 6 presents the simulations and design studies for the proton line, refocusing optics and switchyard. Finally, chapter 7 concludes the thesis and gives several perspectives for continuing work on this sophisticated and ambitious experiment.

Chapter 2

The GBAR experiment

2.1 Principle

GBAR stands for *Gravitational Behavior of Antimatter at Rest.*

As explained in the introduction, the antimatter gravity experiment is best performed using neutral species. However, cooling neutral antihydrogen (needed to minimize the initial velocity) is extremely difficult. The major innovation brought by the GBAR experiment, based on an idea of Walz and Hänsch [100], is the production of antihydrogen in its ionic state (one antiproton with two bound positrons). $\bar{H}^+$ ions can then be sympathetically cooled down to some 10 μK by Coulomb interaction with an easily laser cooled species. An antihydrogen atom is then obtained by photo-detaching the excess positron using a laser pulse. The neutral $\bar{H}$ atom produced is subject only to the gravitational interaction and freely falls.

The acceleration $\bar{g}$ is obtained by measuring the fall time of the antihydrogen. It starts at the moment of the laser shot responsible for the photo-detachment and ends the antihydrogen annihilates at the bottom of the chamber. $\bar{g}$ is determined via the ballistic equation :

$$z = \frac{1}{2}\bar{g}(t_{pd} - t_a)^2 + v_{z0}(t_{pd} - t_a) \tag{2.1}$$

with z, the free-fall distance; t_{pd}, the moment of the photo-detachment laser pulse; t_a, the moment of the annihilation and v_{z0} the vertical z-component of the initial speed. For a vacuum vessel of reasonable size $\sim 1\ m$, the speed of the atoms $\bar{H}$ has to be of the order of 1 m/s which corresponds to energies of about 42 neV (resp.: $T = 5\ \mu K$). Such low energy can only be achieved by mean of laser and sympathetic cooling.

Several methods exist for producing antihydrogen [1, 7]. For GBAR, the $\bar{H}^+$ ions are obtained through a double charge-exchange reaction involving antiprotons and positronium Ps, bound states of an electron and a positron:

$$\bar{p} + Ps \longrightarrow \bar{H} + e^- \tag{2.2}$$
$$\bar{H} + Ps \longrightarrow \bar{H}^+ + e^- \tag{2.3}$$

Unfortunately, cross sections for such reactions are not well known. Many theoretical calculations [101, 102, 103, 104] have be realized to estimate them. Only three experimental points were measured for the first reaction using normal hydrogen [105, 106]. These points are shown in Figure-2.1 with the recent calculations from [103].

The $\bar{H}^+$ production yield can be estimated with :

$$N_{\bar{H}^+} \approx N_{\bar{p}} \times \overbrace{(\sigma_{\bar{H}} n_{Ps} L)}^{1^{st}\ reaction} \times \overbrace{(\sigma_{\bar{H}^+} n_{Ps} L)}^{2^{nd}\ reaction} \tag{2.4}$$

with $N_{\bar{H}^+}$, the number of antihydrogen ion(s) produced; $N_{\bar{p}}$, the number of antiproton(s) passing through the Ps plasma; $\sigma_{\bar{H}}$, the cross section for the first reaction; $\sigma_{\bar{H}^+}$, the cross section for the second reaction; L, the typical length of the Ps converter and n_{Ps} the Ps density.

According to Eq.-2.4, for $N_{\bar{p}} = 10^6$ antiprotons passing through the Ps converter at 6 keV and for positronium atoms in the $1S$ ground state, a density of $n_{Ps} \approx 2.10^{11}\ cm^{-3}$ is required. The commonly used, ^{22}Na isotope decays by positron emission to stable ^{22}Ne and has a half-life of 2.6 yr. Such sources, used by all other AD experiments, are available commercially but are not available with sufficient intensity. To reach such density in less than $100s$, GBAR does not use a ^{22}Na source but a LINAC[1].

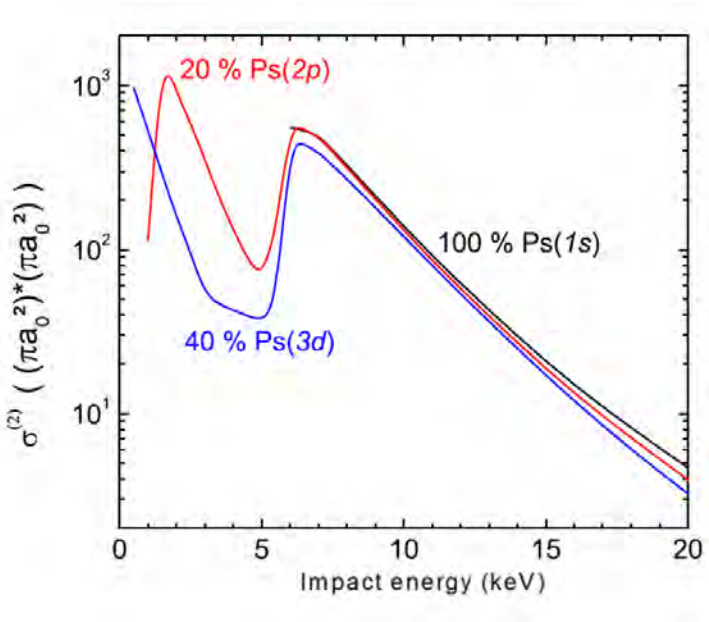

Figure 2.1 Total cross section for the double charge exchange reaction with different laser excitations of the positronium (see section-2.2.2) with $a_0 = 0.529$ Å, the Bohr radius. Plots are from [101] and [102].

Using the numbers above, the $\bar{H}^+$ rate is estimated at about one per AD pulse. About 1500 ions are needed to achieve an accuracy on $\bar{g}$ of about 1%. More details about the general layout and GBAR expectations can be found in the original 2011 proposal [94].

The GBAR experiment is broadly divided into four sections:

1. Positron production and accumulation.
2. Antiproton deceleration and focusing.
3. Antihydrogen synthesis (including laser excitation of positronium).
4. Antihydrogen cooling and preparation, and annihilation detection.

[1]See Section 2.2.1.

A schematic view of GBAR illustrating this functional breakdown is shown in Figure-2.2.

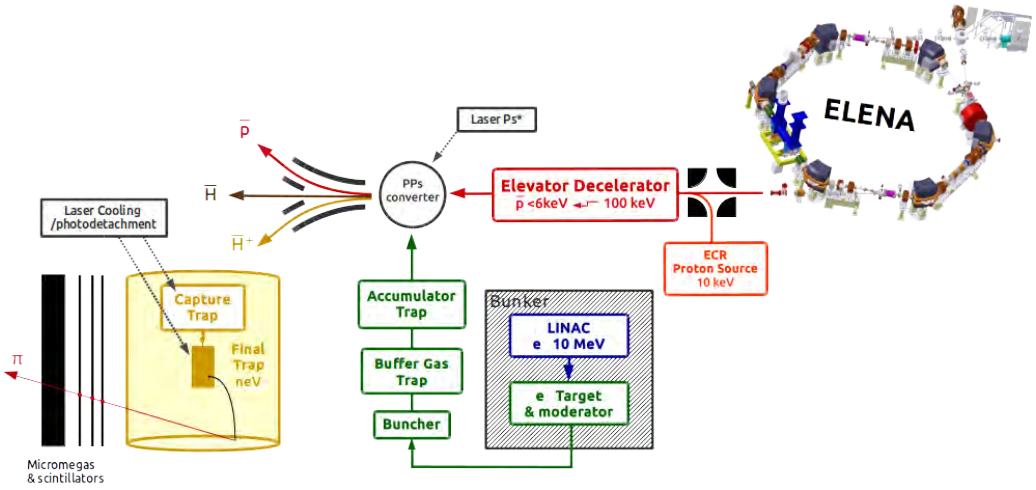

Figure 2.2 Schematic illustration of the GBAR experiment.

The layout of the GBAR experiment in the AD Hall is shown in Figure-2.3.

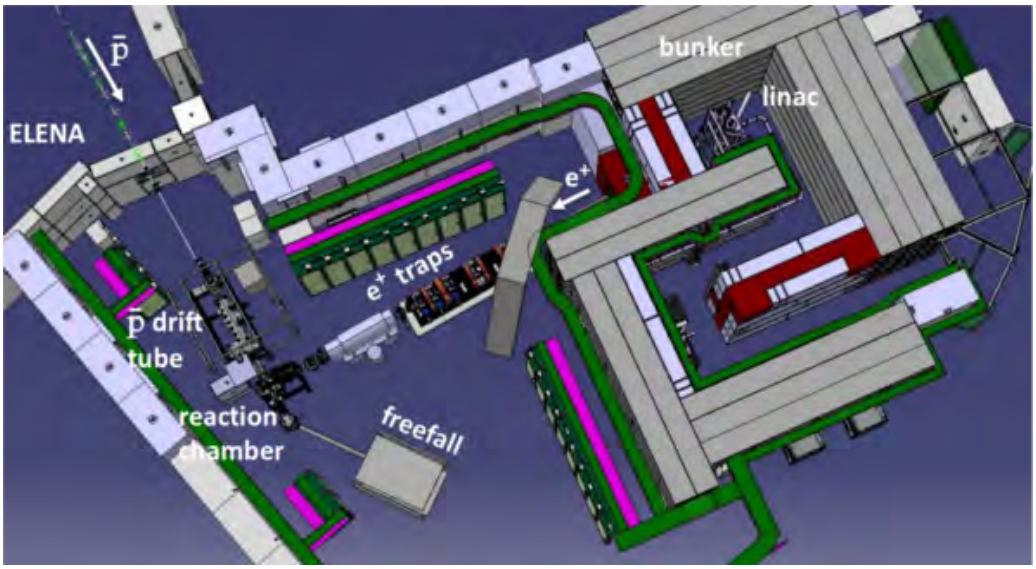

Figure 2.3 Layout of the GBAR experiment in the CERN AD hall.

Step 1 is achieved using the linac and positron traps. Step 2 is performed in parallel by the AD/ELENA rings followed by the $\bar{p}$ pulsed drift tube. Step 3 is via the reaction chamber and Step 4 in the free-fall chamber. The different components are described in the following section.

2.2 Experimental setup

2.2.1 Linac and Positron source

A linac (*linear accelerator*) of 9.5 MeV energy and 300 mA peak current running at 300 Hz repetition rate accelerates electron bunches of a few microseconds length.

Positrons are created by impinging the electrons on a tungsten target. Some of the electrons interact with the target nuclei and emit high energy Bremsstrahlung rays. Gamma rays with a large enough energy can dissociate into electron-positron pairs. Considering an electron to positron conversion of $K(e^- \longrightarrow e^+) \sim 10^{-4}$, a 10^7 $e^+/bunch$ rate is expected behind the target.

The high radiation requires the linac and the tungsten target to be placed in a bunker made of iron and concrete as displayed in Figure-2.3 (without roof). As illustrated in the Figure-2.4, the unusual vertical position of the assembly was chosen to limit the dose depositions.

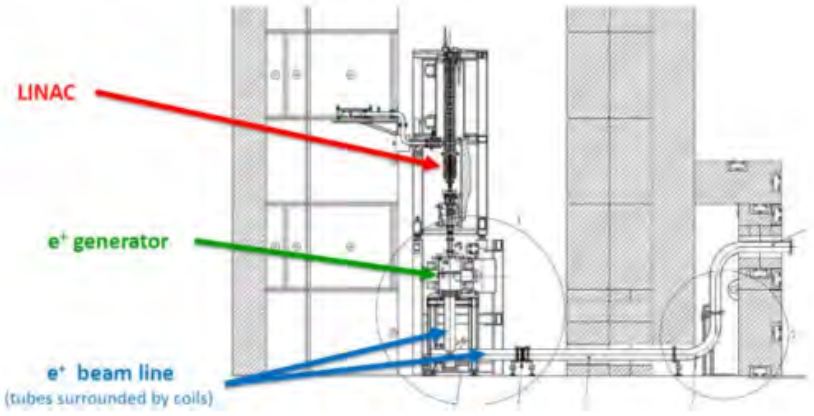

Figure 2.4 Sketch of the linac mounted above the positron tungsten target and moderator inside the GBAR bunker [107]

Since the energy of the newly generated positron is too high, the tungsten target includes a tungsten mesh moderator [108]. Positrons injected into tungsten are slowed down in the metal to thermal energy. The positrons deeply thermalized are annihilated, while the positrons reaching the surface can be re-emitted in vacuum with a few eV energy. A potential difference is applied to the moderator to define the kinetic energy of the beam for downstream transport.

The beam passes through a magnetic separator that selects only the low energy positrons ($\sim 50\ eV$). The beam is guided outside the bunker along a vacuum line covered with a solenoidal winding generating a axial magnetic field of 8 mT that radially confines the positrons. Finally, a buncher compresses the 2.5 m positron pulse in time to inject it into a finite-length trap cavity.

The linac was constructed for GBAR by NCBJ[2] and installed in January 2017 and the first e^+ pulses were generated in November 2017. A average preliminary flux of 3.4 10^5 $e^+/bunch$ was measured.

[2]Narodowe Centrum Badań Jądrowych, Swierk, Poland.

Buffer-Gas Trap

The first step of the positron stacking is carried out using a buffer gas trap (BGT) filled with N_2 gas. Developed by Murphy and Surko in 1992 at the University of San Diego [109], it consists of a 0.1 T Penning-Malmberg trap made of three stages. A scheme of a BGT is shown in Figure-2.5. Positrons are cooled by Coulomb interactions with the electrons of the N_2 molecules. The design of the electrodes and of the vacuum chambers was chosen to optimize the differential pumping. When a maximum of positron bunches have been stacked, the plasma is compressed using the rotating wall technique[3]. The latter consists of inducing angular momentum to the plasma in order to reduce its radius (see Ref.-[113]).

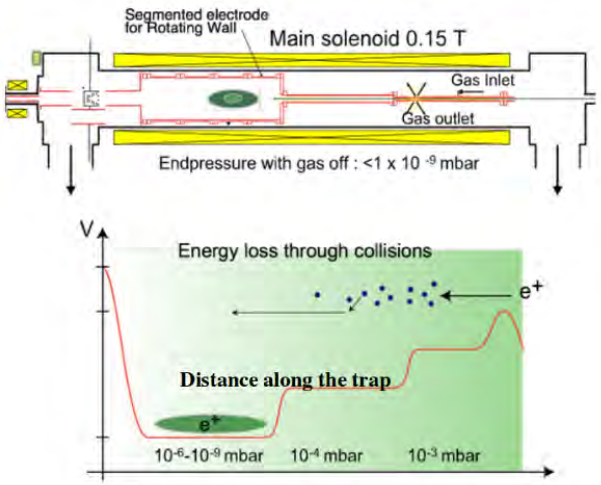

Figure 2.5 Principle scheme of the buffer gas trap. The positron are injected from the left.

Accumulation Trap

The pressure in the last cavity of the BGT is too high for positron accumulation which requires long storage time. Once the rotating wall technique applied, the positrons are sent to a cryogenic 5 T Penning-Malmberg trap. A picture of the trap is displayed in Figure-2.6. Details can be found in Refs.-[114, 115].

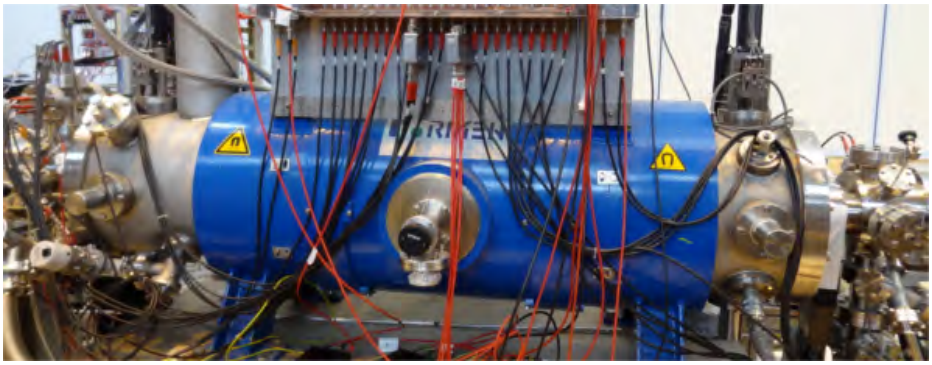

Figure 2.6 Picture of the positron accumulation trap.

[3]Details about this technique can be found in plasma literature like in Refs.-[110, 111, 112].

2.2.2 Reaction Chamber

After accumulating about 10^{10} positrons, the plasma is ejected from the trap with an energy of about 5 keV. It is focused through electrostatic optics onto a silicon cell to produce *positronium*. This cell, named *positron-positronium converter* (*PPs*, also referred as *reaction chamber*), is a bar with an effective rectangular cross section of 1 mm^2 (antiproton beam view) and is 20 mm-long. It is composed of silicon coated inside with nanoporous silicon oxide (SiO_2). A schematic of the reaction target is shown in Figure-2.7.

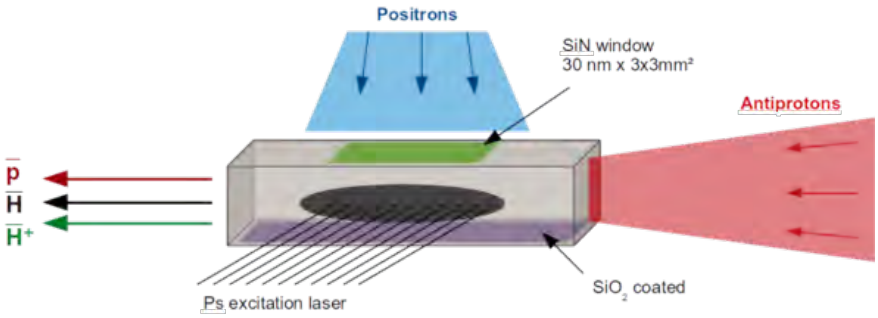

Figure 2.7 Sketch of the $\bar{p} - Ps$ interaction region.

Positrons extracted from the storing trap pass through a first windows made of 30 nm of silicon nitride (SiN), transparent to 5 keV positrons. Thus, they hit the opposite wall of the cell coated with SiO_2. In recent years, the potential for nanoporous insulator materials to be used as highly efficient Ps converters has been recognized and extensively studied [116]. When e^+ are implanted into such a material at kinetic energies of a few keV, they scatter off atoms and electrons in the bulk and are slowed to eV-scale energies within a few ps. With efficiencies of a few tens of percent, the slow positrons capture bound electrons, which tend to accumulate in defects of the material. In the pores, Ps repeatedly bounces off the cavity walls and eventually approaches complete thermalization with the target material. Figure-2.8 shows typical scenarios for the production of positronium in the converter.

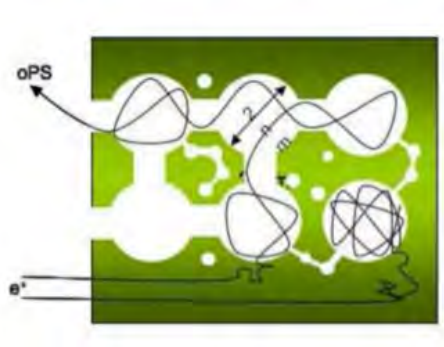

Figure 2.8 Schematic of the ortho-positronium formation principle in the PPs converter. From Ref.-[117].

Two types of positronium atoms are synthesized corresponding to the relative orientations of the spins of the electron and the positron. An anti-parallel spin state $S = 0$, called *para-positronium* (*pPs*),and a parallel spin state $S = 1$, called *ortho-positronium*

(oPs). Both positronium states are meta-stable and annihilate after some time. The main difference between these two states is their lifetime. Para-positronium has a lifetime of almost 250 ps, and does not exist long enough to react with antiprotons. Per contra, ortho-positronium with a lifetime of approximately 150 ns is therefore more favorable to react to form antihydrogen. A 30% efficiency for oPs conversion has been measured with positrons of 3 keV and less [118, 119].

The production of H^+ ions is initiated by the injection of an antiproton pulse into the conversion target, via the two successive reactions Eq.-(2.2) and Eq.-(2.3).

The cross section of the first reaction was measured with its matter equivalent reaction $p + Ps \longrightarrow H + e^-$ for energies of the order of 10 keV for the proton. It is estimated for lower energies in Ref.-[106]. Inversely, the cross section of the second reaction was not measured but estimated for its matter equivalent reaction $H + Ps \longrightarrow H - + e^+$ in the order of 10^{-16} cm^2 [120].

The cross section of the double reaction is shown in Figures-2.1 respectively. The cross section of the second reaction can only occur for $\bar{H}$ atoms with energies higher than 6 keV with ground state Ps. This cross-section increases if the positronium is in an excited state. The laser excitation of the Ps is then investigated as a serious solution to increase the $\bar{H^+}$ production for the states $n = 3$ and $n = 2$.

At CERN, the converter assembly and commissioning is currently in progress. Since the PPs converter is at the crossroad of the positron beam, antiproton beam and laser beams, it has to take into account the different mechanical and electromagnetic constraints. In fact, the converter must be located downstream of the positron storing trap, away from its fringe field influence, in order to not reduce the lifetime of the oPs states [120]. At the same time, the reaction chamber has to be aligned on the antiproton path.

2.2.3 Capture, cooling and free-fall

Capture and precision traps

As detailed in Ref.-[121], $\bar{H}^+$ ions are guided, decelerated[4] and captured into a RF linear trap using sympathetic cooling with laser cooled Be^+ ions. For this purpose, Be^+ ions are loaded into the RF trap and undergo a Doppler laser cooling using UV light at 313 nm. The low-energy Be^+ ions ($\sim$ mK) organize by forming a Coulomb crystal, as shown in Figure-2.9.

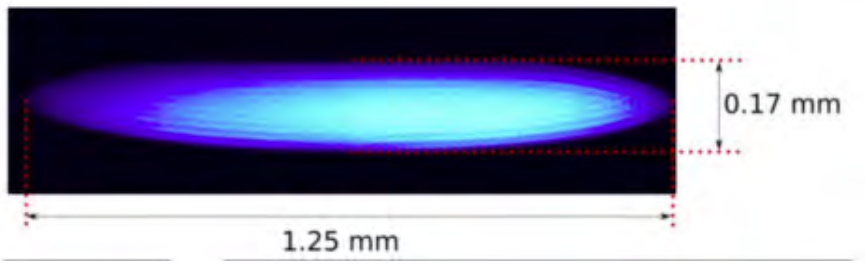

Figure 2.9 Photograph of cold Be^+ ($\sim$ mK) crystals with 4500 ions trapped [107].

[4]The final deceleration process is still under investigation. Hints show that a similar Pulsed Drift Tube technique (this thesis) could be used.

The $\bar{H}^+$ ions arriving from the side of the crystal, loose energy via coulomb interaction with the cooled Be^+ ions. The light ions such as $\bar{H}^+$ tend to concentrate at the center of the coulomb crystal when the heavier ones (Be^+) remain on the periphery. Intensive simulations [122] showed that the capture efficiency of the $\bar{H}^+$ ions is enhanced using specific mass ratios. The possibility of using an intermediate ion species such as HD^+ ions between the Be^+ and $\bar{H}^+$ ions is under investigation. The use of such an intermediate species[5] would reduce the required cooling time (according to [122] $t_{capt} \propto N_{ions}^{-\frac{4}{3}}$).

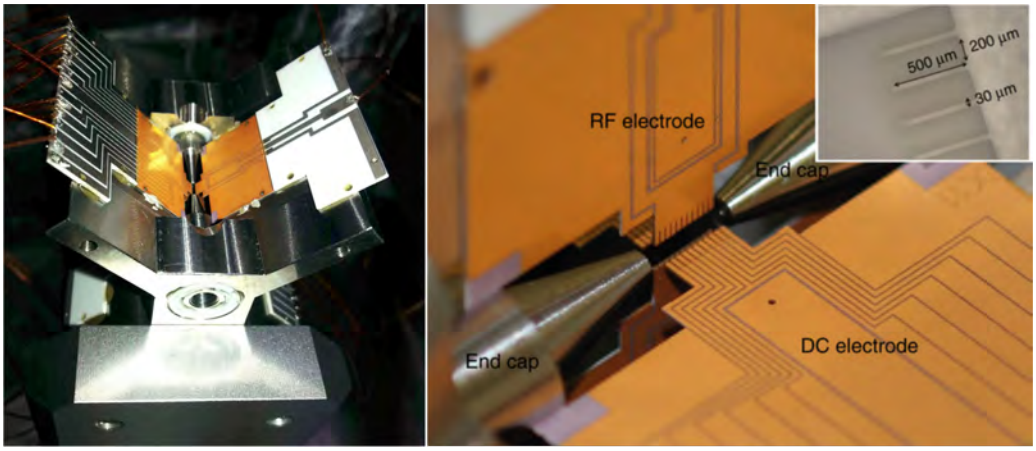

Figure 2.10 Picture of the precision trap (*left*), details on the cavity and x-shaped electrodes of the precision trap (*right*). The gap between the end caps is almost 2 mm [123].

After the capture trap, the $\bar{H}^+$ trip ends in the *precision trap*. The latter consists of an x-shaped, gold coated, micro-fabricated chip trap as shown in Figure-2.10. The x-shaped chips provide a RF trapping field for radial confinement and two DC endcaps for longitudinal confinement. In the trap cavity, Raman sideband cooling is applied, preparing the $\bar{H}^+$ ions in the vibrational ground state at $\sim 10\ \mu K$ (respectively : $\sim 1\ neV$ energy). At the end of all the successive cooling processes, the velocity dispersion of the $\bar{H}^+$ ions is expected of the order of 1 m/s.

Finally, a quasi-at rest $\bar{H}$ atoms are obtained by photo-detaching the excess positron of the $\bar{H}^+$ ions. The laser pulse generating the excess positron ejection, initiates the free-fall time measurement.

Free-fall detection

The capture and precision traps are maintained inside a detection chamber. The design of which is shown in Figure-2.11. A small electrostatic quadruple bender deviates the beam, transported from the reaction chamber, with a 90° angle. This chamber has been designed to sustain UVH vacuum, a homogeneous low magnetic field required for Raman cooling and a high radiation transparency. The chamber is about 1 m tall.

The free-fall is initiated with the photo-detachment laser. The newly produced $\bar{H}$ atoms fall into the chamber and annihilate hitting the bottom plate of the chamber. The chamber is surrounded by several layers of detectors. They detect the position and time of the exiting pions coming from the annihilation of the antiprotons.

Two types of detectors are used. The first ones are Micromegas-type gaseous detectors. Such detectors have a high spatial resolution, but a low time resolution. Three layers

[5] A 10% HD^+ and 90% Be^+ mixture is also considered.

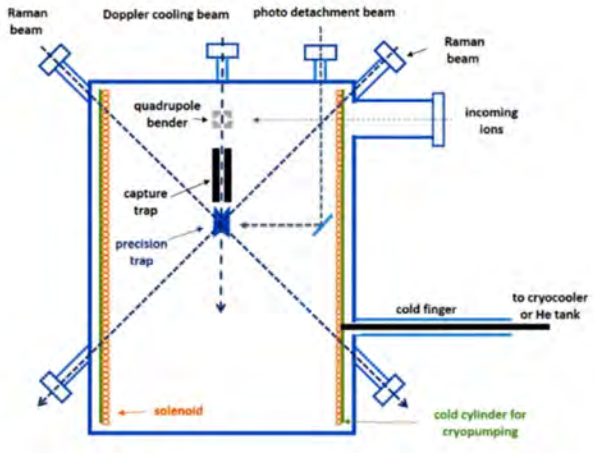

Figure 2.11 Sketch of the free-fall chamber housing the capture and precision traps. The Raman laser beams, the magnetic shielding and the cryo-cooling system are indicated [124].

of Micromegas detector are used to reconstruct the path of the pions to localize the annihilation position. The second are plastic scintillators, with a low spatial resolution but with a high time resolution. These detectors are used to trigger the passage of the pions and reconstruct the free-fall time considering the pion time-of-flight delay. The high resolution of the plastic scintillator allows removing background events such as cosmic rays.

2.2.4 Antiproton decelerator (this thesis)

While the positron beams are being prepared, the $\bar{p}$ are being decelerated in the AD/ELENA to 100 keV.

In the experimental proposal [94], the GBAR collaboration accepted an innovating electrostatic decelerating system whose central element is a *Pulsed Drift Tube* (PDT) decelerating the ion bunches and selecting the downstream energy of the beam. Such a deceleration technique for antimatter has been mentioned for the very first time by Nieto and Goldman in reference-[125].

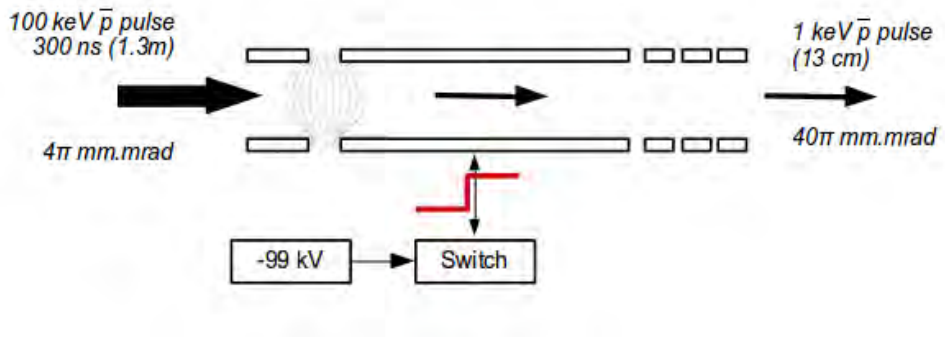

Figure 2.12 Principle scheme of the GBAR decelerator.

Transported at ground potential, the antiproton pulse slows down facing the strong electric field at the entrance of the drift tube. Passing though it, particles reach a local

flat potential distribution and are no longer influenced by strong electric gradients. As illustrated in Figure-2.12, the tube is then switched from a given potential V_{PDT}[6] to ground while they are inside. When exiting the drift tube, antiprotons do not see a re-accelerating potential and retain their residual energy [126] calculated as $E_r = E_i - V_{PDT}$ where E_i and E_r are the initial and residual energies.

The design of the decelerator is inspired from an existing cooler and buncher system used on the ISOLTRAP experiment [127]. In this setup, a 60-keV exotic ion beam is retarded to an energy of a few eV by mean of an electrostatic decelerating field and injected into a linear radiofrequency quadrupole ion trap (*RFQ trap*) filled with a buffer gas.

The ions ejected from the trap fly out with a kinetic energy of a few eV but with an electrostatic potential energy of 60 keV due to the potential reference of the trap. Since the beam travels through the rest of the ISOLTRAP setup at ground potential, a pulsed cavity ensures the transition from the high voltage part to the ground one without any re-acceleration. Because of the need for low-energy injection, all Penning trap facilities use such a device.

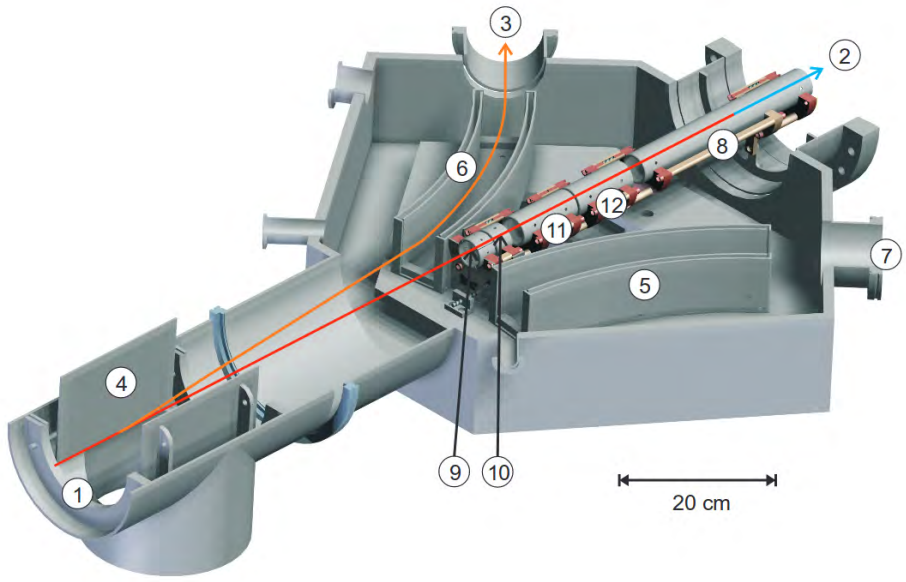

Figure 2.13 Sketch of the switchyard and the pulsed drift tube assembly from the TRIGA-TRAP apparatus [128]. (*1*) Incoming ion pulse, (*2-red line*) 30 keV energy beam and (*blue line*) 1.1 keV energy beam, (*3-orange line*) 30 keV energy bent trajectory, (*4*) horizontal deflector plates, (*5,6*) curved deflectors, (*3,7*) switchyard left and right ports, (*8*) PDT, (*9*) deflector, (*10*) grounded electrode and (*11,12*) deceleration lenses.

A good example of such operational technique can be found in Ref.[128]. For the TRIGA-TRAP experiment, ion bunches delivered at 30 keV are injected into a switchyard chamber. A *Pulsed Drift Tube* (PDT) is used in order to improve the efficiency of trapping by slowing down the ion beam from 30 keV to almost 1 keV. Such apparatus is shown Figure-2.13.

[6] In the case of the GBAR experiment with an expected 1 keV antiproton beam, $V_{PDT} = -99\ kV$.

In all the previous apparatus, a particular attention has been devoted to optics. The decelerating drift tubes are key elements to select the downstream beam energy and/or to ensure the transition between two different electrical potential references along the beam path. One should anyway keep in mind that changing the beam energy impacts the optical properties of the traveling ions. The electric field gradient at the entrance of the PDT leads to a strong focusing of the beam. We will show later that solutions exist to counterbalance this effect.

Following an approach akin to the TRIGA-TRAP experiment which uses two lenses, a design made of a series of six electrostatic, cylindrical lenses followed by a 40 cm-long pulsed drift tube has been proposed in the GBAR framework. Initially held at $-99\ kV$, the PDT is switched to ground and delivers a 1 keV antiproton beam to the rest of the experiment. We show in the following section, that the number of electrodes and the potentials applied on them, and the size and length of the Pulsed Drift Tube can be determined with respect to the properties of the incoming beam in order to maximize the transmission of the antiprotons through Ps converter downstream. Options to decelerate antiprotons to 2 keV and 6 keV have been also investigated to perform spectroscopic measurements. First, in order to clearly understand how does a potential variation impact the beam propagation, the next chapter will come back to electrostatic basics.

Chapter 3

Simulations and electrostatic basics

Electrostatic beam optics are of great importance in low energy electrostatic accelerators. Developed from 1930 to 1955, the theory of electrostatic has been abandoned in favor of simulations made possible by the increase of computing power. However, numerous descriptions and introduction to matrix formalism are available in literature like References-[129, 130, 131, 132, 133][1].

In this chapter, we will introduce the calculation methods used to determine the potential either via the SIMION software[2] or via analytical approximations. Subsequently we will focus on the electrostatic formalism concerning the GBAR decelerator. We will see the impact on the energy of the beam and the ion trajectories. Finally we will arrive at the limits of the study from basic electrostatic simulations.

3.1 Numerical implementation

As detailed in Reference-[134], SIMION is an electrostatic and magnetic field modeling program. It is designed to model the electrostatic and magnetic fields and forces created by a collection of shaped electrodes under given symmetry assumptions. Electrostatic and magnetic fields can be modeled by boundary solutions of partial differential equations, such as *Laplace's equation* or *Poisson's equation*. It may also integrate (when necessary) collective phenomena, such as space charge, occurring within a charged particle beam.

SIMION is renowned in the low energy ion and trapping community. It is interesting here to detail the operation and the methods used by the SIMION software because, as we will see later in this chapter, the main decelerator simulation program has been implemented in Python based on the SIMION software.

3.1.1 Electric Field Calculation

In the past, the solutions of Laplace's equation were provided by a variety of techniques such as resistor networks, conducting paper, electrolytic tank, magnetic analog or conformal transformations[3]. Nowadays, with the explosion of the computation power, numerical methods such as finite-difference or finite-element techniques are achievable.

SIMION is reputed for its efficiency in studying electrostatic optics thanks to a powerful and adaptable calculation of *potential maps*. The computation of such maps is based on a specific finite-difference technique called *over-relaxation*. We won't go into further

[1] These references do not constitute an exhaustive list.

[2] The representations of the ion trajectories in the rest of this work were made from this software.

[3] Chapter 1.1 and 1.3 of Reference-[131], give further details about the mathematical and experimental methods for resolving the Laplace's and Poisson's equation.

details about the suffix 'over', specific to a refinement method speeding up the calculation. Let's focus on the general principle of the so-called *relaxation method*.

The relaxation technique relies on the representation of a $2D$ or $3D$ space by a square base mesh whose nodes carry the value of the local potential. An iterative process computes on each node a new estimate of the potential according to the values on the nearest neighbor nodes. In a classical $3D$ projection, the new estimate is the average value of the six nearest neighbors.[4] In the case of the GBAR decelerator, it is more convenient, in order to save calculation time, to reduce the $3D$ problem to a $2D$ representation including a rotational symmetry. In such representation, since the four nearest points do not contribute equally, a scaling function has to be introduced concerning the radial components.

At the first iteration, the potential on the nodes corresponding to the position of the polarized electrodes is set to a parametric $1\ V$ value. If the electrode is usually grounded, the potential value on the corresponding nodes is set to $0\ V$. The nodes corresponding to electrodes (polarized or grounded) stay fixed during the computation. Over the successive iterations, each nodes is scanned and the potential value it carries is updated with respect to the values on its nearest neighbors. The potential value on each point (except those corresponding to an electrode) change less and less between two successive iterations. The iterative process ends when this change is smaller than a given value. In the case of the GBAR decelerator, the threshold has been set to 10^{-7}.

This iterative process is repeated independently for each charged electrode. A standard potential map is thus generated and stored in separate files. The general potential map is based on the additive solution property of the Laplace's equation. In other words, for each node of the mesh the value of the general potential is the sum of the individual potentials generated by each electrode weighted by the value of the applied voltage.

An important point about the general potential map is the mesh size. Indeed, the smaller the mesh, the more accurate the value of the potential is during the calculation of the trajectory. Unfortunately, the smaller the mesh size and the longer the relaxation calculation time is[5]. In the case of a small mesh size, the search of the potential value in the map is also slightly slowed during the calculation of the trajectory. The impact seems minimal but the very large number of calls causes a noticeable slowdown.

3.1.2 Trajectory computation

Another element to consider in the simulations is the trajectory calculation method and the importance of the initial conditions.

The calculation of the ion trajectory is based on a classical numerical integrator known as the *classical Runge-Kutta method at 4th order* or *RK4* [135, 136]. Such numerical integration method evaluates iteratively the value of a function f, solution of an ordinary differential equation, by temporal successive steps.

The RK4 method is applied twice per step. First, for the integration of the instantaneous speed of the particle. Second, for the integration of the position of the particle. The only force the particles experience is the Lorentz force: $\vec{F} = q\vec{E}$. Then, the evolution of the kinetic variables (acceleration, speed and positions) is deduced from the variation of the potential[6] in the map from the initial position and speed of the particles.

[4] Specific conditions are applied for the nodes on the borders of the mesh following either the Neumann or Dirichlet boundary conditions.

[5] The bigger the size of the storage files as well.

[6] This corresponds to the value of the electric field.

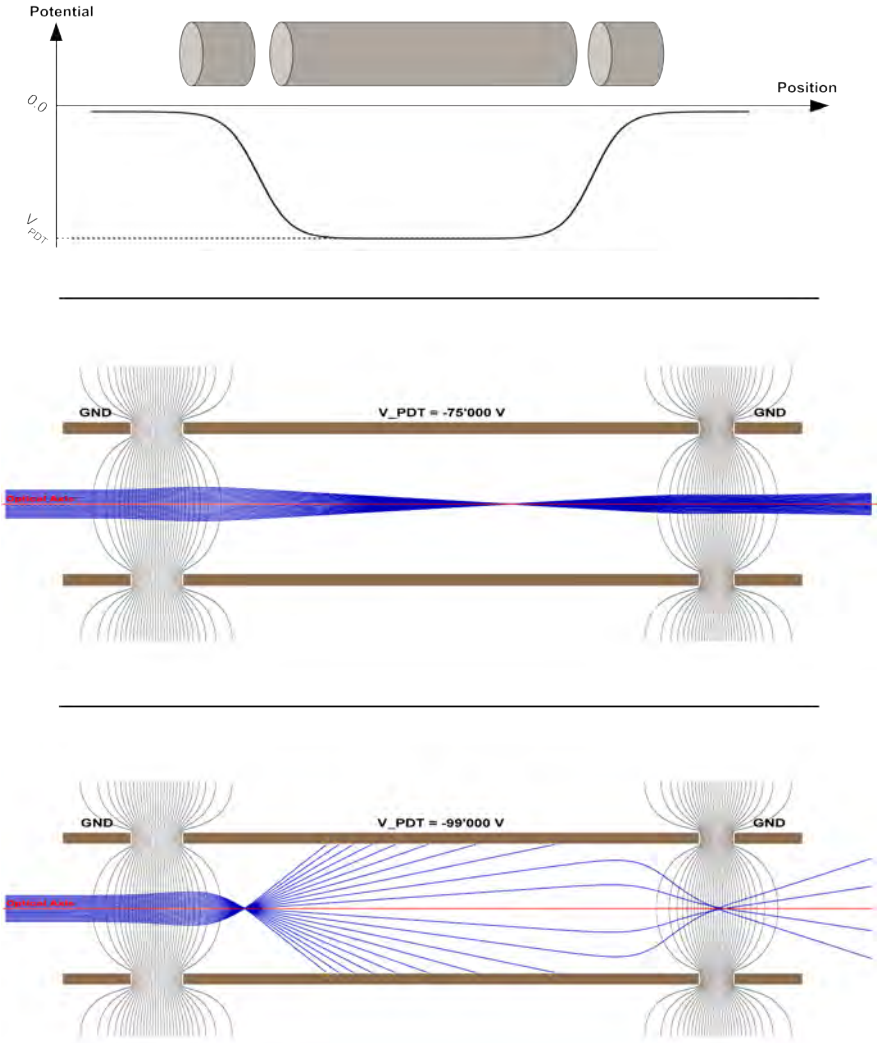

Figure 3.1 (*top*) - Shape of the potential applied on a decelerating tube without switching it to ground. The outermost cylinder electrodes are grounded while the long middle electrode is held at V_{PDT}. The beam travels from left to right. (*middle*) Trajectories of a parallel uniform beam of 100 keV-energy antiprotons through the drift tube polarized at $V_{PDT} = -75\ kV$. Simulated using the SIMION software. (*bottom*) Trajectories of a parallel uniform beam of 100 keV-energy antiprotons through the drift tube polarized at $V_{PDT} = -99\ kV$. Simulated using the SIMION software.

3.2 Electrostatic basics

The accelerating, respectively decelerating, tube lens is a central element of electrostatic ion optics. Figure-3.1 presents two illustrative electrostatic configurations. The paths of $\bar{p}$ particles at exactly 100 keV passing through decelerating tubes polarized at $-75kV$ and $-99kV$ are shown. Here, the beam is idealized by 20 particles homogeneously spaced flying parallel. The entire system is composed of three coaxial cylinders with the same inner radius $R_{in} = 50\ mm$. The outermost electrodes are grounded, the central and longest one is held at potential V_{PDT}. Hereafter, the PDT notation is used even if the drift tube (DT) is initially studied with static potential.

Let's concentrate on the effects on the beam while entering into the polarized decelerating tube that corresponds to the region where the influence of the electric field is the highest. Figure-3.1 shows that the trajectories of the reference ions, originally parallel, is modified by the presence of the strong electric field. Through the first grounded electrode, antiprotons experience a radial force tending to deflect them away from the optical axis, whereas inside the decelerating tube the radial force is directed inward.

We also clearly see from Figure-3.1 (*middle*) that the intensity of the radial component of the field (outward first and then inward) increases with the distance from the optical axis. Indeed, the outermost particles of the bunch suffer a more important deviation than the innermost ones. The combination of the radial dependence of the electric field and the deceleration of the test particles leads to a convergence of the trajectories onto a point called *focal point* or *image point*.

It is worth pointing out that the trajectory of the particles through this electrostatic system is reversible. Thereby test particles flying out the decelerating tube experience an inward force in a first time and are slightly deflected away in a second time. Since they are slower inside the drift tube than outside, the focusing effect is again dominant. This particular case appears in Figure-3.1 (*bottom*) on the right panel of the simulation where the beam is refocused while exiting the drift tube.

Both reasonings applied upstream and downstream the decelerating tube demonstrate that for the same incoming beam energy, the higher the potential difference and then the stronger the electric field, the greater the deflection angle of the deviated particles. Here is the obvious proof that the electric field gradient at the entrance (resp: exit) of a polarized Drift Tube acts as an electrostatic lens. Example Figure-3.1 shows that the one-electrode deceleration leads to important losses. Since the energy of the antiprotons from ELENA (100 keV)[7] is fixed, other optics have to be placed upstream of the decelerator to prevent the beam from blowing up. In a latter section, a more detailed electrostatic study about the pre-decelerating and post-decelerating optics is discussed.

3.2.1 Paraxial-ray approximation

We could try to find an approximated analytical solution of the potential inside the drift tube and deduce the applied force along the particle trajectory. Let's take a general rotational symmetric solution of the Laplace equation $\Delta V = 0$ with :

$$V(r, \phi, z) = \sum_{n=0}^{\infty} (-1)^n \frac{V^{(2n)}}{(n!)^2} \left(\frac{r}{2}\right)^{2n}$$

The potential $V(z, r)$ at radius r of an axially symmetric potential distribution is given

[7] And also latter, for the 10 keV protons generated from the internal GBAR source

by the potential $V(z,0)$ along the optical axis following:

$$V(z,r) \;=\; V(z,0) - \frac{r^2}{4}V''(z,0) + \frac{r^4}{64}V^{(4)}(z,0) - ... \tag{3.1}$$

with $V''(z,0)$ and $V^{(4)}(z,0)$ the second and forth derivative of the potential along the optical axis.

Studying particle trajectories with small angles close to the axis, we can consider the second derivative only:

$$V(z,r) \;=\; V(z,0) - \frac{r^2}{4}V''(z,0) \tag{3.2}$$

The radial force acting on the antiprotons is by definition:

$$F = qE_r = q\frac{\partial V(z,r)}{\partial r} \tag{3.3}$$

Using equation (3.2), the radial gradient becomes:

$$F(r,z) = -\frac{qr}{2}V''(z,0) \tag{3.4}$$

Equation (3.3) and (3.4) show that the radial force applied on a charged particle is proportional to the distance from the optical axis and to the second derivative $V''(z,0)$.

From there, it is possible to establish the equation of motion for a particle traveling on a parallel initial trajectory and at a small radius r from the optical axis into an axisymmetric electric field. This particular case is better known as the paraxial-ray approximation. From (3.4), it is easy to express the Newton's second law of motion [54]:

$$m\ddot{r} = q\frac{\partial V}{\partial r} = -\frac{qr}{2}V''(z,0) \tag{3.5}$$

With :

$$\dot{r} \;=\; r'\dot{z} \tag{3.6}$$

$$\ddot{r} \;=\; r''(\dot{z})^2 + r'\ddot{z} \tag{3.7}$$

where in the small angle approximation $\dot{z}$ is the total velocity and $\ddot{z}$ the instantaneous acceleration in the z-direction.

According to the definition of the electrostatic potential energy and the kinetic energy of a charged particle, $(\dot{z})^2 = 2\eta V(z,r)$ where $\eta = q/m$. If $\ddot{z}$ is the acceleration of the particle in the z direction, we can express it as $\ddot{z} = \eta V'(z,r)$. Replacing into (3.7) and combining with (3.5) in the limit of small radius ($r \approx 0$), it becomes,

$$r'' + \frac{V'(z,0)}{2V(z,0)}r' + \frac{V''(z,0)}{4V(z,0)} = 0 \tag{3.8}$$

A good remark from Ref.[137] is that η doesn't appear in 3.8. Thus, if the mass m or the charge e influence the trajectory of the considered ions, η does not. For instance with $e >> m$, two negatively singly-charged particles (like an antiproton and an electron) undergo the same deceleration and follow the same trajectory through the same potential gap.

Another important element as pointed out by the autors of Refs.[138] and [137] is in the case of two semi-infinite electrodes when particles are flying through the gap. Changing the electrostatic reference by increasing the potential on both electrodes in the same proportion does not modify the shape of the trajectory. It confirms the assumption that only the difference of potential acts on the ion trajectories.

3.3 Electric field at the ends of the Drift Tube

Finding an explicit expression for $V(z,0)$ is something complex because there are no or few models applicable to most electrostatic optics. No ideal analytical solution exists even for one of the simplest electrostatic lenses like the 'Einzel' lens[8]. However, under well-chosen assumptions, it is possible to approach a mathematical solution for $V(z,0)$.

The GBAR decelerator has the advantage of presenting a complete rotational symmetry. A reference method created by Sidney Bertram in 1940 [139, 140] gives an approximate function of $V(z,0)$ in good agreement with numerical solutions as computed by softwares like SIMION. In the configuration shown in Figure-3.1, the gap between the first electrode at ground and the drift tube can be simplified as between two semi-infinite tubes of unit radius R separated a distance S with a potential $V1$ applied on the left tubes and $V2$ on the right one.

A general solution for such electrodes using the Bertram's method is given by:

$$V(z,0) = \left(\frac{V_1+V_2}{2}\right) + \left(\frac{V_2-V_1}{2\omega S}\right) log_e \frac{cosh\ \omega z}{cosh\ \omega(z-S)} \tag{3.9}$$

with $\omega = 1.318$, when $R \neq 1$ then ω becomes $\frac{\omega}{R}$.

A simpler form is found by considering $S \to 0$:

$$V(z,0) = \left(\frac{V_1+V_2}{2}\right) + \left(\frac{V_2-V_1}{2}\right)\ tanh(\omega z) \tag{3.10}$$

This hypothesis remains valid for $S \neq 0$ at a scaling factor, if S is small enough compared to the inner diameter of the tubes[9]. The first and second derivatives are deduced from (3.10):

$$V'(z,0) = \frac{V_2-V_1}{2}\omega\ sech^2(\omega z) \tag{3.11}$$

$$V''(z,0) = -(V_2-V_1)\omega^2\ tanh(\omega z)\ sech^2(\omega z) \tag{3.12}$$

On Figure-3.2, a comparison between the SIMION software and the previous analytical formulas is carried out on both ends of the drift tube. The agreement between the curves and the simulated data is really good. The shaded span highlighted the position of the electrodes. The organization follows the GBAR decelerator design including an upstream electrode 80 mm-long, the drift tube 400 mm-long and a downstream electrode 40 mm-long. The gap between the electrodes and the drift tube on both side is 30 mm. From the electrostatic point of view, the drift tube is held at $-99\ kV$ [10] while the outermost electrodes are kept to ground.

It is interesting to note that the trajectory of the ions as discussed in the previous section and represented in Figure-3.1, finds all its physical meaning through the shape of the second derivative as plotted on Figure-3.2 (*bottom plot*). Taking into account its charge, it is evident here that the radial force applied on an off-axis antiproton is proportional to the product of the distance to the optical axis and $V''(z,0)$. This latter is negative on the left side of the first gap ($z < 5650\ mm$) meaning that an outward force applies and positive on the right side of the same gap ($5650\ mm < z < 5800\ mm$) resulting in an inward force.

[8] An 'Einzel' lens is an electrostatic device made of 3 successive, cylindrical electrodes.
[9] In the decelerator, $\emptyset = 100\ mm$ and $S = 30\ mm$.
[10] The plotted curve for the potential is in absolute value.

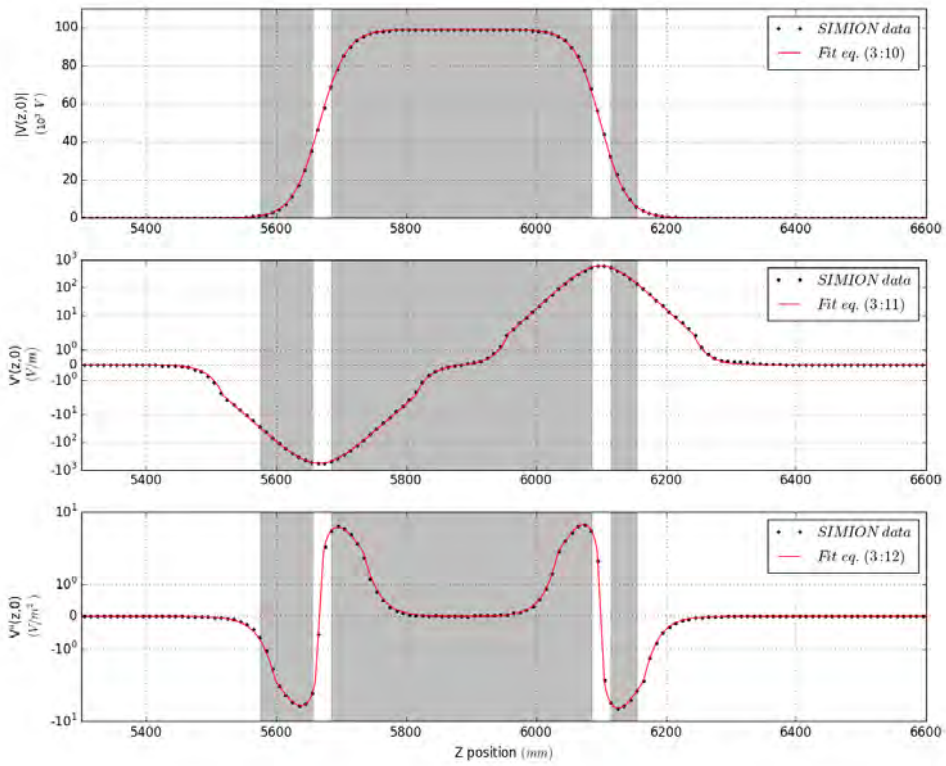

Figure 3.2 Simulated shape of the axial potential $V(z,0)$ (absolute value, *top*) and its first (*middle*) and second derivatives (*bottom*) computed with the SIMION software. For the derivative plots the y-axis is in symmetric logarithmic scale. The gray spans represent the position of the drift tube and on both side the grounded electrodes. The red lines correspond to the fit of the SIMION data using equations (3.10), (3.11) and (3.12).

3.4 Energetic study of the Drift Tube

The definition of the potential along the optical axis through the drift tube offers the possibility to approach the electrostatic deceleration principle from an energetic point of view. It relies on the difference between the initial kinetic energy of an incoming antiproton with respect to the electric potential energy it experiences locally inside the drift tube when this latter is switched to ground. That's why inhomogeneities of the potential map inside the tube impact the energy distribution of the particles downstream.

Since the GBAR antiproton line is based solely on electrostatic optics, the energy spread is of crucial importance. As mentioned above, two particles with different energies do not follow the same path when passing through the same electrostatic lens. The energy distribution of the beam causes optical aberrations referred as *chromatic aberrations*. For instance, a fast antiproton would be less deflected than a slower one through successive lenses. The greater the energy spread, the greater the chromatic aberrations within the particle bunch, and the bigger the beam spot when focusing onto a target as illustrated on Figure-3.3. In GBAR, worsening the energy distribution while decelerating further reduces the transmission rate through the silicon converter and directly impacts the $\bar{H}^+$ production.

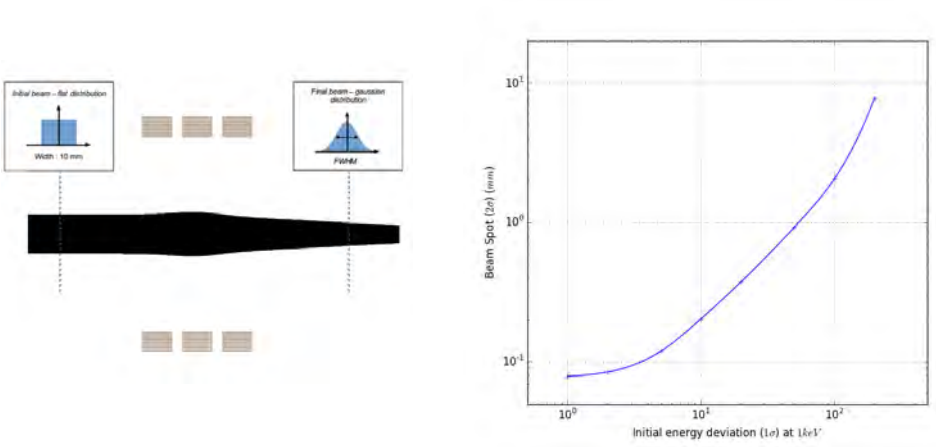

Figure 3.3 Illustration of the chromatic aberration effects in the case of an Einzel lens, performed with SIMION. The beam, flying from left to right, is initially parallel and uniformly distributed over a radius $r = 5\ mm$. The energy distribution is considered as a gaussian center on 1 keV. *On the right*, the curve represents the size of the beam (2σ value) after passing through the lens with respect to the initial energy spread.

As discussed in the previous section, the shape of the potential on the optical axis does not follow a perfect square function. According to (3.10), the potential $V(z, 0)$ on the edge of the drift tube tends asymptotically towards V_{PDT} following a hyperbolic tangent behavior, so-called *penetration field*[11]. This means that if the bunch is located on the edge while switching the drift tube to ground, the outermost antiprotons undergo a lower deceleration than the innermost ones. It is interesting to note that the axial profile of the potential always affects the energy spread towards higher energy values. If this latter is higher than the initial energy spread of the beam, the energy distribution will not be anymore symmetric.

Let's now define δd as the depth from the edge of the tube such as illustrated in Figure-3.4. From the potential function (3.10), we can determine the value of δd over which the potential variation due to the penetration field drops to negligible values compared to the energy distribution of the initial beam. The antiproton pulse must penetrate deeper than δd into the drift tube to not suffer a wider spread of the energy distribution. Obviously, the length of pulsed drift tube has to be extended by twice the length δd.

If we assume σ_E, the maximum acceptable energy spread induced by the deceleration at $z = \delta d$ as:

$$\sigma_E = \frac{\Delta E}{E_f} = \frac{(q)\Delta V}{(q)V_f}$$

where $\Delta V = |V(\delta d, 0) - V_{PDT}|$ and V_f, the final virtual potential directly proportional to the energy of the beam downstream the decelerator.

The switching depth δd can be evaluated from:

$$\delta d = \frac{1}{\omega} argtanh(2\sigma_E \frac{V_f}{V_{PDT}} + 1) \tag{3.13}$$

The energy spread σ_E ($\equiv \Delta V/V_f$) induced by the deceleration is plotted on Figure-3.5 (*dashed line*) with respect to the distance δd from the edge of the drift tube in the case of the GBAR experiment. For example, to make sure that the energy dispersion induced by the deceleration is $|\Delta V/V| < 10^{-4}$, the tail of the antiproton bunch should be located

[11] Electrostatic equivalent to the magnetic fringe field.

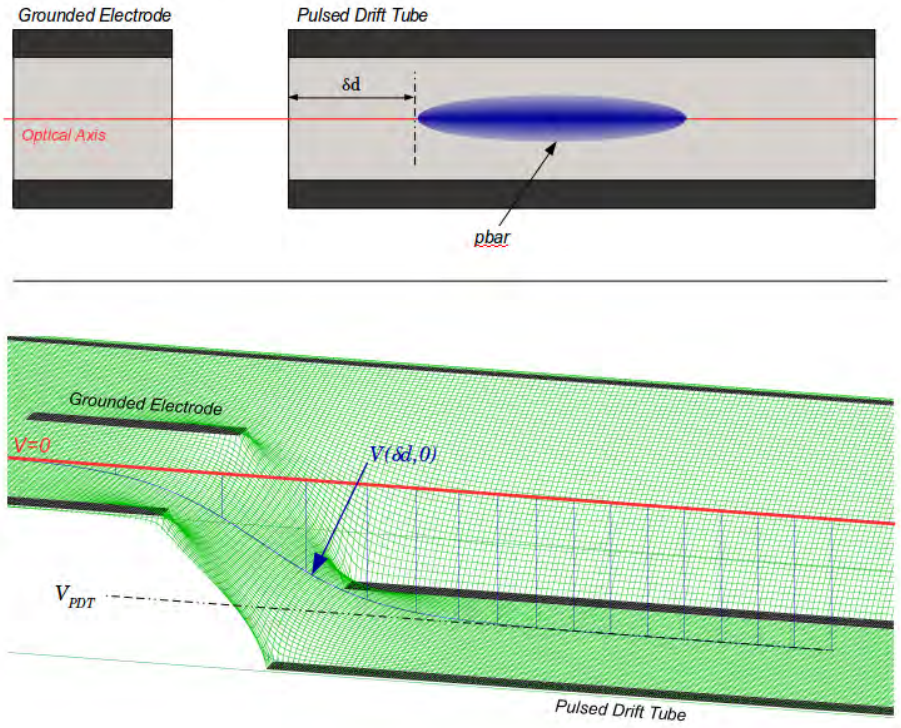

Figure 3.4 (*Top*) - Schematic of the entrance of the drift tube and definition of δd. (*Bottom*) - Potential projection at the entrance of the drift tube and definition of V_{PDT} and $V(\delta d, 0)$.

further than $\delta d = 268\ mm$ from the edge of the drift tube while switching it to ground.

The parameters of the beam provided by ELENA also participate in determining the dimensions of the drift tube. To ensure a constant deceleration, the potential distribution in the drift tube has to remain as flat as possible around $-99\ kV$ over a distance at least as large as the size of the antiproton pulse when decelerated at 1 keV. According to [95], the bunch length is expected to be $\Delta t = 75\ ns$ (r.m.s. value). This latter can be turned into space unit assuming a mean velocity of $v_{(1keV)} = 438\ mm.\mu s^{-1}$. A simple calculation gives a bunch length inside the drift tube of $L_{1keV} = 4\Delta t \times v_{(1keV)} = 131\ mm$ with 2σ significance. In a similar way, we find the bunch length for decelerated beams at 2 and 6 keV such as $L_{2keV} = 186\ mm$ and $L_{6keV} = 322\ mm$.

Let's take the case of GBAR as an example. The initial antiproton beam is expected to be decelerated from 100 keV to 1 keV with an initial energy spread $\Delta E/E = 10^{-3}$. The expected energy variation is then $\Delta E = 100\ eV$. Taking into account the conservative nature of all the forces acting on the bunch[12] while decelerating, the ΔE value should remain the same leading to an energy spread downstream the decelerator of $\Delta E/E_f = 10^{-1}$. Expecting now to decelerate the antiproton bunch without impacting this latter by more than 10% (it means that the energy spread induced by the decelerator should be less than $\sigma_E = 10^{-2}$), the pulsed drift tube in the decelerator should theoretically measure:

$$L_{1keV} + 2 \times \delta d(\sigma_E = 10^{-2}) = 131 + 2 \times 172.4 \approx 476 \text{ mm}$$

[12]The space charge effect and other intra beam scatterings are considered negligible over the 2 m distance of the apparatus.

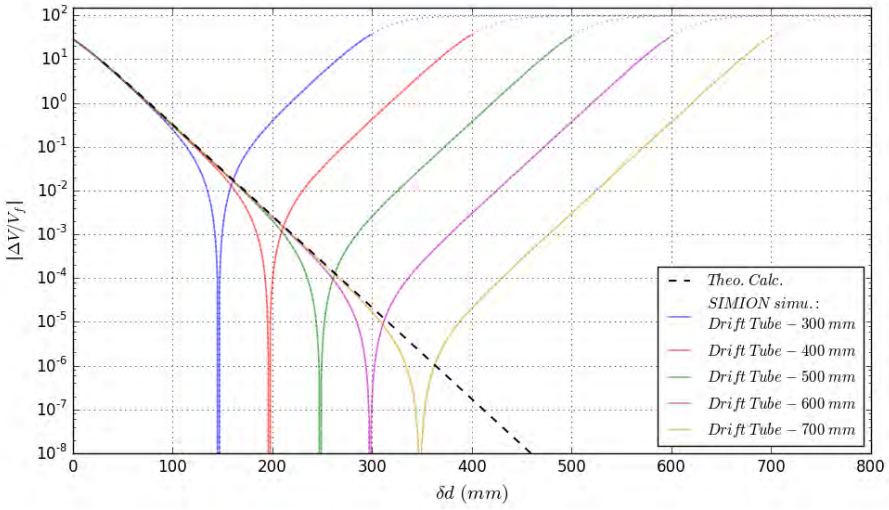

Figure 3.5 Evaluation of the axial potential variation along the pulsed drift tube with respect to the distance δd from the edge of the drift tube. (*dashed line*) - Theoretical estimation for a $R = 50\ mm$ semi-infinite cylinder initially polarized at $V_{PDT} = -99\ kV$. (*solid lines*) - Corresponding simulations of the potential spread for 5 different sizes of drift tubes ($finite\ length,\ R = 50\ mm$) obtained with SIMION.

The relation (3.13) applies only in the case of a semi-infinite, cylindrical electrode. Since working with such an abstract object is impossible, Figure-3.5 illustrates simulated values of $|\Delta V/V_f|$ along tubes polarized at $-99\ kV$ for 5 different finite lengths (300, 400, 500, 600 and 700-mm). We can see that the variation of the potential is in good agreement with the theoretical prediction over the first centimeters in all cases before diverging due to the symmetry of the system. The divergence of the simulated curves in the logarithmic scale marks the middle of the drift tube where $\Delta V = 0$. Taking into account that the antiproton bunch must be at the center of the drift tube while switching it to ground, we can evaluate in the different cases the maximum energy spread it would suffer.

One should keep in mind that the same reasoning applies radially. The potential deformations near the surface of the drift tube induces energy variations as well. This time, since the potential is smaller on the optical axis than in the vicinity of the electrode, the energy distribution is affected towards smaller energy values. The impact of the radial profile of the potential on the energy distribution is however much less important than in the axial case, as shown in Figure-3.6.

In the case of the GBAR decelerator, knowing that the antiproton bunch is 131 mm-long, 10 mm-large at 1 keV inside the 400 mm-long drift, the minimal energy spread is $\sigma_{E,L} \sim 10^{-1}$ axially and $\sigma_{E,R} \sim 5.10^{-4}$ radially. Adding to this the displacement during the 25 ns of switching time corresponding to $\delta d_{switch} = 11\ mm$, ie $\sigma_{E,switch} = 1.10^{-1}$.

It corresponds to an energy downstream the apparatus of :

$$E_f = 1000\ keV\ \pm 100\ eV\ (initial\ spread) \quad \pm {}^{90}_{0.5}\ eV\ (deceleration\ spread) \quad \pm {}^{90}_{0}\ eV\ (switching\ spread) \tag{3.14}$$

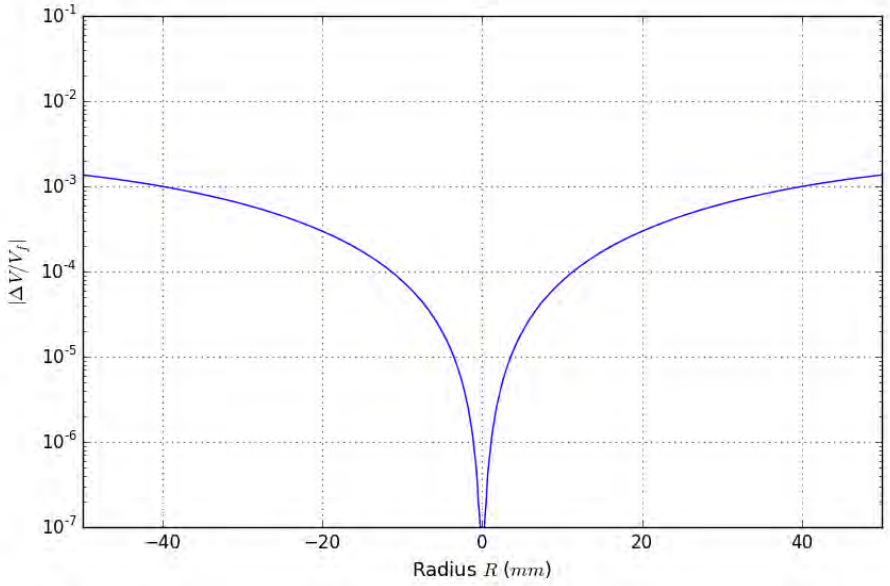

Figure 3.6 Evaluation of the radial potential spread inside the pulse drift tube with respect to the radial position. Simulated for a 400 mm-long drift tube polarized at $V_{PDT} = -99\ kV$. The values are extracted at the middle of the tube ($\delta d = 200\ mm$).

Applying a similar reasoning for deceleration at 2 keV and 6 keV:

$$\begin{aligned} &At\ 2\ keV: \quad E_f = 2000\ keV\ \pm 100\ eV\ (i.s.)\ \pm\ {}^{100}_{0.5}\ eV\ (d.s.)\ \pm\ {}^{100}_{0}\ eV\ (s.s.) \\ &At\ 6\ keV: \quad E_f = 6000\ keV\ \pm 100\ eV\ (i.s.)\ \pm\ {}^{1000}_{0.5}\ eV\ (d.s.)\ \pm\ {}^{1000}_{0}\ eV\ (s.s.) \end{aligned}$$

3.5 Pre-focusing system

In the previous section, we investigated the deceleration from an energetic point of view. We now know that the decelerator is able to decelerate an antiproton bunch from 100 keV to 1 keV (respectively: 2 keV and 6 keV) and evaluated the impact on the energy distribution of the antiproton beam. However, a very important question for GBAR remains: how many of the decelerated antiprotons may reach the Ps converter ? It is important to remind here that the lower energy antiprotons, the higher the cross section for the production of antihydrogen ions (as explained in Chapter 2).

As mentioned in the earlier sections, the electrostatic gradient at the entrance of the DT has a similar effect as an electrostatic lens. One should keep in mind that the transmission through the drift tube is even greater when the paraxial approximation is respected. In other words, it is crucial to keep the beam as parallel as possible with the smallest possible spot inside the pulsed drift tube[13].

The potential on the drift tube determines the energy of the particles downstream the decelerator. It is therefore necessary to compensate for the strong focusing effect with the use of an additional optics. As we have already mentioned at the beginning of this chapter, the simplest one is an Einzel lens. It consists of three cylindrical electrodes whose central electrode is polarized and the outermost electrodes kept grounded. Such

[13]If the beam is too wide, it experiences edge effects near the electrode.

an Einzel lens is then placed upstream of the decelerating tube.

As shown in Figure-3.7, the GBAR decelerator consists of cylindrical electrodes with an inner radius of 50 *mm* and an outer radius of 60 *mm*. At first the beam passes through six electrodes, referred as *pre-decelerating electrodes*, the first and forth electrodes are 50 *mm*-long and the others 80 *mm*-long. These six electrodes are mechanically divided in two groups of three electrodes. Subsequently, it passes through a pulsed drift tube 300 *mm*-long in its preliminary design as exposed in the Figure-3.7. In such a design, the gap between all the electrodes is 30 *mm*.

As described in the previous sections, the choice of such a geometry makes it difficult to construct an analytical approach. Then, in order to avoid the use of difficult non-linear solutions, a numerical approach was preferred. At first glance, intensive simulations seem an easy way out, but as we will see in this chapter, they have their share of complications as well.

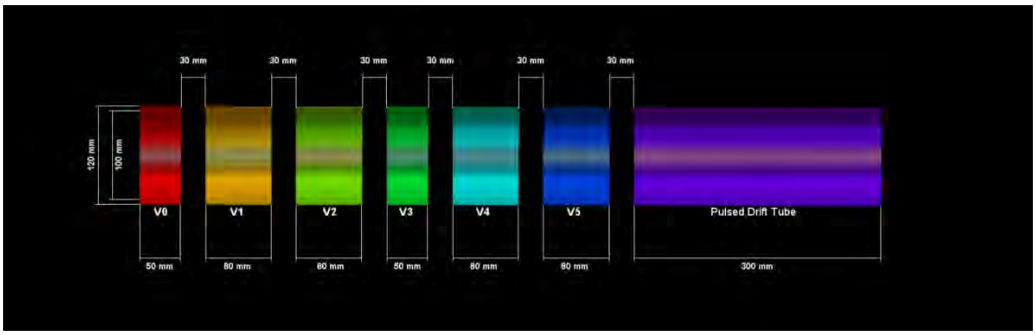

Figure 3.7 Schematic of the pre-prototype shape of the GBAR decelerator as implemented in the preliminary simulations. Colors indicate different voltages applied on the electrodes.

3.5.1 Light optics analogy

For a better understanding, it is interesting to use an analogy with light optics. Indeed, in some aspects, an Einzel lens (or any other cylindrical electrostatic lens) has similarities with a thin lens as employed in light optics. Thus if a charged particle is traveling off axis along a path parallel to the optical axis displaced from it by a distance h, it emerges from the lens with a certain angle. The plane from which the trajectory seems to be deviated is called the *principal plane*. The point where the path of the particle crosses the optical axis is called the *focal point*. Finally, such as in light optics, the distance between the principal plane and the focal point is called the *focal length*. These elements are displayed in Figure-3.8.

As in light optics, each electrostatic lens has two focal points (and two principal planes as well) depending on the direction of the particle through the lens. The first one is the *object focal point* corresponding to the point from where a charged particle seems to come when it emerges downstream the lens on a parallel path. The second one is the *image focal point*, corresponding to the crossing point between the optical axis and the path of a particle originally flying parallel.

It is interesting to note some differences with this analogy. Unlike light optics, the image and object principal planes do not necessarily coincide with the geometric center of the lens. If the electrostatic lens presents a symmetry along the optical axis, the object and image focal points (respectively principal planes) are then equidistant from

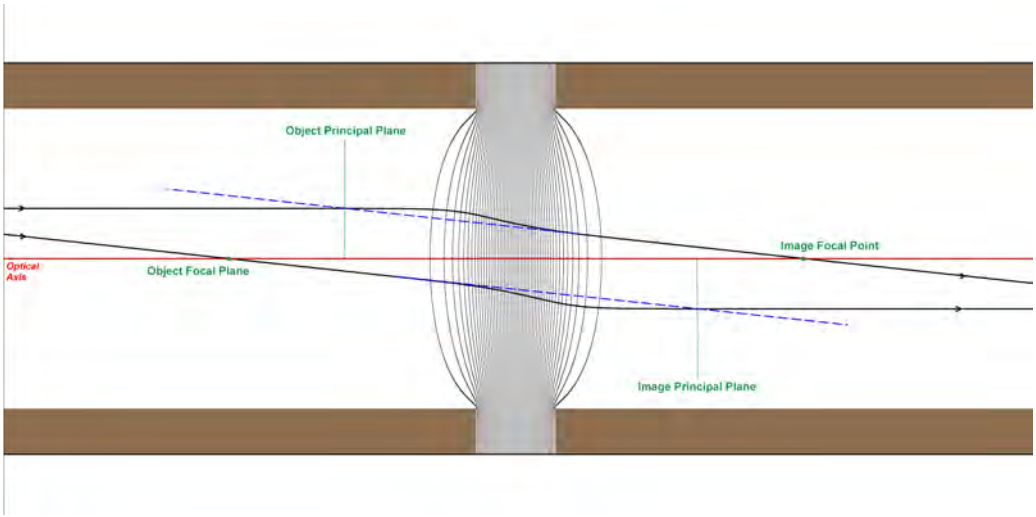

Figure 3.8 Definition of the principal planes and focal points in an electrostatic gap. The grey lines correspond to equipotential lines in the gap.

the midpoint. This is for example the case of a conventional Einzel lens. If the lens is electrostatically asymmetric, such as in the case of the drift tube where the potential is not the same on both side of the gap, the principal planes and focal points are displaced toward the low voltage side of the lens. Figure-3.9 illustrates the position of the focal points and principal planes for the drift tube when polarized at -90, -94, -98 and -99 kV according to the GBAR design.

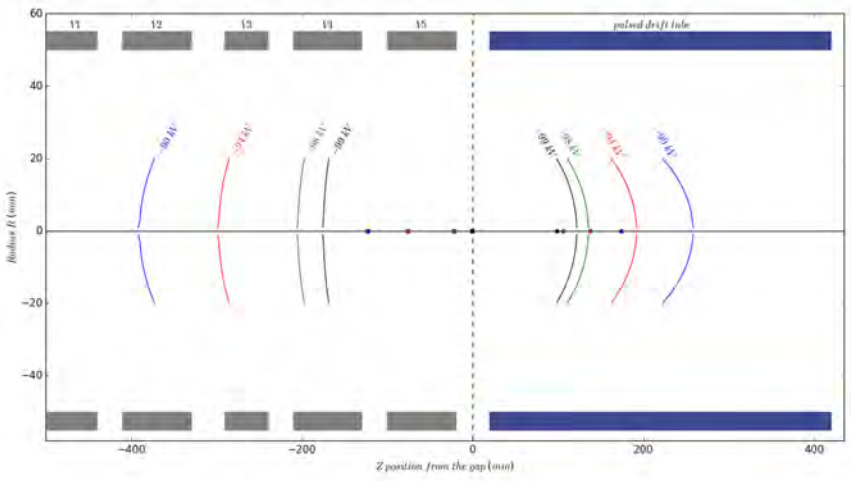

Figure 3.9 Schematic of the principal planes and focal points for the GBAR drift tube for a 100 keV antiproton beam. The square markers correspond to the object focal points and the round marker to the image focal points. Colors correspond to the studied deceleration case. The focal points and principal planes are represented in the limit of the paraxial approximation ($R < 20$ mm). All the electrodes except the PDT (in blue) are grounded.

3.5.2 Telescopic system with an additional lens

Once highlighted the definition of the focal points and planes, a step further in the case of the decelerating drift tube is to look at the addition of an Einzel lens upstream the pulsed drift tube.
With two lenses on the same optical axis, it is possible to realize a *telescopic system*. With such system, if the incoming beam is parallel, it emerges from the last lens parallel as well. The sinequanone condition to implement such telescopic assembly is that the image focal point of the first lens coincide with the object focal point of the second lens. In the case of the GBAR drift tube, it consists in focusing the antiproton beam on the object focus point of the pulsed drift tube as depicted by the square markers in Figure-3.9.

The magnification of the telescopic system can be evaluated the same way as for light optics systems by the ratio of the focal lengths of the optics, $M = \frac{s_f}{s_i} - \frac{f_2}{f_1}$ where s_i and s_f are the initial and final spot sizes of a parallel beam and f_1 and f_2 are the focal length of the first and second lenses. According to the magnification formula, in order to minimize the beam size in the drift tube, a larger focal distance is required for the first lens.

The focal length of an electrostatic lens can be adjusted with the potential applied on the electrode. Then, the longer the distance between both optics elements, the smaller the beam spot inside the drift tube according to the magnification formula. Figure-3.10 shows the cases of a 100 keV antiproton beam decelerated at 1 keV through such a telescopic system with an Einzel lens located upstream the pulsed drift tube at two different distance $L = 500$ mm and $L = 1000$ mm. In both illustrated cases, the beam emerges parallel (the system is really telescopic) but with different spot sizes[14].

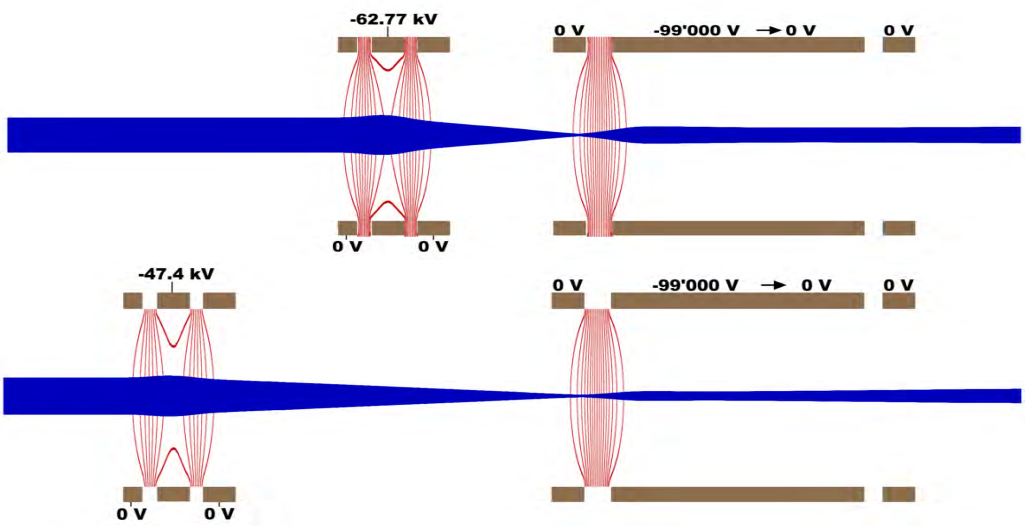

Figure 3.10 Comparison of simulated telescopic systems for a 1 keV deceleration. The apparatus is composed of an Einzel lens and a pulsed drift tube. The initial beam is taken homogeneous over a radius $R = 10$ mm and parallel to the optical axis with an energy of exactly 100 keV. The red lines correspond to the equipotentials with a 5 kV step. (*Top*) - Distance between the Einzel lens and the drift tube $L = 500$ mm. The spot of the emerging beam is 8 mm. (*Bottom*) - Distance between the Einzel lens and the drift tube $L = 1000$ mm. The spot of the emerging beam is 4 mm.

[14]The longer the distance between both optics elements, the lower the potential required to make the focal points coincide.

Such an optical telescopic system is currently considered in the framework of the post-LS2 design of the ASACUSA experiment where the replacement of the RFQD is envisaged in favor of an electrostatic decelerator.

3.5.3 Limits of the light optics analogy

The studies presented so far all focus on homogeneous and parallel incident beams. The reality is of course slightly more complex and the analogy with geometric light optics quickly reaches its limits.

Spherical aberrations

The first limitation is the so-called *spherical aberrations*. They are characterized by axial displacements of the focal point for off-axis particles traveling parallel at different distances from the optical axis. The effects of these aberrations appear in Figure-3.11 for the drift tube. It can be noted that the position of the focal point changes according to the initial position of the particle. To a first order approximation, we can consider this displacement proportional to the square of the lens semi-aperture h of the initial particles.

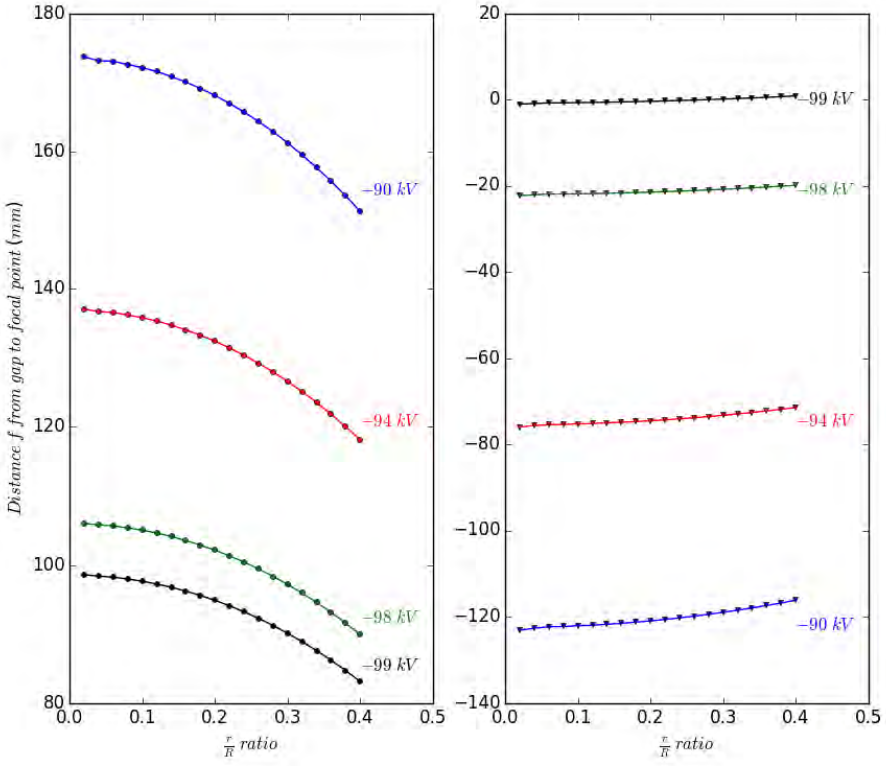

Figure 3.11 Position of the focal point object (*left*) and image (*right*) with respect to the radial position of the incoming particles in the case of the GBAR drift tube. The incident test-particles are traveling parallel with an energy of 100 keV.

Liouville's theorem and phase space definition

Up to now we have treated parallel particle trajectories and properties through optical devices. In fact, we have to deal with a beam of (anti-)particles, i.e. an ensemble of several particles moving on average in the same direction[15]. Thus, a realistic beam does not necessarily obey the paraxial approximation.

To describe such a beam, it is necessary to move to a representation of the beam based on the position of the particles in the phase space. In this representation, a beam takes the form of an ellipse characterizing its size and its divergence in each x and y plane as depicted in Figure-3.12.

Such an ellipse can be described via the emittance ϵ with the expression:

$$\epsilon = \gamma x^2 + 2\alpha x.x\prime + \beta x\prime^2 \tag{3.15}$$

where x is the position, $x\prime$ the first derivative of the position (equivalent to the angle of the particle) and α, β, γ three parameters known as *Twiss parameters*[16]. As shown in the Figure-3.12, the α parameter is related to the beam ellipse tilt , β is related to the beam size and γ to the beam divergence. The γ parameter is not necessarily given since it is dependent on α and β according to :

$$\gamma = \frac{1+\alpha^2}{\beta} \tag{3.16}$$

The *emittance* ϵ is the 2-dimensional phase-space area occupied by the particles of a beam. This parameter gives a measure of the beam quality. The smaller the emittance, the smaller the beam spot, the smaller the beam divergence.

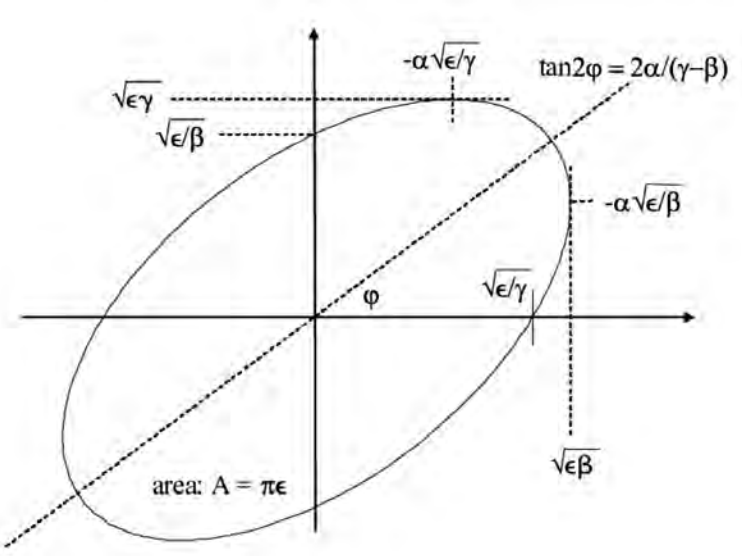

Figure 3.12 Phase space ellipse representation of the beam on one axis. Drawing from Ref.[141].

[15] And in our case, on average at the same speed.
[16] They can be referred as *Courant-Snyder parameters* as well.

In practice, we ideally wish to get a beam with as small an emittance as possible. But physically, the phase-space distribution of the beam is determined by the source of the beam and cannot be modified by accelerator[17]. This is a consequence of the *Liouville's theorem*. According to Ref.[142], this theorem states that, if we have a distribution of points in phase space, described by a density function $\rho(x, x')$ for a two-dimensional phase space, and the motion of the particles in that phase space is determined by a Hamiltonian, then the phase-space density will be constant in time. In other words, in the presence of conservative forces, the area defined by the ellipse of the beam in the phase-space representation is conserved.

Another consequence of the Liouville's theorem is that the emittance ϵ varies as the inverse of the momentum[18]. A decrease in the momentum implies an increase of the emittance. An intuitive way to understand it is to consider the definition of the divergence (average angle of the particles in the beam) as the ratio of the radial component of the speed $v_\perp$ over the axial component $v_\parallel$. Since the deceleration is not isotropic, only the axial component $v_\parallel$ of the speed changes.

In the case of GBAR, the ratio $v_\perp/v_\parallel$ increases by a 10 factor[19]. Therefore, the emittance increases as well, passing from 4π *mm.mrad* in ELENA to 40π *mm.mrad* inside (and downstream) the drift tube. Consequently, the size and the divergence of the beam inside the drift tube can not be infinitely reduced.

3.6 Conclusion

As designed with the six pre-decelerating electrodes, only five of them can be polarized between 0 and 100 kV while the very first one is kept grounded as a potential reference.

The application of an analytical approach as used for the determination of potential (such as the Bertram method) or the telescopic system (such as the light optics analogy) appears difficult. Furthermore, the geometry of the electrodes with a diameter = 100 mm larger than the length of the electrodes $L = 80$ mm does not allow to apply electrostatic rules to first order. The non-linear behavior of the potential (and the need to realize a development to higher order) appears clearly in Figure-3.13. In such an electrostatic configuration, the potential on the optical axis is not only determined by the potential on the electrode N but also depends on the potentials applied on the $N-1$ and $N+1$ electrodes. This latter appears smoothed.

The use of five different potentials appeared to offer a certain flexibility in the deceleration process. However, as a balance, it presents a very large number of applicable electrostatic configurations.

[17] Except some particular cases.

[18] One can also consider the so-called *normalized emittance* referring to the area in the (x, p_x) *canonical phase space* with x the position and p_x the x-momentum. Such normalized emittance is conserved during acceleration/deceleration. This definition is not considered in this document.

[19] The kinetic energy is reduced by a factor 100 and the speed by a factor $\sqrt{100} = 10$.

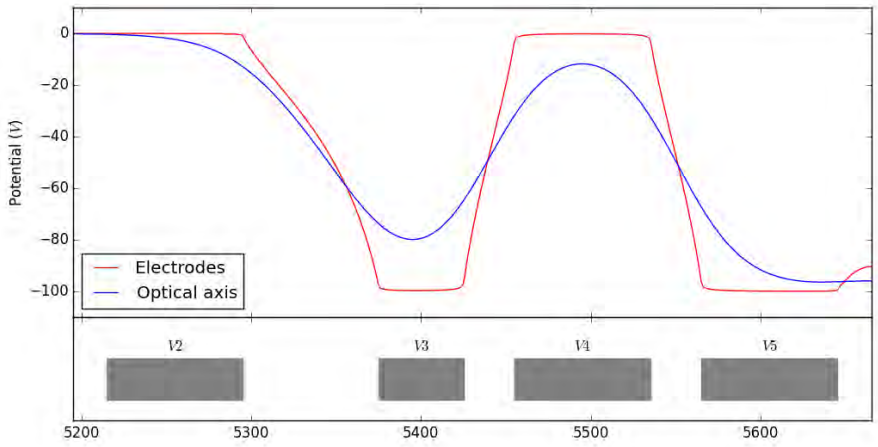

Figure 3.13 Simulation of the influence of the nearest electrodes on the potential along the optical axis. The red curve corresponds to the potential along the electrodes, the blue curve to the potential along the optical axis. The position of the electrodes is illustrated on the bottom part.

Chapter 4

Results using a Genetic Algorithm

4.1 Minimization algorithm

In this chapter, we will show the reasons for choosing an evolutionary algorithm in the electrostatic potential research. We will see how this type of algorithm can find solutions for the GBAR decelerator when associated with simulations of ion trajectories. Finally we will present the results obtained from the preliminary design of the decelerator and the limits of such an algorithm within the GBAR experiment.

4.1.1 Systematic calculation method

The simplest way to look for the best solution is to define a parametric value, called "*metric*", characterizing the expected behavior of the beam. The smaller this value, the closer it is from the best solution. Scanning and evaluating all the possible configurations offers the guarantee to find the minimal value of the metric. According to the metric definition, the dimensionality of the problem can be reduced by encoding each configuration in a unique way through the use of one or two combined variables. For instance, the voltage ratio between two electrodes or the addition of symmetry in the problem can simplify the minimization of the metric.

Unfortunately, such reasoning can not be applied in the case of the decelerator if we consider all the charged electrodes as independent. Indeed, in this case, the system has five independent degrees of freedom offering a very large number of possible combinations.

Let's consider $\Delta V = 100\ V$ as the minimal voltage variation inducing a visible change in the beam propagation, with a voltage range between $0\ V$ and $100\ kV$, each electrode can take 1000 possible values. It means $(10^3)^5 = 10^{15}$ voltage combinations for the decelerator apparatus. If the calculation of the metric function lasts $30\ s$ optimistically[1], the overall simulation for the evaluation of all the possible combinations would last $3.10^{16}\ s$, roughly a billion years. Conversely, the evaluation of all the possible combinations in a reasonable three month time would require a $12'500\ V$ voltage step. This latter is of course too large.

Then it is obvious that such a method, ironically called *bulldozer method*, is unachievable in a reasonable amount of time. When looking for the minimization of the metric, the ergodicity[2] of the method is a necessary condition but not a sufficient condition. It is therefore necessary to use more efficient methods including convergence toward an optimal solution.

[1] For comparative purposes, a realistic simulation time for 5,000 ions is around $85\ s$.

[2] The ergodicity is, in lay terms, the ability of an algorithm or numerical process to reach all the points of the space in which it is defined.

4.1.2 SIMION SimplexOptimizer

The first minimization method studied is already implemented by default with the SIMION software. This module, called *SimplexOptimizer*, is an optimization routine based on the *simplex method* also known as *Nelder-Mead downhill method*. Such a method is a commonly applied numerical method to find an optimum of a given function in multi-dimensional space. This routine is typical in electrode simulations with SIMION when looking for voltages minimizing for instance the beam spot size. Such method applies perfectly in the context of the metric as we defined it before in a solution space with $N > 1$ dimensions.

This routines requires four inputs:

- Starting points, one per dimension of the problem.
- Step sizes, one per dimension of the problem.
- A function characterizing the required parameters for the beam. This is by definition the metric function.
- A minimal metric value, which stops the algorithm.

This Nelder-Mead type method assumes a metric function f defined in a N dimensions space. The initialization of the algorithm consists in generating a non-degenerated simplex[3] with the starting points as inputs. By successive iterations, the algorithm evaluates the value of the metric function for the starting points and repeats the operation for surrounding points within a step size. In every dimension, it modifies the value of the vertices in the direction tending to reduce the metric value. If the step size is too large to reduce further the metric, the algorithm decreases its value to ensure the execution of the next iteration.

Limitations This method enables to cover the solution space in an optimized way without evaluating all the possible configurations. By modifying one, two or three variables at each iteration, the algorithm converges to a solution satisfying the desired conditions. However, this simplex optimization routine has some limitations. This mathematical method tends to converge towards the nearest local minimum. Once the simplex is fixed around a local minimum, the latter becomes an attractor from which the algorithm can not take out. The diversity of the solutions reduces with the iterations. Thus, the probability of finding the global minimum of the metric function (or at least a lower local minimum) is small. Indeed, from the initial points, the algorithm does not scan all the configurations but relies on global trends at each iteration, which does not guarantee a monotonous convergence to a local minimum. Similarly, if the metric function does not allow a minimum (even locally), the algorithm does not converge and loop to infinity[4].

Therefore, such a routine is only useful for more detailed investigations of the voltage values. In the case of the electrostatic configurations of the decelerator, this non-ergodic method appears limited because it requires the execution of a very large number of time the algorithm with different initial points to make sure that the minimum reached by the metric function corresponds to a global minimum. It is important to remember that an ion simulation is performed at each iteration. Thus, the calculation time becomes relatively large even though less important than in the case of the bulldozer method.

[3] Polytope in a N dimension space composed of $N+1$ vertices. In a 2D space, a simplex is a triangle, in a 3D space, a simplex is a tetrahedron.

[4] This method limits the infinite loop risk by introducing a maximum number of iterations.

If the calculation time of the bulldozer method, or the non-ergodic nature of the simplex method represents a real problem in the search of the electrostatic configurations for the GBAR decelerator, it is now possible to implement a technique that guarantees both the ergodicity hypothesis and the fast convergence towards the global minimum (or at least a local minimum with lower metric value). The algorithms providing the best solutions fulfilling those criteria emerge nowadays with the automation of systems and belong for the majority of them to the family of the evolutionary algorithms as we will describe below.

4.2 Genetic algorithm and potential selection

Because of the inherent difficulty of optimizing a system with five variables, an attempt was made to solve the problem using a Genetic Algorithm approach.

4.2.1 Description of Evolutionary Algorithms

In 1860, Charles Darwin published his book, *On the origin of species* [143]. In this work, Darwin rejected old dogmas considering that every species is able to survive in any environment and exposed his theory about the evolution of species. We can summarize it as follows: *under external conditions, species have progressively adapted and selected through breeding processes to live in a specific natural medium.*

In contrast to Lamarckism, Darwinism considers that evolution involves the selection and transmission of survival traits within a population of individuals. It is only during the 20^{th} century that genetics reveals the processes involved in this natural selection of species. The problem of the information processing and the support of heredity has been solved. Computer scientists then studied methods to implement systems spontaneously evolving with respect to new environmental conditions. Such processes are the basement of the evolutionary computation.

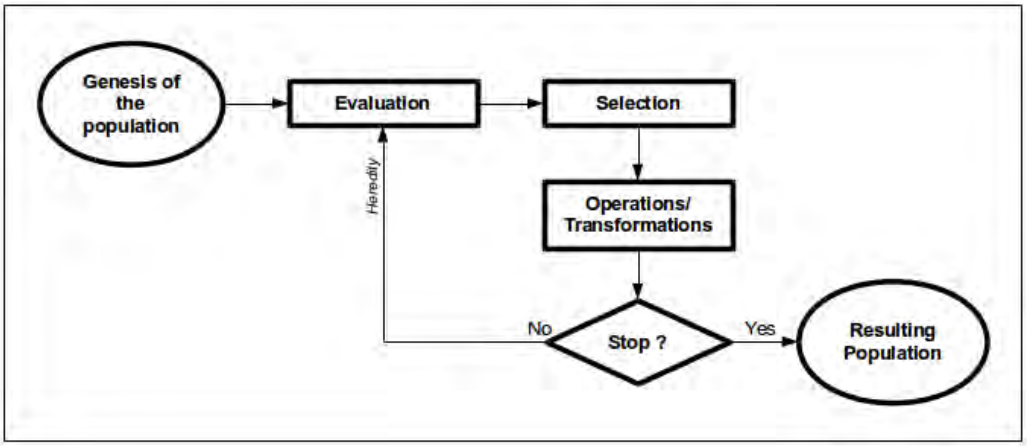

Figure 4.1 Schematic diagram of a typical evolutionary algorithm.

As shown in Figure-4.1, an evolutionary algorithm simulates the evolution of a population of various individuals, randomly generated to which transformations are applied and subject to selection. Temporality is marked by the passage through each of the stages of the algorithm, called a *generation*. If the selection occurs with respect to a specific (and well defined) criteria/function, the population tends to improve from one generation to the next [144, 145, 146].

Such an algorithm does not require any knowledge about the problem itself. According to Ref.-[147], one can see it as a black box with several inputs (*variables*) and several outputs (*objectives*). The algorithm executes defined operations on the inputs and reads the outputs, re-injects them as inputs and repeat the operations in order to improve the successive outputs.

Evolutionary algorithms constitute an original approach in solving information processing problems; no needs to look for analytical solutions, or numerical approximations, but simply for solutions satisfying different criteria the best way. If there is no absolute guarantee to find the unique global optimum (for instance in a multi-dimensional problem), their ability to find such a global optimum (or suitable local optima) in a reasonable amount time is much more better than with other classical computational methods.

During the last decades, the explosion of the worldwide computing power offers opportunities in solving more complex evolving systems without mathematical concepts or requiring too many iterative processes. For instance, in addition to cellular automata, such evolutionary algorithms are used to simulate the complex flight of bird groups or the movement of barchan dunes in the desert. With the development of neuron networks, they give birth to the basement of the artificial intelligence (AI) and to the automatic optimization (AOp) [148].

Today the *Evolutionary Computation* includes several types of algorithms among which three are mainly represented:

- the *Evolutionary programming* [145]
- the *Evolution Strategy* [149]
- the *Genetic Algorithm* [150, 151]

With its chromosome representation, this latter offers the best perspective in solving the potential distribution problem for the GBAR decelerator. In the next section, the classical operation of a genetic algorithm with a biological analogy is presented with particular bounds to the electrostatic deceleration optics problem.

4.3 Genetic algorithm

Genetic algorithms (GA) are at the crossroad of computation science, evolution theory and modern genetics. The combination of these last two is today designated as *Neo-Darwinism*. They provide solutions to problem without analytically calculable solutions in reasonable time. The difference with a classical evolutionary algorithm lays on three main transformations: the *crossover*, the *mutation* and the *selection*.

Basically, a GA can be defined as a computer code looking for an extremum (resp: extrema) of a function defined on a specific data space. Five elements are required to use it:

- A way to code the characteristics of the individuals inside the population. It consists in attributing to each point of the data space an unique set of coordinates. In the case of the decelerator, the coding principle is an array composed of five values corresponding to the potentials applied on the five pre-decelerating electrodes. The idea is to explore as much as possible the space of the solutions offered by the different values of potentials.
- A genesis mechanism of the population. This mechanism is crucial to avoid the generation of a homogeneous population increasing the convergence time towards the global optimum.

- An evaluation function for the individuals of the population. This function returns a value called *fitness*. We can compare this with the study of the beam in the drift tube with the selection criterion based on the spot size, the beam divergence or a combination of both defined as the metric.
- Transformations also called *operators* to explore the data space or diversify the population.

While executing a GA, thousand of solutions answering the problem are randomly generated. These *genotypes* undergo an evaluation process estimating the relevance of such solutions following the species selection theory. It means that the more fitting the solutions are, the higher is the probability for these solutions to 'survive'[5]. The population (the group of solutions) evolves in successive generations via crossovers of the best solutions and via random mutations. By reiterating this process several times, the population evolves towards an optimal solution.

A pseudo-code for a typical GA is:

1. Initialize the population P
2. Evaluation process on P
3. "While" optimal solution found "then":
   a) New population $P\prime$ = parents selection in P
   b) $P\prime\prime$ = *Crossover* on $P\prime$
   c) $P\prime\prime\prime$ = *Mutation* on $P\prime\prime$
   d) P replaced by progeny $P\prime\prime\prime$ and new *Individuals*
   e) Evaluate P again
4. EndOf "While"

Following this formal definition and composition of GAs, questions remain: what is the general format of the information ? how does the selection mechanism occur ? how does the population diversify ?

4.3.1 Coding a GA

No need to be a specialist in genetics or biology to understand the selection process of a GA. As described above, a GA is based on a population of solutions. Each solution can be associated to *genes*. The different values they can take are called *alleles*. Coding each allele in an unique form is absolutely crucial.

At a higher level, a sequence forms a *chromosome*. It can be unique. Finally, a group of chromosomes represents an *individual*. All the generated individuals form the population.

Let's now define the genetic equivalence in the case of the optics problem for the decelerator. The investigated solutions are obviously the electrostatic configurations applied on the pre-decelerating electrodes, considering the potential values as genes and the different values of each potential as alleles. The potential values are coded over 17-bit binary values between "*00000000000000000*" (0.0) and "*11000011010100000*" (100'000.0). The different solutions are expressed as 85-bit chromosomes consisting of 5 concatenated genes.

[5]Stay in the process.

For example, according to the following potential values:

$$\begin{aligned} BIN(86778) &= 10101001011111010 \\ BIN(74026) &= 10010000100101010 \\ BIN(46870) &= (0)1011011100010110 \\ BIN(11800) &= (000)10111000011000 \\ BIN(50733) &= (0)1100011000101101 \end{aligned}$$

The chromosome becomes:

$$[86778, 74026, 46870, 11800, 50733] \Leftrightarrow {}'10101001011111010100100001001010100101101110001010110000101110000110000110000110001011011'$$

Selection

The selection operator determines which individuals of the population P survive to the next generation defining a new population $P\prime$. For n individuals in P, $n/2$ individuals are selected in $P\prime$ (the remaining $n/2$ individuals are generated by the crossover process).

This operator is crucial to ensure the convergence to the optimal solution. It directly impacts the population deciding which element of $P\prime\prime\prime$ survives, dies or breeds. The probability of survival of an individual is supposed to be directly related to its effectiveness in the population to meet the selection rule. The relevance of an individual in the population is materialized by the *fitness* value. Let's develop here three selection methods[6]:

- The *roulette wheel selection* or *fitness proportionate selection*. It is the most commonly used method where the survival probability is directly proportional to the performance of the individual in the population. Such selection offers a big variance (*dispersion*) of the individuals. Nevertheless, this kind of selection is intimately dependent on the random sampling adopted. Thus, two deviances may appear:
  - A *high fitness deviance*, where only a few individuals are selected several times as having a high fitness.
  - A *low fitness deviance*, where the selection of only low fitness individuals happens.

  Both led to a stagnation situation of the genetic code or at least seriously slowed down its execution. The selection of a specific seed value in the pseudo-random processing and the introduction of the *replacement*[7] operator ruled out this problem by generating new combinations of potentials.
- The *elitism* or *elitist selection*, retaining only the best individuals in a generation P for the next generation $P\prime$. In this selection, the variance is almost zero and the diversity of the individuals seriously impacted. It can be used as confirmation tool for the best solutions found. The crossover and mutation probability have however been proven to prevent any premature convergence.
- The *tournament selection*, the fairest and most relevant selection. In this latter, a random sampling with replacement operates between two individuals of the population P. If the sampling results have a value p such as $0.5 < p < 1.0$ then the

[6] These methods have been selected successively to operate in the framework of the potential configurations of the decelerator.

[7] Cf. later in the text

tournament duelists with the highest fitness is selected for the population $P\prime$. The variance and diversity of this selection is high and the selection pressure can be adjusted by changing the selection range of p.

For unfixed reasons, the tournament method caused a slowdown in the execution of the code requiring the use of the roulette method or the elitist method with enhanced mutation and crossover rates to obtain a greater diversity of results.

Crossover

The *crossover* or *recombination* in the GAs is the computational transposition of the natural mechanism leading to the biological bases of heredity. This operation occurs after the selection on P. The new generation $P\prime$ is then composed of $n/2$ individuals. $n/4$ couples are randomly generated and 'breed'. Chromosomes from the parents are copied and recombined to generate new individuals.

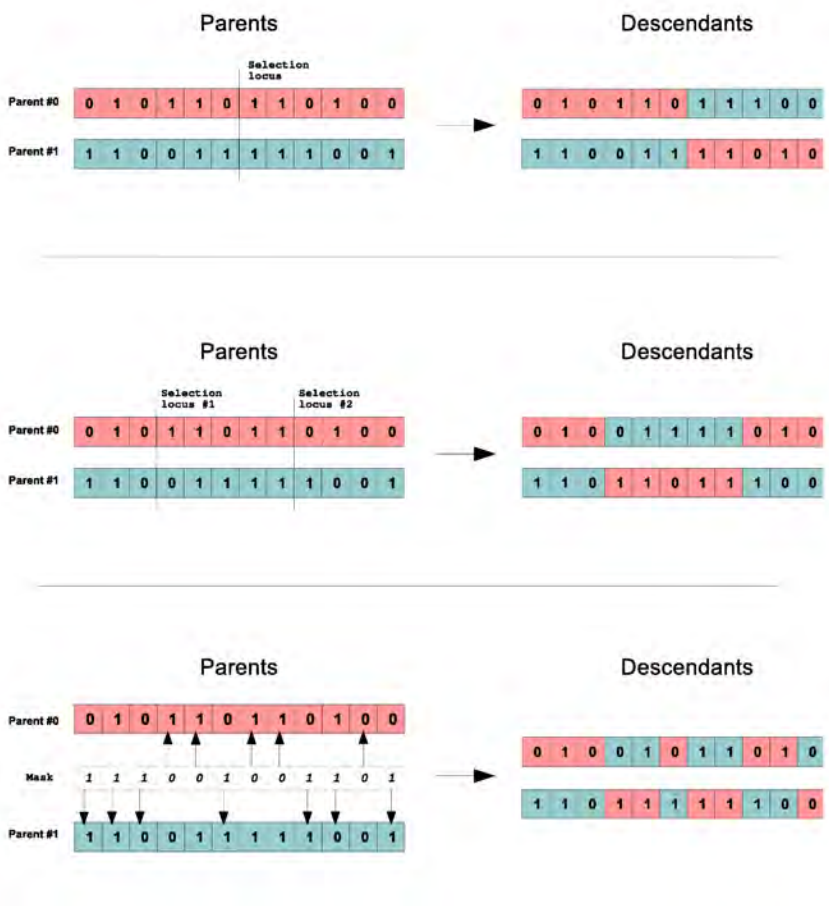

Figure 4.2 Examples of crossover processes: (*up*) Single-point crossover, (*middle*) Multi-point crossover, (*down*) Uniform crossover. Figure based on Ref.-[152]

After the creation of a chromosome pair, both parent chromosomes are copied[8]. The recombination of the chromosome can then follow various ways.

[8]To continue on a genetic analogy, there are cloned

A first way is to randomly select one locus on both chromosome copies delimiting segments. According to the crossover probability P_c, the segments are exchanged with their counterparts on the opposite chromosome as shown on Figure-4.2 (*up*). Such crossover is called *Single-point crossover*. It is possible to apply this operation on more than one separation locus (cf Figure-4.2 (*middle*)). In this case, it is called *Multi-point crossover*. By increasing the number of selection loci, a better diversity appear. Indeed, the higher the number of selection loci, the higher the probability a crossover appends, the larger the diversity is. At the beginning, only one locus was chosen. Thereafter, the number of loci was increased to 2 or 3 in order to increase the number of solutions.

Another way is to generate a binary mask with the same length as the parent chromosomes. Each byte of this mask codes for one gene on both elements of the chromosome pairs. It determines from which parent the first descendant chromosome inherits the gene in the corresponding locus. For instance, if the mask presents a '0' value, the first descendant inherits from parent chromosome #0, else if the mask presents a '1' value, it inherits from parent chromosome #1. Symmetrically, the second descendant inherits from the complement of the mask. Such recombination is referred as *uniform crossover*. An example is found on Figure-4.2 (*down*).

The crossing operator, as in genetics, ensures the mixing of the coding material and allows the reproduction of favorable alleles. In more concrete terms, this operator creates new combination of parameters and guarantee the possibility to reach any point on the data space.

Anyway, the common action of selection and crossover do not participate in creating new genes. Indeed, if the ensemble of the chromosomes in a generation carry a non-favorable allele, there is no way following the selection or recombination rules to generate this favorable allele. This is why a new operator is introduced, the *mutation*.

Mutation

The *mutation* operator consists in changing the allele of a gene according to a given probability P_m. It modifies the characteristics of a solution randomly and maintains diversity inside the population. The mutation introduces kind of "noise" as a local perturbative function.

Such operator limits the *genetic drift*. This latter occurs when some alleles of the gene are randomly favored and tend to spread among the population until all chromosomes present the same.

In addition with the crossover, the mutation guarantee the *ergodicity* of the GA. Intuitively, it means that in a reasonable amount of time, any point of the data space can be reached. Since a mutation can happen anywhere randomly on a chromosome, a GA offers mathematically the opportunity to reach the global optimum.

Replacement

The *replacement* is the easiest step in a GA. It consists in generating the new generation according to the previous operations. The main goal is to determine which part of the previous generation is kept or not.

A first method consists in replacing a part or even the entire P population by the new P''' generation without any consideration for the fitness value of the new individuals with respect to the previous generation. This method introduces a great diversity but exposes the GA to a genetic drift. Indeed, a low fitness individual from the P''' population may

replace a high fitness individual from the P population. The risk of drift increases with the replacement of the entire generation P, also known as *generational replacement*.

Another method consists in sorting the P population and introducing only the descendants whose fitness is better than the parents. This strategy is a better way to ensure the GA convergence. It is known as the *elitist replacement*.

But as always with elitism, the risk is to see a premature convergence of the solutions. The possibility to introduce a few new individuals generated via a pure random process is a good way to keep the engine of diversity active. It is interesting to cite another existing process called **overcrowding**, consisting in the increasing the population size but this process has not been used in this framework.

4.3.2 Example of a simple GA

In order to test the GA code without the complexity of the SIMION-like simulations, a simpler case has been encoded. Such a code is useful to benchmark the different randomizers and seeds possible and to highlight the undesired behavior of the GA. It is also the only opportunity to set the different values of mutation, crossover and replacement probabilities.

Let's consider the simple example of a population of endemic birds on an island. This initial bird population has 3 different phenotypes in the following proportions:

Phenotype		Chromosome: [Allele 1, Allele 2]		Code		Initial proportion
black plumage	⇔	[black, black]	⇔	[1,1]	⇔	25%
white plumage	⇔	[white, white]	⇔	[0,0]	⇔	25%
grey plumage	⇔	[black, white]/[white, black]	⇔	[1,0]/[0,1]	⇔	50%

Table 4.1 Initial bird population

The GA description of the bird colony starts with the genesis of the population. Here a randomize function generates the individuals of the first generation with respect to the ratios given in Table-4.1. The diversity of such first generation is crucial to avoid *founder effect* where a random reduction of the genetic characteristics leads to an undesired convergence. In specific cases, the choice of a good randomize function may be critical.

Let's apply on the initial population the crossover and replacement operators but without any selection. The randomize function and its seed have been chosen in order to avoid the founder effect. Figure-4.3 (*top*) shows the typical evolution of a bird population in such a case. The three species almost keep the same proportion over time. This test is a good way to see if the individuals suffer genetic drift originally. As shown in Figure-4.3 (*middle*), a genetic drift may lead to an undesired convergence favoring here the *white* population. Comparing the two first plots, one can appreciate the crucial impact an initial genetic drift may engender with respect to the selection criterion.

Let's imagine that a natural predator of the birds is now introduced on the island. This predator eliminates certain individuals over generations from a selection criterion, for instance defined as: "The more white birds are, the less chance they have to survive". Following the criterion, the phenotype "black plumage" must then be favored.

Figure-4.3 (*bottom*) presents an ideal case of convergence. The main difference compared to Figure-4.3 (*middle*) is the non variability of the final solution. While a genetic drift may favor the "grey plumage" or "white plumage" phenotypes, the GA converges

toward an unique solution in almost 100% cases where only the *black* population survive (*whites* disappear first and *greys* thereafter).

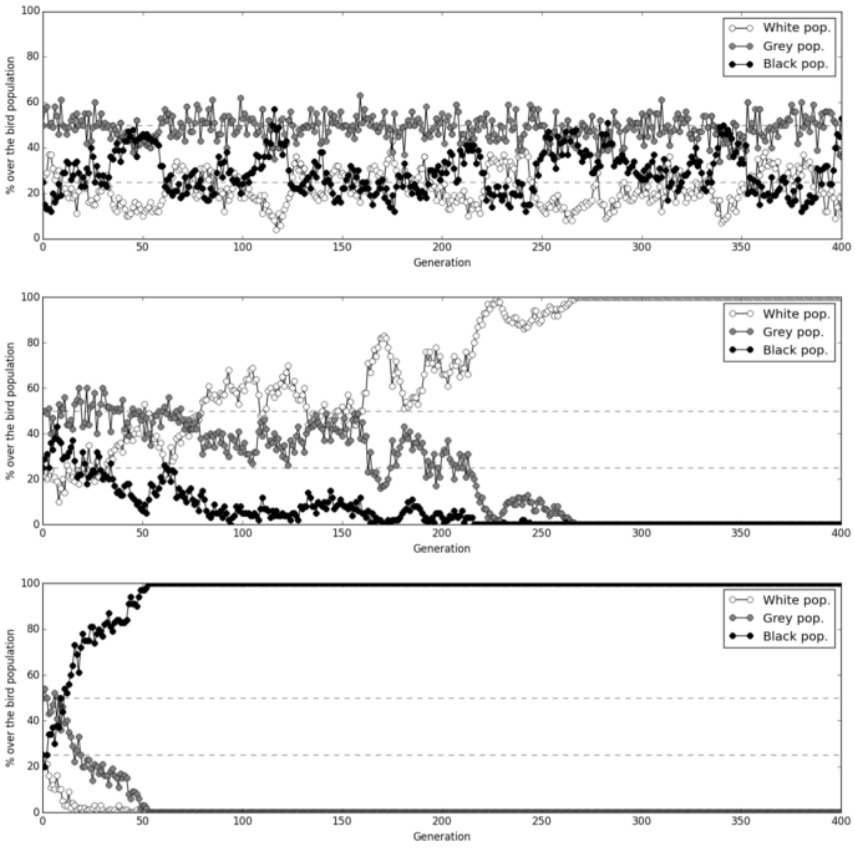

Figure 4.3 Evolution of the phenotype ratios in the bird population over 400 generations integrating the crossover and replacement processes. (*top*) Careful randomize function with optimal random seed. No genetic drift appears. The mean values of the different ratios : $\widehat{W} = 0.23$, $\widehat{B} = 0.29$ and $\widehat{G} = 0.49$. (*middle*) Classical uniform randomize function without seed selection. Genetic drift appears with extinction of the *grey* and *black* population (undesired convergence). (*bottom*) Ideal GA convergence with crossover, mutation, replacement and selection operators.

4.3.3 Applying Genetic Algorithm to potential search

From SIMION to Python

Despite its frequent use, SIMION has a significant disadvantage. It is based on a language not commonly used in physical simulation, the *LUA* language. Such a language, optimized for the deployment and development on embedded systems, is an inconvenient to implement a code as complex as a genetic algorithm. For more ease in the coding of the genetic algorithm, the LUA language [153] has been abandoned in favor of *Python 2.7*.

This program is based on a "Pythonian" transcript of the main functions of SIMION as previously described. The calculation of the potential from the finite difference method is carried out for a mesh of 0.25 *mm* size. Each of the six pre-deceleration electrodes and the drift tube were integrated following the original design shown in Figure-3.7. The potential map for each electrode is stored in a separate binary files of type *npy* using the *cPickle* Python module. In the same way, the integration of the trajectories with the RK4 method is done with a fixed step of 10 *ns*.

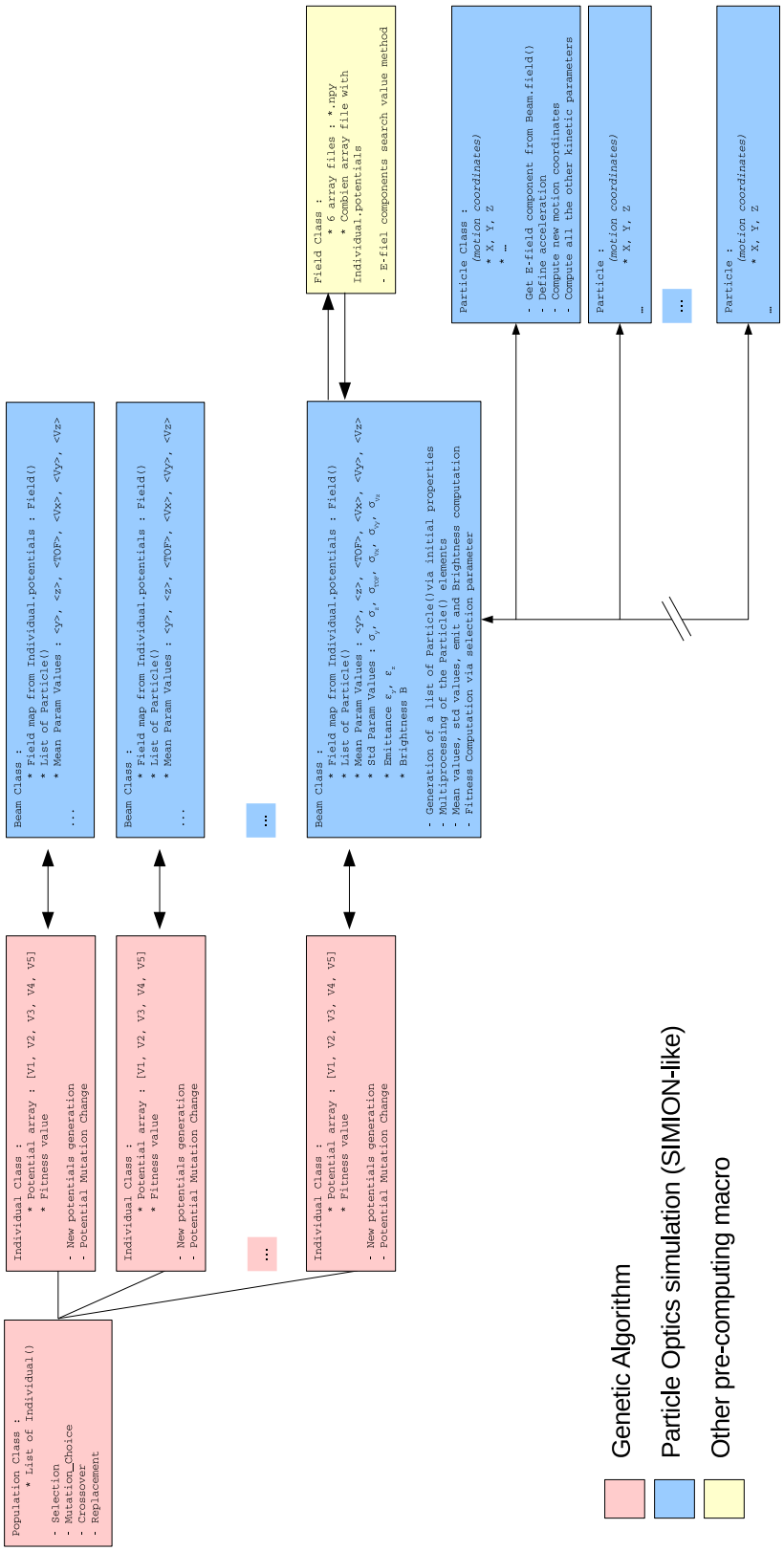

Figure 4.4 Schematic of the search algorithm.

An advantage of Python is its ability to be used to parallelize a code. Indeed, the use of a GA requires a very large number of calls for the same functions such as for the integration of trajectories and the repetition of these functions for the different configurations in the individual population generated. With the Python *multiprocessing* package, it is possible to perform simultaneously the trajectory integration of several particles at the same time before gathering all the final kinematic parameters in the drift tube. The calculation speed is then increased. This option is not available in SIMION or LUA language.

General organization of the GA method

Figure-4.4 summarizes the general organization of the potential search method with the genetic algorithm and the trajectory simulation.

The method has two sides, on one hand the organization of the selection following the GA principle and on the other hand, the integration of the trajectories of the ions for each configuration. For this, we benefit from the efficiency of object-oriented programming. The structure of the method is therefore divided into two blocks.

The first block is fully dedicated to the GA and the generation of the electrostatic configurations. *Individual* objects are generated by a master object, called *Population*. At each generation, the *Population* object classifies the *Individuals* according to their fitness value and selects from it the *Individuals* which survive, mutate, breed or are replaced. The *Population* object contains 100 *Individuals* randomly chosen thanks to a randomizer whose seed value has been carefully determined to avoid any original genetic drift. The *Population* object manages the GA selection mechanism. It is at the *Population* level that the selection parameters are adjusted (the mutation rate, the probability of crossing, the probability of replacement, the number of survivors).

Individual objects carry the characteristics of the problem. Each *Individual* receives as attributes the voltage values applied on the pre-decelerating electrodes. These values are obtained randomly (new Individuals or replacement) or by modifying previous values (mutation or crossover). *Individuals* also carry methods applying the mutation, crossover, or replacement operators when ordered by the master *Population* object. It is also from this object that the second part of the search code is called.

The second block is entirely dedicated to the trajectory modeling, the execution of ion flight simulations through the decelerator and the calculation of the fitness value from the final parameters of the simulation.
The central element of this block is the *Beam* object. This latter has several crucial functions:

- It manages the generation of the potential maps via the *Field* object.
- It generates 200 *Particles*[9] objects according to the defined beam parameters.
- It calculates the fitness value from the final states of the *Particle* objects.

The *Field* object carries as attributes the corresponding unitary potential maps for each electrode. The methods specific to the *Field* object are dedicated to calculating the potential maps and the corresponding electric fields. Thus, before the start of the GA, the unitary potential maps are generated with the relaxation method and saved in binary files. During the execution of the GA, the *Field* object loads the unitary potential maps from these files, receives the voltage values of the *Beam* object and returns the general

[9]200 *Particles* is a compromise between the desired 1000 particles simulation and the calculation time.

potential map. It is also this object which is in charge of returning the value of the potential (and the electric field) at the coordinates of the ion at each step of the trajectory integration.
Finally, the objects *Particle* carry as attributes the kinematic parameters of the simulated antiprotons. They also carry the RK4 integration method that modifies the attributes step by step.

The advantage of creating a master *Beam* object is to group the *Particles* and *Field* objects. It also manages the parallelism in the execution of the integration method for each *Particle* object. At the end of the simulation, it brings together the final parameters of the *Particles* and pools these elements to extract the fitness value. Finally, it returns this value to the *Individual* who generated it.

To summarize, the program generates a *Population* object. This latter integrates 100 *Individual* objects carrying an unique electrostatic configuration.
At the creation of each *Individual*, a *Beam* object is created. It generates a general map of potential following the attributes of the *Individual* who generated it and creates 200 *Particle* objects with respect to the desired beam parameters. These *Particles* integrate the RK4 method as well as the kinematic parameters of the simulated antiprotons.
Once the integration of the trajectory is performed by each *Particle* object, the final parameters of the simulation are pooled by the *Beam* object that evaluates the fitness value. The latter is returned to the *Individual* level.
When all the *Individuals* received their fitness value, the *Population* object orders them with respect to their fitness and applies the various GA operators.
A new generation then starts, and new *Individual*'s (or those who have been chosen for mutation or crossover) generate a *Beam* object and so on...

Remarks on the execution of the search algorithm The main problem of this architecture is that the parallelism is restrictive at the level of the *Particle* object. Indeed, despite the parallel computation of the trajectories, the block managing the selection of the electrostatic configurations (in pink on the Figure-4.4) stays in stand-by as long as the *Beam* object has not finished the integration of all its *Particle* attributes. Then, the main cause of slowdown comes from the simulation block. To improve the efficiency of the search algorithm, the entire simulation block could be replaced by an electrostatic analytical solution[10] which does not require to simulate the propagation of a beam through a simulated decelerator.

Extracted potential configurations

The GA method is run several times with different initial populations[11]. It returns a list of Individuals containing electrostatic configurations classified by increasing fitness.

Because of the slowness of the program (despite the parallelization), it is difficult to expect total convergence every time. The idea is then to pay attention to the intermediate stages of the runs. After 100 generations, 70% of the population is concentrated around the same values of potentials (convergence toward a local or general minimum). We can then highlight the points of fixation/convergence even temporary during the execution of the GA.

For this, an independent routine checks the population at each generation before applying the mutation, crossover and replacement operators, and extracts a weighted

[10] At least, an electrostatic approximation.
[11] The seed of the randomizer is carefully changed to avoid initial genetic drift.

average configuration of the first 50 Individuals. If the average configuration does not change more than 1000V (1% of the maximum voltage) for each gene on half of the Population for at least 10 generations, the values are saved. The configurations used in the next section have accounted for 50% of the population for at least 10 generations.

Initial conditions As explained in the previous chapter, the evolution of the beam through the decelerator is strongly correlated with the initial conditions of the particles. From basic information communicated at the time, we were not able to simulate a beam with precise parameters. The essential information known then was the emittance about 4π *mm.mrad*. From such an emittance, it is possible to generate a beam whose profile in the phase space is a square whose width corresponds to the maximum hypothetical size of the beam 4 *mm* and the height corresponds to the maximum hypothetical divergence of 4 *mrad*. Since the system is axisymmetric, the beam is generated in only one transverse direction in a first time[12].

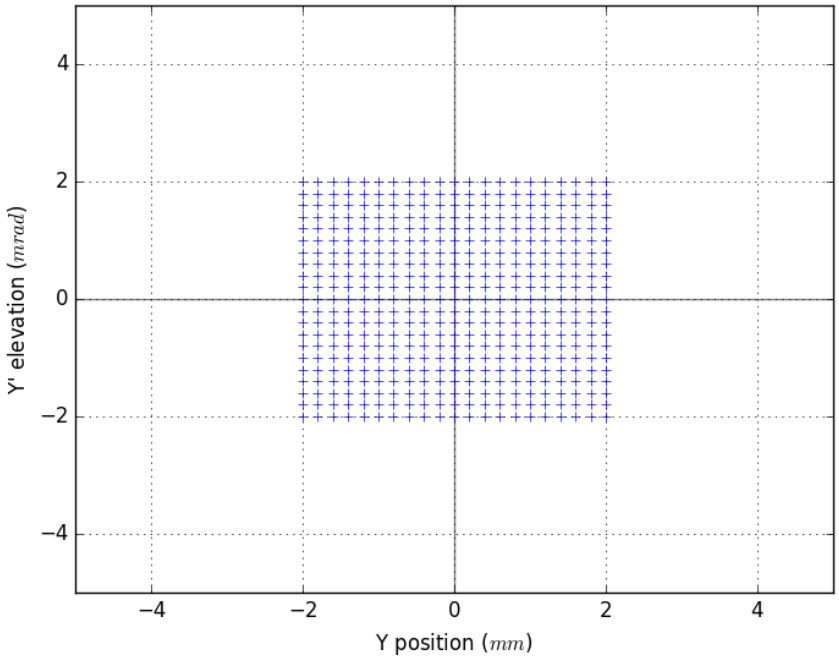

Figure 4.5 Phase space distribution of the simulated beam.

Subsequently, we obtained the Twiss parameters of the beam (see Table-4.2) resulting from beam simulations in the ELENA ring. These parameters are still preliminary but give a good idea of what the beam from ELENA should be at nominal.

The simulated beam configurations downstream the ELENA ring can be divided in two types:

- A configuration type referred as "*Minimize Alpha*" which tends to minimize the Twiss parameter α. The ellipse of the beam in the phase space is then flat.
- A configuration referred as "*Minimize beam size*" which tends to minimize the size of the beam spot.

[12]Dissociation for the X- and Y- axis performed latter with the parameter shared by ELENA.

These configurations are presented for three different distances from the GBAR handover point: 2 m, 3 m and 4 m. The handover point corresponds to the sector valve between the ELENA ring and the GBAR experiment. It marks the position from where the beam enters the GBAR experimental zone.

Case	α_x	α_y	β_x	β_y	D_x	D'_x
2m Min. beam size	-0.2888	0.6457	1.221	1.573	-1.546	-0.573
2m Minimise α	1.02e-9	-9.25e-10	4.636	8.396	-1.64	-0.556
3m Min. beam size	-0.3564	0.2945	1.878	1.658	-1.918	-0.531
3m Minimise α	-8.15e-2	-6.17e-3	4.486	10.488	-0.525	-0.587
4m Min. beam size	-0.421	-0.0357	2.658	1.897	-2.28	-0.504
4m Minimise α	-0.2336	-0.0225	5.607	9.649	-2.466	-0.509

Table 4.2 Preliminary Twiss parameters of the beam ejected from ELENA as generated by the madx software [154]. The emittance of the beam is $\epsilon_x = 4.10^{-6}$ $m.rad$ horizontally and $\epsilon_y = 6.10^{-6}$ $m.rad$ vertically. The momentum spread $\Delta p/p = 2.5e-3$.

Stopping conditions The objective of these simulations is to find the electrostatic configuration that allows us to have a parallel beam with a small spot size, taking into account the physical limitations as explained in the previous chapter.

In a first step, simulations are performed statically (the voltages on the electrodes stay unchanged during the simulation). For simplicity, to consider only the optical effects upstream the decelerator, all the simulated ions stop at the center of the DT[13]. For the same reasons, effects on the ion time-of-flight distribution are not taken into account and the ions are generated at the same time in the simulation.

In a second step, a more realistic beam is simulated for the most interesting electrostatic configurations. These simulations then integrate an energy and temporal dimension. In the following, the initial conditions are much more studied.

Metric The best solution to characterize the beam shape satisfying the desired conditions is to define a unitless parameter called *metric*. This metric behaves as a variable that must be minimized (resp: maximized) to converge towards an optimal solution. It is the computational equivalence of the fitness value considered in the GA.

In the case of GBAR, we can use the following definition to characterize the size and divergence of the beam inside the DT:

$$metric \;=\; \alpha \times \left(a\frac{r}{r_0} + b\frac{x'}{x'_0} \right) \tag{4.1}$$

with r the beam radius (1σ-value), $r_0 = 10$ mm the characteristic (best expected) beam radius, x' the beam divergence, $x'_0 = 10$ $mrad$ the characteristic (best expected) beam divergence, α a factor related to the transmission rate through the drift tube[14] and a,b weighting coefficients (usually $a = b = 1$).

This definition of the metric offers a unitless variable that must be minimal when the beam is small and has a small divergence. Hereafter, the entire simulation process and the metric estimation is referred as a *metric function* by analogy with mathematics.

[13]Effects related to switching or to energy dispersion are not considered.

[14]This factor has to be equal to 1 when the transmission rate is 100% and large $\alpha >> 1$ when the transmission rate tends to zero.

4.4 Results

4.4.1 GA outputs

The solutions presented in the Table-4.3 are the weighted average configurations on the majority of individuals for 10 non-successive generations. Configurations are rounded to 100V. The initial simulated beam follows the phase space distribution as shown in Figure-4.5. After a post-analysis, similar solutions are brought together.

V1 (kV)	V2 (kV)	V3 (kV)	V4 (kV)	V5 (kV)	Spot Size 1σ(mm)	Divergence 1σ(mrad)	Fitness (unitless)
69.3	59.4	53.6	**71.0**	0.0	2.54	6.81	2.34
63.5	0.	29.1	48.9	**70.7**	3.78	6.24	2.51
69.5	60.0	53.4	12.1	12.5	2.43	7.61	2.51
63.6	1.1	0.1	2.0	10.9	2.25	8.02	2.57
34.0	**74.9**	10.2	22.1	30.7	2.93	8.24	2.79
14.6	**79.2**	12.1	50.1	**94.8**	9.24	3.03	3.07
10.3	37.4	**84.5**	0.5	1.2	4.94	14.899	4.960
12.4	15.0	25.1	95.4	89.3	16.08	7.73	5.95
14.3	45.6	**99.1**	0.3	**100.5**	6.43	20.42	6.71
13.7	44.9	92.6	77.8	27.9	2.07	47.13	12.30

Table 4.3 Solutions proposed by the execution of the Genetic Algorithm with the corresponding 1σ-value of the beam spot and beam divergence at the center of the drift tube. The last column shows the fitness value taking into account in all the presented cases a 100% transmission rate through the whole decelerator structure. Potentials are expressed in absolute values.

It is important to note that the smallest fitness solutions have repeatedly be the terminal solutions of the GA when its execution was stopped manually. Unfortunately, the lack of history on the execution of the GA does not allow to determine clearly how many times for each one.

Through the ten configurations presented in Table-4.3, the first six have fitness values $f \leq 3$ while the last four have higher fitness values. The last four configurations are not the best solutions but show good results either for the spot size or for the divergence, but not both at the same time.

Concerning the first six rows of the table, we can identify three different combinations as highlighted by the colors. The first kind is composed of a "plateau", identified in green, whose voltages vary between $-55\ kV$ and $-70\ kV$. Such configurations end with small potential values below $-12.5\ kV$. The second kind has the $V1$ voltage fixed at $-63\ kV$, in red, and ends with a ramp, coloured in blue, with two different terminal value ($-70\ kV$ for the first and $-11\ kV$ for the second). Last but not least, the third kind shows two successive ramps. The first ramp, in purple, ranges from $0\ V$ (if we consider the first grounded electrode) to $-80\ kV$ in both cases and the second ramp, coloured in blue, presents different terminal values.

By using these configurations as inputs in a corresponding SIMION simulation, we realize that the potentials of higher values have a much more influence than the potentials of low values. As we saw, all combinations have 1, 2 or 3 strong potentials dominating the configuration. The most evident strong potentials appear in bold in Table-4.3. The influence of the other potentials being minor, they can be considered as weak potentials. So varying the value of a strong potential changes much more the fitness value than the one of a weak potential. The value of the weak potential only slightly impacts the prop-

agation of the beam as long as it does not reach approximately 75% of the value of the closest strong potential.

By injecting beam parameters as expected from ELENA[15], two configurations differ from those in Table-4.3. Both selected configurations have two strong potential and seem to show the ratios for the weak potentials. In order to study their relative influences, we empirically extrapolate formulas to determine the applied voltages.

The first one is found to be : $[-63.5,\ 0.0,\ -29.1,\ -48.9,\ -70.7]$.
Approximated relations for such voltage configurations, hereafter referred as $1P1R$ (*1 Peak, 1 Ramp*), are:

$$V1,\ V5 \in [-100kV, 0[\text{ and } V2 = 0V,$$
$$V3 = \frac{1}{3}V5,\ V4 = \frac{2}{3}V5 \tag{4.2}$$

The second one is found to be: $[-34.0,\ -74.5,\ -10.2,\ -22.1,\ -30.7]$.
Approximated relations for such voltage configuration, hereafter referred as $1R1R$ (*1 Ramp, 1 Ramp*), are:

$$V2, V5 \in [-100kV, 0[$$
$$V1 = \frac{1}{2}V2,\ V3 = \frac{1}{3}V5,\ V4 = \frac{2}{3}V5 \tag{4.3}$$

The remaining solutions highlighted in green in the Table-4.3 behave like a telescopic system with several electrodes holding the same voltage. As we saw in Chapter 3 with the light optics analogy, the further the first lens electrode(s), the better the focusing into the drift tube. This may explain why they haven't been selected after SIMION studies.

4.5 Choice of the preliminary beam configuration

Both "*Minimize Alpha*" and "*Minimize Beam Size*" configurations are tested for the three different distances proposed, see Table-4.2. In the case of both selected configurations $1P1R$ and $1R1R$, 2000 particles are simulated. The Tables-4.4 & 4.5 present the beam spot and beam divergence in the drift tube for the different cases.

1P1R	Beam spot X $1\sigma_X$ (mm)	Beam div. X $1\sigma_{X'}$ (mrad)	Beam spot Y $1\sigma_Y$ (mm)	Beam div. Y $1\sigma_{Y'}$ (mrad)
Distance 2m				
Min. Alpha	3.74	23.0	4.22	21.50
Min. Beam Size	5.41	35.66	5.59	29.74
Distance 3m				
Min. Alpha	3.92	26.64	4.30	21.62
Min. Beam Size	5.08	18.54	4.95	17.56
Distance 4m				
Min. Alpha	2.34	5.88	1.90	4.25
Min. Beam Size	2.48	6.76	1.96	4.22

Table 4.4 Beam parameters in the drift tube for the $1P1R$ electrostatic configuration.

The electrostatic configurations $1P1R$ and $1R1R$ are tested without refinement of the voltages. As we will see, these values can be improved.

[15]See previous section for details.

1R1R	Beam spot X $1\sigma_X$ (mm)	Beam div. X $1\sigma_{X'}$ (mrad)	Beam spot Y $1\sigma_Y$ (mm)	Beam div. Y $1\sigma_{Y'}$ (mrad)
Distance 2m				
Min. Alpha	2.07	38.70	2.55	37.46
Min. Beam Size	2.95	68.73	3.32	60.23
Distance 3m				
Min. Alpha	2.03	44.41	2.63	37.69
Min. Beam Size	3.11	39.80	3.24	35.00
Distance 4m				
Min. Alpha	1.63	10.52	1.29	8.96
Min. Beam Size	1.81	11.31	1.52	5.86

Table 4.5 Beam parameters in the drift tube for the $1R1R$ electrostatic configuration.

4.5.1 Optics modification

For technical reasons, the original design shown in Figure-3.7 has evolved. The distance between the $V2 - V3$ electrodes and between the electrode $V5$ and the drift tube have been enlarged as shown on Figure-4.6. Furthermore, the length of the PDT changed from 300 mm to 400 mm. This new design was used for the deceleration prototype in Orsay.

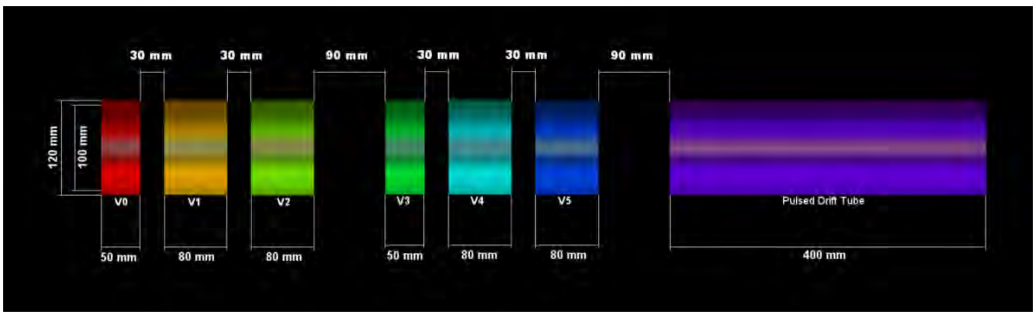

Figure 4.6 Schematic of the prototype design of the decelerator.

The modification of the distances between the optics inevitably impacts the trajectory of the ions. It is then necessary to modify the electrostatic configuration to compensate for the changes. The problem is to know if these changes have a strong impact on the value of the voltages compared to those applied for the original design. As we saw in the previous chapter, the system is highly correlated. In other words, changing the potential on one electrode can lead to changing the potentials on all the other electrodes.

We re-implemented the configurations found by the GA in SIMION with the new organization. We considered a gaussian beam following the "4m Minimize Alpha" configuration. The ion-flight simulation is exectued ion-per-ion and stop 500 mm downstream the drift tube. To not take into account temporal effects, the drift tube is switched to ground when the ion passes at the center of the tube. Figure-4.7 summarizes the ion trajectories comparing the preliminary and prototype designs with the configurations $1P1R$ and $1R1R$ as found by the GA. Figures-4.7-B1/B2 show beams with higher divergence downstream the PDT. They mark in both cases, the necessity to change some of the voltages.

Starting from the GA solutions, we then used the simplex method to find out if the prototype design displays new electrostatic configurations. As the simplex method

converges towards the nearest minimum, we assume that the new form of potential is relatively close to that found by GA. We applied the simplex method several times and found the following average configurations:

$$1P1R^* : \quad [-61.5, -4.5, -24.9, -44.7, -66.5] \tag{4.4}$$
$$1R1R^* : \quad [-30.3, -69.7, -0.5, -19.5, -32.5] \tag{4.5}$$

We can see that the $1P1R^*$ and $1R1R^*$ configurations are very close to the $1P1R$ and $1R1R$ initial voltages. The changes applied to the original design have a relatively small impact. The main change occurs on the first strong potential $V1$ for $1P1R^*$ and $V2$ for $1R1R^*$. Again, the weak potentials do not play an important role if they stay at less than 75% of the closest strong potential.

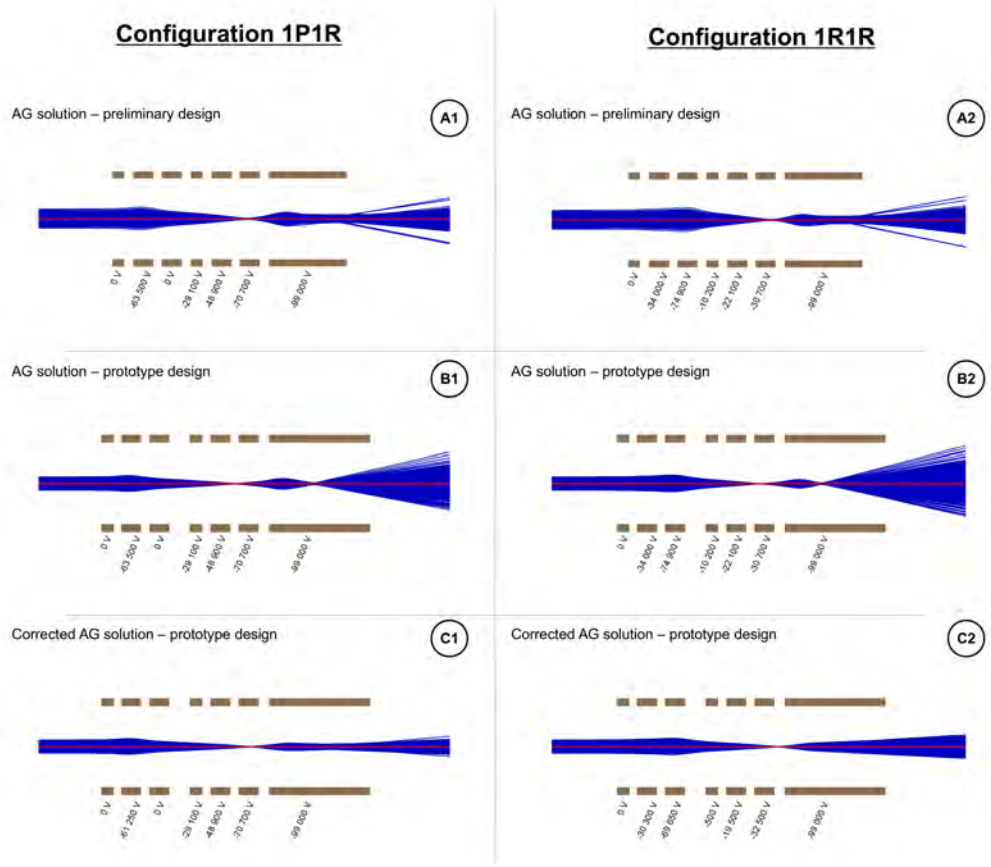

Figure 4.7 Comparison of the "4m Minimize Alpha" beam through the preliminary design (*Ax*) and through the prototype design (*Bx, Cx*) with the initial electrostatic configurations $1R1R$ and $1P1R$ (*Ax, Bx*) and with the corrected voltages as found with the simplex method (*Cx*). The voltage indicated below the drift tube is switched to ground when the particles reach the middle of the tube.

"Simplicity is the ultimate sophistication." (L. Da Vinci)

To summarize, from a multitude of configurations with 5 independent variables, the GA returned two main configurations, $1P1R$ and $1R1R$. Via extrapolations, we reduced the number of independent variables to only 2. These variables correspond to the value of the strong potentials carried by the electrodes (V1, V5) for the $1P1R$ configuration and the electrodes (V2, V5) for the $1R1R$ configuration. The other potentials, called "weak", do not participate significantly in the focusing of the beam in the drift tube. By the simplex method, we confirmed that the two voltage schemes found with the GA are also valid for the prototype design despite different inter-electrode gaps.

After deducing empirical relations between the strong and weak potentials, as expressed by the formulas Eq.-(4.2) and Eq.-(4.3), one may raise the question of the dependence between both strong potentials. In other words, are there other couples of solutions for $(V1, V5)|_{1P1R}$ and $(V2, V5)|_{1R1R}$, except Eq.-(4.4) and Eq.-(4.5), verifying the same beam conditions or improving them ?

In order to establish the correlation between the strong potentials, we performed a systematic calculation. We concentrated on the $1R1R$ configuration since it has the best results concerning the beam spot size in the drift tube. Following the same protocol as in the simulation in the Figure-4.7, we performed the simulation ion-per-ion stopping the flight of the ions 500 mm downstream the drift tube. When the particle flight is stopped, the X- and Y-positions as well as the elevation and azimuth angles are saved. If a simulated antiproton ends before reaching the downstream 500 mm limit, the latter is not counted. 5000 antiprotons are simulated following the "4m Minimize Alpha" beam configuration.

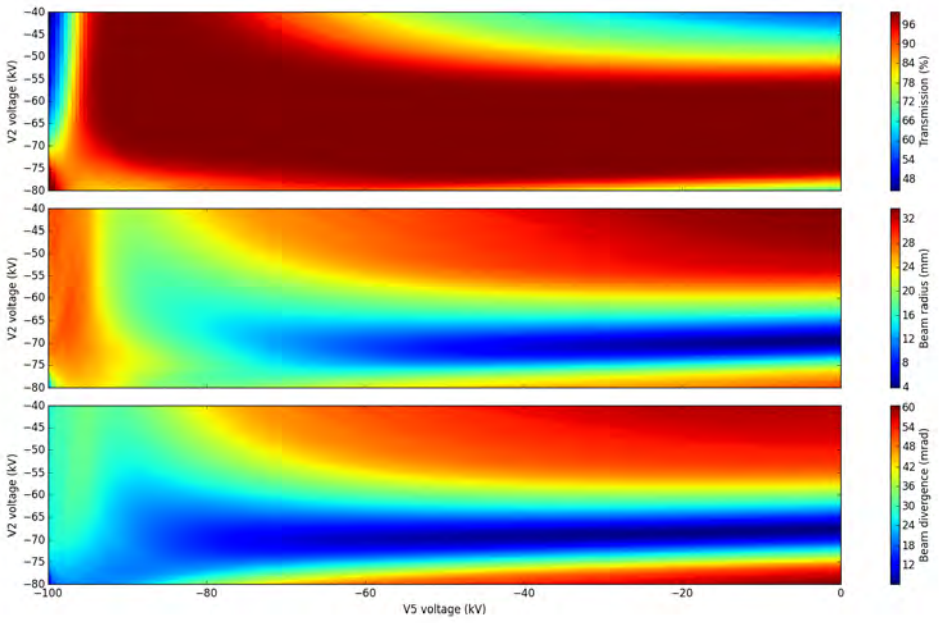

Figure 4.8 Systematic calculation method for the $1R1R$ electrostatic configuration through the prototype design of the decelerator depicted Figure-4.6. The transmission (*top*) is estimated from the ratio between the number of antiprotons in a $R < 50$ mm radius, 500 mm downstream the DT, with 5000 initial particles. The beam spot values (*middle*) and divergence values (*bottom*) correspond to the 1σ-values.

The result of the systematic calculation method is shown in Figure-4.8. The transmission rate through the decelerator apparatus (*top*) corresponds to the number of antiprotons reaching the end of the simulation (500 mm downstream the drift tube) with a radius $R < 50\ mm$[16]. The beam size (*middle*) and the beam divergence (*bottom*) values correspond to the 1σ-values.

We see from the top plots in the Figure-4.8 that the maximum transmission rate (100% for 5000 particles) coincide rationally when the beam size is small and the beam divergence is low. If we do not take into account the temporal effects and the impact on the energy distribution, the transmission is very good (above 96%) for $-75\ kV < V2 < -55\ kV$ and $-93\ kV < V5 < 0\ V$.

Regarding the middle plot in the Figure-4.8, we note that the beam size is minimal for V2 between $-65\ kV$ and $-73\ kV$. It reaches a minimum for $V2 = -69.250\ kV$. Conversely, the beam size does not depend strongly on the voltage applied to V5 for $V5 < -70\ kV$. For $-60\ kV < V5 < 0\ V$, the beam spot is smaller than 8 mm (1σ-value). However, the beam size slightly decreases with respect to V5. It reaches a minimum value (4 mm) when the latter tends to 0 V.

According to the bottom plot in the Figure-4.8, the same behavior is observed with respect to the beam divergence. Thus, we find that the beam divergence depends mainly on the value of V2. Similarly, the divergence decreases when V5 tends to 0 V.

The same development also applies to the $1P1R$ configuration. The strong potential V1 is then $V1 = -61.5\ kV$. The difference between the strong potential $V1 = -61.5\ kV$ in the $1P1R$ configuration and the strong potential $V2 = -69.25\ kV$ in the $1R1R$ configuration is easily explained by the distance between the electrode on which the strong potential is applied and the object focal point of the drift tube.

We can then imagine that a configuration with the $V1$ or $V2$ electrode polarized while all the others are grounded offers the best solution. Such solution is identical to the telescopic system proposed in the Chapter-3.

4.5.2 Discussion

It is pleasant to note how right was Edward Teller : *"Physics is, hopefully, simple."*[17]. The best solution appears to be a telescopic electrostatic system such as described in Chapter 3. It would be interesting to run the GA again with the prototype dimensions in order to see if after more than 100 generations, a similar result is found.

Energy of the beam In the case of GBAR, the initial energy of the antiproton beam passing through the decelerator is fixed at 100 keV and those of the proton beam at 10 keV. As previously seen, the decelerator is supposed to decelerate antiproton beams from 100 keV to 1 keV. It must also be able to offer antiproton pulses to the rest of the GBAR experiment within an energy range between 1 keV and 10 keV. When working with the matter equivalent charge exchange reaction, the decelerator is also supposed to decelerate the 10 keV proton pulses from the GBAR internal source to 1 keV. A remaining question is : what are the potentials we have to apply when decelerating pulses to higher energies ? What are the voltages when the initial energy of the beam is not 100 keV ?

[16] $R = 50\ mm$ corresponds to the radius of the beam pipe downstream the decelerator cavity.
[17] E. Teller continued : "... Physicists are not."

At first sight, it seems easy to establish the electrostatic configuration for decelerating an antiproton pulse from 100 keV to 10 keV starting from the configurations found in Eq.-4.2 and Eq.-4.3. But the idea that a correction factor[18] should be applied to all the voltages is not true. Such a mathematical shortcut would be effective only if all the initial parameters of the beam are modified by the same factor. Indeed, cross-multiplying appears to not be a good solution and a practical example of such a problem is exposed in Chapter-5 with the particular case of the Orsay decelerator prototype tested with a 50 keV source.

Back to the simplest telescopic solution, one can find that reducing the potentials cross-multiplying with the potential on the PDT worsens the transmission through the decelerator. Indeed, when decreasing the potential on the DT, the object focal point of the DT moves away from the tube (cf Chapter-3, Figure-3.9). To compensate for the upstream displacement of the object focal point, the voltage on the lens must be increased.

Downstream refocusing According to the previous sections, we found the best configuration to be a telescopic configuration with $V1 = -61.5\ kV$. The Figure-4.9 shows a comparison of a 100 keV antiproton beam through such an electrostatic configuration considering an additional Einzel lens downstream the PDT.

The design used in these SIMION simulation correspond to the prototype design as illustrated in the Figure-4.6. The beam is composed of 5000 antiprotons are generated 3 m away from the decelerator following the initial "4m Minimize Alpha" beam configuration. While passing through the pulsed drift tube, antiprotons are decelerated from 100 keV to 1 keV. The potential on the drift tube is switched from $-99\ kV$ to ground at $t = 2.29\ \mu s$.

The following plots illustrate the beam profile as expected 500 mm downstream the PDT. Without refocusing system, the beam spot is 32 mm on the X-axis and 26 mm on the Y-axis with 95% confidence level. By introducing an Einzel lens between, the beam spot measures then 19.7 mm on the X-axis and 17.0 mm on the Y-axis with 95% confidence level.

We will see in the next chapter that the refocusing system behind the PDT has been investigated using other type of optics in order to improve the transmission through the Ps converter.

[18] Found to be the ratio between the desired final potential on the PDT with the initial $-99\ kV$ potential.

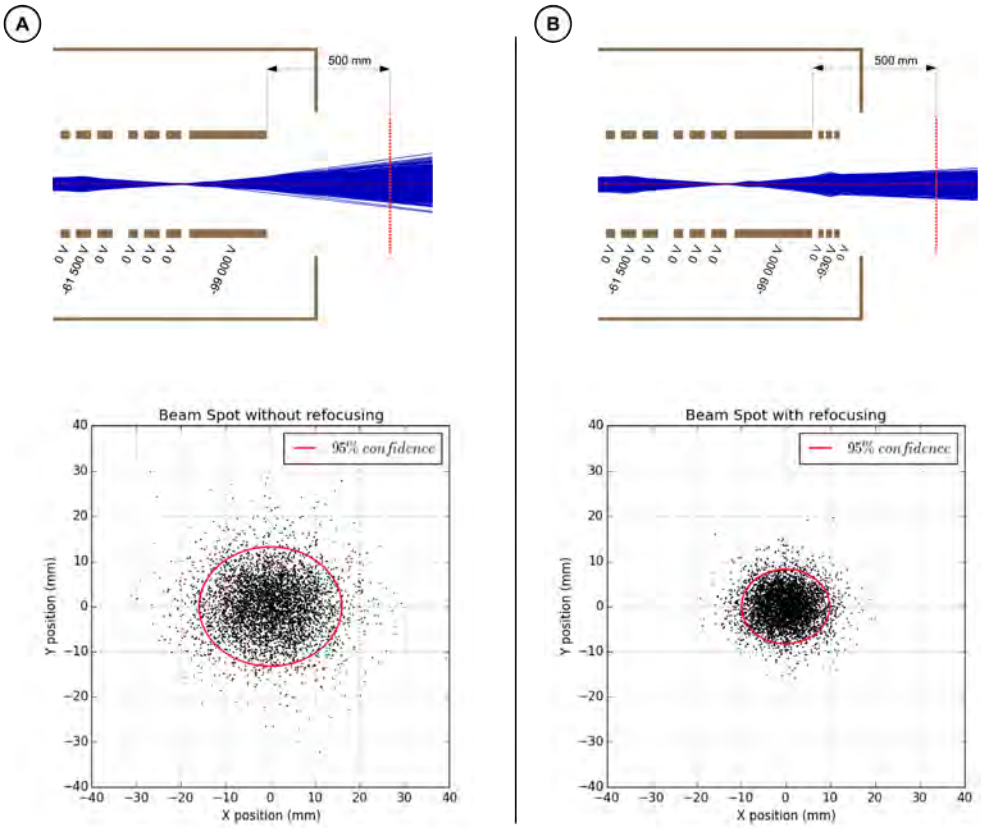

Figure 4.9 Comparison of the refocusing impact downstream the PDT. In the top figures, the red dashed lines correspond to the place where the beam profile is taken. In the bottom plots, the red circles correspond to the 95% confidence ellipse. (A) Trajectories without refocusing system. (B) Trajectories with an Einzel lens for refocusing. The potential applied on the center electrode of the Einzel is $V = -930V$.

Chapter 5

GBAR Antiproton Decelerator Setup & Results

5.1 Prototype off-line test bench and measurements

To pursue the study of the deceleration principle, an off-line prototype of the decelerator had been tested up to 50 keV with beam provided by a Penning-type discharge source.

As elaborated in Chapter 3 and 4, we proposed a decelerating system made of a series of six electrostatic, cylindrical lenses followed by a 300 mm-long drift tube. The geometry of the electrodes has been chosen in order to minimize the risk of arcs. The cylindrical symmetry (axisymmetry) guarantees good resistance to high voltage by limiting coronal discharges.

Following the design presented in Figure-4.6, the pre-decelerating electrodes are divided in two triplets (see Figure-5.1). As shown in Figure-5.2, they are insulated from

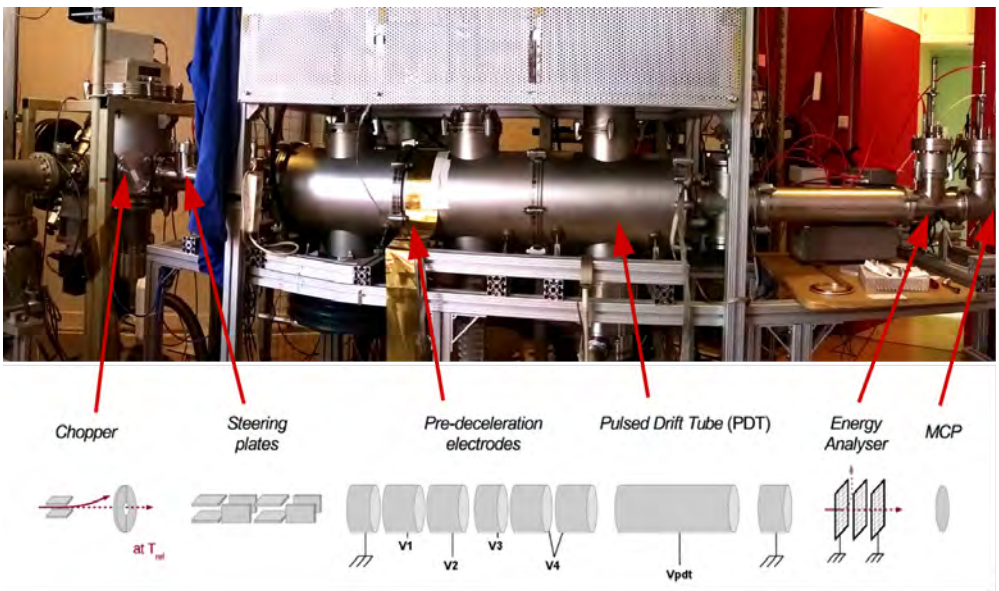

Figure 5.1 Picture and schematic of the prototype off-line decelerator test bench as installed in Orsay from 01/2016 to 08/2016. The ion beam is flying from left to right over 3 m.

Figure 5.2 Triplet of pre-decelerating electrodes mounted on the aluminum frame with Macor rods.

the beam pipe by Macor rods. The whole triplet structure is supported by an aluminum frame. The gap between the triplets of electrodes is determined by the size of these frames and fixed to 90 mm.

Due to lack of space, we were not able to use a refocusing system downstream the pulsed drift tube. We then chose to install the diagnostic part directly downstream of the PDT with enough distance to resolve the different species of ions in time and not to pick up the electromagnetic noise while switching the tube. Although the refocusing problem was partly solved by increasing the potential on the upstream electrodes, as we will see, the beam signal suffered from a too low intensity downstream the PDT.

The decelerated beam energy was scanned with the use of the energy analyzer made of three successive meshes installed on a movable support as shown in Figure-5.3. In addition to this energy analyzer, a Faraday Cup (*FC*) allowed to measure the beam current. Finally, a MCP detected the beam at the end of the line and sends the signal through a low-pass filter and an amplification chain to an oscilloscope coupled with a monitoring computer.

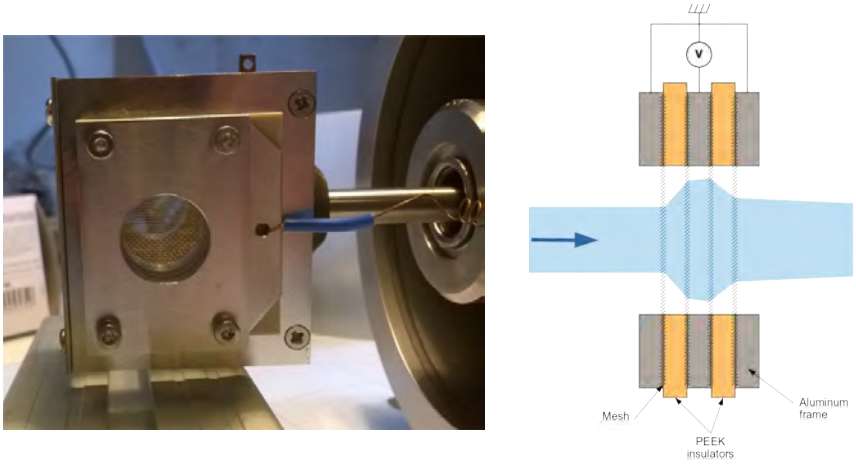

Figure 5.3 (*left*) - Picture of the energy analyzer used in the prototype of the decelerator. (*right*) - Schematic of the energy analyzer detector. The beam is displayed in blue, the insulating parts are beige and the conducting parts are grey.

5.1.1 Orsay proton source

The source used to test the Orsay decelerator prototype is a Penning-type ion source. Developed since the first discharge experiments performed by Penning in 1936 [155], it consists of a DC discharge generating ions in a so-called *plasma cavity*. In our case, such an ion source is filled with H_2 gas. As shown in Figure-5.4, the DC high voltage V_d is applied between the anode (in green) and the cathode (in yellow) and is typically of the order of $V_d = 3.0\ kV$. The electric field induced by the difference of potential V_d forces the ionizing electrons to oscillate between the cathodes.

The path of the ionizing electrons is further increased by the addition of a magnetic field along the axial direction of the discharge chamber. The magnetic field induces a Larmor gyration of these electrons around the magnetic field lines with a frequency:

$$2\pi f = \omega = \frac{eB}{m_e} \tag{5.1}$$

with a radius :

$$r = \frac{m_e v_\perp}{eB} \tag{5.2}$$

with m_e the electron mass, B the axial magnetic field and $v_\perp$ transverse velocity of the particle.

For electrons in the Orsay Penning-type ion source, it corresponds to a frequency of $1.10^{10}\ rad/s$ ($\approx 1.6\ GHz$) and a Larmor radius of $1.8\ mm$, respectively, based on an axial magnetic field strength of $580\ G$. Since the Larmor radius is smaller than the dimension of the discharge chamber, the ionizing electrons are then radially trapped by the axial magnetic field and longitudinally trapped by the potential difference between the cathodes and the anode.

Electrons in the neutral gas are accelerated by the applied electric field and undergo collisions with the H_2 molecules. If the electron has sufficient energy, it removes one or

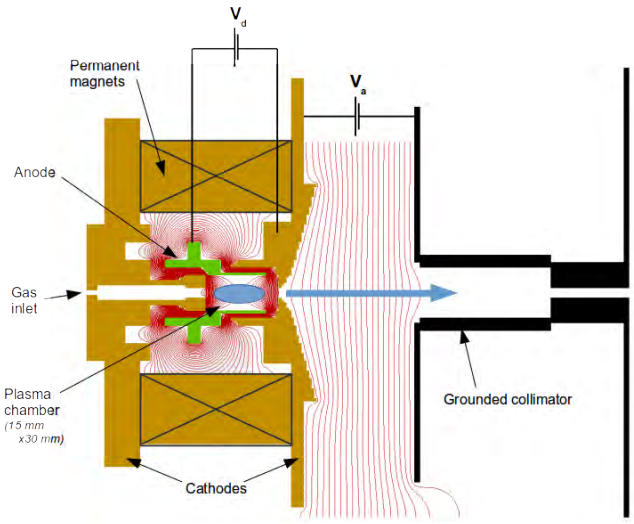

Figure 5.4 Schematic of the Orsay Penning-type discharge source. The green piece corresponds to the anode, the yellow one to the cathode and the black one to the grounded collimator playing also the role of extraction electrode. The magnetic field is longitudinal. The plasma cavity is $\emptyset 15\ mm \times 30\ mm$. The electrostatic configuration is $V_d = 3.0\ kV$ and $V_a = 5.0\ kV$. The red lines correspond to equipotentials with $100\ V$ steps. The blue ellipse corresponds to the trapped electron region.

more electrons from the neutral atoms, resulting in secondary electrons increasing further the number of ionizing electrons. The plasma is then ignited and sustained by these multiple collisions.

$e^- + H_2$	$\longrightarrow$	$e^- + H + H$	8.8 eV
$e^- + H$	$\longrightarrow$	$e^- + e^- + H^+$	13.6 eV
$e^- + H_2$	$\longrightarrow$	$e^- + e^- + H_2^+$	15.4 eV
$e^- + H_2$	$\longrightarrow$	$e^- + e^- + H + H^+$	18 eV
$e^- + H_2$	$\longrightarrow$	$e^- + e^- + e^- + H^+ + H^+$	46 eV

Table 5.1 Ionization processes in hydrogen gas with respect to the electron impact energy. Data from Ref.[156].

The Table-5.1 lists the various collision processes and products for electrons in a hydrogen gas environment. The dominant ionization process is the electron impact ionization of the hydrogen molecule. The created protons and H_2^+ ions are much more massive than the electrons and are not confined by the axial magnetic field. They are swept to the two cathodes by the symmetric potential distribution within the discharge region and accelerated by the applied electric field.

For the Orsay source, an aperture of 4 mm diameter in one cathode allows the ions to exit the discharge chamber. The ion source components (yellow and green in the Figure-5.4) are floated at high voltage. The application of an electric gradient V_a between the plasma chamber and a grounded (extraction) electrode produces a beam and accelerates it for the final application with a energy $E = qV_a$. The collimator is located 75 mm from the cathode with a 4 mm aperture and is 30 mm long (see Figure-5.5 (*left*)). The extracted ion current is a function of both the plasma density within the ion source and the size of the extraction aperture.

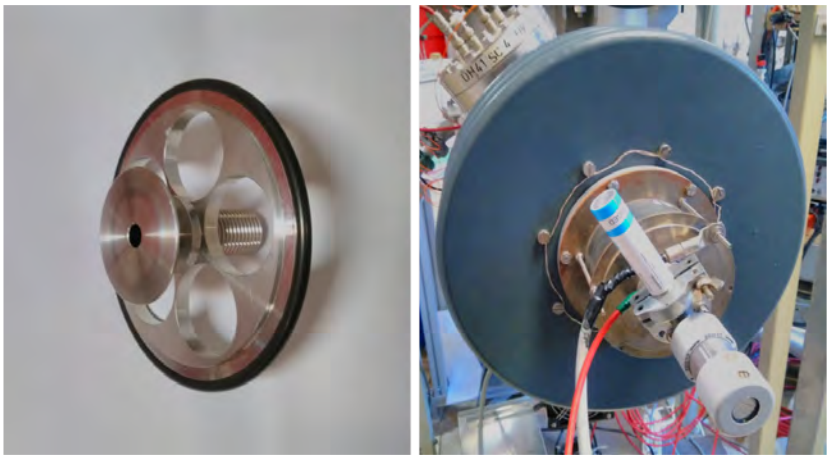

Figure 5.5 (*Left*) - Picture of a collimator and extraction electrode. (*Right*) - Picture of the Orsay source. The blue and white bottle is the *Hydrostik* hydrogen reservoir.

For a fixed magnetic field and applied discharge voltage, the source operates in several modes that depends on the pressure within the plasma cavity. The discharge current is generally proportional to the source operating pressure motivating the use of the Penning discharge for pressure gauge [157]. Higher or lower pressures within the discharge chamber result in higher neutral density and the mean free path for ionization electrons decreases. Operation in these regimes requires frequent pressure adjustment and can become unsta-

ble[1]. As the gas pressure in the plasma cavity is quite hard to measure, an indirect setting for the pressure has to be employed. The pressure in the plasma chamber is evaluated qualitatively from the pressure indicated by the closest gauge directly downstream the source[2]. In absence of mass flow regulator, a full investigation of the different regimes for the Orsay source was not possible but the best parameters for long time operations were found to be $V_d = 3.0\ kV$ with the pressure read on the closest gauge $p = 1.10^{-6}\ mbar$. With such settings, the routinely extracted current was around $1 - 2\ \mu A$ at $5\ keV$.

Working with hydrogen, the atomic ion fraction[3] in the extracted beam is low, on the order of $1\% - 15\%$. According to Ref.[161], the low atomic ion fraction can be explained by the low electron density (and thus the low plasma density) and short mean free path of molecular H_2^+ ions in the plasma chamber. Furthermore, additional secondary electrons are emitted from the grounded collimator under ion impacts. These secondary electrons are accelerated back into the discharge region and represent a serious problem for H and H_2 recombination. The possibility to use electron repelling plates has been investigated but spark generation for $V_a > 10\ kV$ was observed and complicated the source operation.

Another explanation for the low atomic ion fraction can be found in Ref.-[156]. At primary electron energies relevant to such a source of the order of 1000 eV, the cross-section for the creation of a molecular H_2^+ ion is one order of magnitude higher than the one for the creation of an atomic H^+ ion when both originate from molecular H_2. The H^+ ion is formed from electron impact on the atomic H neutral, but this event requires the prior dissociation of neutral H_2. More detailed investigations to improve the atomic ion fraction can be found in literature as in Refs.-[162, 163].

The source is supplied with gas provided by a hydrostik cell of 10L (see the blue cell on the right picture in Figure-5.5). In order to study the species distribution extracted from the Penning-type ion source, two mass spectroscopic techniques have been used.

Wien filter Developed in 1898 [164, 165], it consists in two independent electrodes face to face operated in a magnetic field. By applying in addition a difference of potential between both electrode plates, an electric field is generated perpendicular to the magnetic field. For $V_\perp = 0\ V$, the charged particles are deflected by the magnetic field with a force $\vec{F} = q\vec{v} \times \vec{B}$ with q the charge of the particles, $\vec{v}$ the velocity of the particles and $\vec{B}$ the magnetic field. By applying, a difference of potential V, the deflection of the ions can be counterbalanced depending on their speed.

$$\vec{F}_{mag} = q\vec{v} \times \vec{B} \tag{5.3}$$
$$\vec{F}_{elec} = -q\vec{E} \tag{5.4}$$
$$\tag{5.5}$$

with $\vec{F}_{mag} + \vec{F}_{elec} = \vec{0}$, then:

$$E = vB \tag{5.6}$$

with $\vec{E}$ the electric field between the electrode plates.

In the case of the Orsay Penning-type source, a 5000 G magnetic field is provided by two permanent magnets. Since the generated ions are supposed to be single-charged ions and since the accelerating potential ramp is fixed in time, the initial speed of the particles depends directly from the initial energy and then from their mass.

[1] Detailed explanation of major instability processes in these regimes may be found in Refs.-[158, 159, 160].

[2] It follows the principle of the calibrated leak technique.

[3] Defined in Ref.[156] as the fraction of atomic versus molecular ions.

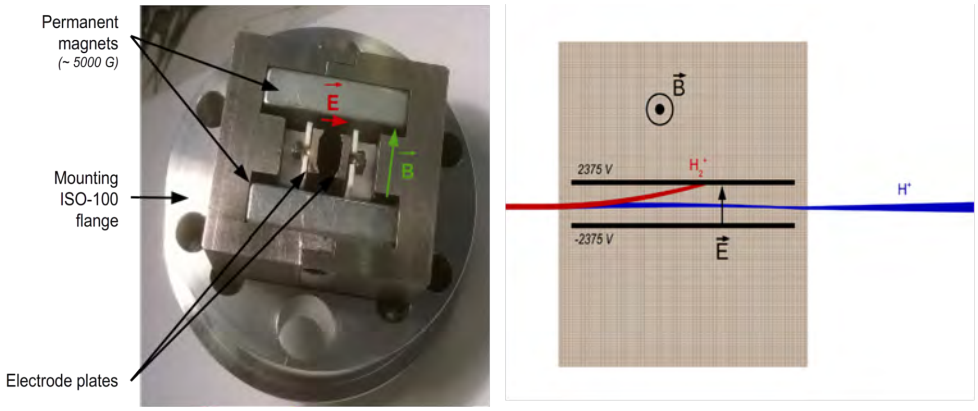

Figure 5.6 (*Left*) - Picture of the Wien filter on its mounting flange. (*Right*) - SIMION simulation of the Wien filter for a 10 keV H^+/H_2^+ beam example. The initial beam is here 2.5 mm-large and parallel.

The relation between the difference of potential ΔV and the mass becomes:

$$\frac{\Delta V}{d} = \sqrt{\frac{2K}{m_i}} B\ (c) = \sqrt{\frac{2qV_{acc}}{m_i}} B\ (c) \tag{5.7}$$

with ΔV, the difference of potential between the Wien filter electrodes; $d = 7\ mm$, the distance between the plates; $K = qV_{acc}$, the initial kinetic energy proportional to the accelerating potential V_{acc}; q, the charge of the ion and c, the speed of light.

Figure-5.6 presents the Wien filter used in Orsay with trajectory examples made with SIMION.

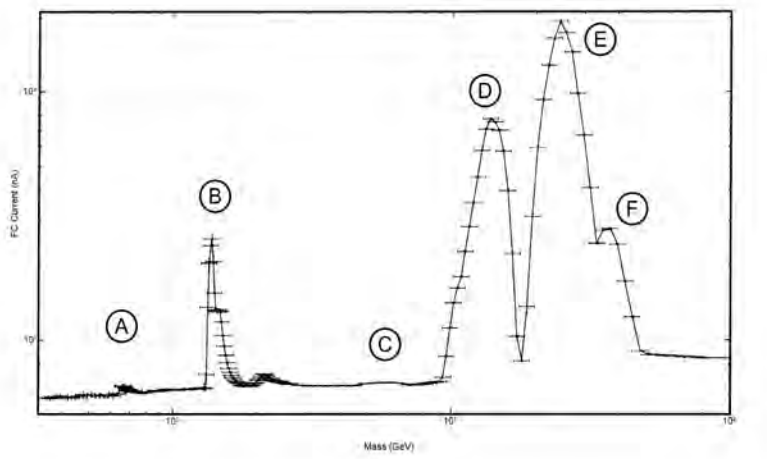

Figure 5.7 Wien filter spectrum of the Penning-type source.

Studying the species distribution consists to scanning the mass domain by changing the potential applied on the electrodes of the Wien filter. Such a technique is advantageous because it does not require a pulsed beam. The signal is acquired on the Faraday Cup at the end of the line and related to the difference of potential applied between the Wien filter electrodes.

From the Wien filter spectrum shown in Figure-5.7, we can identify ion species such as H^+ (A), H_2^+ (B), CH^+ (C), H_2O^+ (D), CO^+/N_2^+ (E) and O_2^+ (F) according to their mass assuming a slight shift (especially for the smallest masses).

Time-of-flight spectrum Another method used to establish the species distribution of the Penning-type source consists in pulsing the beam in order to perform time-of-flight (TOF) measurements. Such a technique requires to let the pulses fly over a sufficient distance to differentiate between species.

The beam is chopped with a pair of deflector plates followed by a 15 mm aperture (see Figure-5.1). The applied voltage is pulsed by a switch[4] with a 1 second repetition period. For all measurements, the initial time T_{ref} is defined when the potential on the deflector plates is turned off. Four pairs of steering plates, two for each direction, allow to center the ion pulses.

Here, a 20 keV pulse, 1 μs-long, is generated through the decelerator off-line prototype. The signal is acquired after 3 m of flight on a Multi-Channel Plate (MCP). This technique was used to obtain the TOF spectrum in Figure-5.8. A comparison is realized with SIMION to identify the different species. The results with the flight time method corroborate those obtained with the Wien filter.

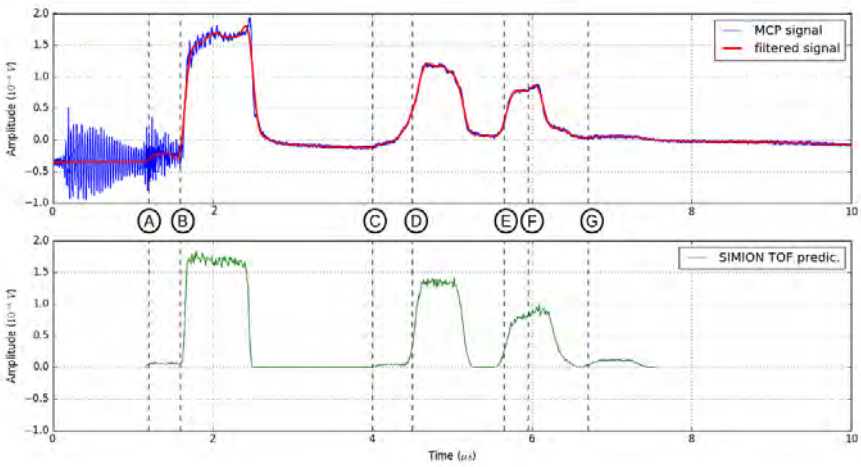

Figure 5.8 (*top*) - Signal acquired on the MCP (*blue*). The noise on the left part of the signal is coming from the high voltage switch used to pulse the beam. A numerical low-pass filter is applied (*red*) to emphasize the signal shape. (*bottom*) - Corresponding SIMION simulation. The vertical dashed mark on both plots the different species simulated with SIMION for comparison: (A) - H^+ ions, (B) - H_2^+, (C) - CH^+, (D) - H_2O^+, (E) - CO^+, (F) - N_2^+ and (G) - O_2^+. The amplitude of the species in the simulation has been adapted a posteriori to fit with the signal shape and check the identification.

Advantages and disadvantages The Penning-type source used in Orsay for the decelerator off-line prototype is a multi-species source. Unfortunately, the atomic ion fraction is very low and does not allow a pure proton deceleration. However, this distribution of species offers the opportunity to test the deceleration on the CO^+ and N_2^+ ions while keeping the others species as references for TOF measurements. A difficulty remains the bad repeatability of the measurement over long time because of pressure variations in the plasma chamber.

[4]Push-Pull GHTS 10kVDC-100A BEHLKE model.

5.1.2 High Voltage circuit

Ion trajectories through the decelerator were shown in Chapter 3 and 4 while simulating the pulsed drift tube. Constructing a real system that holds 100 kV and switches it to ground in less than 200 ns is far from trivial. Extrapolated from the ISOLTRAP experiment, running typically at only 30 kV, we believe this is the first such system working at 100 kV. Here, we describe the HV switch, circuit and protection system.

From an electrical point of view, a charged cylindrical electrode storing electrical potential energy placed into a grounded tube and isolated by vacuum, is equivalent to a capacitor. A measure of the capacitance was found to be $C_{proto} = 100\ pF$ for the decelerator in its off-line prototype design with a 300 mm-long drift tube and $C_{final} = 25\ pF$ for its on-line design with a 400 mm-long drift tube.

Pushing this reasoning, pulsing the drift tube potential and quenching the electrostatic potential energy consists of operating a capacitor discharge. To perform a correct deceleration, the drift tube has to be switched to ground when the bunch flies through. Considering a 300 ns long bunch decelerated to 1 keV, it represents a fall-time lower than 175 ns. Such operation appears easy when dealing with low-voltage devices but it becomes more complex when tensions reach 100 kV.

VHV switches

The main problem of the discharge operation is the transition from the polarized state to the unpolarized state[5]. To perform such switching, two Very High Voltage (VHV) MOSFET[6] switch devices have been specially designed by the BEHLKE company.

The first one is a HTS 1501-20-LC2 as presented in Figure-5.9. This MOSFET device performs 150 kV switching with a maximum current acceptance of 200 A and a minimum turn-on time of 10 μs. This switch is a *one-way* switch also referred as *single pole, single throw* switch ($SPST$). This name corresponds to a simple on-off switch with two terminals, either connected together or disconnected from each other. For simplicity, the SPST denomination will be used hereafter.

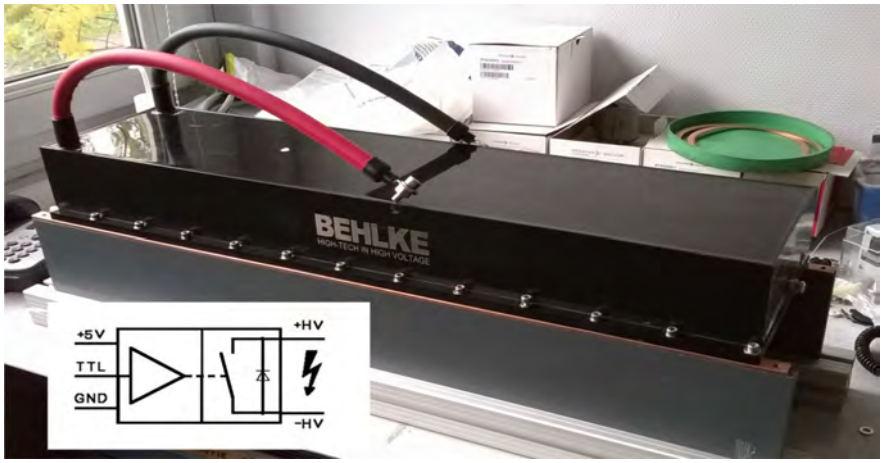

Figure 5.9 Picture of the BEHLKE HTS 1501-20-LC2 single pole, single throw (very) high voltage switch. The switch is presented mounted on insulated plastic supports.

[5]Here, (un)polarized means that the component is (un)charged.
[6]Standing for Metal-Oxide-Semiconductor Field-Effect Transistor.

The second switch is a HTS 1401-20-GSM as presented in Figure-5.10. It performs $2 \times 140\ kV$ switching with a maximum current acceptance of 200 A and a minimum turn-on time of 10 μs. This switch is a *two-way* switch also referred as *single pole, double throw* switch (*SPDT*). The latter corresponds to a simple break-before-make changeover switch where a *COM* pole can be connected either to a positive polarity or to a negative polarity pole. For simplicity again, the SPDT denomination will be used hereafter.

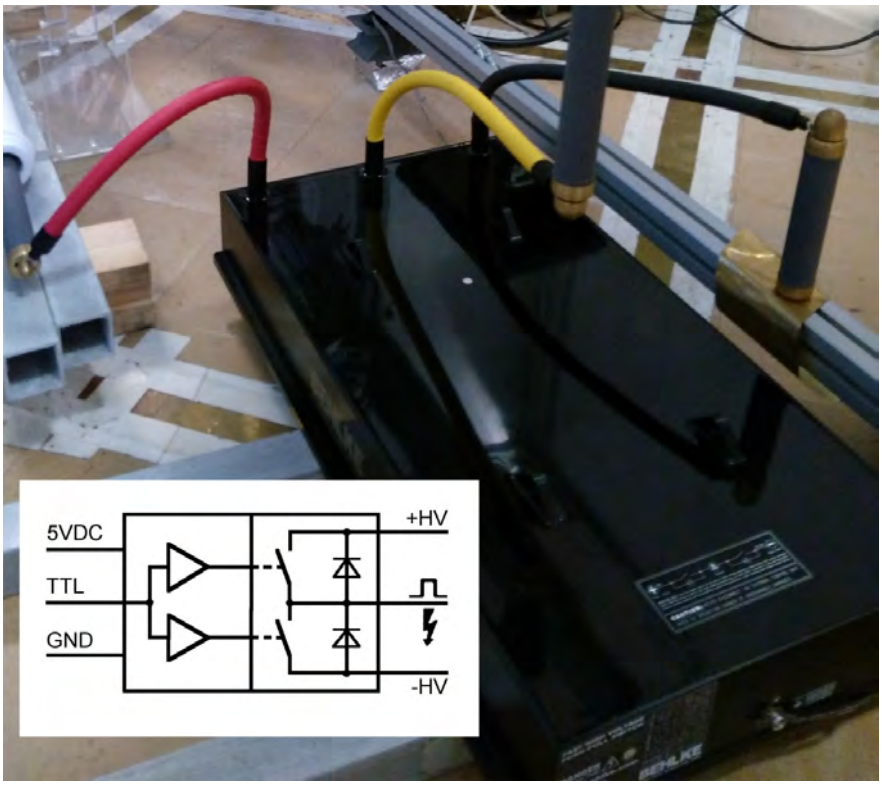

Figure 5.10 Picture of the BEHLKE HTS 1401-20-GSM single pole, double throw (very) high voltage switch.

The SPST switch allows us to build a simple pulsed HV circuit where the drift tube is switched from $\pm 100\ kV$ to ground. It is an ideal tool for fast switching tests and commissioning. In the future, the SPST switch can be replaced by the SPDT switch. The double-throw switch will enable to change the polarity of the drift tube. It will be possible, for 100 keV $\bar{p}$ beam deceleration, to switch from $-49\ kV$ to $+50\ kV$[7], when a single SPST switch can only switch the PDT to ground. Then, techniques, such as rebunching and time-focus, will be achievable by applying a ramping positive potential.

In the following HV circuit description, the polarity of the system is positive to perform proton deceleration. The design of the HT circuit in negative polarity for the deceleration of the antiprotons is strictly identical except for the connections to the BEHLKE switch. The latter must be reversed to accommodate negative voltages.

HV pulsing circuit

The 100 kV tension to charge the drift tube is delivered by a bipolar Spellman power supply SL150. According to the technical data from Spellman, this power supply can deliver a maximum current of $I_{max} = 1.5\ mA$. A resistor $R_{supply} > 35\ M\Omega$ is used to

[7]The current SPDT circuits displayed in Figure-5.12 needs to be modified to support the transient.

limit the current when switching the DT to ground. In our case, a resistor $R_{supply} = 1\ G\Omega$ (see Figure-5.12), has been chosen in order to increase the complete rise time to $t_{load} = 5 \times R_{supply}C = 0.5\ s$[8]. Such high value resistance limits the corona effect when re-polarizing the DT.

According to BEHLKE technical data, the optimal operating current should not excess (with safety margins) 150 A. Then, a resistor in series with the switch limits the current flowing through it when depolarizing the DT. Considering the maximum operating voltage $V = 150\ kV$, the resistor has to be $R_{limit} > 1.0\ k\Omega$ (cf. Figure-5.12). To avoid impacting the fall time, the smallest resistance value has be chosen ($R_{limit} = 1\ k\Omega$).

From those values, one can estimate the discharge time constant τ for both off-line prototype and on-line designs. Neglecting the parasitic inductive and capacitive effects, the latter is evaluated as $\tau = R_{limit} \times C_i$ where the C_i correspond to the capacitance in each case. The discharge time constants are found to be $\tau_{proto} = 100\ ns$ for the off-line prototype design and $\tau_{final} = 25\ ns$ for the final on-line design.

These values are still lower than the 175 ns time required for the bunch to cross the entire drift tube at 1 keV. While switching from the polarized state to the unpolarized state, the 1 keV bunch moves over a 78 mm distance. The Figure-5.11 shows a complete 1 s cycle.

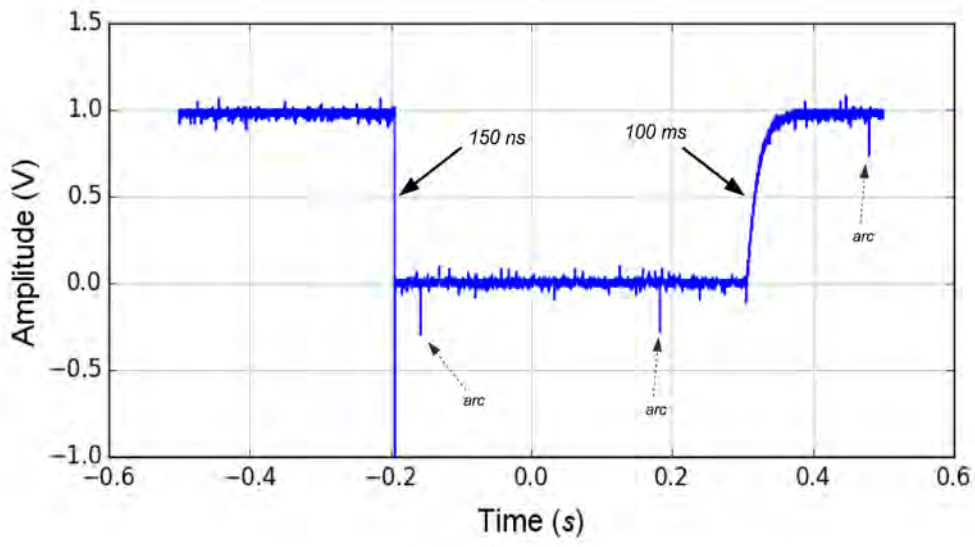

Figure 5.11 PDT potential measured through a $1 : 10'000$ divider probe during a complete $1s$ switching cycle on the decelerator. The potential applied on the pulsed drift tube is 10 kV with the SPST configuration as illustrated in Figure-5.12a. The overshoot at $t = -0.2s$ is induced by the resistive nature of the probe. Three undesired arc signals are visible.

Another element to point out from BEHLKE technical data is the leakage current $I_{leak} < 20\ \mu A$ through the MOSFET switch in *closed* mode. Such a leakage current induces an error on the actual value of the potential applied on the DT. With a current of 20 μA and an initial voltage of 100 kV, the actual voltage applied on the DT is only 80 kV. To suppress the effect of the leakage current, a low value resistor $R_{over} = 120\ \Omega$

[8] $t_{load} = 0.125\ s$ for the final on-line design of the decelerator.

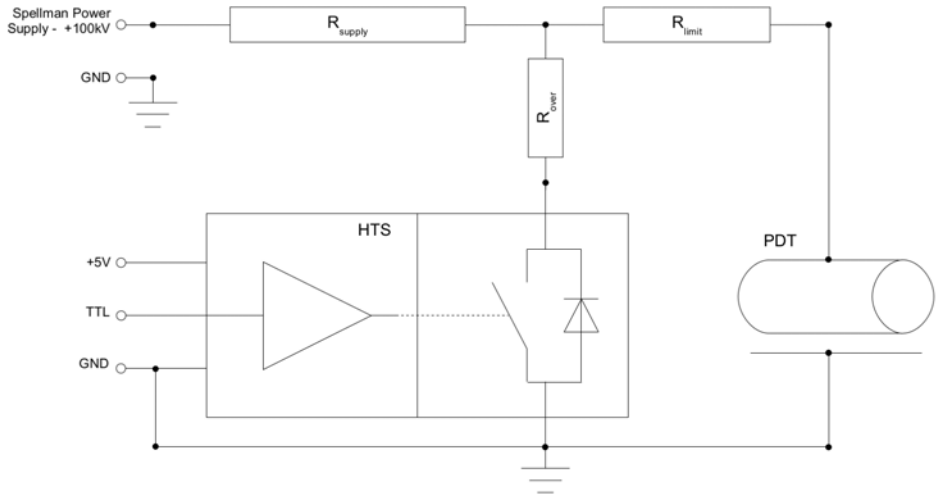

(a) SPST switch design.

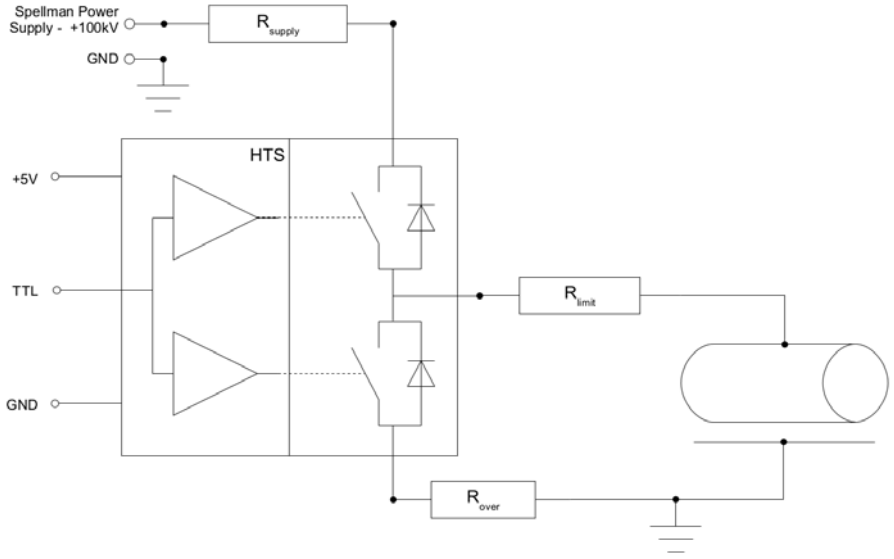

(b) SPDT switch design.

Figure 5.12 Schematic of the pulsed high voltage circuit when working with (a) - the SPST switch or (b) - the SPDT switch. The schematic corresponds to the design for proton beam deceleration and accept only positive polarity. The connection to the switch must be reversed to accept negative polarity. $R_{supply} = 1\ G\Omega, R_{limit} = 1\ k\Omega,\ R_{over} = 120\ \Omega$.

is introduced in series with the resistor R_{supply} and the switch. The value of such resistor has been chosen in order to limit the overshoot phenomena associated with parasitic inductive effects. With $R_{over} = 120\ \Omega$, overshoots are limited to less than 10% of the voltage step.

A schematic of the pulsed HV circuit with the SPST switch and an equivalent design for work with the SPDT switch can be found in the Figure-5.12.

High Voltage protection

The realization of such a pulsed high-voltage circuit is a real technical challenge. Indeed, we must take into account mechanical, electrical and safety constraints.

As presented in the Figure-5.13, the resistors R_{supply}, R_{limit} and R_{over} are specific non-inductive, ceramic resistors dedicated to pulsed high voltage purposes. They are connected to each other through large brass connectors carefully machined with no protruding edges that would cause corona (or sparking).

To avoid any deleterious capacitive effect, all the pulsed parts of the HV circuit have to remain unshielded. Protection of users and electromagnetic compatibility is ensured by a copper Faraday cage. For mechanical reasons, the entire pulsed system (Faraday cage plus high voltage components) is placed under the decelerator chamber and the Faraday cage is included in the decelerator chamber frame.

According to the safety rules [166, 167, 168], any live equipment must be protected from direct or indirect[9] electrical contact with grounded elements. For this purpose, it is common to place the exposed electrical equipment in environments with a high dielectric strength such as, in SF_6 gas, refined oil or insulating cast resin. However, these solutions represent a particular difficulty for maintenance in case of component failure.

Therefore, a simple air-insulated installation has been chosen. According to Ref.-[169], the dielectric strength of dry air at $25°C$ is almost 3 $kV.m^{-1}$. For safety reasons, this value is lowered to $1kV.m^{-1}$ when designing electrical equipment. Air-insulate live components held at 100 kV requires 10 cm distance for flat surfaces (i.e. homogeneous fields).

Corona discharge Even if the risk of electric arc can be diminished by respecting a safe distance, it is not enough to suppress *corona discharge* in the Faraday copper box. Corona discharge occurs in the vicinity of a charged component when locally the strength of the electric field is high enough to ionize the molecules of the surrounding gas (or fluid) but when the closest path through the surrounding medium is too long to initiate an electric arc or breakdown. In our case, corona is an undesired effect since it induces current leakage in the circuit, limits the applied voltage and produces ozone.

The corona effect can be extinguished by taking care to reduce the strength of the local electric fields at the surface of the high voltage components. Indeed, corona discharge occurs mainly on surfaces with sharp edges or points, where the electric field lines converge. The design of the high voltage circuit encased in the Faraday cage consisted of smoothing the charged surfaces, increasing contact areas and conductor size, and building of a dielectric barrier (see Figure-5.14).

[9] Inductive or capacitive effects.

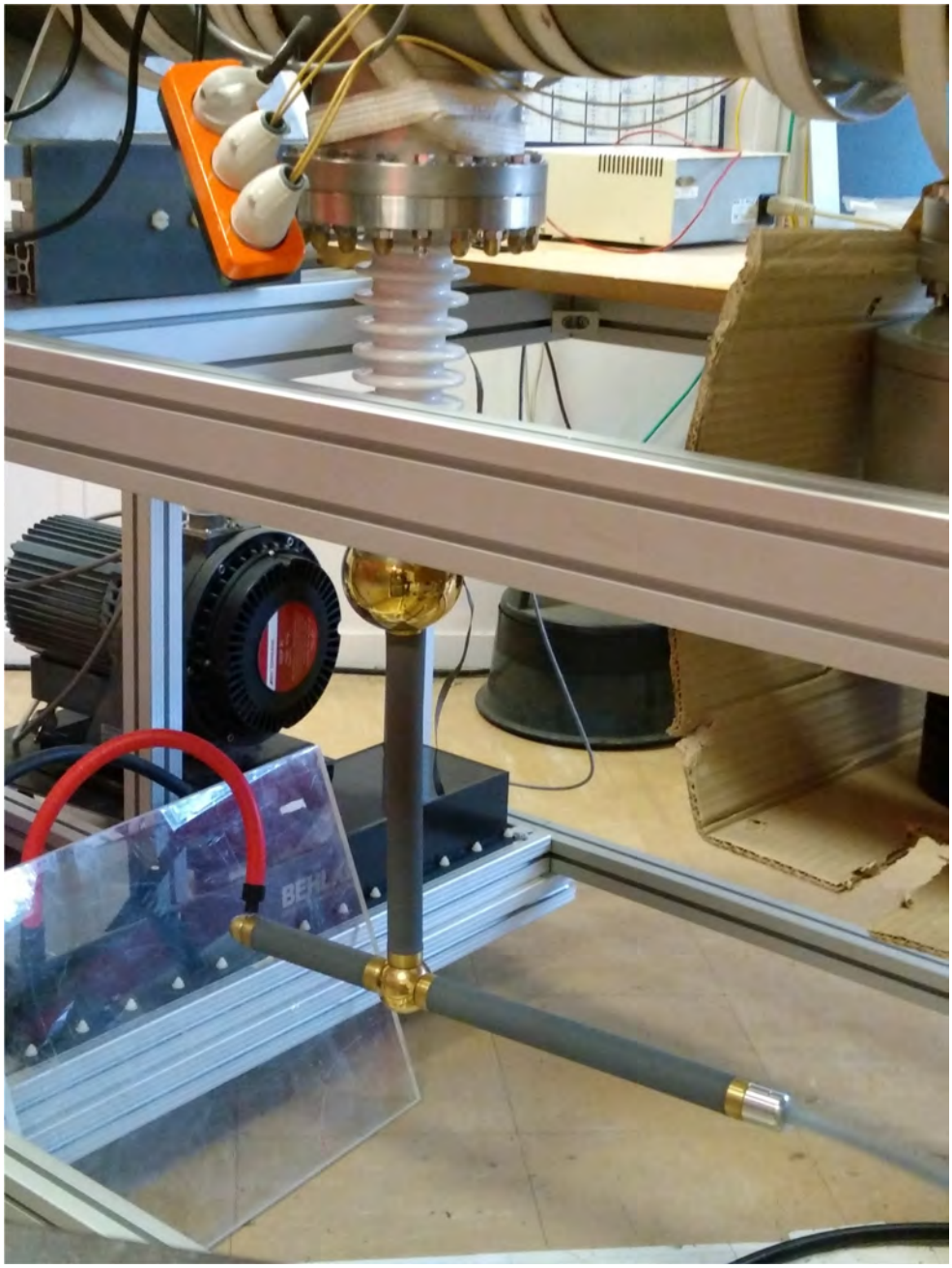

Figure 5.13 Picture of the high voltage assembly in the SPST configuration. The grey bars are the high voltage ceramic resistors. The cable on the right provides the 100 kV tension. The circuit is connected on the upper part through the white ceramic feedthrough to the drift tube . In the background on the left, behind a Plexiglas plate, the SPST switch is connected to the system on one branch and to the earthed chassis on the other one. The feedthrough connection is made inside a hollow brass ball to avoid corona.

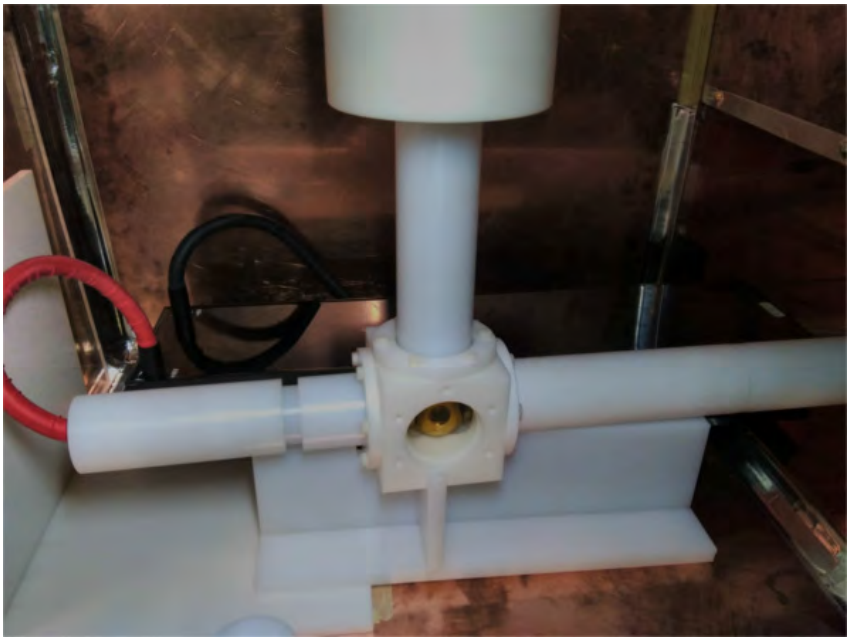

Figure 5.14 Picture of the pulsed high voltage circuit (Figure-5.12) embedded in its dielectric shield inside the copper Faraday cage. Resistors and special connections are visible in Figure-5.13.

In this purpose, special brass ball connectors have been installed at the crossing point of the high voltage ceramic resistors (see Figure-5.13). The large radius of this ball enables a larger contact with the resistors and imbed the assembly screws whose threads are obvious sources of corona. In a similar manner, new cable-to-feedthrough contacts have been realized to protect the end of the ceramic high voltage feedthroughs. These contacts cover the threads of the feedthroughs and avoid the appearance of corona discharge. At the same time, they have been designed to connect the high voltage cables from the top. An examples of such contacts appears at the end of the white ceramic feedthrough in the Figure-5.15.

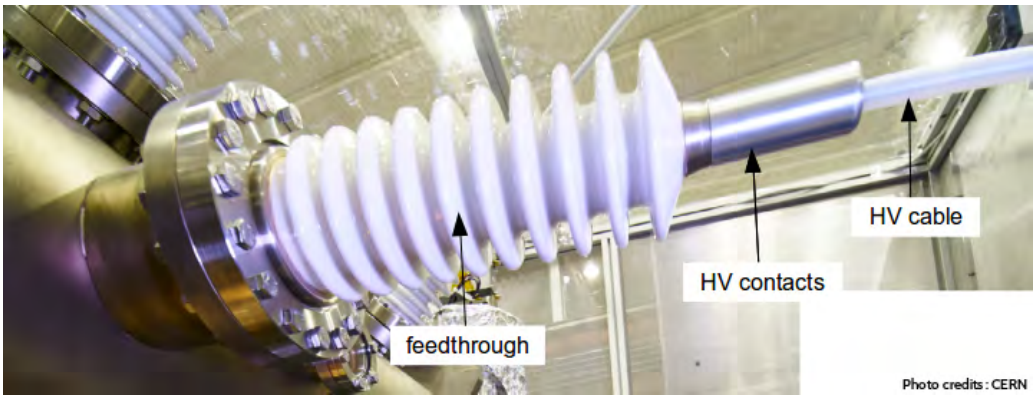

Figure 5.15 Photograph of a high voltage feedthrough mounted on the decelerator chamber. The feedthrough is connected to the cable with a new high voltage contact.

In addition, a complete dielectric shield made of Teflon covers the high voltage components. Such a high dielectric layer reduces the formation of corona by increasing the closest path to generate arcs (see Figure-5.14).

Earthing Special attention was paid to the earthing of the structure. Indeed, during the switching, current loops can appear locally. These loops represent a danger for the diagnostic and control devices, especially if they are generated by an undesired spark. To ensure sufficient earthing, all electrical installations were placed on and connected to a ground floor. This ground floor serves as an electrical reference for the entire system.

Finally, connected from lattice of brass strips, a protective cage encompasses the entire decelerator chamber. This cage is an essential element for user safety. According to Ref.-[168], an *IP3X* classification is required for such enclosure [166, 167]. IP3X testing involves pressing a standardized test probe, in the form of a 2.5 mm steel wire, against all openings in the enclosure, with a force of 3 N. For acceptance, the probe must not enter the enclosure.

5.1.3 Orsay prototype setup

We set the source acceleration potential to 50 kV. The resulting energy of the exiting particles was measured to 48 keV with an energy spread of 250 eV[10]. This spread is mainly due to the discharge potential applied to generate ions. The current was measured before applying any potential at 4.6 $\mu A \pm 0.25$ μA due to the fluctuating gas pressure inside the plasma chamber. The geometrical emittance of the source through the whole line was estimated at roughly 25π $mm.mrad$.

A bunch length of 2 μs was used to reduce the distortion phenomena induced by too short impulsion on the electronic trigger of the transistor switch. In order to perform a deceleration of the beam from 48 keV to 1 keV, the PDT is first held at 47 kV. The switching of the drift tube is synchronized on the chopper cycle with a delay time of 1.8 μs. For a 47 kV potential, fall-times of order 135 ns were recorded (slightly longer than the 100 ns expected).

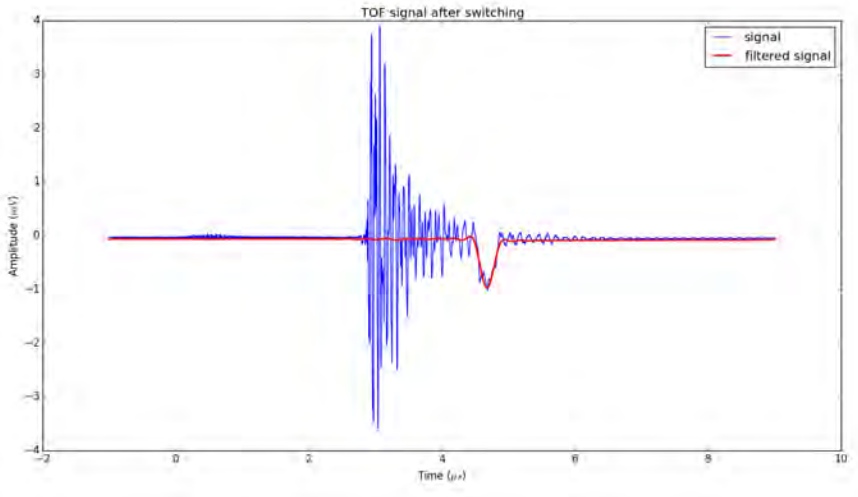

Figure 5.16 MCP signal while decelerating from $\sim$ 50 keV to 1 keV. (*blue line*) - Pre-amplified MCP signal as displayed on the scope screen. The noise is coming from the SPST when switching 35 kV. (*red line*) - The same signal filtered with a Savitzky-Golay algorithm.

[10]Measure performed by rising the potential applied on an Einzel until the disappearance of the beam spot. The measure was cross-checked by TOF estimations.

The signal is acquired at the end of the deceleration line on the MCP, amplified and sent to an oscilloscope. Despite a maximum distance of 1 m between the MCP and the drift tube, the signal is partly included in high frequency noise induced by the switching operations (chopper and/or SPST). A numerical post analysis ends to filter the residual high frequency noise using a Savitzky–Golay filter algorithm[11]. An example of such filter is shown in Figure-5.16.

The energy analyzer is located 10 cm upstream the MCP, placed off-axis with a movable system. As mentioned in the first section of this chapter, no refocusing elements were used for the test of the off-line decelerator prototype. The potential on the pre-decelerating electrodes were found starting from the incorrect cross-multiplication hypothesis. By changing iteratively the values, the best configuration to optimize the transmission was found as $(V1, V2, V3, V4, V5) = (35\ kV,\ 5\ kV,\ 20\ kV,\ 43\ kV,\ 43\ kV)$. According to the simulations, the transmission rate through this apparatus is evaluated to 36% taking into account a Gaussian beam profile and the geometry of the energy analyzer.

Results

Even without refocusing, the transmission is still quite acceptable: 48% of the beam remains downstream the drift tube and the energy scanner. This value is better than expected, probably because the beam profile is slightly different than the Gaussian profile we have used in the simulations. By stopping the chopper cycle, we confirmed that the observed signal was not electronic noise due to the pulse on the drift tube.

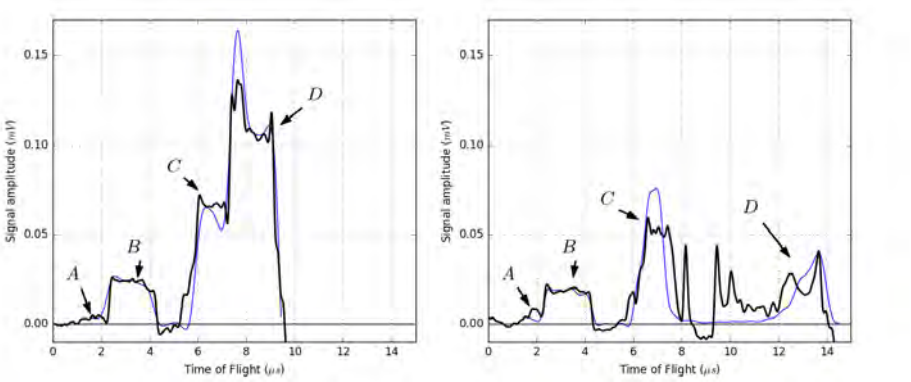

Figure 5.17 Time of flight spectra from the discharge source successively non-decelerated and decelerated. The blue lines are the predicted signals from SIMION simulations. The peak A corresponds to H^+ ions, B to H_2^+ ions, C to CO^+ and H_2O^+ ions and D to CO^+ and N_2^+ ions. (*Left*) - 48 keV beam without switching. (*Right*) - After the deceleration process. The ions of the peaks A, B and C remain at 48 keV while the ions in the peak C are partly decelerated to 1 keV.

During the data acquisition, a first TOF spectrum was achieved with the PDT polarized at 47 kV (Figure-5.17-*left*) and another one by switching the PDT from 47 kV to ground (Figure-5.17-*right*). Between both sets of measurements, the potential on the pre-decelerating electrodes was adjusted to compensate the optic changes and maximize the signal on the MCP.

[11] Further details about such a filtering algorithm can be found in the Refs.-[170, 171, 172, 173].

As the Figure-5.17 shows, four square signals are clearly resolved on the time-of-flight spectra before the beginning of the deceleration. Considering the distance $d = 3.4\ m$ between the chopper and the MCP, the obtained spectra are in good agreement with the predicted values based on SIMION simulations and the previous spectra obtained with the Wien filter or the TOF technique. Since the pulse length was extended to 2 μs, the CH^+ and H_2O^+ signals are not resolved (respectively C and D in Figure-5.8) as well as those of the CO^+ and N_2^+ ions (resp. E and F in Figure-5.8).

The deceleration is applied on the D peak while the others are kept unchanged as time-of-flight references. In Figure-5.17-(*left*), almost 35% of the remaining ions in the D peak are decelerated. According to their lower time-of-flight, part of the ions between 10 and 12 μs are not completely decelerated to 1 keV. This can be explained by the difficulty to synchronize the PDT switching on the passage of the ions in the tube. Indeed, the bunch length (2 μs) is barely smaller than the time required for the ions to pass through the DT ($\sim 2.45\ \mu s$). Taking into account the edge of the potential at the ends of the DT, part of the ions are not correctly decelerated. A shorter bunch would have improved this measurement.

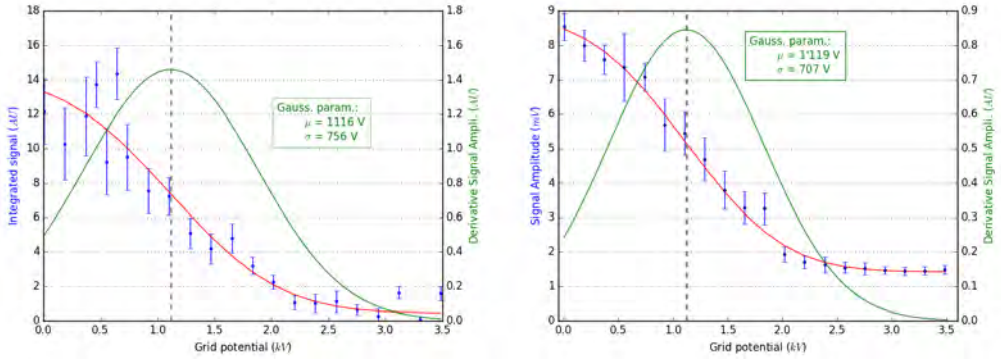

Figure 5.18 Energy spectra after the deceleration. Plots illustrate the integrated signal (*left*) and the amplitude of the signal (*right*) with respect to the potential V_{mesh} affected by their respective statistical error for 100 samples. Red lines are the corresponding error function fit curves. Green lines correspond to the derivative of the fit curves. Derivatives follow a gaussian distribution $D = A.\exp(-(x-\mu)^2/2\sigma^2)$.

During a second test, the remaining energy of the ions in peak D was investigated. The beam was directed through the energy analyzer. The potential on it was raised step by step until the disappearance of the last peak on the TOF spectrum. The potential configuration of the source, the PDT and on the pre-deceleration electrodes were kept unchanged.

Both the amplitude and the integrated signal of the D peak were recorded and fitted with an error function. The derivative of the fit curve gives us the energy profile of the decelerated ions (see Figure-5.18). The centroid values are found to be $\mu_{integ} = 1'116 \pm 292\ V$ (fit error) and $\mu_{ampl} = 1'119 \pm 35\ V$ (fit error). They confirm an effective deceleration from 48 keV to $1.1 \pm 0.7\ keV$.

5.1.4 Refocusing

To produce antihydrogen ions, it is not enough to decelerate ions from 100 keV to a few keV. Indeed, it is also necessary that antiprotons interact with the positronium atoms.

As seen in Chapter 2, positronium atoms are formed as a dense plasma inside the PPs converter. The shape of this cell has been studied to optimize the formation of such a plasma. It is 20 mm long with a square cross section of 1 mm^2.

We study here the possibility to focus through the PPs converter using different optics.

Einzel doublet

The first idea to refocus the beam downstream the decelerator was to make a telescopic system with a doublet of Einzel lenses, similar to the pre-deceleration electrodes.

The mechanical constraints require shorter electrodes than for the pre-deceleration electrodes. They were designed using the same cylinders (100 mm internal radius and 120 mm outer radius) but are 30 mm long and are separated by a gap of 10 mm. The refocus assembly is shown in Figure-5.19. To optimize the size of the spot, the distance between the lenses was enlarged up to 200 mm.

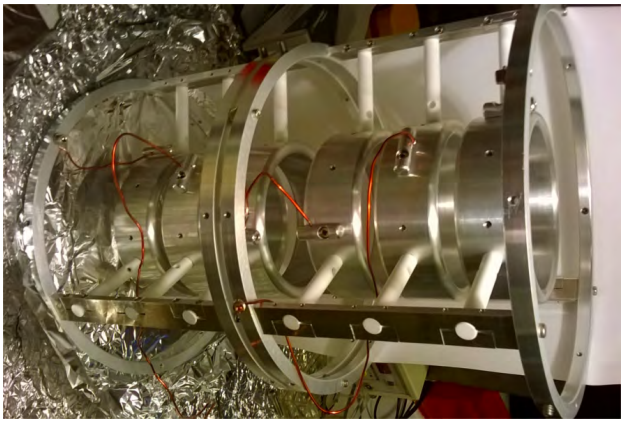

Figure 5.19 Photograph an Einzel lens doublet as used for the refocusing system.

As displayed in Figure-5.20, the lenses were installed inside vacuum chambers on the Orsay test bench. The discharge-type source was set to provide a 2 keV beam with a average current of 0.89 μA. At the end of the beam line, the intensity of the beam is measured on the order of 0.55 μA and the geometrical emittance is estimated of the order of 67π $mm.mrad$[12] (bigger than the 40π $mm.mrad$ theoretically expected thanks to the Liouville's theorem downstream the PDT).

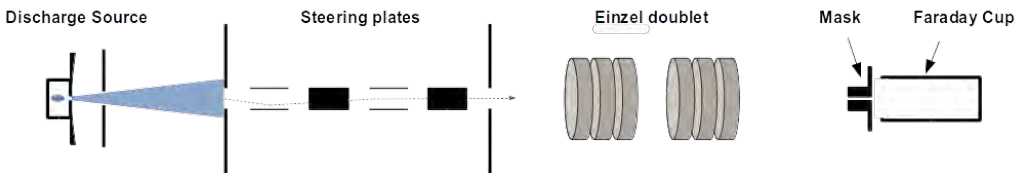

Figure 5.20 Schematic of the refocusing test bench. The measurements are performed with 2 keV proton beam.

[12]The geometrical emittance was determined by the apertures of the extraction electrode and the collimator elements along the beam path.

The beam is detected after 2.3 m flight through the Einzel lenses using a Faraday cup. In order to simulate the passage of antiprotons through the PPs converter, a hat-shaped mask was placed in front of the FC, as shown in Figure-5.21. This mask is 20 mm long with a 2 mm diameter hole (minimum size achievable). The mask is isolated in order to measure the current of the beam hitting it as well. Figure-5.22 shows a 2D plot of detected current on the mask and in the cup as a function of the two Einzel lens voltages.

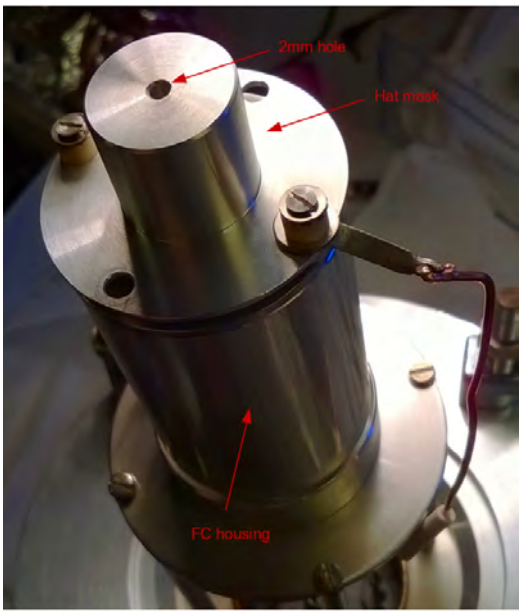

Figure 5.21 Photograph of the hat-shaped mask mounted in front of the Faraday Cup detector.

According to Figure-5.22, the total current measured behind the mask is at most 92 $nA \pm 3nA$ (error corresponding to the measure instability). The transmission rate is therefore $0.092/0.5 = 16.7\%$.

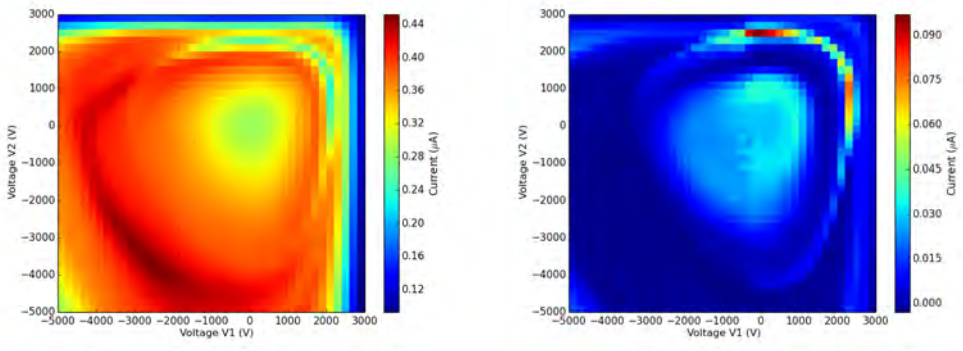

Figure 5.22 Beam current as measured on the hat-shaped mask (*left*) and in the Faraday Cup (*right*) for a $2 - keV$ proton beam. The color is proportional to the current value. The electrode are identified as #1 and #2 corresponding respectively to the first and second lens.

A sizeable fraction of the beam is lost on the collimator mask. In the case of GBAR, since the section of the cell is 1 mm^2, a lower transmission rate can be expected (depend-

ing on the initial beam emittance).

Concerning the design of the refocusing system, we can see that maximum transmission rates are reached when one of the lenses is turned off. The best transmission rate is for $V_{Einzel1} = 0\ V$ and $V_{Einzel2} = 2350\ V$. Therefore, only one Einzel lens is required to ensure the transmission of the beam through the PPs converter. As shown in Figure-5.34, a single lens was included in the on-line version for ELENA.

Alignment issue The first attempts to perform the transmission rate measurement through the PPs converter lead to unexpected results. As shown in Figure-5.23, diagrams present important distortions.

After investigations, the reason of the distortion had been attributed to the misalignment of the electrodes of one of the lenses. The simple displacement of an electrode with respect to the optical axis leads to poor focusing in the reaction chamber. This is proof that particular attention must be paid to the installation and positioning of the electrodes in the GBAR optical line.

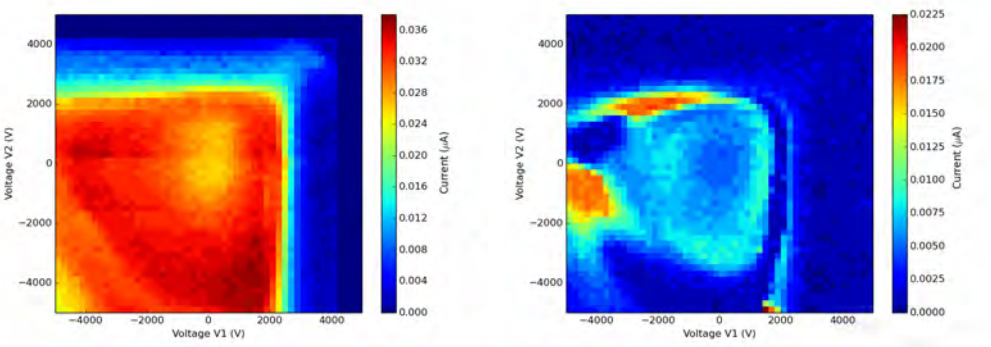

Figure 5.23 Beam current as measured on the hat-shaped mask (*left*) and in the Faraday Cup (*right*) for a $2 - keV$ proton beam. The color is proportional to the current value. The electrode are identified as #1 and #2 corresponding respectively to the first and second lens. The second Einzel lens suffers a misalignment.

5.2 On-line decelerator for ELENA

5.2.1 Vacuum improvement

CF Chamber - "Clarinette"

As shown in the Figure-5.1, the entire off-line decelerator prototype was made from ISO-KF type vacuum chambers sealed with viton gaskets. This technology notably offered a great modularity necessary with regard to the modifications brought to the first version of the decelerator. For all the tests having been carried out with ions of matter (such as protons) an Ultra High vacuum (UHV) was not necessary. In the off-line prototype, the typical pressure within the main cavity containing the PDT was $10^{-7}\ mbar$. In addition, the electrical operations on the switch were achievable without any risk for pressures below $10^{-6}\ mbar$. The pumping system consisted of a scroll pump in series with turbomolecular pumps (TBM). The delay of intervention on such a KF apparatus was greatly reduced.

This level of pressure is not sustainable when trapping antimatter particles (in a trap or in a storage ring). For comparison, the level of vacuum required in the ELENA ring

is in the order of $10^{-11} - 10^{-12}$ *mbar* depending on the sector of the machine. The 10^{-11} *mbar* limit is necessary in order to maintain the antiproton beam in the ring for a duration of about one minute[13]. To avoid contaminating the storage ring, the antiproton line in GBAR must reach a maximum pressure of 5.10^{-10} *mbar*.

The decelerator electrodes were reassembled inside a Conflat-type (*CF*) vacuum chambers shown on the left of the Figure-5.24. Copper gaskets are used to seal the chamber enabling to reach ultra-high vacuum where the outgassing of the elastomer gaskets (as for ISO-KF type system) could be a significant gas load.

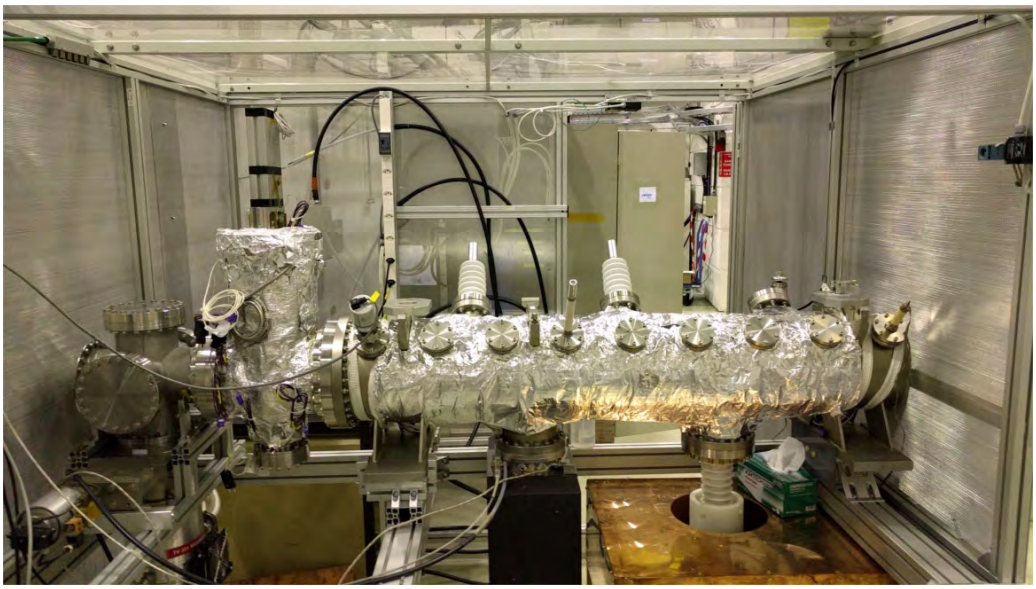

Figure 5.24 Photograph of the on-line decelerator in the AD Hall. The (anti)proton beams are coming from the left and the GBAR reaction chamber is away on the right. The first cross on the left is dedicated to pumping and the second chamber houses a Beam Position Monitor from CERN. The IP/3X protection cage is all around.

In order to reach $p < 10^{-9}$ pressure, a $\sim 200°$ baking during a 24 *h* period is required. Such a thermal conditioning activates the surface outgassing. At the same time, we operate an electrical conditioning of the electrodes. The electrical conditioning is the process consisting in gradually increasing the voltage on the electrodes after venting. This first power up has the effect of accelerating the outgassing on the polarized electrodes. Finally, a 300 l/s ion pump was placed under the main decelerator tank to complete pumping for pressures $p < 10^{-7}$.

The main chamber used for the on-line design of the decelerator was an old copper coated, RFQ cavity, $1'555$ *mm* long, 250 *mm* large. It was not custom developed to accommodate the pre-deceleration electrodes and the drift tube. Therefore, adjustments were necessary.

First, a new PDT was installed into the chamber, maintained by two wide disks made of PEEK[14]. This insulating polymer is considered as vacuum compatible and resists to high temperature. Such a polymer has been preferred to a ceramic system because of the weight of the PDT made of stainless steel. High voltage ceramic feedthroughs were ordered depending on the ports on the side of the chamber and the maximum achievable

[13]The time to operate the deceleration and cooling of the antiprotons.
[14]PEEK stands PolyEtherEtherKetone.

voltage. As seen in Figure-5.24, four different kinds of the feedthroughs have been used.

On the side of the chamber, flat flanges (illustrated in Figure-5.25a) were sealed using special aluminum O-rings, referred as $Helicoflex$. The rings offered a cheap and time-conserving solution compatible with UHV. In addition, their flexibility allowed to bake the chamber while maintaining a proper seal.

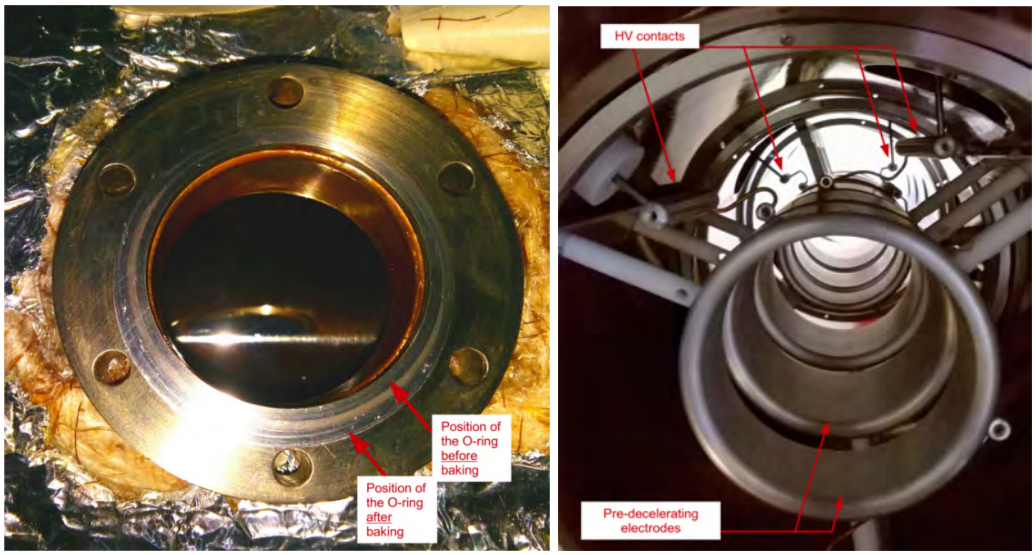

(a) Side of the decelerator chamber. (b) Inside the decelerator chamber.

Figure 5.25 (*left*) - Picture of a flat port on the side of the in-line decelerator chamber after baking at 200°. The mark of the Helicoflex O-ring before and after the baking are visible. (*right*) - Picture of the inside of the in-line decelerator chamber with the high voltage in-vacuum connections. The in-vacuum connections appear on the top of the picture for the pre-decelerating electrodes.

On the vacuum side, the ports of the chamber did not correspond with the position of the electrode inside the chamber. Specific custom high voltage terminals have been machined to connect the end of the feedthrough rods with the corresponding electrode. The shape of these terminals has reduced the risk of arc inside the chamber. Examples of such terminal connections are illustrated in Figure-5.25b.

Finally, to support the 200 kg apparatus, a new frame has been designed as shown on the bottom of the Figure-5.24. Mounted on rails, the chamber could slide off-axis to allow maintenance inside the cavity.

Problems

Unfortunately, the vacuum level reached in the on-line decelerator chamber never dropped below 10^{-8} $mbar$, which was insufficient to open the valve between the ELENA ring and the GBAR antiproton line. After several days of pumping, baking at 200° and electrical conditioning of the electrodes, no improvements were observed. After investigations, several elements explained such a failure/situation:

- A 10^{-8} $mbar.l.s^{-1}$ leak was found on an all-metal valve used to vent the chamber.
- Several Helicoflex O-rings were deformed and displaced during the baking. Then the sealing of the chamber was impacted.

- Even if vacuum compatible, the large PDT supports made of PEEK were probably outgassing a lot.

First, the old CF "Clarinette" chamber was removed. As shown in Figure-5.26, a new design replaced it including four CF chambers custom developed for the decelerator. A new ion pump has been placed upstream the new cavities to increase the pumping power and act as a differential pumping stage reducing the residual gas flow towards ELENA. Finally, concerning the in-vacuum plastic elements, the PDT supports made of PEEK have been replaced by a ceramic cradle (see Figure-5.26 inset).

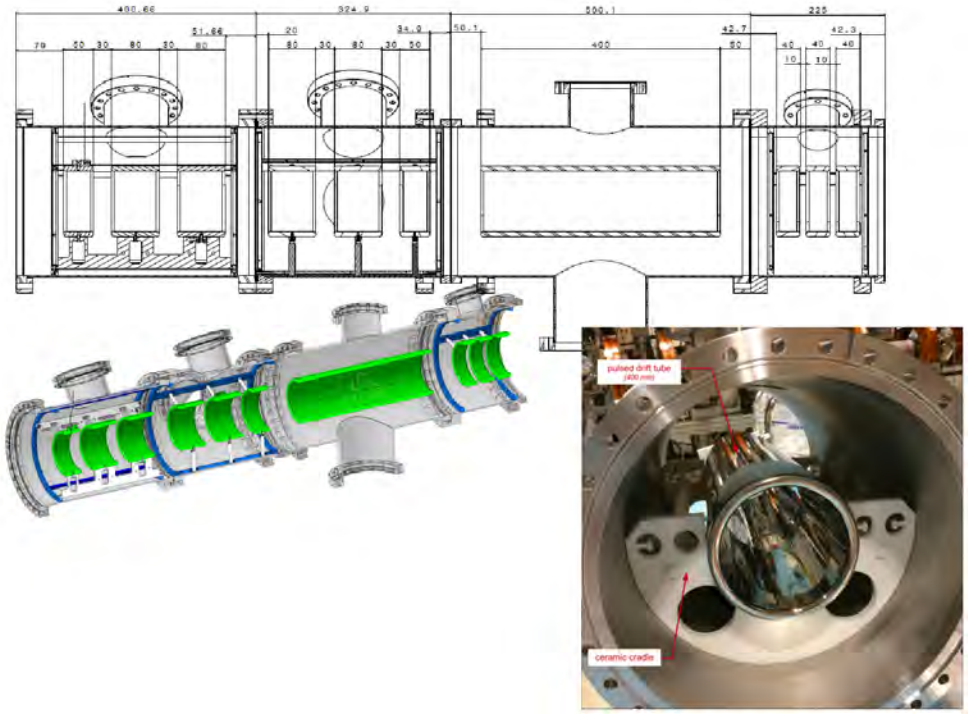

Figure 5.26 Schematic of the on-line decelerator in the new chambers with the electrode positions and dimensions. (*Inset*) - Photograph of the stainless 400 *mm* pulsed drift tube inside the new decelerator chamber. The PDT is mounted on the ceramic cradle.

5.2.2 MCP energy anaylzer

The MCP energy analyzer (*MCP-EA*) used with the off-line prototype decelerator allowed us to prove the feasibility of the deceleration. However, the latter suffers from defects:

- the small aperture makes it difficult to focus the beam through. A significant part of the beam was lost ($\sim 52\%$). It was difficult to consider such a high level of loss when working with only 10^7 antiproton pulses at CERN.
- The energy analyzer was independent of the detection system. The remote diagnostic induces additional loss and optical effects on the beam.

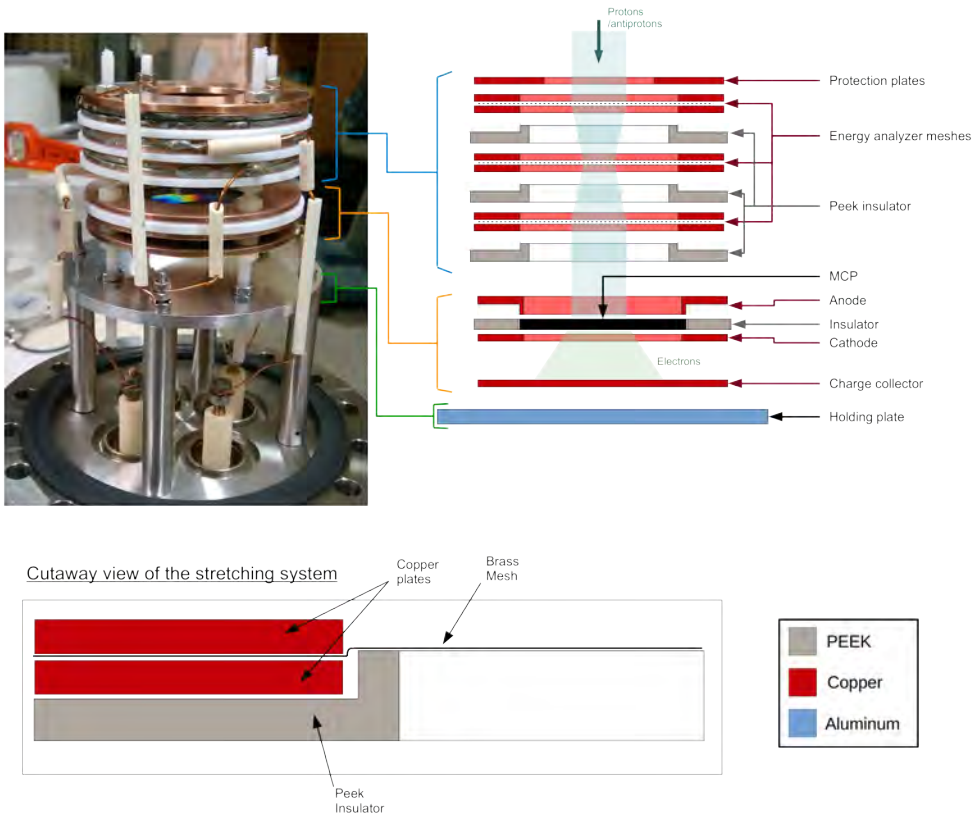

Figure 5.27 Schematic and picture of the improved energy analyzer.

Therefore, we developed a new diagnostic device limiting losses. Based on the same stacking principle as the commercial MCP design from TOPAG. The energy analyzer and the MCP detector are mounted on the same support (see Figure-5.27). This diagnostic is composed of:

- A grounded protecting plate that prevents the beam from touching (and charging) the insulating plastic parts.
- A series of three meshes. Brazed on copper disks, they have an inner radius of 21.5 *mm* and an outer radius of 34 *mm*.
- Insulating disks made of PEEK. They insulate the components held at different potentials. These disks have a protrusion that ensures a slight stretch on the meshes to keep them as flat as possible.

- A sensitive part made of one MCP detector with a charge collector behind.

The outermost meshes are grounded when the middle one is held at a variable voltage. In the same way as for the off-line decelerator prototype, the potential V_{mesh} applied on the middle mesh increases and blocks the particles with an energy $E < qV_{mesh}$. The advantage of this design is the small distance between the mesh triplet and the MCP. By shortening this distance, we highly reduce the beam loss.

Likewise, this new diagnostic is directly connected through voltage feedthroughs to a readout electronics and placed outside the beam pipe. In this way, we prevent outgassing from in-vacuum electrical components and complex re-openings of the diagnostic chamber to switch the polarity of the readout chain when changing from positively to negatively charged particles.

The MCP-EA device has been tested in Orsay following the scheme shown in Figure-5.28. An ion gun source has been used with increasing energies up to 1 keV. The ions generated by this source are potassium ions with virtually no energy dispersion. The results of these tests are shown in Figure-5.29 with four different energy values. The beam is pulsed using a quadrupole electrostatic deflector. It deviates the beam by an angle of 90° for 1 μs towards the diagnostic element. For all the studied energies, the amplitude and the integrated signal are saved with respect to the V_{mesh} voltage, see Figure-5.29. The curves obtained are interpolated according to radial basis function approximations (RBF) [174].

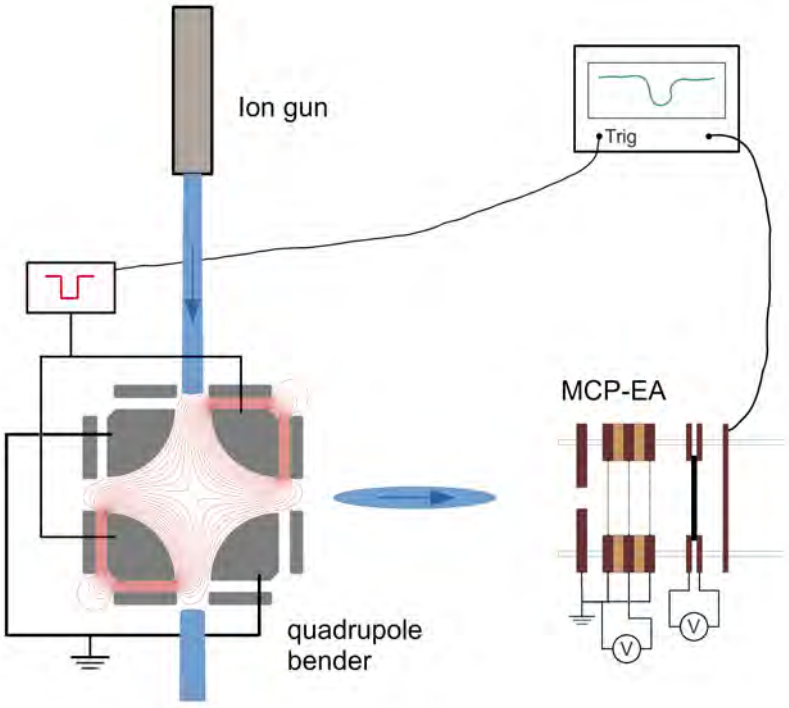

Figure 5.28 Schematic of the MCP-EA test bench.

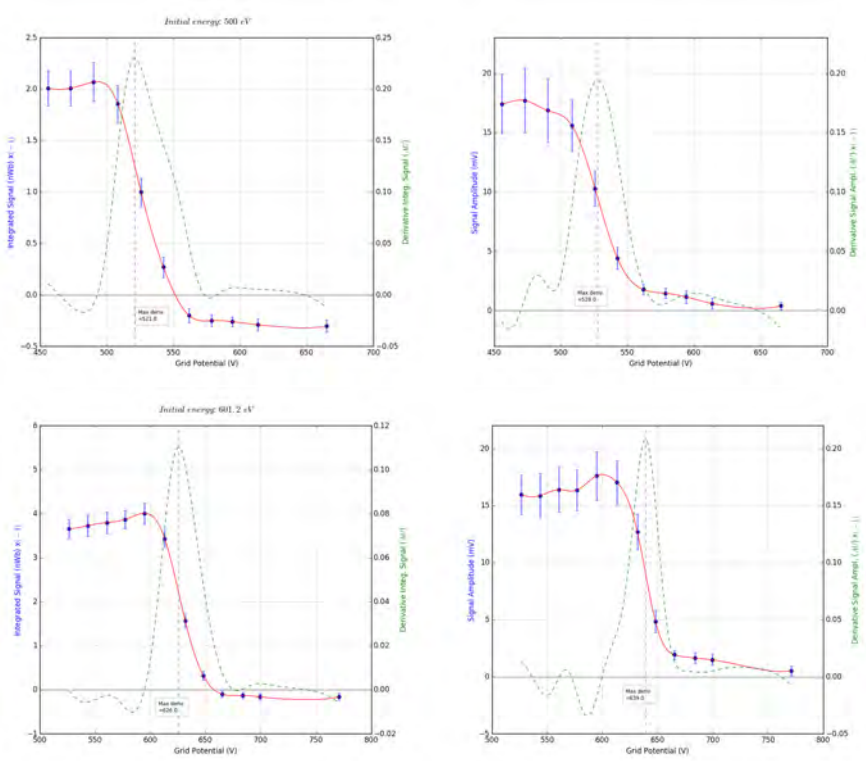

Figure 5.29 Test of the MCP-EA with different beam energies. The plots illustrate the integrated signal and the amplitude of the signal while rising the potential V_{mesh}. The initial beam energy in the different cases is : (*up*) - $E_i = 500\ eV$; (*bottom*) - $E_i = 600\ eV$.

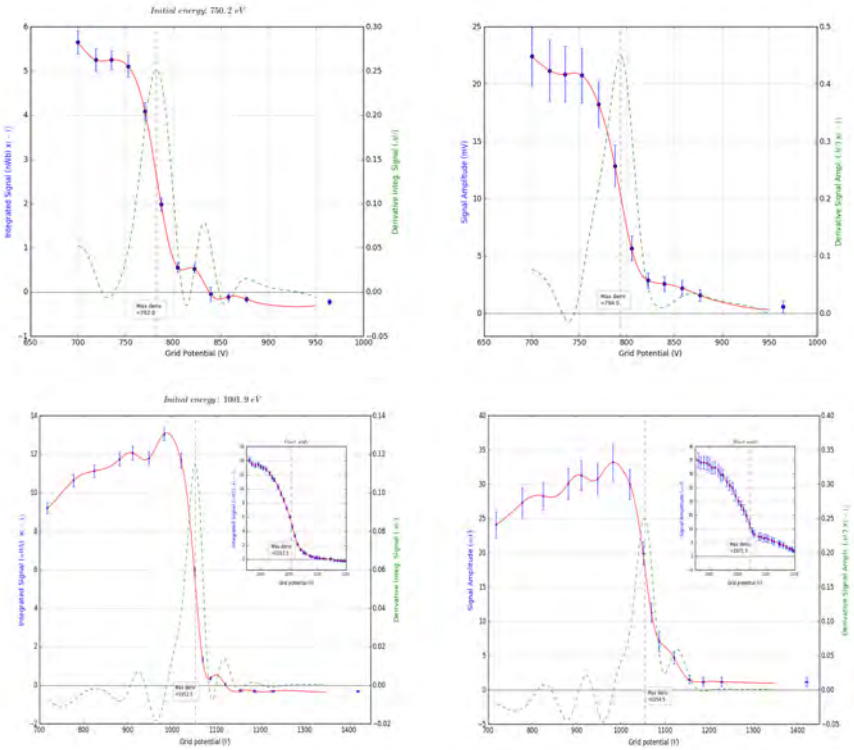

Figure 5.30 Test of the MCP-EA with different beam energies. The plots illustrate the integrated signal and the amplitude of the signal while rising the potential V_{mesh}. The initial beam energy in the different cases is : (*up*) - $E_i = 750\ eV$; (*bottom*) - $E_i = 1000\ eV$.

5.3 Deceleration of the 100-keV ELENA H^- and $\bar{p}$ beams

Testing of the decelerator was done in parallel with the commissioning of the ELENA ring (see Figure-5.31). ELENA receives antiproton pulses decelerated (and electron cooled) to 5.5 MeV from the AD, every 109.2 seconds. In ELENA, the antiprotons are further decelerated, by magnetic ramping and more electron cooling, to 100 keV and ejected into the LNE50 beam line that connects GBAR. For a description of the AD and ELENA, see Ref.-[95]. The ELENA ring is also equipped with an "off-line" H^- cusp-type source for operating independently of the AD. This source can deliver beam with a much higher repetition rate (about every 5 s) and is nominally designed to work at 100 kV, however continuing problems with an isolation transformer significantly reduced the amount of commissioning time.

Figure 5.31 The 30.4 m circumference ELENA synchrotron ring. ELENA receives 100 keV H^- beam from a source (*bottom left*) or 5.3 MeV antiproton beam from the AD (*bottom*) and circulates clockwise. The beams are extracted from the LNE50 beam line (*top right*).

The electrostatic-optics LNE50 extraction line is shown in Figure-5.32. Downstream of the ELENA kicker is a fast-closing valve (actuated by a gauge inside the GBAR decelerator), followed by a first quadrupole doublet, a set of (horizontal and vertical) steering plates, a beam-profile monitor (BPM), a longitudinal beam pickup monitor, a kicker-bender section (to send the beam to another experiment) and another quadrupole, steerer, BPM assembly, followed by a gate valve.

On the GBAR side (see Figure-5.33) there is an ion pump, followed by a 2.4 m drift section[15]. This is followed by another ion pump and a switchyard (equipped with a valved-off turbomolecular pump) that houses a quadrupole bending element to merge a proton beam into the GBAR line (see section-6.2). In front of the first decelerator electrodes, is a vertical $CF200$ chamber containing the ELENA-standard BPMs. The four $CF250$-standard chambers housing the decelerator electrodes and decelerated-beam Einzel lens follow.

Figure-5.34 shows the positions of the various optical elements and the detectors used to monitor the ELENA beams. For H^- ions, obvious only a MCP coupled to a phosphor screen (PS) can be used. For the antiproton beam, scintillators were installed near the

[15]It will be used to accommodate the antiproton trap – see section-6.1.3.

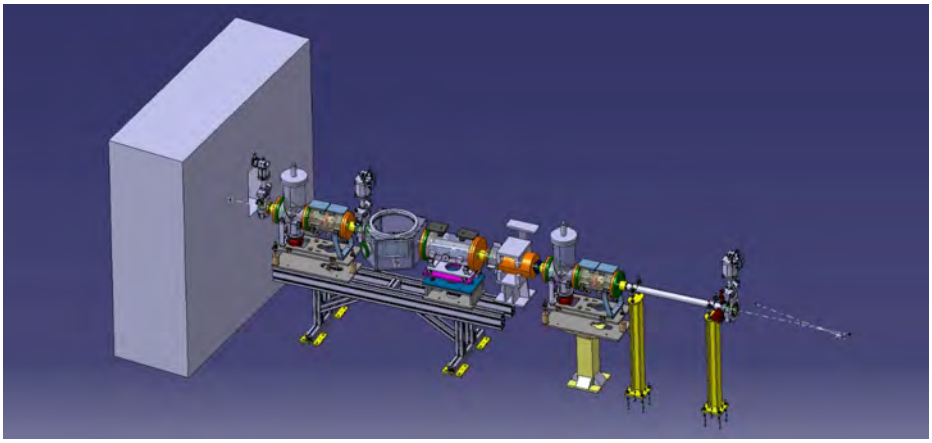

Figure 5.32 The ELENA extraction line (*LNE50*) that delivers beam to GBAR. Beam comes from right to left from the ELENA kicker through the electrostatic optical elements (see the text).

quadrupole bender, and immediately upstream and downstream of the MCP/PS just before the Ps chamber.

Figure-5.35 shows a picture of the beam line itself. The Spellman power supplies for each decelerator lens (and the Fug supply for the Einzel lens) were controlled by analog voltages from a National Instrument compact RIO system[16]. Remote control of the entire system was required since no one is allowed in the GBAR zone when antiprotons (or even H^- ions) are sent.

For the first test, there were no BPM units available so the only diagnostic was an MCP and phosphor screen, with which a first image was obtained with an H^- beam using the nominal optics settings in LNE50 and no deceleration. Even though it was eventually possible to focus and move the beam, without the BPM's it was very difficult to inject the beam along the optical axis.

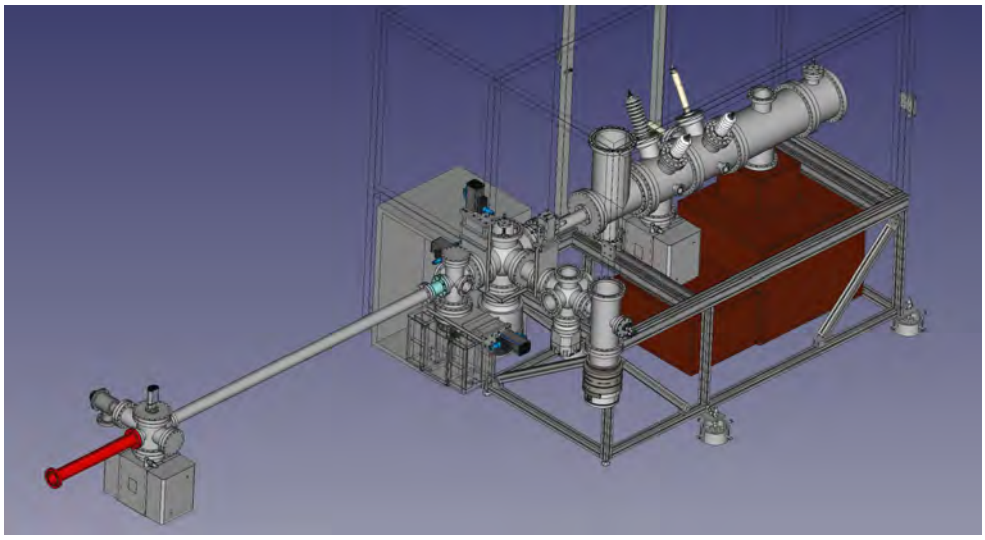

Figure 5.33 The GBAR injection line that receives beam (coming from the left) from the ELENA LNE50 extraction line. The red-colored beam pipe is located inside the wall shown in Figure-5.32.

[16]Implemented by Dr. B.-H. Kim

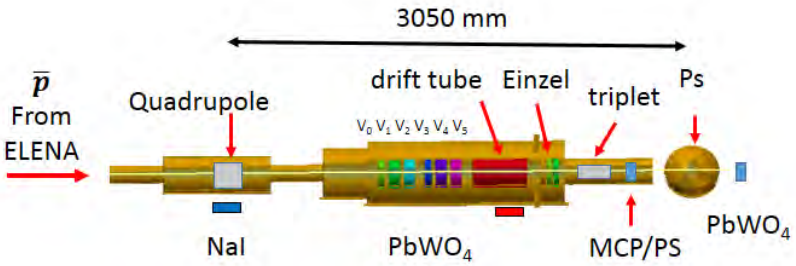

Figure 5.34 Schematic diagram of the antiproton line, showing the positions of the optical elements and different detectors (NaI and PbWO4 are the scintillators; MCP/PS is the multi-channel plate with phosphor screen).

The next step was to use antiprotons. Despite the disadvantage of the long (almost 2 minutes) period between shots, antiprotons have the enormous advantage of revealing where their positions when annihilating. By placing scintillating crystals along the beam line (including at the MCP position) it was possible to discover where the beam was being lost. The first problem was the quadrupole bender located in the merging cross in front of the decelerator, which has a 12 *mm* aperture. If the beam is off axis then the deceleration tends to accentuate the angle, preventing transport of the beam to the detector.

During the tests with H^- beam, the effect of each decelerator lens on the beam was checked (except V_0, which is grounded in the chamber). Lens V_4 is suspected to be mis-

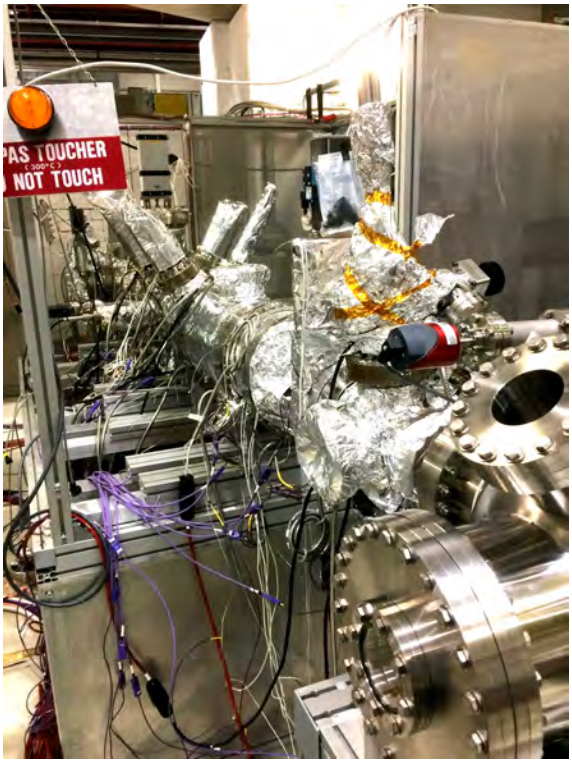

Figure 5.35 Photograph of the antiproton beam line with the new decelerator chambers (during baking and before reconstructing the high-voltage safety cage). The BPM actuator is visible upper left and the reaction chamber is visible at lower right.

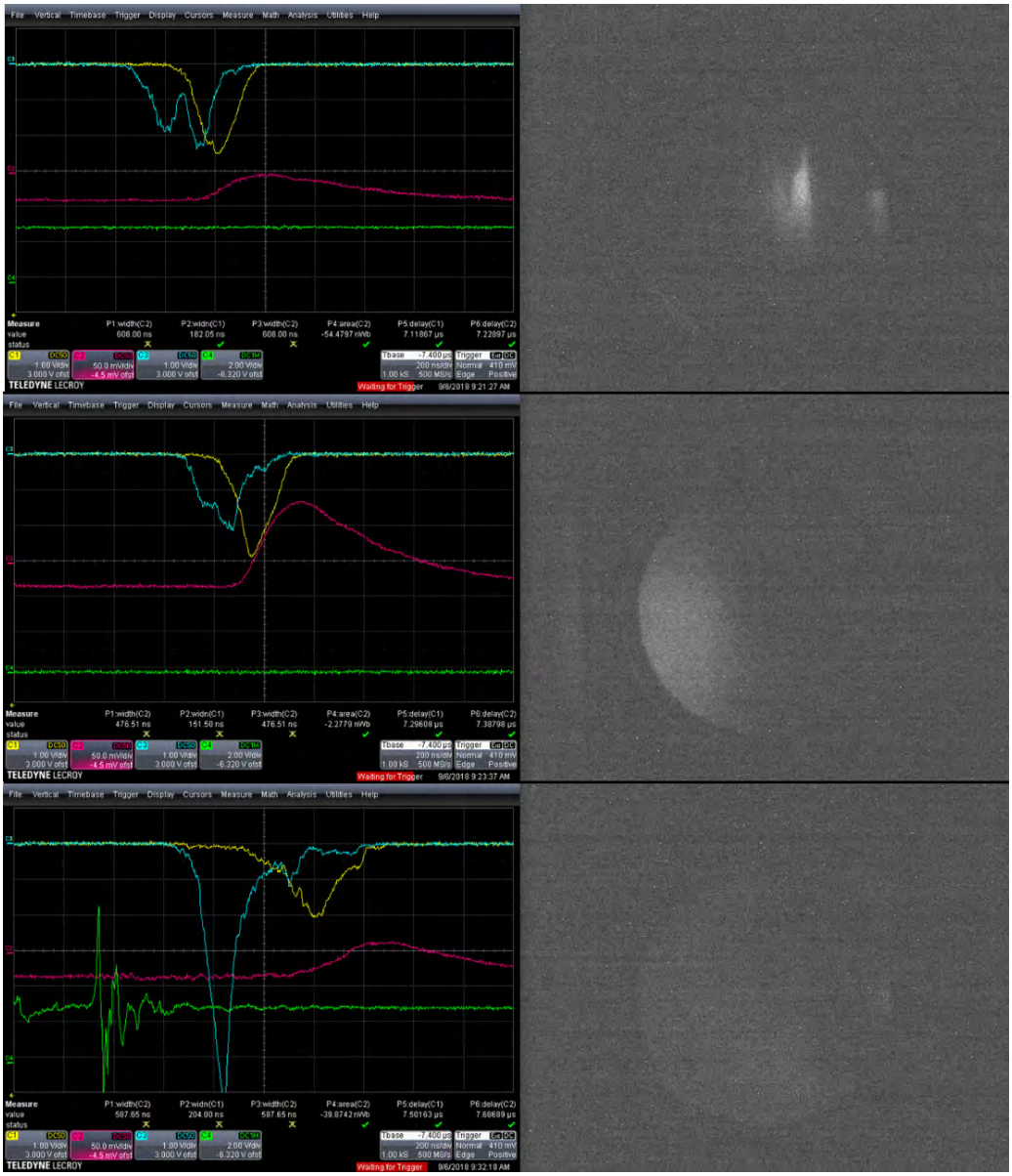

Figure 5.36 (*right*) MCP/PS image of the antiproton beam; (*left*) oscilloscope traces showing the HV-switch trigger (*green*), MCP charge signal (*red*), upstream scintillator (*blue*) and downstream scintillator (*yellow*). The voltage on the drift tube is 95 kV and the timing is: (*top*) too early, so that the beam sees the drift tube at ground; (*middle*) too late, so the beam is decelerated but then re-accelerated when leaving the drift tube – this is called "*static*" mode; (*bottom*) while the beam pulse is inside. The oscilloscope timebase is 200 ns/div.

aligned since when polarizing it, the beam quickly disappeared. Therefore the V_4 electrode was connected to the V_5 one to avoid a gradient between them.

The results of the first antiproton tests are shown in Figure-5.36. Having verified the influence of the different lenses and the drift tube, a test of the switch timing was performed. The trigger for GBAR is derived (using a Labview-interfaced SRS gate and delay generator) from the the so-called ELENA-W1 (1 *ms* warning) ejection signal that turns on the kicker inside the ring and deviates the beam pulse into LNE50. In all tests, only the drift tube was polarized.

The upper panel in Figure-5.36 shows something blocking the beam. Indeed, the upstream scintillator (*blue trace*) shows annihilation somewhere in the triplet electrodes (which have only a 30 *mm* aperture). The static-mode (*middle panel*) shows a slightly higher electrical signal (*red trace*) which is slightly delayed in time. This indicates that the drift tube acts as a (*static*) Einzel lens. The delay is from the deceleration and corresponds exactly to simple calculation[17]. The lower panel in Figure-5.36 shows a diffuse beam. This is compatible with a decelerated beam that will diverge and has not been focused (Einzel lens was zero). The annihilation signal in the triplet (*blue*) is much bigger, which is also consistent with a divergent beam. The downstream scintillator (*yellow*) shifts in coherently with the electrical signal (*red*) due to the longer time of flight of the decelerated antiproton beam.

After these tests, a new movable MCP/PS was installed inside the reaction chamber so as to monitor the beam position as close as possible to the positronium cloud. The reaction chamber and MPC mounting are shown in Figure-5.37.

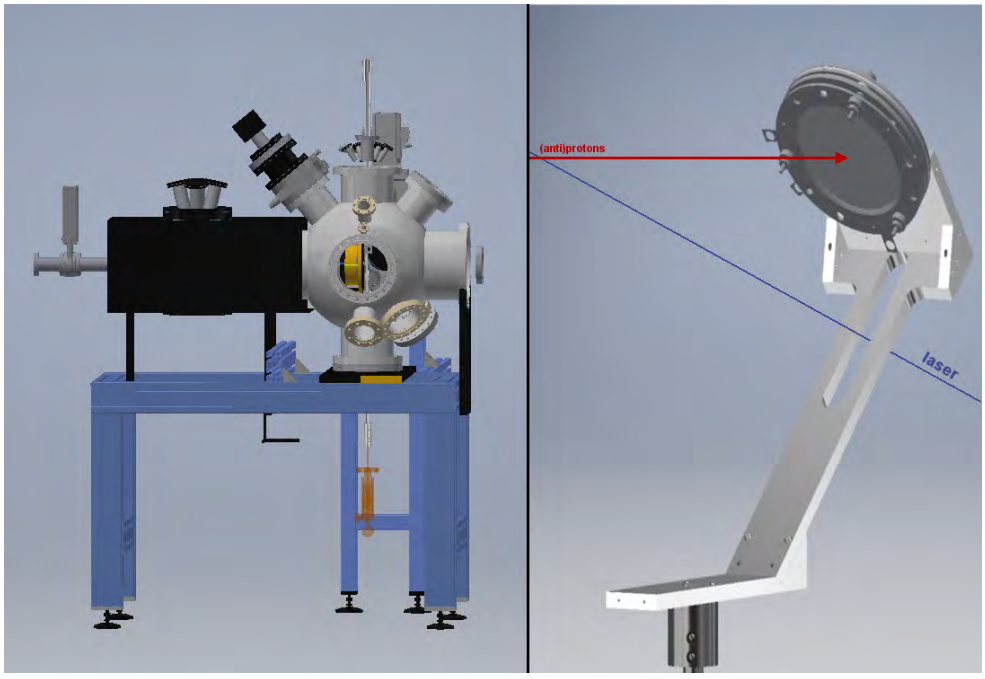

Figure 5.37 (*left*) Reaction chamber showing the end of the positron line (positrons arrive from the left) and the MCP mounted inside (in its retracted position – the antiprotons arrive from the front). (*right*) detail of the MCP mounting showing the angle required for passage of the laser beam for exciting the Ps cloud.

[17] A 100 keV antiproton beam travels one meter in 228 ns.

The results of a test with antiprotons is shown in Figure-5.38, with the MCP/PS signal on the right and the oscilloscope traces of the trigger, MCP and scintillator signals on the left. The drift-tube voltage was set to 95 kV, resulting in 90 kV with the leakage current. The other lens voltages (V_1, V_2, V_3, V_4, V_5) were (20 kV, 70 kV, 40 kV, 40 kV, 60 kV) kilo-volts. These voltages are relatively close to the GA solution C2 shown in Figure-4.7. The timing of the HV switch trigger was varied to try and maximize the later time-of-flight signals of the MCP and downstream scintillator. The images on the top are with no Einzel-lens voltage while the images on the bottom are with the maximum voltage (20 kV). Again, in addition to the time-of-flight difference between the 100 keV and 10 keV beams (about 0.6 μs; the oscilloscope timebase is set to 1 $\mu s/div$) the 20 kV Einzel lens has no effect on the 100 keV beam but focuses somewhat the 10 keV beam.

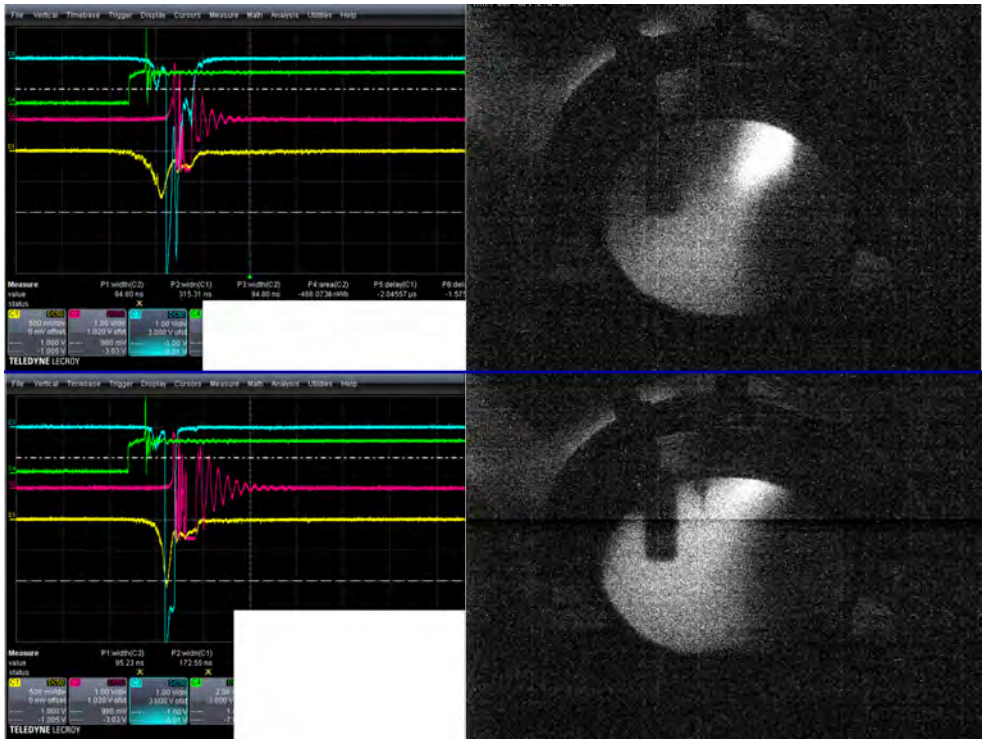

Figure 5.38 (*right*) MCP/PS image of the antiproton beam; (*left*) oscilloscope traces showing the HV-switch trigger (*green*), MCP charge signal (*red*), upstream scintillator (*blue*) and downstream scintillator (*yellow*). Top panel is with no Einzel-lens voltage and bottom with 20 kV. The shadow of the Ps support (see Figure-5.37) is visible.

While there is still a major component of undecelerated antiproton beam, the decelerated component is about 25% and can be focused using the Einzel lens, as seen in Figure-5.34. There are two reasons which might explain this.
The imperfect alignment of the beam axis with the mechanical axis (likely a combination of imperfect mechanical alignment and an uncorrected beam angle) can lead to a time spread since the beam is dispersed over different angles. While efforts were made by ELENA to reduce the time of the bunch, in many cases it appeared to be larger than 300 ns and hence, is not within the drift tube while it is pulsed down. There was also some jitter in the trigger signals, which could explain the problem since the deceleration window is very narrow. Unfortunately there was not enough time to study these points in detail before the end of the AD run. Nevertheless, some deceleration has been achieved and it is encouraging to see that the instrument functions as it was intended.

Chapter 6

Ion transport through GBAR

6.1 Post Deceleration

6.1.1 Antimatter charge state switchyard

In this section, we detail the simulations performed for the GBAR charged state switchyard. This crucial element in the GBAR experiment is supposed to separate the different products exiting the reaction chamber and guide them through the post-decelerator part of the GBAR experiment.

The selection is based on the charge of the different products: $\bar{H}^+$, neutral $\bar{H}$ and negative $\bar{p}$.

Three different geometries were studied, hereafter denominated as:

- Three Plate Pairs (*T2P*) : consisting on three parallel plates deviating the beam according to the charge of the particles.
- Curved Plate Bender (*CPB*) : consisting on two long plates curved along the beam path with two repetition plates inside.
- Corrected CPB (*CCPB*) : consisting on a CPB design with larger electrodes and grounded gates at the entrance and at the exit of the chamber.

These geometries present an evolution in the design according to the simulation results. They also take into account the chamber space and the opportunity of exploiting the neutral $\bar{H}$ beam.

For all the simulations, 5000 particles are randomly generated with respect to the position and divergence parameters of the beam downstream the decelerator. The following results are displayed using the SIMION beam orientation where the X-axis corresponds the beam propagation axis and the Y-axis is the horizontal axis (see Figure-6.1).

For such a simulation the number of independent voltages is quite small, a GA is thus not necessary. We optimized the voltage parameters using the *SimplexOptimizer* function. This function, part of the SIMION software, performs simulations changing step-by-step the potential values on the electrodes following a simplex algorithm. As we already pointed out, for each step, the function selects the best potential set minimizing an adjustable value, so called “metric”.

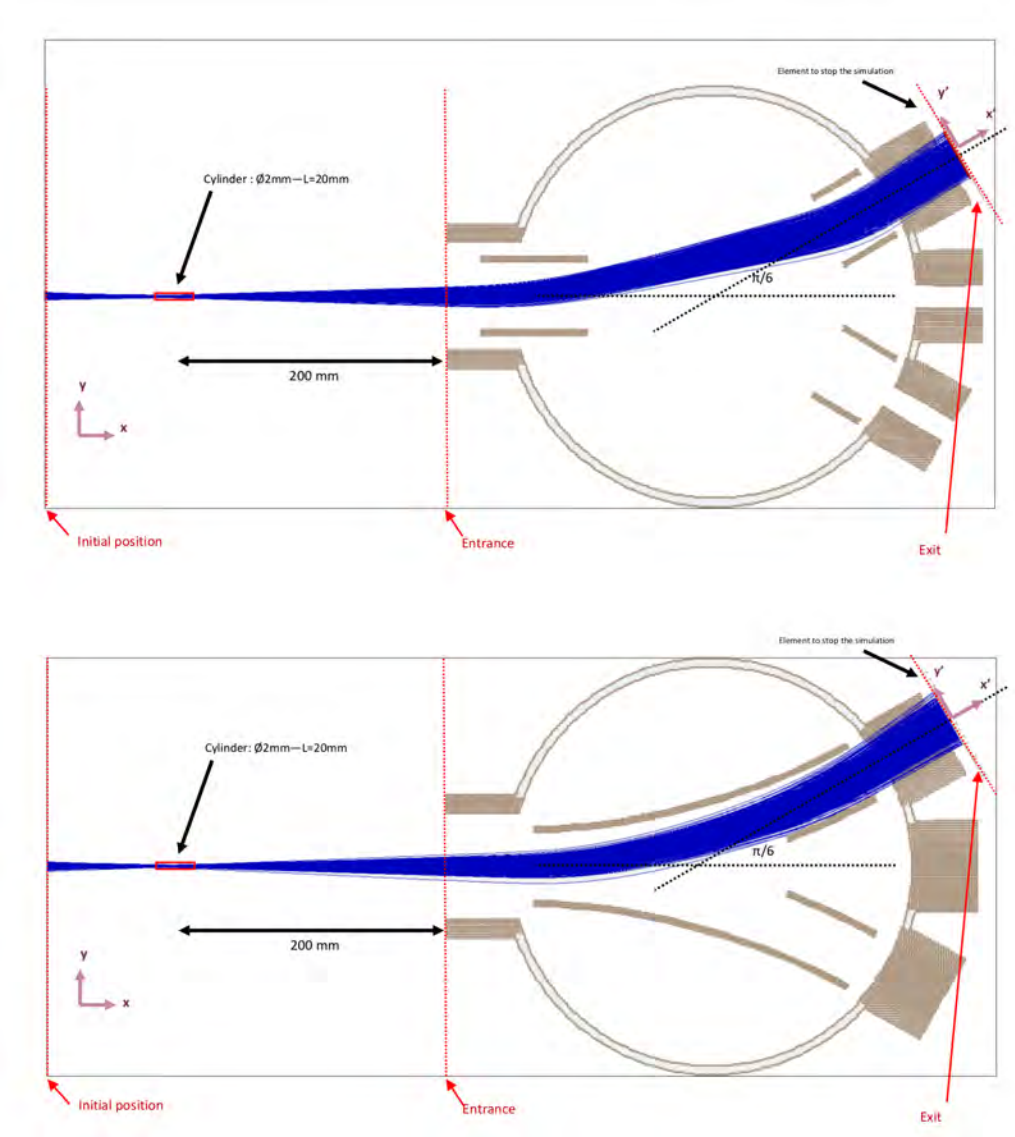

Figure 6.1 Geometry of the T2P (*top*) and CPB (*bottom*) designs as modeled in SIMION. The blue lines correspond to antiprotons flying from left to right through the bender. The red rectangle displays the PPs converter position. The CCPB design is not represented but is equivalent to the CPB design (*top*) with grounded gate at the entrance and exit of the beam. Note the particular orientation where the X-axis corresponds to the beam propagation direction.

In the present case, the metric is defined as:

$$m = \frac{|\theta - \theta'|}{\theta'} + \frac{|r - r'|}{r'} \tag{6.1}$$

with θ, the mean angle of the particles exiting the switchyard; θ', the expected exiting angle, here 30°; r, the mean radius of the beam; r', the expected mean radius downstream the switchyard (maximized in this case to 5 mm).

The selection criteria appears not to be very sensitive to the beam radius since the switchyard does not focus the beam. We then changed for a simplified metric given by:

$$m = \frac{|\theta - \theta'|}{\theta'} \tag{6.2}$$

We considered the potential values returned by this function as reference.

In the present case, the particles exiting the switchyard must travel through a 4 m-long beam pipe to reach the free-fall chamber. Taking into account that a focusing/re-accelerating system is essential, we looked at the beam size, divergence and transverse speed to determine the best electrode shape.

	δy (2σ) (mm)	δz (2σ) (mm)	δDy (2σ) $(mrad)$	δDz (2σ) $(mrad)$	δE (2σ) (eV)	δV_y (2σ) $(mm/\mu s)$	δV_z (2σ) $(mm/\mu s)$
Entrance	4.95	5.04	22.48	22.62	100	9.7	9.9
G1-T2P	20.4	13.3	79.8	42.41	98.2	33.5	16.4
G2-CPB	22.8	10.6	102.2	14.2	93.5	42.9	5.4
G3-CCPB	22.9	12	107.7	12.0	80.5	46.2	4.8

Table 6.1 Beam parameters for the different designs proposed for the switchyard

T2P is the simplest design to perform a 30° bend. As expected with such a system, we can see in the Figure-6.2 that the beam profile at the exit of the switchyard spreads on the X-axis into a wedge shape. This is typical from an electrostatic deviation for a beam with such a large energy distribution ($\sim 1\%$).

In addition, a spread of the transverse speed distribution on the Y-axis also appears in Figure-6.3.

Taking into account the energy spread and the beam profile, we can easily understand this behaviour. A particle at the centre of the entrance beam pipe with an energy slightly lower than 1 keV will be more deviated by the field and then appears on the left part of the beam profile. Inversely, a particle with an energy slightly higher than 1 keV will more deeply penetrate into the field and then experience a stronger deviation.

Since most of the particles out of a radius $r > 10$ mm are lost, we study a new design with a continuous ramp potential all along the deviation.

CPB is an improved design of T2P. We can see in Figure-6.4 that we reduced the wedge transverse profile of the beam exiting the switchyard by using an electrode following the trajectory of the particles.

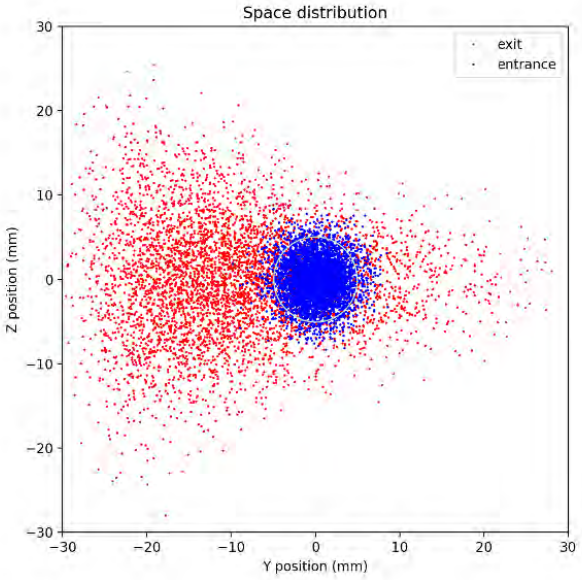

Figure 6.2 Beam Profile comparison between the beam at the entrance (*blue*) and exit (*red*) of the T2P design switchyard with respect to the optical axis.

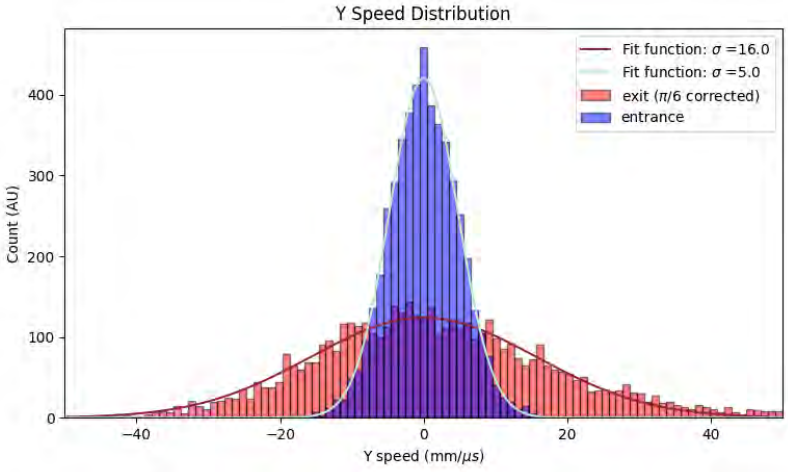

Figure 6.3 Transverse (Y-)speed distribution comparison at the entrance (*blue*) and exit (*red*) of the T2P design. Distributions are fitted with a gaussian function. The standard deviation value σ is indicated in each case in the corresponding legend.

The CCPB design is based on the CPB design but with an even better definition of the potential at the entrance and at the exit of the switchyard with the use of grounded gates. No major effects compare to the CPB design. However, we can notice a small change in the horizontal Y phase space diagram where particles on the edge of the 'bow tie' are less affected, see the comparison in Figure-6.5 of the vertical phase space between the CPB design and the CCPB design.

The initial beam parameters are directly extracted from the SIMION decelerator sim-

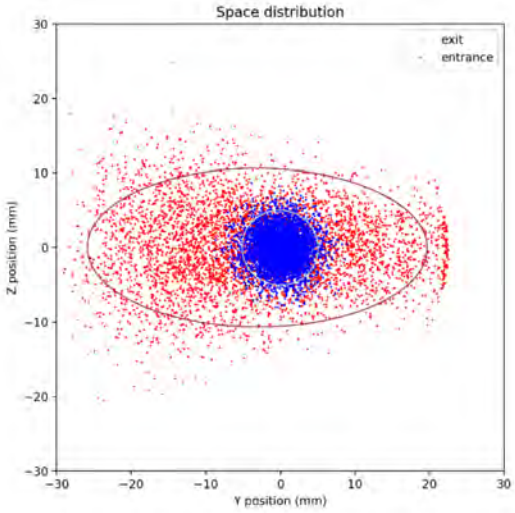

Figure 6.4 Beam Profile comparison between the beam at the entrance (*blue*) and exit (*red*) of the CPB design with respect to the optical axis.

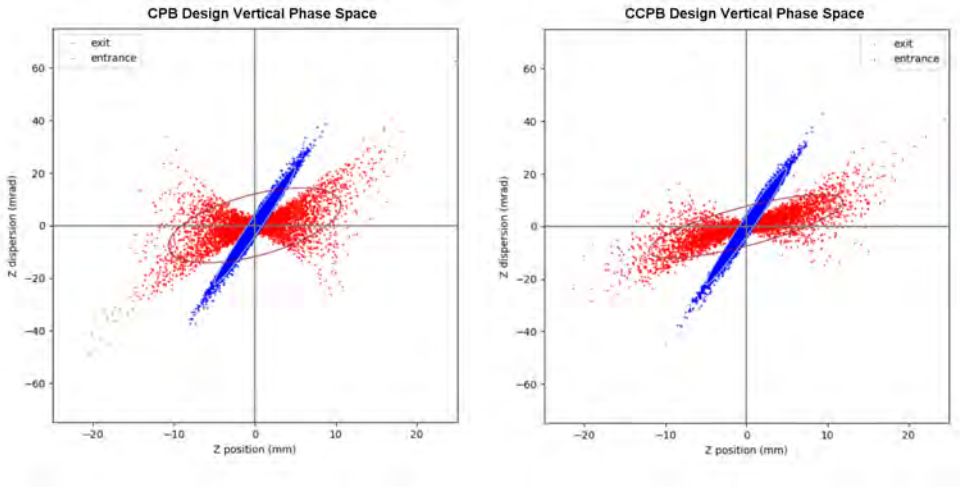

Figure 6.5 CPB and CCPB phase space diagrams comparison.

ulations through a 1 *mm*-radius and 20 *mm*-long cylinder (simulating the Ps converter). 642 particles are fired through the system. The design of the electrodes follow the CPB design with corrective grounded gates (so called 'CCPB'). According to this simulation, we conserved 100% of the beam downstream.

The small number of particles generated by this program do not permit to study the impact of the different design on the beam. That is the reason why we performed it only with the finalized CCPB geometry.

Starting from a basic system made of two successive bending plate electrodes. We found that a continuous electrode should be preferred to limit the wedge profile of the beam and reduce 'bow tie' effect.

A design with 100mm-large electrodes completed with grounded gates was found to be

	δy (2σ) (mm)	δz (2σ) (mm)	δDy (2σ) $(mrad)$	δDz (2σ) $(mrad)$	δE (2σ) (eV)	δV_y (2σ) $(mm/\mu s)$	δV_z (2σ) $(mm/\mu s)$
Entrance	4.95	5.04	22.48	22.62	100	9.7	9.9
G1-CCPB	20.4	13.3	79.8	42.41	98.2	33.5	16.4

Table 6.2 Results for the switchyard with a better defined initial beam

an optimal design. Taking into account the initial energy spread, the electrostatic induces a spread in velocity and divergence on the Y-axis, while it minimizes these parameters on the Z-axis.

Switchyard chamber Therefore, this design was adopted and engineered[1] along with the CF vacuum chamber. As shown in Figure-6.6, the chamber containing the switchyard consists of a 300 mm-diameter tank (CF standard) with an entry port 100 mm wide ($CF100$) and three exit ports 63 mm wide. The height of the chamber has been fixed to 250 mm for space occupancy. The entire chamber was modeled in the simulations in order to define the ground potential reference around the charged electrodes.

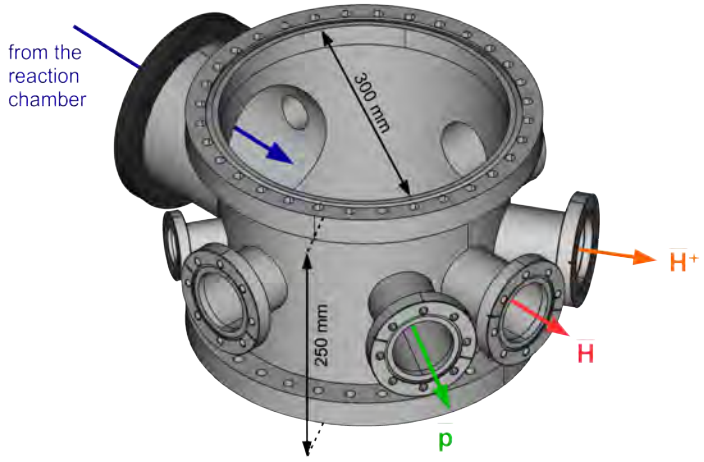

Figure 6.6 Drawing of the switchyard vacuum chamber DN300CF standard with ±30° port plus 0° other ports.

[1]By P. Tetaz under the supervision of D. Pierrepont

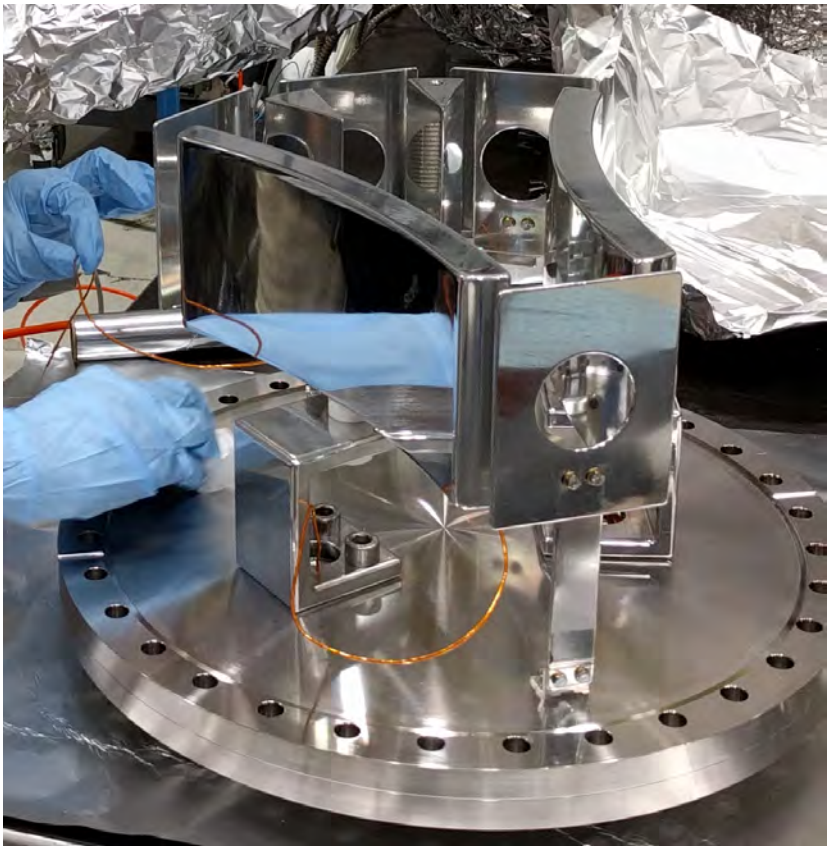

Figure 6.7 Picture of the switchyard optics mounted in their vacuum chamber. In the foreground, the ground gate marks the entrance of the switchyard.

6.1.2 Time-varying voltage on the drift tube

As we saw in the Section-5.2.1, the use of a SPDT switch offers the possibility to change the polarity of the drift tube. By applying a time-varying potential on the PDT, (anti)proton pulses can be tailor to the positron pulse in order to maximize the temporal overlap of Ps and antiprotons or simply compress to increase the rate of trapped particles.

If we assume the antiproton velocity spread to be $\sigma(v)$ and that such a spread is linearly correlated to the position of the ion in the bunch. We can define the speed of the particles with respect to their position in the bunch as :

$$v_p - \bar{v} = \alpha(x_p - \bar{v}) \tag{6.3}$$

where v_p, the speed of the considered particle; $\bar{v}$, the mean speed of the bunch; x_p, the position of the considered particle; $\bar{x}$, the mean position of the bunch and α the linear correlation factor.

We can connect the Eq.-6.3 to the time t_p at which the considered particle passes the center of the gap between the PDT and the grounded electrode behind.

$$v_p \approx \bar{v}(1 - \alpha t_p) \tag{6.4}$$

By changing the value of the potential on the PDT, we can change the kinetic energy of the (anti)protons so that all of them (from the head to the tail of the bunch) enter into the downstream trap cavity. We can thus estimate the required change in energy as :

$$\Delta E = \bar{E} - E_p = \frac{m_p}{2}(\bar{v}^2 - v_p^2) = m\bar{v}(\bar{v} - v_p) \approx 2E\alpha t_p \tag{6.5}$$

If we assume a potential $V(z,t)$ on the optical axis to be linear (at the first order).

$$V(z,t) = V_{PDT}(t)\left(1 - \frac{|z|}{L}\right) \tag{6.6}$$

where V_{PDT}, the potential on the PDT; z, the position from the edge of the PDT and L, the gap between the PDT and the grounded electrode behind.

We integrate the force applied on a particle of charge q along the gap between the PDT and the grounded electrode:

$$\Delta E = -q\int_0^L \frac{\partial V(z,t)}{\partial z} dz \tag{6.7}$$

Supposing $\sigma(v) << \bar{v}$, Eq.-6.7 becomes :

$$\Delta E = \frac{q}{L}\int_0^{L/\bar{v}} V_{PDT}(t(z))dt \tag{6.8}$$

According to Ref.-[175], a general solution is :

$$V_{PDT}(t) = V_{PDT}^0[1 - (t/T_p)^k] \tag{6.9}$$

where T_p is the half-period of the bunching pulse; V_{PDT}^0, the potential applied on the PDT after switching and $k \in \mathbb{N}$ is the time-bunching factor.

SIMION simulations have been performed applying $\bar{p}$ time-bunching in order to maximize the 'at-target' density while minimizing subsequent energy spread [176]. An example of such bunching simulation is shown in Figure-6.8. It has been shown that an increase in $\bar{H}^+$ formation of approximately an order of magnitude could be expected by implementing such bunching with $k = 2$.

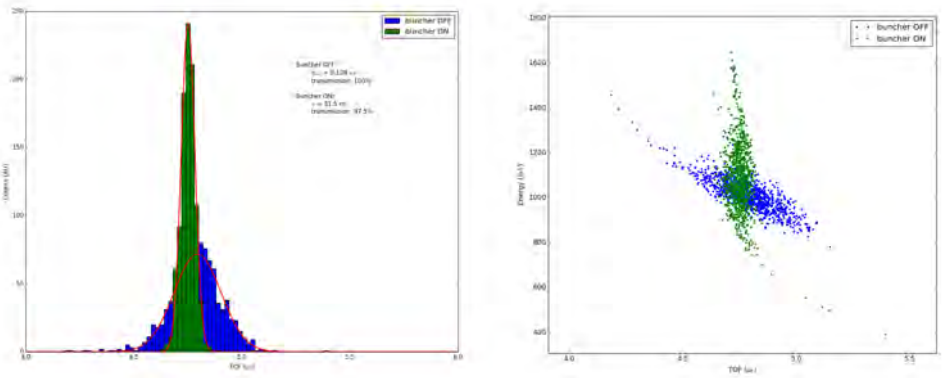

Figure 6.8 TOF spectrum (*left*) and TOF versus energy diagram (*right*) of a time-focused antiproton beam 2.4 m downstream the decelerator simulated with SIMION.

6.1.3 Antiproton trap

As shown in Figure-6.9 from Ref.-[104], reducing the proton impact energy leads to a considerable gain in the $\bar{H}^+$ production cross section. Therefore, during the LS2, the upgrade program involves the installation of a Penning-Malmberg cryogenic trap between the decelerator and the reaction chamber. It will trap, accumulate and cool down antiproton bunches once decelerated. Such an antiproton trap will also aim to increase the number of $\bar{p}$ crossing the PPs converter and decouple the experiment from the AD-ELENA cycle.

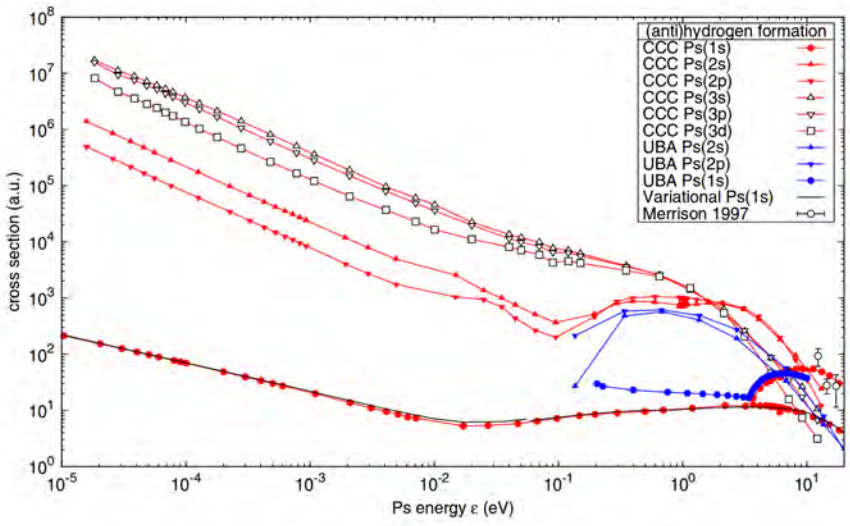

Figure 6.9 Total cross sections for positronium atoms, in the specified initial state nl, scattering on (anti)protons to form (anti)hydrogen calculated by using the CCC methods, more details in Ref-[104]. The three experimental points are due to Merrison et al. [106].

The trap is built following the example of the MUSASHI trap in the ASACUSA experiment [177]. As shown in Figure-6.10, a series of cylindrical electrodes of 10.5 mm inner radius are assembled within a cryogenic magnet generating a high homogeneity magnetic field of 7 T. The electrodes are maintained in a cryogenic vacuum chamber guaranteeing a maximum vacuum of 10^{-11} $mbar$ to preserve the antiprotons and to improve the thermalization of the plasma.

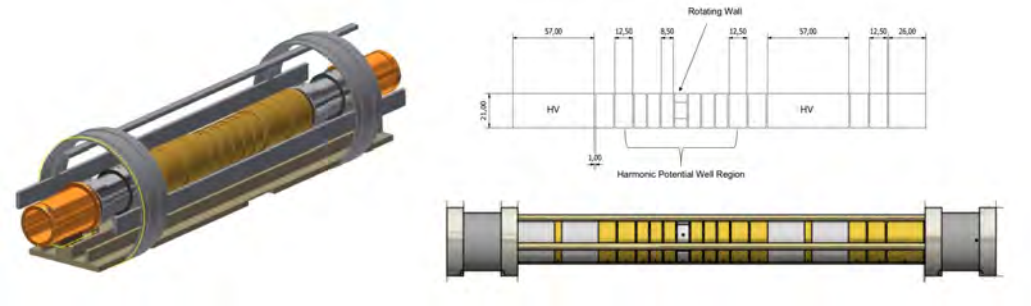

Figure 6.10 GBAR antiproton trap electrodes.

Different cooling techniques will be studied including sympathetic cooling with a preloaded electron plasma. The capture of antiprotons will allow rotating wall compression as for the positron line (see Chapter 2). The latter reduces the spot size of the antiproton beams crossing the PPs converter. On a basis of comparison with the MUSASHI trap [98, 99, 177, 178], one can expect pulses of 10^5 antiprotons with an energy spread of $\sim 0.1\ eV$.

Injection electrodes

In order to guarantee that the maximum number of $\bar{p}$ is trapped despite the energy dispersion, SIMION simulations have been realized. The main difficulty relies on the injection into the cavity of the trap taking into account the effects related to the magnetic field. The first is the magnetic mirror effect. It occurs when the incident particles have an excessive angle and are then deflected by the magnetic field lines. They are reflected at the entrance of the trap.

The antiprotons that are not reflected spiral in the magnetic field. The radial component of their speed is transformed into cyclotron motion. Only the longitudinal component is retained. This results in a spread of the $\bar{p}$ bunch.

Only part of the $\bar{p}$ are trapped in the cavity. Simulations carried out was aimed at improving the injection optics in the trap. Two cases were investigated:

- the first with a simple Einzel lens corresponds to the one described in the previous section
- the second relates to the addition of a second lens at the entrance of the trap (out of the magnetic field).

The simulated beam follows the configuration "2m Minimize Alpha" (see Table-4.2). This configuration tends to minimize the divergence of the beam 2 m downstream the GBAR handover point (separation valve between ELENA and GBAR) and is more suitable than the "4m Minimize Alpha" configuration used so far. The magnetic field introduced in SIMION simulation corresponds to the measured field map of the cryogenic magnet.

The trap electrodes can withstand voltages up to 5 kV. Then the $\bar{p}$ beam is decelerated to 2 keV to keep the definition of the beam good enough. The decelerator electrodes are set according to the recommendations seen in Chapter 2, i.e. a telescopic setting where the PDT is polarized to $-98\ kV$ and the $V2$ lens (strong potential) to $-68.4\ kV$.

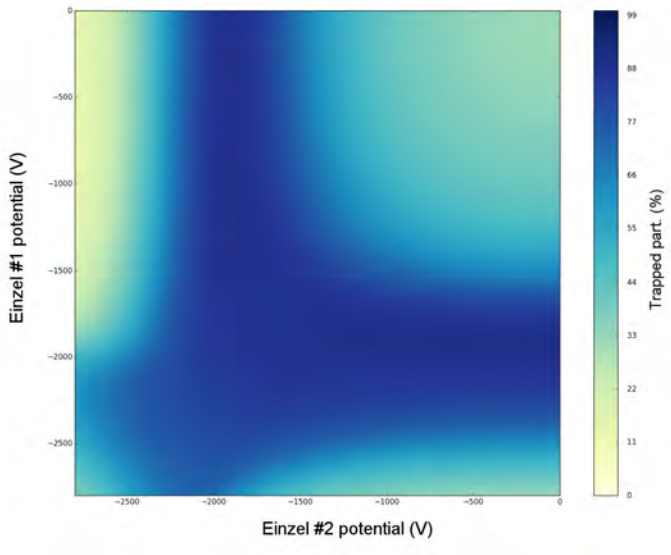

Figure 6.11 Fraction of trapped antiprotons according to SIMION simulations using two lenses. Einzel #1 corresponds to the lens directly downstream the decelerator and Einzel #2 corresponds to an additional lens placed upstream the cryogenic $\bar{p}$ trap (out of the magnetic field).

Trapping is simulated in stages. In a first step by applying a $-3\ kV$ potential on the last electrode. After an optimized time, the potential on the first electrode is also raised to $-3\ kV$ to complete the potential well. An antiproton is thus considered trapped if it enters the cavity and performs at least 10 round trips in the potential well. The result is given as a percentage of the 5000 particles initially generated, as seen in Figure-6.11 with respect to the potentials on the focusing electrodes.

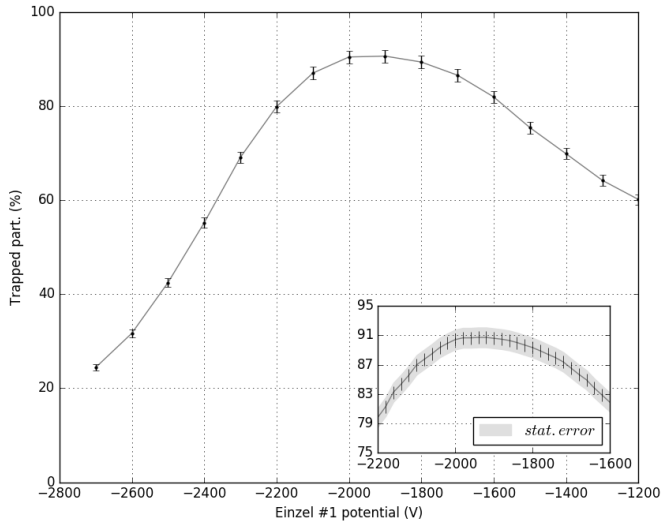

Figure 6.12 Fraction of trapped antiproton according to SIMION simulations using a single lens downstream of the decelerator. The inset corresponds to a finer voltage step.

First, the use of two lenses is of limited interest. Indeed, maximum trapping is obtained when one of the two lenses is off. If we compare the situations $V_1 = 0\ V$ or $V_2 = 0\ V$, the case $V_2 = 0\ V$ is slightly more favorable with a maximum transmission of 90.7% trapped for $V_1 = -1940\ V$. A more detailed simulation for $V_2 = 0\ V$ is presented in Figure-6.12.

Considering the 73% transmission through the quadruple bender of the GBAR proton source, the decelerator and the quadruple triplet, it corresponds to $73\% \times 90.7\% = 66\%$ of the antiproton beam in the trap. This value is to be compared with the results obtained with the today techniques where only 0.01% are trapped.

6.2 GBAR proton source

In anticipation of the Long Shutdown 2, a proton source has been devised to provide the GBAR experiment with protons in the absence of antiproton beams. Such a source will allow experiments and measurements complementary to that of the antimatter free fall.

During the LS2, this source will be the corner stone of the development program. It will allow the development of the electrostatic optics along the antiproton line. The first element to be tested is the injection into the cryogenic antiproton trap whose installation is also scheduled during the LS2. The protons will also allow to commission the cryogenic trap and test the different cooling techniques. When high energy beams at CERN will restart, these techniques will then be applied to antiprotons as part of the free fall measurement.

The proton source will be used to carry out a measurement program as well, concerning the cross-section for the production of hydrogen atoms and hydrogen ions following the single or double charge exchange reaction (matter equivalent of Eq.-2.2 and Eq.-2.3):

$$p + Ps \longrightarrow H + e^+ \tag{6.10}$$

$$H + Ps \longrightarrow H^- + e^+ \tag{6.11}$$

This cross-section measurement is based on the work of Merrisson et al [105, 106]. The GBAR collaboration will be engaged in demonstrating the impact of laser excitation of the positronium on the production cross-section. All this matter-based study program is an essential preliminary step in anticipation of the restart of antiproton beams at CERN.

6.2.1 Source characteristics

The source is an *Electron Cyclotron Resonance* source (ECR)[2]. H_2 gas is injected into the plasma chamber of the source immersed in a magnetic field. A 2.45 GHz radio-frequency wave excite the electrons in the plasma. The frequency of the RF coincides with the cyclotron frequency of the electron and exhausts the ionization of the gas. In the same way as for the discharge source used with the off-line prototype(see Section-5.1.1), the cavity is placed at a floating potential allowing extraction and initial acceleration of the ions.

A schematic of the source is shown in Figure-6.13. This source has the advantage of being compact while delivering intense beams up to 600 μA current.

[2]Model TES35 from *Polygon Physics*

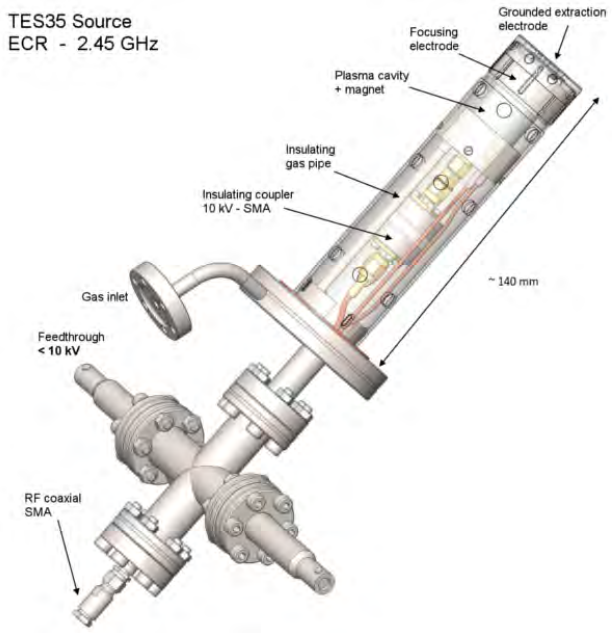

Figure 6.13 Schematic of the TES35 proton source integrated in the GBAR experiment. Data from the Polygon Physics company.

6.2.2 Proton source line design

Operation with hydrogen gas imposes particular conditions in order to create a plasma especially in terms of gas flow. Priming and maintaining the plasma impose a high gas flow of the order of 12 $sccm$[3]. This results in a high pressure between 10^{-3} and 10^{-4} $mbar$ in the source enclosure.

Such pressure is incompatible with the maximum expected pressure of 10^{-8} $mbar$ in the first decelerator chamber[4]. In order to minor the impact of the source, a three stage differential pumping line has been developed as illustrated in Figure-6.14.
Vacuum basic calculations give an estimation of the expected pressures in the successive cavities. The pressure in the intermediate cavity is expected to be $p_2 = 2.10^{-6}$ $mbar$. The conductivity between two successive cavities is limited by adding pumping restrictions. A more detailed simulation with the Molflow software, presented in Figure-6.14 confirmed the geometry of the proton line.

Since the TES35 operates with hydrogen, the beam is essentially made of single-charged positive ions H^+, H_2^+ and H_3^+, and neutral species H, H_2 and H_3 (see Table-6.3). Indeed, the charged species composing the extracted beam collide with the residual gas atoms in the chamber and neutralize. The Figure-6.15 shows the deviation of the charged particles extracted from the TES35 proton source when passing in the vicinity of a magnet. The proportions of each of the species were estimated from the light intensity profile. The contribution of each charged species for the $600\mu A$ current follows :

[3] $sccm$ means *Standard cubic Centimeters per Minute*, 1 $sccm = 0.016$ $mbar.l/s$.
[4] A higher pressure in the decelerator would impact the pressure in the reaction chamber as well and disrupt the production of positronium and antihydrogen.

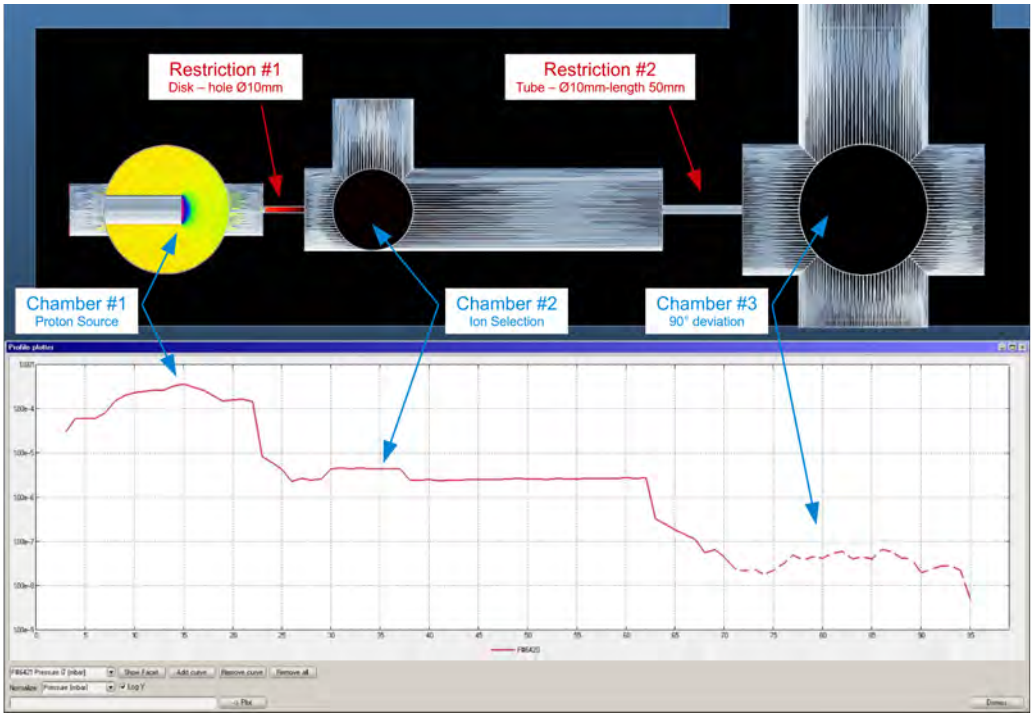

Figure 6.14 Molflow simulation of the GBAR proton source line. The simulation presents the three stage differential pumping simplified geometry (*top*) and the corresponding simulated pressure (*bottom*). The proton source is located in the left cavity. In the bottom plot, the distance on the X-axis is in *cm* and the pressure on the Y-axis is in *mbar*. Since the number of simulated events in the third cavity is not enough, the dashed line illustrates a maximum limit of the pressure.

Charged species	Rate (%)
H^+	5
H_2^+	58
H_3^+	37

Table 6.3 Proportion of the charged species extracted from the TES35 source for a current of $600\mu A$ except the neutral species. Data given by the Polygon Physics company.

Optics along the proton line As previously described, the source provides ions of H^+, H_2^+ and H_3^+. Some of these ions collide with the gas atoms in the source enclosure and neutralize, producing neutrals of H, H_2 and H_3. A dedicated electrostatic system has been developed to select only the H^+ ions as depicted in the Figure-6.16.

First, a flat Einzel lens focuses the beam into the gap of a Wien filter[5]. The Wien filter selects in mass the H^+ ions. The principle is equivalent as in Section-5.1.1. The others species (H_2^+, H_3^+) are dumped into the second chamber. The amount of neutrals produced in the second cavity has been taken into account for the design of the differential pumping system. In addition to the Wien filter, a pair of electrostatic plates chop the beam to get 300 *ns* bunches.

Upon entering the third chamber, the pulse is composed of H^+ ions and neutrals elements. The selection of the remaining charged particles is done using a quadruple

[5]The same Wien filter as presented in the Figure-5.6.

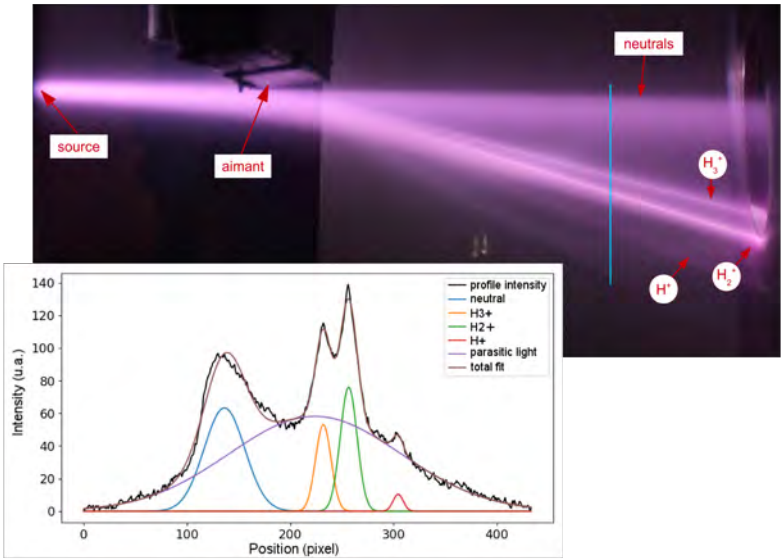

Figure 6.15 Photograph of the separation of the different species extracted from the TES35 source by a magnet placed at the nearest beam during preliminary tests conducted by Polygon Physics. The insert represents the profile of the light intensity of the beam picture along the blue line. Data from the Polygon Physics.

bender. The protons are deflected at a 90° angle when neutrals continue without being deflected. Once again, the amount of neutral stopping in the third cavity has been taken into account.

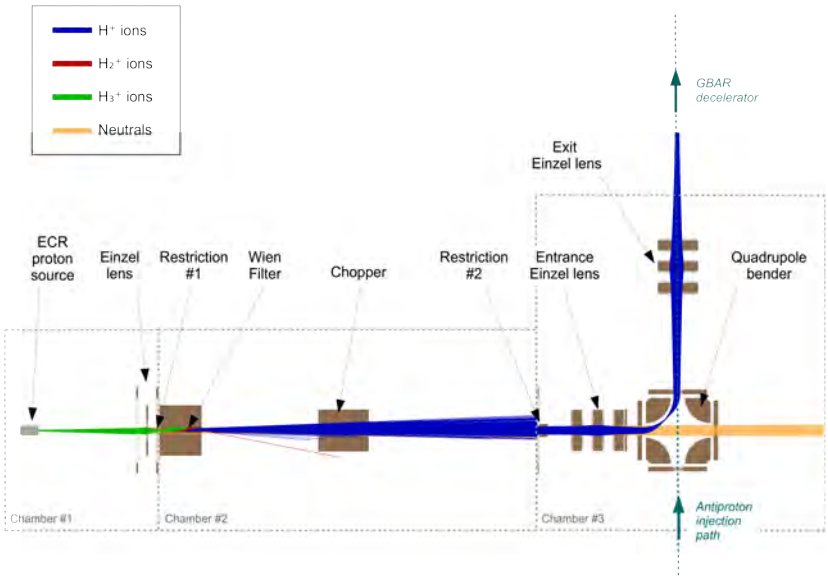

Figure 6.16 SIMION simulation of the GBAR proton line optics. The simulated beam is composed of H^+, H_2^+ and H_3^+ ions and neutrals elements. The initial beam energy is set to 10 keV.

Last but not least, to enhance the transmission through the bender, two small Einzel lenses are positioned upstream and downstream. The position of the last Einzel lens on the proton was investigated to ensure the best transmission through the decelerator. The case of a segmented Einzel lens was also simulated to compensate the vertical distortion of the beam when passing through the electrostatic quadruple bender. The projection of the proton beam profile at the first pre-decelerating electrode of the decelerator is shown in Figure-6.17.

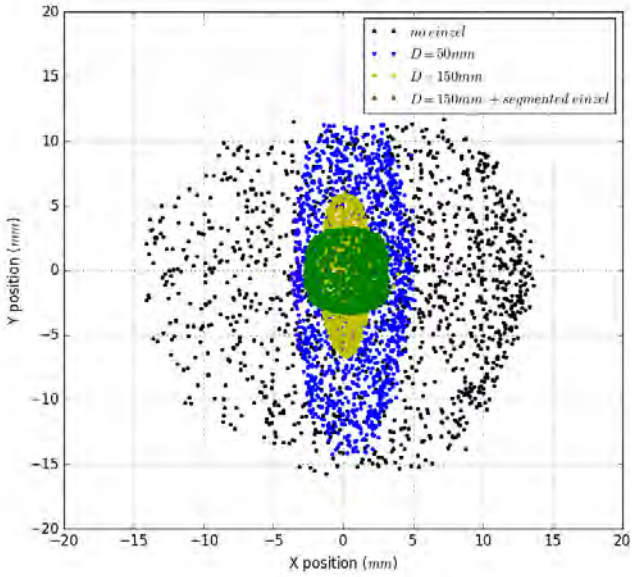

Figure 6.17 Profiles of the proton beam 1 m downstream the quadruple bender in the decelerator chamber. The profile is taken at the first pre-decelerating electrode. The four cases correspond to a 90° deflection into the antiproton line without downstream Einzel lens (*black*), with the downstream Einzel lens at 50 mm (*black*), at 150 mm (*yellow*) and with a segmented Einzel lens for vertical/horizontal discrimination (*green*)

Chapter 7

Conclusion & Perspectives

7.1 Conclusion

Numerous experimental investigations prove that the gravitational mass and the inertial mass of ordinary matter are equivalent. Given the lack of evidence considering the gravitational behaviour of *antimatter* systems, GBAR will first synthesize antihydrogen ions using laser-excited positronium. These ions are then captured and cooled to few neV before being dropped into a detection chamber to measure $\bar{g}$.

The production of such ions relies on a double charge-exchange reaction for which antiproton energies below a few keV are predicted to be most favourable. The new extra low-energy antiproton ring ELENA will extend the deceleration capacity of the CERN Antiproton Decelerator (AD) providing 100 keV antiproton beams for experiments devoted to antihydrogen, including GBAR. If 100 keV is still quite high for the reactions producing antihydrogen ions, this regime allows the use of electrostatic devices.

We reported here the design of a new electrostatic device to further decelerate antiprotons from 100 keV to about 1 keV which avoids losses from the use of energy-degrading foils. This decelerating system is made of a series of six electrostatic, retarding lenses followed by a 400 mm long drift tube held at -99 kV, which is switched to ground while the antiprotons are inside and avoid the re-acceleration of the antiprotons while exiting.

The electric field gradient at the entrance of the pulsed drift tube leads to a strong focusing of the beam. The 5 deceleration electrodes upstream are set to potentials ensuring a parallel transport through the tube. These potentials have been simulated with the SIMION software. Considering the very large number of combinations possible, a dedicated genetic algorithm (GA) has been implemented to select the best configurations, two of which have been retained. To our knowledge, this is the first application of a GA to a problem in low-energy beam transport.

In addition to this computational work, we reported the first test of deceleration for a proton beam from 48 keV to 1.4 keV. The deceleration as well as the final energy have been confirmed by two different techniques (TOF and Grid analyzer) with ions generated from a discharge-type source integrated into a test bench built in Orsay. The results corroborate the expected value simulated with the SIMION software.

After the encouraging preliminary results, a complete decelerator stage implementing an air-insulated 100 kV pulsed system respecting the physical constraints of the deceleration as well as the CERN safety policy, was connected to the ELENA ring and commissioned. Antiproton beams have now been decelerated to energies below 10 keV without using foils for the first time.

The first results obtained in 2018 commissioning at CERN are encouraging. Indeed, the comparison of the results in terms of decelerating voltage configurations calculated using the GA was difficult since the conditions were not exactly the same. The ELENA injection optics were different, the beam was not on axis, and the electrode (and beam line) alignment was not perfect. But now, some data are available.

7.2 Perspectives

Some ideas are put forward to improve the apparatus and the whole experiment.

As we saw in Chapter 2, the number of $\bar{H}^+$ produced depends on the number of positrons and antiprotons introduced inside the PPs converter. The antiproton trap (as discussed in Chapter 6) should increase the number of low energy, cooled antiprotons. However, the very low cross section for producing even $\bar{H}$ remains a problem. Indeed, almost 99% of the antiprotons do not interact and are lost downstream the switchyard. If several experiments expressed interest in the use of this manna of unused antiprotons, it is clear that this is a significant loss taking into account the time required for AD and ELENA to provide a new antiproton pulse to GBAR.

Re-using $\bar{p}$ pulses would offer a significant advantage in making $\bar{H}$ production independent of the AD/ELENA cycles. Furthermore, even with low efficiency, recycling would significantly reduce the time of accumulation of antiprotons.

Based on the principle of a reflectron [179], the first case would reverse the direction of travel of the ions. With the cooling applied inside the trap the energy spread of the antiprotons is low enough. However, reflecting the beam seems to concentrate the problems on the reaction chamber. Indeed, in such a case, the antiproton pulse would go back and forth through the PPs converter (and through the input collimator) reducing the number of antiprotons recycled. According to the energy spread, bypassing the PPs converter on the way back to the trap is possible using deflector plates as used in Ref.-[180] to trap the particles in a closed path.

Moreover, the energy spread of the downstream $\bar{H}^+$ beam is still a major problem for their capture into the RF Paul trap (see Chapter 2). The idea of using an Electrostatic Ion Beam Trap has been proposed as a solution [181].

The next steps are to carefully simulate the real conditions, also including the annihilation/scintillator data. This, in addition to the measurement of the cross sections and building the free-fall chamber, will certainly occupy the GBAR collaboration during LS2.

Nomenclature

Acronyms / Abbreviations

AD Antiproton Decelerator

AI Artificial Intelligence

AOp Automatic Optimization

BGT Buffer Gas Trap

CERN Organisation Européenne pour le Recherche Nucléaire

CF Comflat technology

CCPB Corrected CPB design

CPB Curved Plate Bender design

CPT Symmetry CPT: Charge, Parity, Time (reversal)

$\bar{d}$ Antideuterium

ECR Electron Cyclotron Resonance

EEP Einstein Equivalence Principle

ELENA Extra Low ENergy Antiproton ring

EP Equivalence Principle

FC Faraday Cup

GA Genetic Algorithm

GBAR Gravitational Behavior of Antimatter at Rest

GR General Relativity

$^2\bar{H}^+$ or $\bar{d}$ Antideuteron (antideuterium nucleus)

$^3\bar{H}^+$ Antitriton (antitritium nucleus)

Hbar ($\bar{H}$) Antihydrogen

$^3\bar{H}e^{(2+)}$ Antihelium-3

$^4\bar{H}^{(2+)}$ Antihelium-4

HV High Voltage

$^3_{\bar{\Lambda}}\bar{H}^+$ Antihypertriton

ΛCDM model Standard Cosmological Model, Lambda-Cold Dark Matter model

LEAR Low Energy Anti-proton Ring

LLI Local Lorentz Invariance

LPI Local Position Invariance

LS2 Long Shutdown 2

MCP-EA MCP detector with Energy Analyzer

MCP Multi Channel Plate detector

nbar ($\bar{n}$) Antineutron

oPs Ortho-positronium

pbar ($\bar{p}$) Antiproton

PDT Pulsed Drift Tube

pPs Para-positronium

PPs Positron-Positronium converter

RFQD Radio-Frequency Quadrupole Decelerator

RK4 Runge-Kutta method at 4^{th} order

SEP Strong Equivalence Principle

SME Standard Model Extension

SM Standard Model

SPDT Single Pole, Double Throw

SPST Single Pole, Single Throw

T2P Three Plate Pairs design

TOF Time-Of-Flight

UCN Ultra-Cold Neutron

UFF Universality of Free-Fall

UHV Ultra High Vacuum

VHV Very High Voltage

WEP Weak Equivalence Principle

Bibliography

[1] G. Gabrielse, N. S. Bowden, P. Oxley, A. Speck, C. H. Storry, J. N. Tan, M. Wessels, D. Grzonka, W. Oelert, G. Schepers, T. Sefzick, J. Walz, H. Pittner, T. W. Hänsch, and E. A. Hessels. Background-free observation of cold antihydrogen with field-ionization analysis of its states. *Phys. Rev. Lett.*, 89:213401, Oct 2002.

[2] D. Hanneke, S. Fogwell, and G. Gabrielse. New measurement of the electron magnetic moment and the fine structure constant. *Phys. Rev. Lett.*, 100:120801, Mar 2008.

[3] G. Gabrielse, R. Kalra, W. S. Kolthammer, R. McConnell, P. Richerme, D. Grzonka, W. Oelert, T. Sefzick, M. Zielinski, D. W. Fitzakerley, M. C. George, E. A. Hessels, C. H. Storry, M. Weel, A. Müllers, and J. Walz. Trapped antihydrogen in its ground state. *Phys. Rev. Lett.*, 108:113002, Mar 2012.

[4] B. Radics, S. Ishikawa, N. Kuroda, D. J. Murtagh, Y. Nagata, M. Tajima, S. Van Gorp, Y. Abo, P. Dupre, Y. Higashi, C. Kaga, M. Leali, V. Mascagna, L. Venturelli, N. Zurlo, H. Breuker, H. Higaki, Y. Kanai, E. Lodi Rizzini, Y. Matsuda, S. Ulmer, and Y. Yamazaki. Antihydrogen synthesis in a double-cusp trap towards test of the cpt-symmetry. *Hyperfine Interactions*, 237(1):156, Nov 2016.

[5] Y. Nagata, N. Kuroda, P. Dupre, B. Radics, M. Tajima, A. A. Capon, M. Diermaier, C. Kaga, B. Kolbinger, M. Leali, E. Lodi Rizzini, C. Malbrunot, V. Mascagna, O. Massiczek, T. Matsudate, C. Sauerzopf, M. C. Simon, K. Suzuki, J. Zmeskal, H. Breuker, H. Higaki, Y. Kanai, Y. Matsuda, S. Ulmer, L. Venturelli, E. Widmann, and Y. Yamazaki. Progress of antihydrogen beam production using a double cusp trap. *JPS Conf. Proc.*, 18:011007, 2017.

[6] C. Malbrunot, C. Amsler, S. Arguedas Cuendis, H. Breuker, P. Dupre, M. Fleck, H. Higaki, Y. Kanai, B. Kolbinger, N. Kuroda, M. Leali, V. Mäckel, V. Mascagna, O. Massiczek, Y. Matsuda, Y. Nagata, M. C. Simon, H. Spitzer, M. Tajima, S. Ulmer, L. Venturelli, E. Widmann, M. Wiesinger, Y. Yamazaki, and J. Zmeskal. The asacusa antihydrogen and hydrogen program: results and prospects. *Philosophical Transactions of the Royal Society of London A: Mathematical, Physical and Engineering Sciences*, 376, 2018.

[7] G. B. Andresen et al. Trapped antihydrogen. *Nature*, 468:673–676, 2010.

[8] G. B. Andresen et al. Confinement of antihydrogen for 1000 seconds. *Nature Phys.*, 7:558–564, 2011.

[9] M. Ahmadi et al. An improved limit on the charge of antihydrogen from stochastic acceleration. *Nature*, 529(7586):373–376, 2016.

[10] P.A.M. Dirac. The quantum theory of the electron, part i. *Proceedings of the Royal Society of London. Series A.*, 117:610, 1928.

[11] P.A.M. Dirac. The quantum theory of the electron, part ii. *Proceedings of the Royal Society of London. Series A.*, 118:351, 1928.

[12] H. Weyl. Elektron und gravitation. i. *Zeitschrift für Physik*, 56:330–352, 1929.

[13] P.A.M. Dirac. A theory of electrons and protons. *Proceedings of the Royal Society of London. Series A.*, 133:60, 1930.

[14] J.R. Oppenheimer. On the theory of electrons and protons. *Physical Review*, 35:562, 1930.

[15] C. Anderson. The apparent existence of easily deflectable positives. *Science*, 76:238, 1932.

[16] P. Blackettandand G. Occhialini. Some photographs of the tracks of penetrating radiation. *Proceedings of the Royal Society of London. Series A.*, 139:699–726, 1933.

[17] C. Anderson. The positive electron. *Physical Review*, 43:491, 1933.

[18] I. Curie and F. Joliot. Nobel prize speech. 1935.

[19] J. Chadwick. Possible existence of a neutron. *Nature*, 129:402, March 1932.

[20] E. Hayward. Ionization of high energy cosmic-ray electrons. *Phys. Rev.*, 72:937, 1947.

[21] H.S. Bridge, H. Courant, H. DeStaebler, Jr. Rossi, and B. Rossi. Possible example of the annihilation of a heavy particle. *Nuovo Cimento*, 95:1101, 1954.

[22] E. Amaldi, C. Castagnoli, G. Cortini, C. Franzinetti, and A. Manfredini. Unusual event produced by cosmic rays. *Nuovo Cimento*, 1:492–500, 1955.

[23] O. Chamberlain, E. Segrè, C. Wiegand, and T. Ypsilantis. Observation of antiprotons. *Phys. Rev.*, 100:947, 1955.

[24] B. Cork, G.R. Lambertson, O. Piccioni, and W.A. Wenzel. Antineutrons produced from antiprotons in charge-exchange collisions. *Phys. Rev.*, 104:1193, 1956.

[25] D.E. Dorfan, J. Eades, L.M. Lederman, W. Lee, and C.C. Ting. Observation of antideuterons. *Phys. Rev. Lett.*, 14(24):1003, 1965.

[26] T. Massam, T. Muller, B. Righini, M. Schneegans, and A. Zichichi. Experimental observation of antideuteron production. *Nuovo Cimento A*, 63(1):10–14, 1965.

[27] Yu.M. Antipov, S.P. Denisov, S.V. Donskov, Yu.P. Gorin, V.A. Kachanov, V.P. Khromov, V.M. Kutyin, L.G. Landsberg, V.G. Lapshin, A.A. Lebedev, A.G. Morozov, A.I. Petrukhin, Yu.D. Prokoshkin, E.A. Razuvaev, V.I. Rykalin, R.S. Shovalov, V.I. Soljanick, D.A. Stoyanova, N.K. Vishnevsky, F.A. Yetch, A.M. Zajtzev, and G.D. Zhilchenkova. Observation of antihelium-3. *Nuclear Physics B*, 31:235–252, 1971.

[28] N.K. Vishnevsky, M.I. Grachev, V.I. Rykalin, V.G. Lapshin, V.I. Solyanik, Yu.S. Khodyrev, V.P. Khromov, B.Yu. Baldin, L.S. Vertogradov, Ya.V. Grishkevich, Z.V. Krumsztein, R. Leiste, Yu.P. Merekov, V.I. Petrukhin, D. Pose, A.I. Ronzhin, I.F. Samenkova, V.M. Suvorov, G. Chemnitz, N.N. Khovansky, B.A. Khomenko, M. Zawlowski, G.A. Shelkov, and J. Schuler. Observation of antitritium [in russian]. *Yad.Fiz.*, 20:694–708, 1974.

[29] G. Baur, G. Boero, A. Brauksiepe, A. Buzzo, W. Eyrich, R. Geyer, D. Grzonka, J. Hauffe, K. Kilian, M. LoVetere, M. Macri, M. Moosburger, R. Nellen, W. Oelert, S. Passaggio, A. Pozzo, K. Röhrich, K. Sachs, G. Schepers, T. Sefzick, R.S. Simon, R. Stratmann, F. Stinzing, and M. Wolke. Production of antihydrogen. *Physics Letters B*, 368:251–258, 1996.

[30] STAR Collaboration. Observation of an antimatter hypernucleus. *Science*, 328:58–62, 2010.

[31] STAR Collaboration. Observation of the antimatter helium-4 nucleus. *Nature*, 473:353–356, 2011.

[32] ALICE Collaboration. Precision measurement of the mass difference between light nuclei and anti-nuclei. *Nature Physics*, 11:811–814, 2015.

[33] J. Adam et al. Production of light nuclei and anti-nuclei in *pp* and pb-pb collisions at energies available at the cern large hadron collider. *Phys. Rev. C*, 93:024917, Feb 2016.

[34] P.A.M. Dirac. The quantum theory of the emission and absorption of radiation. *Proceedings of the Royal Society of London. Series A.*, 114:243, 1927.

[35] C.S. Wu, E. Ambler, R.W. Hayward, D.D. Hoppes, and R.P. Hudson. Experimental test of parity conservation in beta decay. *Phys. Rev.*, 105:1413–1415, 1957.

[36] R.L. Garwin, L.M. Lederman, and M. Weinrich. Observations of the failure of conservation of parity and charge conjugation in meson decays: The magnetic moment of the free muon. *Phys. Rev.*, 105:1415–1417, 1957.

[37] J.H. Christenson, J.W. Cronin, V.L. Fitch, and R. Turlay. Evidence for the 2π decay of the k_2^0 meson system. *Phys. Rev. Lett.*, 13:138, 1964.

[38] A. Alavi-Harati et al. (KTeV Collaboration). Observation of direct cp violation in $k_{S,L} \to \pi\pi$ decays. *Phys. Rev. Lett.*, 83:22, 1999.

[39] V. Fanti et al. (NA48 Collaboration). A new measurement of direct cp violation in two pion decays of the neutral kaon. *Phys. Lett. B*, 465:335–348, 1999.

[40] R. Aaij et al. (LHCb Collaboration). First observation of violation in the decays of mesons. *Phys. Rev. Lett.*, 110:221601, May 2013.

[41] J. DiSciacca, M. Marshall, K. Marable, G. Gabrielse, S. Ettenauer, E. Tardiff, R. Kalra, D. W. Fitzakerley, M. C. George, E. A. Hessels, C. H. Storry, M. Weel, D. Grzonka, W. Oelert, and T. Sefzick. One-particle measurement of the antiproton magnetic moment. *Phys. Rev. Lett.*, 110:130801, Mar 2013.

[42] S. Ulmer et al. High-precision comparison of the antiproton-to-proton charge-to-mass ratio. *Nature*, 524(7564):196–199, 2015.

[43] Masaki Hori, Hossein Aghai-Khozani, Anna Sótér, Daniel Barna, Andreas Dax, Ryugo Hayano, Takumi Kobayashi, Yohei Murakami, Koichi Todoroki, Hiroyuki Yamada, Dezső Horváth, and Luca Venturelli. Buffer-gas cooling of antiprotonic helium to 1.5 to 1.7 k, and antiproton-to–electron mass ratio. *Science*, 354(6312):610–614, 2016.

[44] M. Ahmadi et al. An improved limit on the charge of antihydrogen from stochastic acceleration. *Nature*, 529(7586):373–376, 2016.

[45] M. Ahmadi et al. Observation of the 1S-2S transition in trapped antihydrogen. *Nature*, 541:506–510, 2016.

[46] C. Smorra et al. A parts-per-billion measurement of the antiproton magnetic moment. *Nature*, 550(7676):371–374, 2017.

[47] M. Ahmadi et al. Observation of the hyperfine spectrum of antihydrogen. *Nature*, 548(7665):66–69, 2017.

[48] H. Nagahama et al. Sixfold improved single particle measurement of the magnetic moment of the antiproton. *Nature Commun.*, 8:14084, 2017.

[49] M. Tanabashi et al. (Particle Data Group). The review of particle physics (2018). *Phys. Rev. D*, 98:030001, 2018.

[50] Andrei Sakharov. Violation of cp invariance, c asymmetry, and baryon asymmetry of the universe. *JETP Lett.*, 5:24–27, January 1967.

[51] A. Benoit-Lévy and G. Chardin. Introducing the Dirac-Milne universe. , 537:A78, January 2012.

[52] Luc Blanchet. Gravitational polarization and the phenomenology of MOND. *Classical and Quantum Gravity*, 24(14):3529–3539, jul 2007.

[53] Paul S. Wesson. *Five-dimensional Physics*. World Scientific, 2006. ISBN: 981-256-661-9.

[54] Isaac Newton. *Principia- Philosophiae naturalis principia mathematica; Book III, Proposition VI, Theorem VI.* Univ. of California Press [english translation], 2016. ISBN: 9780520290884.

[55] R.v. Eötvös. *Math. Naturwissenschaft*, 8:65, 1890.

[56] R.v. Eötvös, D. Pekár, and E. Fekete. *Ann. Phys.*, 68:11, 1922. English translation for the U.S. Department of Energy by J. Achzenter et al., University of Washington preprint 40048-13-N6.

[57] P.G. Roll, R. Krotkov, and R.H. Dicke. The equivalence of inertial and passive gravitational mass. *Ann. Phys.*, 26:442–517, 1964.

[58] I. Shapiro, C. Counselman, and R.W. King. Verification of the principle of equivalence for massive bodies. *Phys. Rev. Lett.*, 36:555–558, 1976.

[59] T.M. Niebauer, M.P. McHugh, and J.E. Faller. Galilean test for the fifth force. *Phys. Rev. Lett.*, 59:609–612, August 1987.

[60] C.W. Stubbs, E.G. Adelberger, B.R. Heckel, W.F. Rogers, H.E. Swanson, R. Watanabe, J.H. Gundlach, and F.J. Raab. Limits on composition-dependent interactions using a laboratory source: Is there a "fifth force" coupled to isospin? *Phys. Rev. Lett.*, 62:609–612, February 1989.

[61] E.G. Adelberger, C.W. Stubbs, B.R. Heckel, Y. Su, H.E. Swanson, G.L. Smith, J.H Gundlach, and F.W. Rogers. Testing the equivalence principle in the field of the earth: Particle physics at masses below 1 μev? *Phys. Rev. D*, 42:3267–3292, November 1990.

[62] S. Baeßler, B.R. Heckel, E.G. Adelberger, J.H. Gundlach, U. Schmidt, and H.E. Swanson. Improved test of the equivalence principle for gravitational self-energy. *Phys. Rev. Lett.*, 83(18):3585–3588, November 1999.

[63] V.V. Nesvizhevsky, H.G. Börner, A.M. Gagarski, A.K. Petoukhov, G.A. Petrov, H. Abele, S. Baeßler, G. Divkovic, F.J. Rueß, Th. Stöferle, A. Westphal, A.V. Strelkov, K.V. Protasov, and A.Yu. Voronin. Measurement of quantum states of neutrons in the earth's gravitational field. *Phys. Rev. D*, 67:102002, May 2003.

[64] MICROSCOPE Collaboration. Microscope mission : First results of a space test of the equivalence principle. *Phys. Rev. Lett.*, 119:231101, December 2017.

[65] M. Nieto and T. Goldman. The arguments against antigravity and the gravitational acceleration of antimatter. *Phys. Rep.*, 205:221–281, July 1991.

[66] C. Will. *Theory and Experiment in Gravitational Physics*. Cambridge University Press, 1993. ISBN: 0521439736, 9780521439732.

[67] M.L. Good. ${K_2}^0$ and the equivalence principle. *Phys. Rev.*, 121(1):311–313, January 1961.

[68] I.R. Kenyon. A recalculation of the gravitational mass difference between the k^0 and $\bar{K}^0$ mesons. *Phys. Lett. B*, 237(2):274–277, March 1990.

[69] G. Gabrielse, X. Fei, L.A. Orozco, R.L. Tjoelker, J. Haas, H. Kalinowsky, T.A. Trainor, and W. Kells. Thousandfold improvement in the measured antiproton mass. *Phys. Rev. Lett.*, 65(11):1317–1320, September 1990.

[70] G. Gabrielse, A. Khabbaz, D.S. Hall, C. Heimann, H. Kalinowsky, and W. Jhe. Precision mass spectroscopy of the antiproton and proton using simultaneously trapped particles. *Phys. Rev. Lett.*, 82(16):3198–3201, April 1999.

[71] R.J. Hughes and M.H. Holzscheiter. Constraints on the gravitational properties of antiprotons and positrons from cyclotron-frequency measurements. *Phys. Rev. Lett.*, 66(7):854–857, February 1991.

[72] G. Chardin and J.-M. Rax. Cp violation. a matter of (anti)gravity ? *Phys. Lett. B*, 282(3):256–262, May 1992.

[73] R.M. West, A. Lauberts, H.-E. Schuster, and H.E. Jorgensen. Astrometry of sn 1987a and sanduleak-69 202. *Astronomy and Astrophysics*, 177:L1–L3, March 1987.

[74] K.S. Hirata, T. Kajita, M. Koshiba, M. Nakahata, Y. Oyama, N. Sato, A. Suzuki, M. Takita, Y. Totsuka, T. Kifune, T. Suda, K. Takahashi, T. Tanimori, K. Miyano, M. Yamada, E.W. Beier, L.R. Feldscher, S.B. Kim, A.K. Mann, F.M. Newcomer, R. Van Berg, W. Zhang, and B. G. Cortez. Observation of a neutrino burst from the supernova sn1987a. *Phys. Rev. Lett.*, 58(14):1490–1493, April 1987.

[75] K.S. Hirata, T. Kajita, M. Koshiba, M. Nakahata, Y. Oyama, N. Sato, A. Suzuki, M. Takita, Y. Totsuka, T. Kifune, T. Suda, K. Takahashi, T. Tanimori, K. Miyano, M. Yamada, E.W. Beier, L.R. Feldscher, W. Frati, S.B. Kim, A.K. Mann, F.M. Newcomer, R. Van Berg, W. Zhang, and B. G. Cortez. Observation of a neutrino burst in coincidence with supernova 1987a in the large magellanic cloud. *Phys. Rev. D*, 38(2):448–458, July 1988.

[76] R.M. Bionta, G. Blewitt, C.B. Bratton, D. Casper, A. Ciocio, R. Claus, B. Cortez, M. Crouch, S.T. Dye, S. Errede, G.W. Foster, W. Gajewski, K.S. Ganezer, M. Goldhaber, T.J. Haines, T.W. Jones, D. Kielczewska, W.R. Kropp, J.G. Learned, J.M. LoSecco, J. Matthews, R. Miller, M.S. Mudan, H.S. Park, L.R. Price, F. Reines, J. Schultz, S. Seidel, E. Shumard, D. Sinclair, H.W. Sobel, J.L. Stone, L.R. Sulak, R. Svoboda, G. Thornton, J.C. van der Velde, and C. Wuest. Observation of a neutrino burst in coincidence with supernova 1987a in the large magellanic cloud. *Phys. Rev. Lett.*, 58(14):1494–1496, April 1987.

[77] J.M. LoSecco. The case for neutrinos from sn1987a. *Phys. Rev. D*, 39(4):1013–1019, February 1989.

[78] L.M. Krauss and S. Tremaine. Test of the weak equivalence principle for neutrinos and photons. *Phys. Rev. Lett.*, 60(3):176–177, January 1988.

[79] S. Pakvasa, W.A. Simmons, and T.J. Weiler. Test of equivalence principle for neutrinos and antineutrinos. *Phys. Rev. D*, 39(6):1761–1763, March 1989.

[80] M. Gasperini. Experimental constraints on a minimal and nonminimal violation of the equivalence principle in the oscillations of massive neutrinos. *Phys. Rev. D*, 39(12):3606–3611, June 1989.

[81] H. Minakata and H. Nunokawa. Testing the principle of equivalence by solar neutrinos. *Phys. Rev. D*, 51(12):6625–6634, June 1995.

[82] T. Brando, A. Fainberg, T. Kalogeropoulos, D. Michael, and G. Tzanakos. Observations of low-energy antineutrons in a time-separated neutral beam. *Nucl. Instrum. Methods*, 180:461–467, April 1981.

[83] F.C. Witteborn and W.M. Fairbank. Experimental comparison of the gravitational force on freely falling electrons and metallic electrons. *Phys. Rev. Lett.*, 19(18):1049–1052, October 1967.

[84] F.C. Witteborn and W.M. Fairbank. Experiments to determine the force of gravity on single electrons and positrons. *Nature*, 220:436–440, November 1968.

[85] F.C. Witteborn and W.M. Fairbank. Apparatus for measuring the force of gravity on freely falling electrons. *Rev. Sci. Instrum.*, 48(1):1–11, January 1977.

[86] T.W. Darling, F. Rossi, G.I. Opat, and G.F. Moorhead. The fall of charged particles under gravity: A study of experimental problems. *Rev. Mod. Phys.*, 54(1):237–257, January 1992.

[87] P. Dyer, J.Camp, M.H. Holzscheiter, and S. Graessle. Falling antimatter: An experiment to measure the gravitational acceleration of the antiproton. *Nucl. Instrum. Methods B*, 40-41:485–488, April 1989.

[88] Nelson Jarmie. A measurement of the gravitational acceleration of the antiproton: An experimental overview. *Nucl. Instrum. Methods B*, 24-25:437–441, April 1987.

[89] Dragan Slavkov Hajdukovic. Do we live in the universe successively dominated by matter and antimatter? *Theoretical essay, CERN PH Division*, June 2011. arXiv: 1106.1260.

[90] A.P. Mills Jr. and M. Leventhal. Can we measure the gravitational free fall of cold rydberg state positronium? *Nucl. Instrum. Methods B*, 192:102–106, May 2002.

[91] D. B. Cassidy and S. D. Hogan. Atom control and gravity measurements using rydberg positronium. *International Journal of Modern Physics: Conference Series*, 30:1460259, 2014.

[92] G Yu Drobychev, P Nédélec, D Sillou, G Gribakin, H Walters, G Ferrari, M Prevedelli, G M Tino, M Doser, C Canali, C Carraro, V Lagomarsino, G Manuzio, G Testera, S Zavatarelli, M Amoretti, A G Kellerbauer, J Meier, U Warring, M K Oberthaler, I Boscolo, F Castelli, S Cialdi, L Formaro, A Gervasini, G Giammarchi, Antonio Vairo, G Consolati, A Dupasquier, F Quasso, Hinko Henry Stroke, A S Belov, S N Gninenko, V A Matveev, V M Byakov, S V Stepanov, D S Zvezhinskij, M De Combarieu, P Forget, P Pari, L Cabaret, D Comparat, G Bonomi, A Rotondi, N Djourelov, M Jacquey, M Büchner, G Trénec, J Vigué, R S Brusa, S Mariazzi, S Hogan, F Merkt, A Badertscher, P Crivelli, U Gendotti, and André Rubbia. Proposal for the AEGIS experiment at the CERN antiproton decelerator (Antimatter Experiment: Gravity, Interferometry, Spectroscopy). Technical Report CERN-SPSC-2007-017. SPSC-P-334, CERN, Geneva, Jun 2007.

[93] Jeffrey S Hangst. Addendum to the ALPHA Proposal; The ALPHA-g Apparatus. Technical Report CERN-SPSC-2016-031. SPSC-P-325-ADD-1, CERN, Geneva, Jul 2016.

[94] P. Perez for the GBAR collaboration. Proposal to measure the gravitational behaviour of antihydrogen at rest. *SPSC Committee Papers*, September 2011. Report Number: CERN-SPSC-2011-029 ; SPSC-P-342.

[95] Stephan Maury, Walter Oelert, Wolfgang Bartmann, Pavel Belochitskii, Horst Breuker, Francois Butin, Christian Carli, Tommy Eriksson, Sergio Pasinelli, and Gerard Tranquille. Elena: the extra low energy anti-proton facility at cern. *Hyperfine Interactions*, 229(1):105–115, Oct 2014.

[96] C. Smorra et al. BASE – The Baryon Antibaryon Symmetry Experiment. *Eur. Phys. J. ST*, 224(16):3055–3108, 2015.

[97] Y. Bylinsky, A.M. Lombardi, and W. Pirkl. Rfqd - a decelerating radio frequency quadrupole for the cern antiproton facility. August 2000. arXiv: hep-ex/0008030.

[98] N. Kuroda, H.A. Torii, K. Yoshiki Franzen, Z. Wang, S. Yoneda, M. Inoue, M. Hori, B. Juhász, D. Horváth, H. Higaki, A. Mohri, J. Eades, K. Komaki, and Y. Yamazaki. Confinement of a large number of antiprotons and production of an ultraslow antiproton beam. *Phys. Rev. Lett.*, 94, January 2005.

[99] N. Kuroda, H.A. Torii, Y. Nagata, M. Shibata, Y. Enomoto, H. Imao, Y. Kanai, M. Hori, H. Saitoh, H. Higaki, A. Mohri, K. Fujii, C.H. Kim, Y. Matsuda, K. Michishio, Y. Nagashima, M. Ohtsuka, K. Tanaka, and Y. Yamazaki. Development of a monoenergetic ultraslow antiproton beam source for high-precision investigation. *Phys. Rev. ST Accel. Beams*, 15, February 2012.

[100] Jochen Walz and Theodor W. Hänsch. A proposal to measure antimatter gravity using ultracold antihydrogen atoms. *General Relativity and Gravitation*, 36(3):561–570, Mar 2004.

[101] Pauline Comini and Paul-Antoine Hervieux. $\bar{H}$ and $\bar{H}^+$ production cross sections for the gbar experiment. *Journal of Physics: Conference Series*, 443(1):012007, 06 2013.

[102] P Comini and P-A Hervieux. $\bar{H}^+$ ion production from collisions between antiprotons and excited positronium: cross sections calculations in the framework of the gbar experiment. *New Journal of Physics*, 15(9):095022, 2013.

[103] Pauline Comini, Paul-Antoine Hervieux, and François Biraben. $\bar{H}^+$ production from collisions between positronium and kev antiprotons for gbar. *Hyperfine Interactions*, 228(1):159–165, Oct 2014.

[104] A. S. Kadyrov, C. M. Rawlins, A. T. Stelbovics, I. Bray, and M. Charlton. Antihydrogen formation via antiproton scattering with excited positronium. *Phys. Rev. Lett.*, 114:183201, May 2015.

[105] J. P. Merrison. Hydrogen formation using positronium. *Hyperfine Interactions*, 100(1):65–69, Dec 1996.

[106] J.P. Merrison, H. Bluhme, M. Charlton, H. Knudsen, and M.R. Poulsen. Experimental demonstration of hydrogen formation following the interaction of protons with positronium. *Hyperfine Interactions*, 109(1):313–321, Aug 1997.

[107] P Pérez. AD-7/GBAR status report for the 2018 CERN SPSC. Technical Report CERN-SPSC-2018-006. SPSC-SR-228, CERN, Geneva, Jan 2018.

[108] D. A. Fischer, K. G. Lynn, and D. W. Gidley. High-resolution angle-resolved positron reemission spectra from metal surfaces. *Phys. Rev. B*, 33:4479–4492, Apr 1986.

[109] T. J. Murphy and C. M. Surko. Positron trapping in an electrostatic well by inelastic collisions with nitrogen molecules. *Phys. Rev. A*, 46:5696–5705, Nov 1992.

[110] G. B. Andresen, W. Bertsche, P. D. Bowe, C. C. Bray, E. Butler, C. L. Cesar, S. Chapman, M. Charlton, J. Fajans, M. C. Fujiwara, R. Funakoshi, D. R. Gill, J. S. Hangst, W. N. Hardy, R. S. Hayano, M. E. Hayden, R. Hydomako, M. J. Jenkins, L. V. Jørgensen, L. Kurchaninov, R. Lambo, N. Madsen, P. Nolan, K. Olchanski, A. Olin, A. Povilus, P. Pusa, F. Robicheaux, E. Sarid, S. Seif El Nasr, D. M. Silveira, J. W. Storey, R. I. Thompson, D. P. van der Werf, J. S. Wurtele, and Y. Yamazaki. Compression of antiproton clouds for antihydrogen trapping. *Phys. Rev. Lett.*, 100:203401, May 2008.

[111] J. R. Danielson and C. M. Surko. Torque-balanced high-density steady states of single-component plasmas. *Phys. Rev. Lett.*, 94:035001, Jan 2005.

[112] T.R. C, M. Niels, and K. Martina. *Physics With Trapped Charged Particles: Lectures From The Les Houches Winter School.* World Scientific Publishing Company, 2014.

[113] Amelia Mafalda Maia Leite, Yves Saquin, and Dirk van der Werf. *Development of a buffer gas trap for the confinement of positrons and study of positronium production in the GBAR experiment. Développement d'une piège à "buffer gas" pour le confinement de positrons et l'étude de la production de positronium dans l'expérience GBAR.* PhD thesis, Dec 2017. Presented 27 Oct 2017.

[114] Pierre Dupré. *Piégeage de positons dans un piège de Penning Malmberg, en vue de leur accumulation avec un faisceau pulsé.* PhD thesis, 2011. Thèse de doctorat dirigée par Pérez, Patrice Physique des particules Paris 6 2011.

[115] Pierre Grandemange. *Trapping and accumulation of positrons from a pulsed beam produced by a linear accelerator for gravitationnal interaction of antimatter study.* Theses, Université Paris Sud - Paris XI, December 2013.

[116] David W. Gidley, Hua-Gen Peng, and Richard S. Vallery. Positron annihilation as a method to characterize porous materials. *Annual Review of Materials Research*, 36(1):49–79, 2006.

[117] Ulisse Gendotti. *Design of an experiment to search for invisible decays of ortho-positronium in vacuum and ortho-positronium formation studies in mesostructured silica films.* PhD thesis, 2010. Doctoral Thesis supervised by André Rubbia and Günther Dissertori - ETHZ.

[118] L. Liszkay, C. Corbel, P. Perez, P. Desgardin, M.-F. Barthe, T. Ohdaira, R. Suzuki, P. Crivelli, U. Gendotti, A. Rubbia, M. Etienne, and A. Walcarius. Positronium reemission yield from mesostructured silica films. *Applied Physics Letters*, 92(6):063114, 2008.

[119] Paolo Crivelli, Ulisse Gendotti, Andre Rubbia, Laszlo Liszkay, Patrice Perez, and Catherine Corbel. Measurement of the ortho-positronium confinement energy in mesoporous thin films. *Phys. Rev.*, A81:052703, 2010.

[120] H. R. J. Walters and C. Starrett. Positron and positronium scattering. *physica status solidi c*, 4(10):3429–3436.

[121] Laurent Hilico, Jean-Philippe Karr, Albane Douillet, Paul Indelicato, Sebastian Wolf, and Ferdinand Schmidt Kaler. Preparing single ultra-cold antihydrogen atoms for free-fall in gbar. *International Journal of Modern Physics: Conference Series*, 30:1460269, 2014.

[122] Nicolas Sillitoe. *Production of state-selected H2+ ions and numerical simulations of sympathetic cooling in RF traps.* Theses, Université Pierre et Marie Curie - Paris VI, November 2017.

[123] D Lunney. AD-7/GBAR status report for the 2014 CERN SPSC. Technical Report CERN-SPSC-2014-011. SPSC-SR-136, CERN, Geneva, Mar 2014.

[124] D Lunney. AD-7/GBAR status report for the 2017 CERN SPSC. Technical Report CERN-SPSC-2017-001. SPSC-SR-201, CERN, Geneva, Jan 2017.

[125] M. Nieto and T. Goldman. Experiments to measure the gravitational acceleration of antimatter. *Nucl. Instrum. Methods B*, 112(6):437–440, May 1982.

[126] D. Lunney, P. Dupré, P. Grandemange, V. Manea, T. Mortensen, S. Cabaret, S. Pitrel, P. Comini, P. Debu, L. Liszkay, P. Lotrus, P. Pérez, J.-M. Reymond, N. Ruiz, Y. Sacquin, B. Vallage, D. Brook-Roberge, and Ph. Hard. Beam preparation for studying the gravitational behavior of antimatter at rest (gbar). *Hyperfine Interact.*, 229, October 2014.

[127] F. Herfurth, J. Dilling, A. Kellerbauer, G. Bollen, S. Henry, H.-J. Kluge, E. Lamour, D. Lunney, R.B. Moore, C. Scheidenberger, S. Schwarz, G. Sikler, and J. Szerypo. A linear radiofrequency ion trap for accumulation, bunching, and emittance improvement of radioactive ion beams. *Nucl. Instr. Meth. A*, 469:254–275, 2001.

[128] C. Smorra. *High-precision Q-value and mass measurements for neutrino physics with TRIGA-TRAP and commissioning of an on-line ion source for TRIGA-SPEC.* PhD thesis, Ruperto-Carola-University of Heidelberg, July 2012.

[129] R. Gans. *Z. Tech. Phys.*, 18, 1937.

[130] Mortimer M. Elkind. Titan's digital rfq ion beam cooler and buncher, operation and performance. *Rev. Sci. Instrum.*, 24(129):129–137, February 1953.

[131] A. Galejs and P.H. Rose. *Optics of electrostatic accelerator tubes, in Focusing of Charged Particles*, volume II. Academic Press, New York, a. septier edition, 1945.

[132] V.K. Zworykin, G.A. Morton, E.G. Ramberg, J. Hillier, and A.W. Vance. *Electron Optics and the Electron Microscope.* Wiley, New York, 1967.

[133] J.D. Lawson. *The Physics of Charged-particle Beams.* Clarendon Press, Oxford, 2 edition, 1988. ISBN: 9780198517191.

[134] D. Manura and D.A. Dahl. *SIMION Version 8.0/8.1 User Manual : Covering SIMION Version 8.1.0.31*, volume 1. Scientific Instrument Services Inc. & Idaho National Laboratory, November 2011.

[135] J.C. Butcher. A history of runge-kutta methods. *Applied Numerical Mathematics*, 20(3):247 – 260, 1996.

[136] Wensheng Tang and Yajuan Sun. Construction of runge–kutta type methods for solving ordinary differential equations. *Applied Mathematics and Computation*, 234:179 – 191, 2014.

[137] M.Y. Bernard, P. Durandeau, C. Fert, J.C. Francken, C. Germain, M.E. Haine, K.J. Hanszen, P.W. Hawkes, R. Lauer, D. Linder, T. Mulvey, E. Regenstreif, and C. Weber. *Focusing of Charged Particles*, volume 1. Academic Press Inc., albert septier edition, 1967. ISBN: 0323147186, 9780323147187.

[138] J.W. Gewartowski and H.A. Watson. *Principles of electron tubes: including grid-controlled tubes, microwave tubes, and gas tubes.* Bell Telephone Laboratories series. Van Nostrand Reinhold Inc.,U.S., May 1965. ISBN: 0442026501, 978-0442026509.

[139] *Determination of the Axial Potential Distribution in Axially Symmetric Electrostatic Fields*, volume 28, September 1940.

[140] S. Bertram. Calculation of axially symmetric fields. *J. Appl. Phys.*, 13:496–502, August 1942.

[141] C. Biscari. Transverse beam dynamics. Accelerator Physics UAB - 2014/2015, 2014-2015.

[142] W. T. Weng and S. R. Mane. Fundamentals of particle beam dynamics and phase space. *AIP Conf. Proc.*, 249:3–45, 1992.

[143] Charles Darwin. *On the origin of species - By means of natural selection.* November 1859. OCLC: 352242.

[144] T. Bäck, U. Hammel, and H.-P. Schwefel. Evolutionary computation: Comments on the history and current state. *IEEE TRANSACTIONS ON EVOLUTIONARY COMPUTATION*, 1(1), April 1997.

[145] T. Bäck, D.B. Fogel, and Z. Michalewicz. *Evolutionary algorithms in theory and practice: evolution strategies, evolutionary programming, genetic algorithms.* Oxford University Press, NY, 1996. ISBN: 0195099710, 9780195099713.

[146] T. Bäck. *Handbook of evolutionary computation.* Institute of Physics Pub., 1997. ISBN: 0750303921, 9780750303927.

[147] D. Whitley. A genetic algorithm tutorial. *Statistics and Computing*, 4, June 1997.

[148] T. Geijtenbeek, M. van de Panne, and A.F. van der Stappen. Flexible muscle-based locomotion for bipedal creatures. *ACM Transactions on Graphics*, 32(6), November 2013.

[149] Hans-Paul Schwefel. *Numerical Optimization of Computer Models.* Wiley, 1981. ISBN: 0471099880.

[150] J.H. Holland. *Adaptation in Natural and Artificial Systems: An Introductory Analysis with Applications to Biology, Control, and Artificial Intelligence.* MIT Press, 1992. ISBN: 0262581116, 9780262581110.

[151] J.H. Holland. Outline for a logical theory of adaptive systems. *Journal ACM*, 9, July 1962.

[152] David E. Goldberg. *Genetic Algorithms in Search, Optimization and Machine Learning.* Addison-Wesley Longman Publishing Co., Inc., Boston, MA, USA, 1st edition, 1989.

[153] R. Ierusalimschy, L.H. de Figueiredo, and W. Celes. *Lua 5.1 Reference Manual.* Lua.org, August 2006. ISBN: 85-903798-3-3.

[154] CERN BE/ABP Accelerator Beam Physics Group. Mad - methodical accelerator design, 2012.

[155] F.M. Penning. Die glimmentladung bei niedrigem druck zwischen koaxialen zylindern in einem axialen magnetfeld. *Physica*, 3(9):873 – 894, 1936.

[156] H Tawara, Y Itikawa, H Nishimura, and M Yoshino. Cross sections and related data for electron collisions with hydrogen molecules and molecular ions. 19:617–636, 05 1990.

[157] L. Vályi. *Atom and ion sources.* Wiley-Interscience Publications. Akademiai Kiado, 1977.

[158] F C. Hoh. Instability of penning-type discharges. 6:1184–1191, 08 1963.

[159] K I. Thomassen. Rotational instability in a penning-type discharge. 14:587–589, 04 1965.

[160] K I. Thomassen. Turbulent diffusion in a penning-type discharge. 9:1836–1842, 09 1966.

[161] Felix K. Chen. Investigation of the striking characteristics of a penning ion source. *Journal of Applied Physics*, 56(11):3191–3197, 1984.

[162] A. Sy, Q. Ji, A. Persaud, O. Waldmann, and T. Schenkel. Novel methods for improvement of a penning ion source for neutron generator applications. *Review of Scientific Instruments*, 83(2):02B309, 2012.

[163] S. Amy. *Advanced Penning-type ion source development and passive beam focusing techniques for an associated particle imaging neutron generator*. PhD dissertation, University of California, Berkeley, 2013.

[164] H. H. Rose. TOPICAL REVIEW: Optics of high-performance electron microscopes. *Science and Technology of Advanced Materials*, 9(1):014107, April 2008.

[165] A. Galejs. Focusing and dispersing properties of a stigmatic crossed-field energy analyzer. *Journal of Vacuum Science Technology*, 15:865, May 1978.

[166] Décret n°95-608 du 6 mai 1995 - art. 30 jorf 7 mai 1995 en vigueur le 1er janvier 1997. https://www.legifrance.gouv.fr.

[167] Article r4226, décret n°2010-1016 du 30 août 2010 - art. 1. https://www.legifrance.gouv.fr.

[168] Cern - code c1 - code de sécurité relatif à l'électricité, 1990.

[169] S. RAY. *An introduction to high voltage engineering*. PHI Learning, 2004.

[170] Abraham. Savitzky and M. J. E. Golay. Smoothing and differentiation of data by simplified least squares procedures. *Analytical Chemistry*, 36(8):1627–1639, 1964.

[171] Jean. Steinier, Yves. Termonia, and Jules. Deltour. Smoothing and differentiation of data by simplified least square procedure. *Analytical Chemistry*, 44(11):1906–1909, 1972. PMID: 22324618.

[172] Peter A. Gorry. General least-squares smoothing and differentiation by the convolution (savitzky-golay) method. *Analytical Chemistry*, 62(6):570–573, 1990.

[173] Chandra Shekhar. On simplified application of multidimensional savitzky-golay filters and differentiators. *AIP Conference Proceedings*, 1705(1):020014, 2016.

[174] See:.

[175] F.J. Lynch, R.N. Lewis, L.M. Bollinger, W. Henning, and O.D. Despe. Beam buncher for heavy ions. *Nuclear Instruments and Methods*, 159(2):245 – 263, 1979.

[176] D. A. Cooke, A. Husson, D. Lunney, and P. Crivelli. Enhanced anti-hydrogen ion production. In *3rd International Workshop on Antimatter and Gravity (WAG 2015) London, UK, August 4-7, 2015*, 2016.

[177] Naofumi Kuroda et al. Development of MUSASHI, a Mono-energetic Ultra-slow Antiproton Beam Source. *Conf. Proc.*, C100523:THPEC058, 2010.

[178] N. Kuroda, H. A. Torii, M. Shibata, Y. Nagata, D. Barna, M. Hori, D. Horváth, A. Mohri, J. Eades, K. Komaki, and Y. Yamazaki. Radial compression of an antiproton cloud for production of intense antiproton beams. *Phys. Rev. Lett.*, 100:203402, May 2008.

[179] S.G. Alikhanov. A new impulse technique for ion mass measurements. *Soviet Phys. JETP*, 4, 4 1957.

[180] J. Bernard, G. Montagne, R. Brédy, B. Terpend-Ordacière, A. Bourgey, M. Kerleroux, L. Chen, H. T. Schmidt, H. Cederquist, and S. Martin. A "tabletop" electrostatic ion storage ring: Mini-ring. *Review of Scientific Instruments*, 79(7):075109, 2008.

[181] Synopsis de stage, May 2014. Master 2 internship report.

[182] Alexandre Vallette. *Dynamique d'ions multichargés dans un piège électrostatique.* PhD thesis, 2011. Thèse de doctorat dirigée par Indelicato, Paul Physique Paris 6 2011.

Appendix A

Application of the Bertram method to a multi-potential system

Today, with the development of more and more intensive digital resolution methods for electrostatic systems, analytical approximations are increasingly neglected.

The latter nevertheless offers a non-negligible advantage in the methods of research and optimization of potential. An approximate analytical solution can considerably reduce the computation time.

In this appendix, we will review the Bertram calculation method and we will introduce an optimization of the genetic algorithm from a multi-potential (multi-electrode) approximated solution.

A.1 Classical Bertram's Method

We concentrate on the axial potential distribution for axisymmetric electrostatic electrodes. This section follows the Bertram's articles [139, 140].

Starting from the Laplace's equations in cylindrical coordinates:

$$\nabla^2 V = \frac{\partial^2 V}{\partial r^2} + \frac{1}{r}\frac{\partial V}{\partial r} + \frac{\partial^2 V}{\partial z^2} = 0 \tag{A.1}$$

where $V = V(r, z)$ is the potential at a radius r from the axis and at a distance z from a reference plane.

A particular solution is a linear combination of Bessel functions of the first kind $J_0(kr)$. A general solution is then a Fourrier-Bessel-type function:

$$V(r, z) = \frac{1}{2\pi}\int_{-\infty}^{+\infty} a(k) J_0(kr) e^{ikz} dk \tag{A.2}$$

where the terms $a(k)$ have to be determined to integrate. We assume the potential on the electrodes at radius R as $V(R, z)$. The inverse Fourier transform is :

$$a(k) J_0(ikR) = \int_{-\infty}^{+\infty} V(R, z) e^{-ikz} dz \tag{A.3}$$

The cylindrical system is cut into slices of thickness $d\zeta$ carrying a contribution $U(R, \zeta)$ (See Figure-A.1.). With $U(R, z) = 0$ everywhere except in $z = \zeta$ where $U(R, z) = 1$. Equation (A.3) becomes :

$$a(k) J_0(ikR) = \int_{-\infty}^{+\infty} U(R, \zeta) d\zeta e^{-ikz} dz = \int_{\zeta}^{\zeta + d\zeta} e^{-ikz} dz = \frac{i}{k}\left[e^{-ik(\zeta + d\zeta)} - e^{-ik\zeta}\right]$$

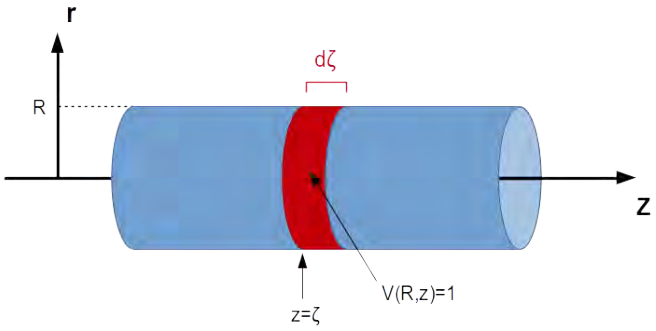

Figure A.1 The unitary potential electrode divided in $d\zeta-$large slices.

With $e^{-ikd\zeta} \underset{d\zeta\to 0}{\longrightarrow} 1 - ikd\zeta$:

$$a(k) = \frac{e^{-ik\zeta}}{J_0(ikR)}d\zeta \tag{A.4}$$

Equation (A.2) can now be expressed for the differential cylinder potential $U(R,\zeta)d\zeta$:

$$U(r,z)d\zeta = \frac{1}{2\pi}\int_{-\infty}^{+\infty}\frac{e^{-ik\zeta}}{J_0(ikR)}d\zeta.J_0(kr)e^{ikz}dk \tag{A.5}$$

By taking all dimensions in terms of R, so that $R = 1$, we have for the potential along the axis $r = 0$, (giving $J_0(0) = 1$):

$$\begin{aligned} U(0,z) &= \frac{1}{2\pi}\int_{-\infty}^{+\infty}\frac{e^{ik(z-\zeta)}}{J_0(ik)}dk \\ &= \frac{1}{2\pi}\int_{-\infty}^{+\infty}\frac{e^{ik\xi}}{J_0(ik)}dk, \text{ with } \xi = z-\zeta \end{aligned} \tag{A.6}$$

Developing for $-2\pi < k < 2\pi$:

$$\frac{1}{J_0(ik)} = \sum_{n=0}^{+\infty} A_n cos(\frac{nk}{2})$$

Injecting into equation-A.6:

$$U(0,z) = \frac{1}{2\pi}\sum_{n=0}^{+\infty} A_n \int_{-2\pi}^{2\pi} cos(\frac{nk}{2})(cos(k\xi) + isin(k\xi))dk \tag{A.7}$$

After developments using trigonometric formulas[1] and integrating, we find:

$$U(0,z) = \frac{\xi}{\pi}sin(2\pi\xi)\sum_{n=0}^{+\infty}\frac{A_n(-1)^n}{\xi^2 - \frac{n^2}{4}}. \tag{A.8}$$

The latter can be approximated to :

$$\boxed{V(0,z) = \frac{\omega}{2}\int_{-\infty}^{\infty} V(1,\zeta)sech^2(\omega\xi)d\zeta} \tag{A.9}$$

[1]Reminder: $sin(2\pi(\xi \pm \frac{n}{2})) = (-1)^n sin(2\pi\xi)$

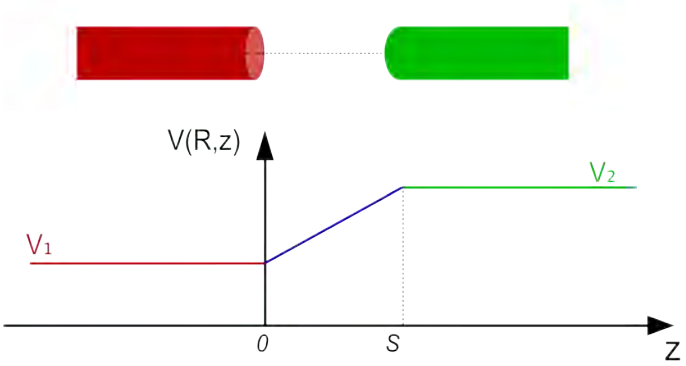

Figure A.2 Infinitely long conducting cylinders with finite separation S; potential along cylinder surface.

with $\omega \approx 1.32$ and $V(1,\zeta)$ the potential on the electrode a $z = \zeta$.
For $R \neq 1$, ω becomes $\frac{\omega}{R}$.

Let's take a simple example with tube semi-infinite tubes polarized at V_1 and V_2 separated by a distance S. We can approximate the potential on and between the electrodes to:

$$V(1,\zeta) = \begin{cases} V_1 & \zeta < 0 \\ V_1 + \left(\frac{V_2 - V_1}{S}\right)\zeta & 0 < \zeta < S \\ V_2 & \zeta > S \end{cases}$$

The equation-(A.9) becomes after integrating:

$$V(0,z) = \left(\frac{V_1 + V_2}{2}\right) + \left(\frac{V_2 - V_1}{2\omega S}\right) log_e \left(\frac{cosh\ \omega z}{cosh\ \omega(z - S)}\right) \tag{A.10}$$

From the potential on the optical axis, we can determine the solution of the Laplace's equation at r with:

$$\boxed{V(r,z) = \sum_{n=0}^{+\infty} \frac{(-1)^n}{(n!\ 2^n)^2} r^{2n} V^{(2n)}(0,z)} \tag{A.11}$$

A.2 Generalization to N electrodes and gaps

Let's consider now three successive concentric electrodes of different lengths and separated by different gap sizes. In a first approximation, the potential on the electrodes is considered exactly flat and linear in the in-between gap, as displayed in Figure-A.3.

An attempt of such generalization has been proposed in Reference-[182]. Here, we proposed a more developed calculus.
The potential can then be divided in two part :

- constant parts of the potential
- linear parts of the potential

The potential on the optical axis can then be expressed as:

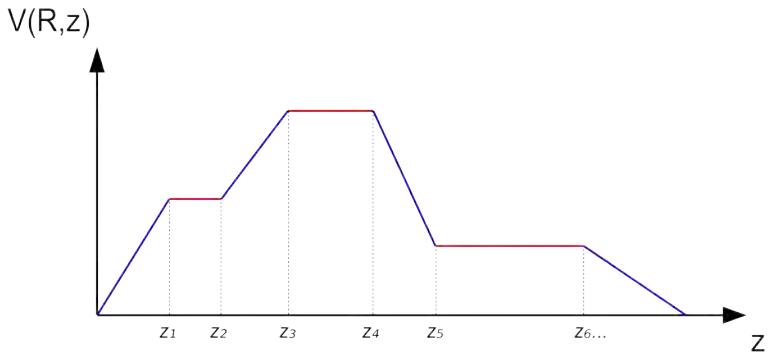

Figure A.3 Example of potentials along a concentric multi-electrode system.

$$V(0,z) = \sum_{i,constant\ parts} \frac{\omega}{2} V_i \int_{z_i}^{z_{i+1}} sech^2(\omega\xi).d\zeta \tag{A.12}$$

$$+ \sum_{j,linear\ parts} \frac{\omega}{2} \int_{z_j}^{z_{j+1}} \left[V_j + \left(\frac{V_{j+1} - V_j}{z_{j+1} - z_i} \right) \zeta \right] .sech^2(\omega\xi) d\zeta \tag{A.13}$$

Substituting $\zeta = z - \xi$ and $d\zeta = -d\xi$, and integrating, Eq-(A.12) becomes:

$$V(0,z)\Big|_{constant} = -\sum_i \frac{V_i}{2} .tanh\left(\omega(z - z_{j+1})\right) - tanh\left(\omega(z - z_i)\right) \tag{A.14}$$

Idem for the linear parts, after a long integration by parts, we found Eq-(A.13) to be:

$$\begin{aligned} V(0,z)\Big|_{linearpart} &= \sum_j \frac{1}{2} \left\{ V_j + \left(\frac{V_{j+1} - V_j}{z_{j+1} - z_j} \right) z \right\} \times \left\{ \frac{sinh\Big(\omega(z_{j+1} - x_j)\Big)}{cosh\Big(\omega(z - z_{j+1})\Big).cosh\Big(\omega(z - z_j)\Big)} \right\} \\ &+ \sum_j \frac{V_{j+1} - V_j}{2\omega(z_{j+1} - z_j)} \omega \times \left\{ - z_{j+1}.tanh\Big(\omega(z - z_{j+1})\Big) + z_j.tanh\Big(\omega(z - z_j)\Big) \right. \\ &\quad + z \left[\frac{sinh\Big(\omega(z_{j+1} - z_j)\Big)}{cosh\Big(\omega(z - z_{j+1})\Big).cosh\Big(\omega(z - z_i)\Big)} \right] \\ &\quad \left. + log_e\Big(cosh\big(\omega(z - z_j)\big)\Big) - log_e\Big(cosh\big(\omega(z - z_{j+1})\big)\Big) \right\} \end{aligned}$$

Appendix B

Differential Pumping Approximate Calculation

Following the approximate gas flow calculations as detailed in the instructions of the IQE 12/38 from the SPECS company.

B.1 Application note

Conductance C : maximum flow of gas caused by a pressure difference through any limiting device, such as apertures or hoses. Measured in liters per second (l/s).

The conductance of a thin aperture can be estimated using the following formula:

$$C = d^2\sqrt{\frac{\pi RT}{32M_{mol}}} \tag{B.1}$$

with d, the diameter of the aperture; R, the gas constant; M_{mol}, the molecular mass of the gas and T, the temperature.

The conductance of a long tube can be estimated by :

$$C \sim 0.125\frac{d^3}{L} \tag{B.2}$$

with d, the diameter of the tube in mm and L, the length of the tube in mm.

Mass Flow Q : actual flow of gas at a given pressure. Measured in $mbar \times l/s$. For large pressure differences, the mass flow can be estimated as $Q = p \times C$.

The pumping speed S of a pump is reduced by any device with the conductance C that connects it to the chamber. For example, the effective pumping speed of a 60 l/s pump connected to a chamber by a 63/16CF adapter with $C = 24l/s$ is reduced to $S_{eff} = 18l/s$.

B.2 Application to the GBAR proton source

To produce the Ps state in the GBAR reaction chamber, UHV conditions are required with pressure $p < 10^{-9}$ $mbar$ when the TES proton operates with operational pressure $p = 10^{-3}$ $mbar$.

A three stage differential pumping system has been designed as exposed on the following schematic:

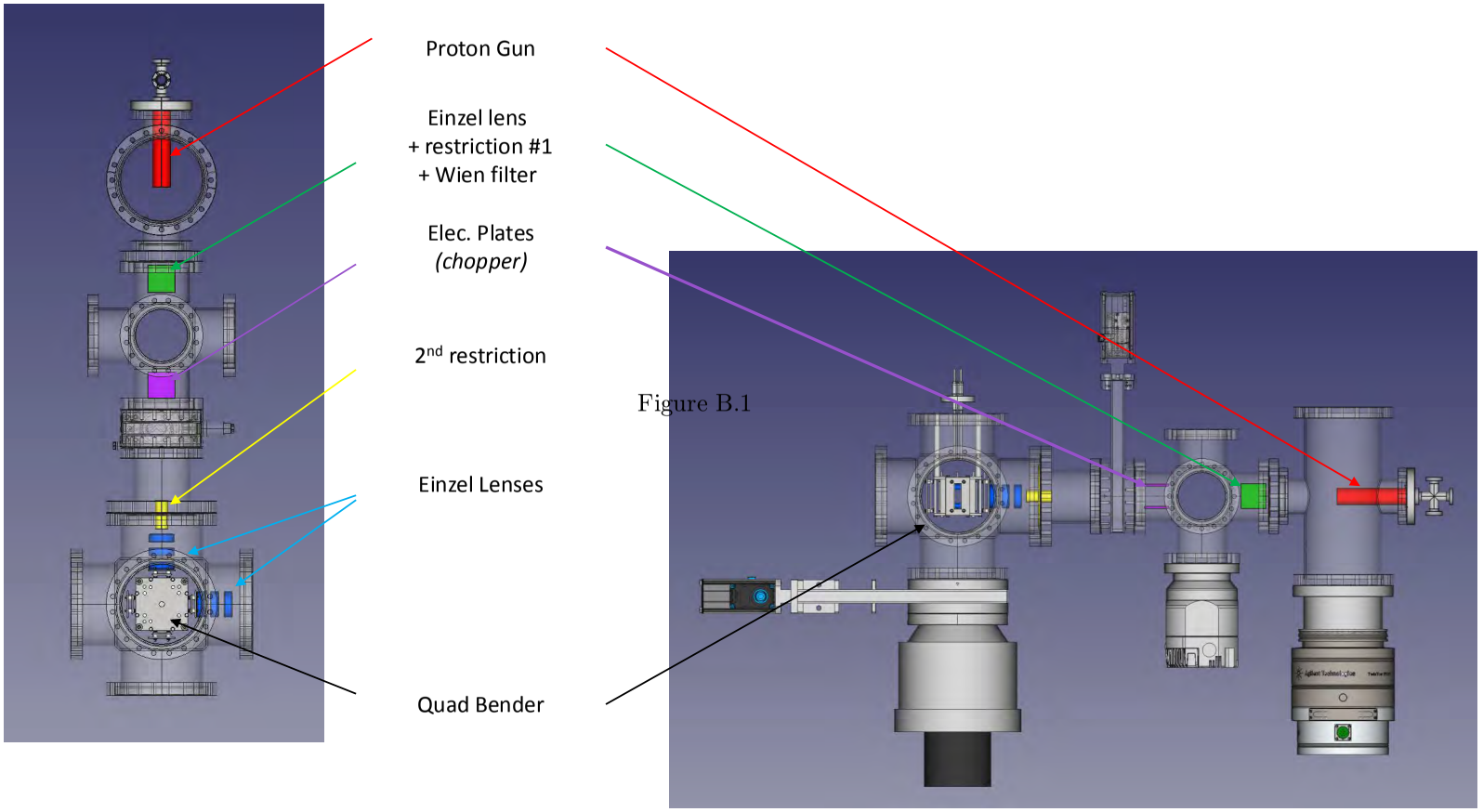
Proton Gun
Einzel lens
+ restriction #1
+ Wien filter
Elec. Plates
(chopper)
2nd restriction
Einzel Lenses
Quad Bender

Figure B.1

Tubes restrictions are used to limit the conductance between the chambers. The restrictions are tubes designed in order to keep the pressure in the first chamber at 10^{-3} *mbar* and 10^{-8} *mbar* in the last chamber. The principle of the differential pump system is shown in the following diagram :

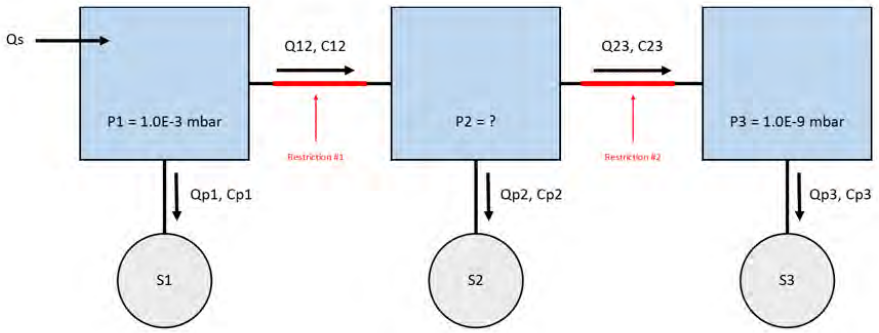

Figure B.2 Differential pumping diagram.

The Table-B.1 summarizes the expected conductance, pumping speed, gas flow and pressure through the different chambers. The initial hydrogen mass flow in the proton source is set to maintain the pressure in the first chamber at 10^{-3} *mbar*. The pumping speed values are given from the pump technical data for hydrogen gas.

Conductance l/s		Flow $mbar.l/s$		Pressure $mbar$	
		Q_s	$4.63\ 10^{-1}$		
C_{p1}	462.42	Q_{p1}	$4.62\ 10^{-1}$	$p1$	10^{-3}
C_{12}	0.49	Q_{12}	$4.93\ 10^{-4}$		
C_{p2}	244	Q_{p2}	$4.86\ 10^{-4}$	$p2$	2.10^{-6}
C_{23}	3.57	Q_{23}	$7.12\ 10^{-6}$		
C_{p3}	712.49	Q_{p3}	$7.12\ 10^{-6}$	$p2$	10^{-8}
$S1$	510				
$(Navigator\ 550\ Varian)$		$Source\ mass\ flow = 28.93\ sccm$			
$S2$	280				
$(Edwards\ nEXT\ 300)$					
$S3$	1000				
$(TurboVAC\ 1000)$					

Table B.1 Evaluation of the conductance, gas flow and pressure through the differential pumping line.

The size of the restrictions is set as:

	Diameter (mm)	*Length (mm)*
Restriction #1	7.5	107.5
Restriction #2	15.5	100

Appendix C

Study of a two-stage deceleration system

Based on the design of the TRIGA trap experiment [128], a decelerator apparatus has been simulated. It is composed as exposed in Figure-C.1 with three long 100 mm-long pre-decelerating electrodes, 500 mm-long drift tube and an Einzel lens. Only two of the pre-decelerating electrodes are polarized when the first one is grounded. The drift tube is pulsed from -99 kV to ground when the antiproton pulse is inside.

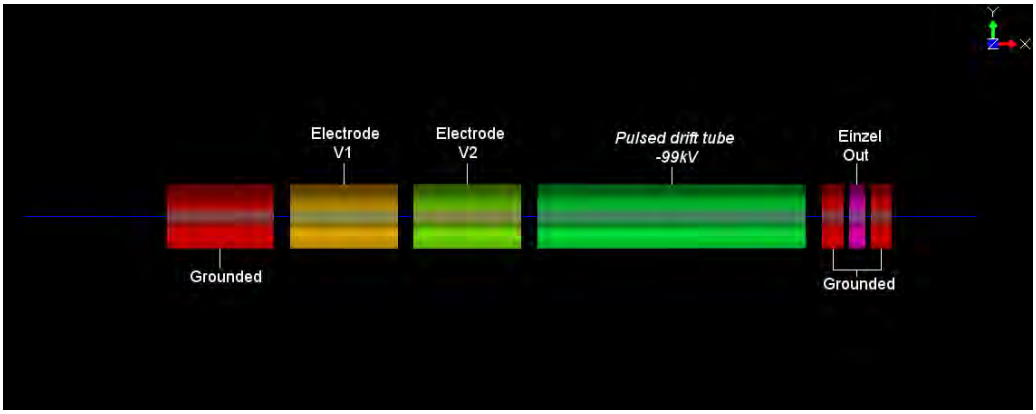

Figure C.1 Design of the two-stage deceleration apparatus. Colors depict the potentials applied on the electrodes, red correspond to grounded parts.

The simulation are performed following the $4mMinimizeAlpha$[1] configuration with a 100 keV antiproton beam. Conserving the symmetry of the ratios between $V0$ and $V1$, and between $V2$ and the PDT, the potentials can be found as:

$$V_2 = V_{PDT} - V_1 \tag{C.1}$$

The two-dimensional system is reduced to a $1D$ system. The best solution is found by scanning the potential value V_2 and simulating it with the SIMION software.

[1] See Chapter-4.

The Figure-C.2 represents the expected transmission, the beam radius and the beam divergence of the beam at the place of the reaction chamber. The best solution is found for :

$$V_1 = -68791\ V \tag{C.2}$$
$$V_2 = -30268\ V \tag{C.3}$$

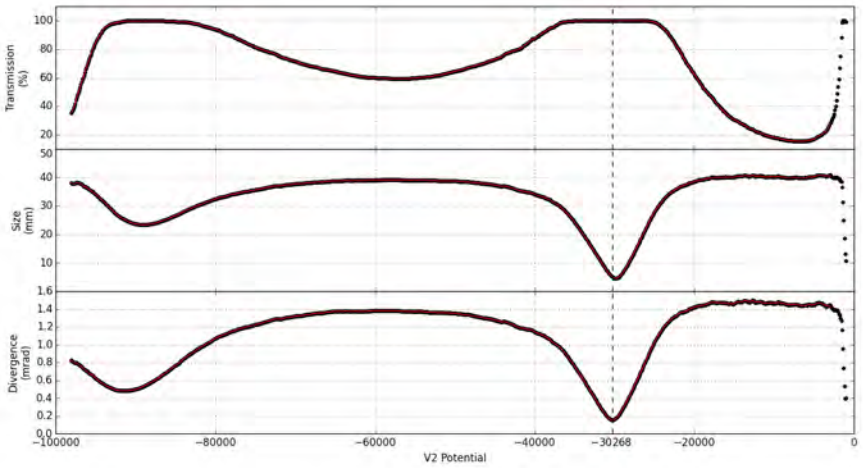

Figure C.2 Beam characteristics through the two-stage deceleration apparatus.

Appendix D

Technical Drawings

The technical drawings for the GBAR decelerator chambers:

- GBAR decelerator, first chamber
- GBAR decelerator, second chamber
- GBAR decelerator, Pulsed Drift Tube chamber
- GBAR decelerator, Einzel lens chamber

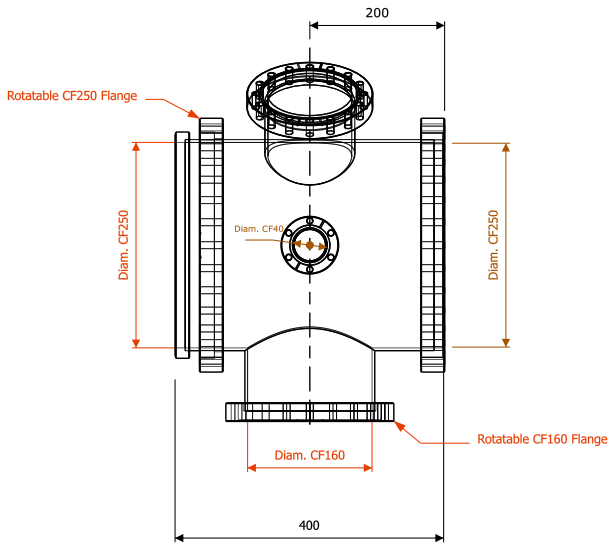

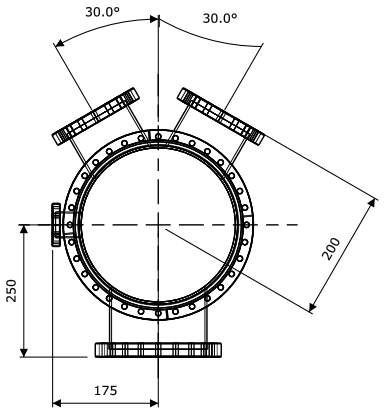

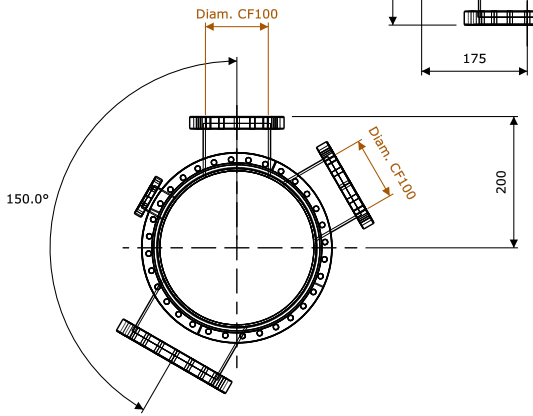

Figure D.1

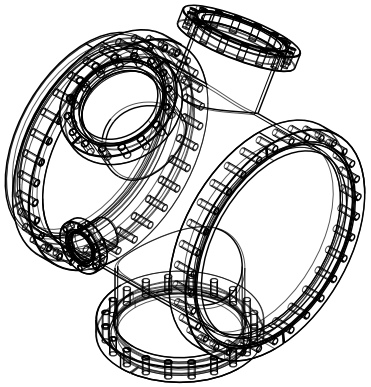

DESIGNED BY: Audric HUSSON DATE: 06/12/2017 CHECKED BY: J.-Y. ROUSSE DATE:	Decelerator Chamber Einzel 1 Chamber		I _ H _ G _ F _ E _ D _ C _ B _ A _
SIZE A3			
SCALE	WEIGHT (kg)	DRAWING NUMBER DECEL_002	SHEET 1

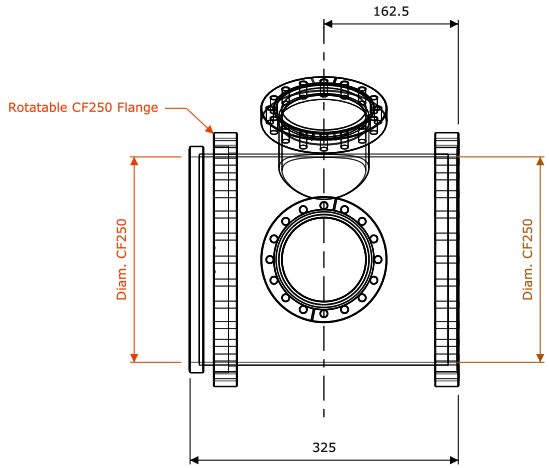

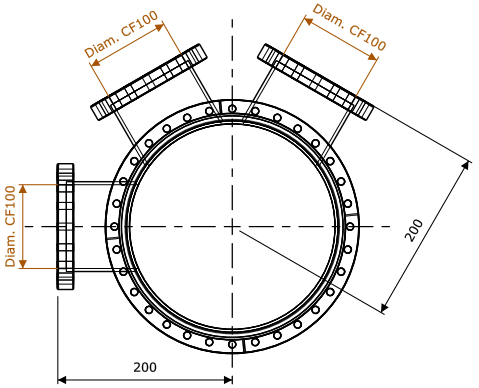

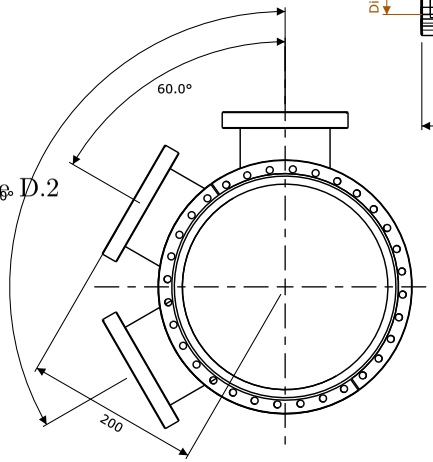

Figure D.2

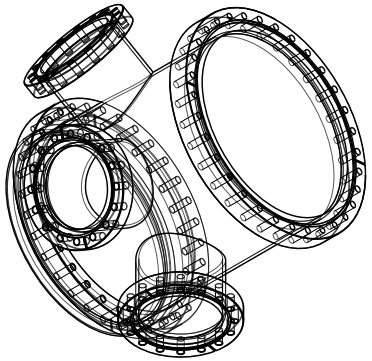

DESIGNED BY: Audric HUSSON	Decelerator Chamber		I _
DATE: 06/12/2017	Einzel 2 Chamber		H _
CHECKED BY:			G _
DATE:			F _
SIZE A3			E _
			D _
SCALE	WEIGHT (kg)	DRAWING NUMBER DECEL_003 / SHEET 1/1	C _
			B _
			A _

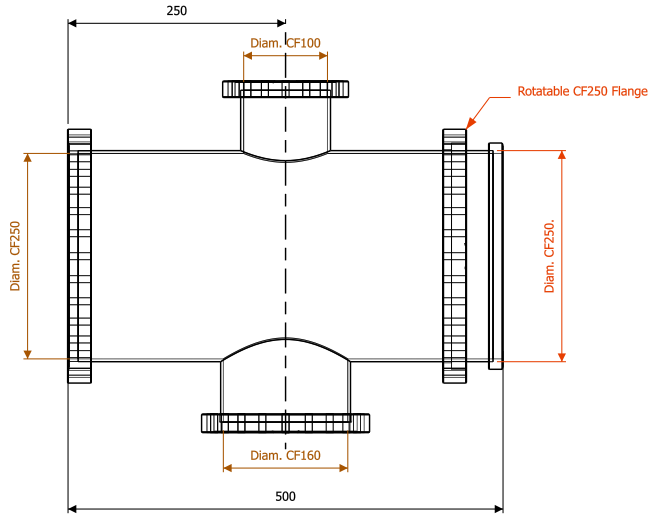

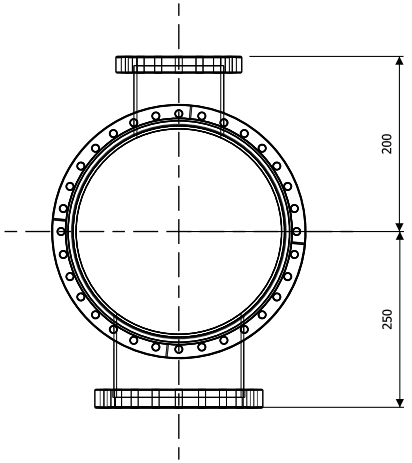

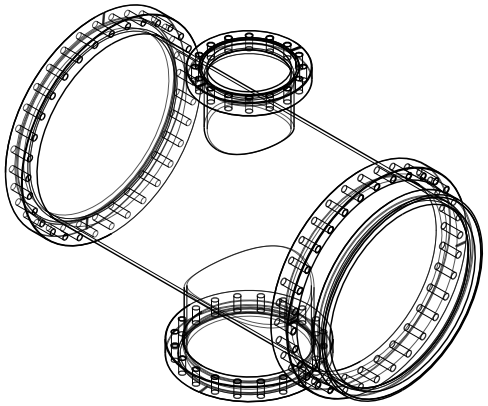

Figure D.3

DESIGNED BY: Audric HUSSON DATE: 22/11/2017 CHECKED BY: J.-Y. ROUSSE DATE:	Decelerator Chamber Drift Tube Chamber		
SIZE A3			
SCALE	WEIGHT (kg)	DRAWING NUMBER: DECEL_001	SHEET: 1

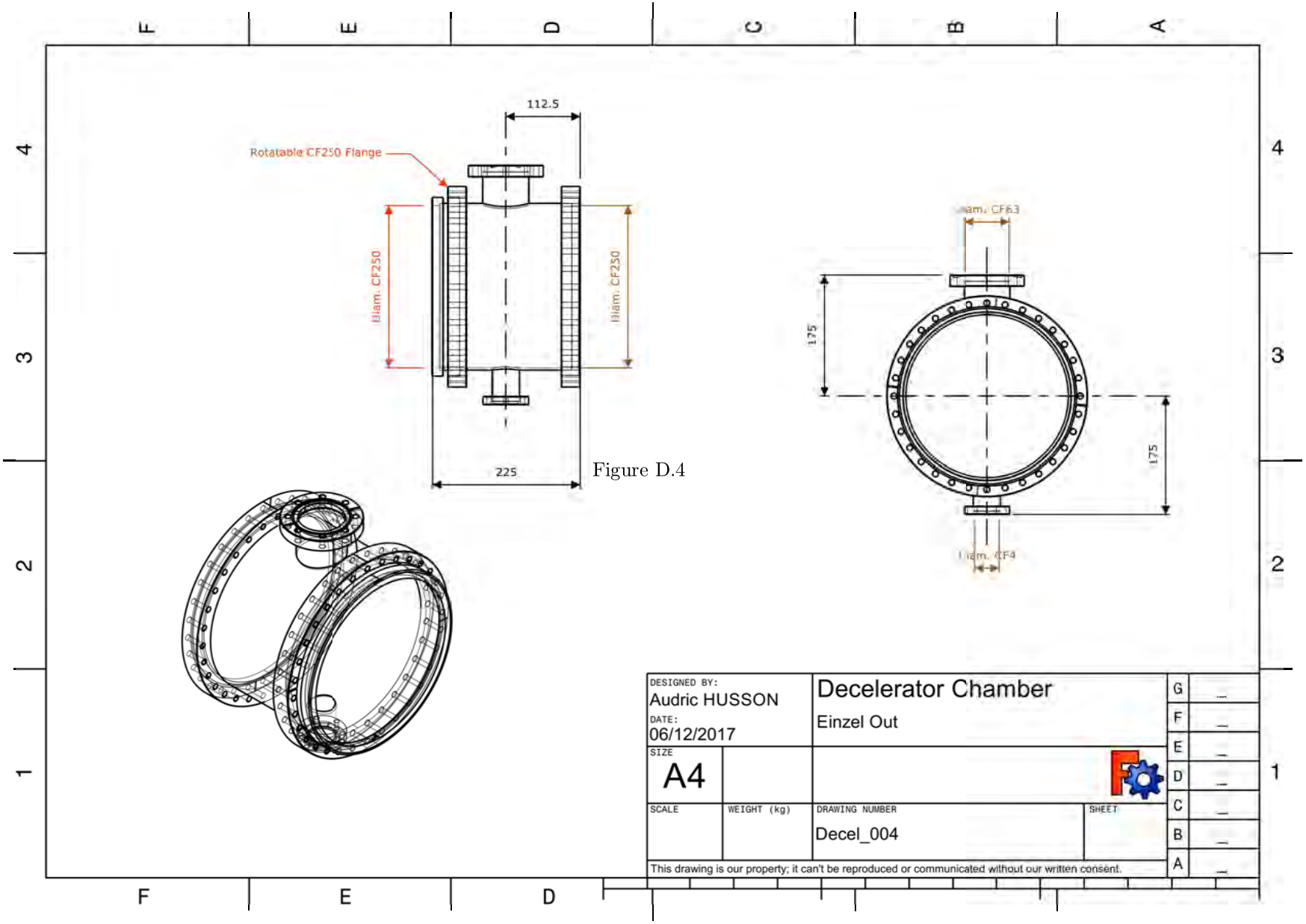
112.5
Rotatable CF250 Flange
Diam. CF250
Diam. CF250
225
Diam. CF63
175
175
Diam. CF4
DESIGNED BY:
Audric HUSSON
DATE:
06/12/2017
Decelerator Chamber
Einzel Out
SIZE
A4
SCALE
WEIGHT (kg)
DRAWING NUMBER
Decel_004
SHEET
This drawing is our property; it can't be reproduced or communicated without our written consent.

Figure D.4

The technical drawings for the High Voltage circuit elements limiting corona discharges:

- High voltage brass ball connector
- High voltage feedthrough connector
- High voltage resistor-cable connector
- Teflon High Voltage circuit support (Part I, Part II & Part III)

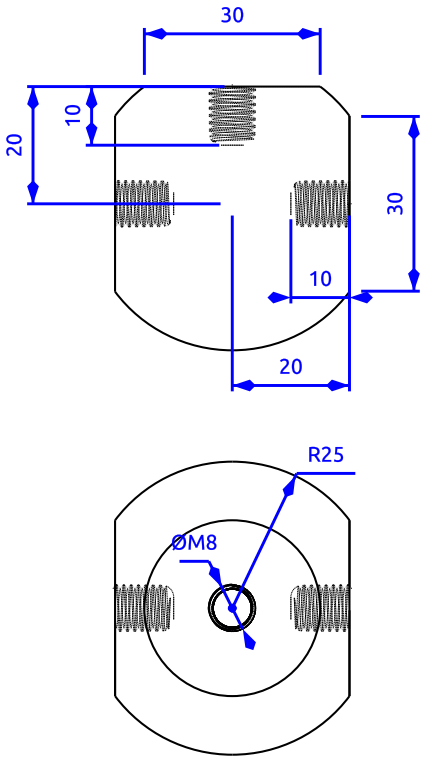

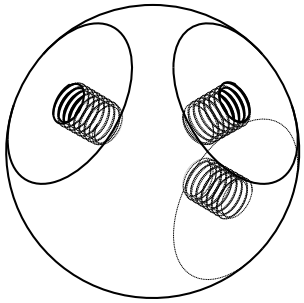

Figure D.5

Created by: HUSSON Audric	Title: Connecteur circuit HT	Size: A4	Sheet: 1 / 1	Scale: (mm)
Supplementary information: Segment central de connection haute tension pour résistances céramiques Nicrom		Part number: 1 Drawing no.: 01		
		Date: 19/12/2016		Revision: REV A

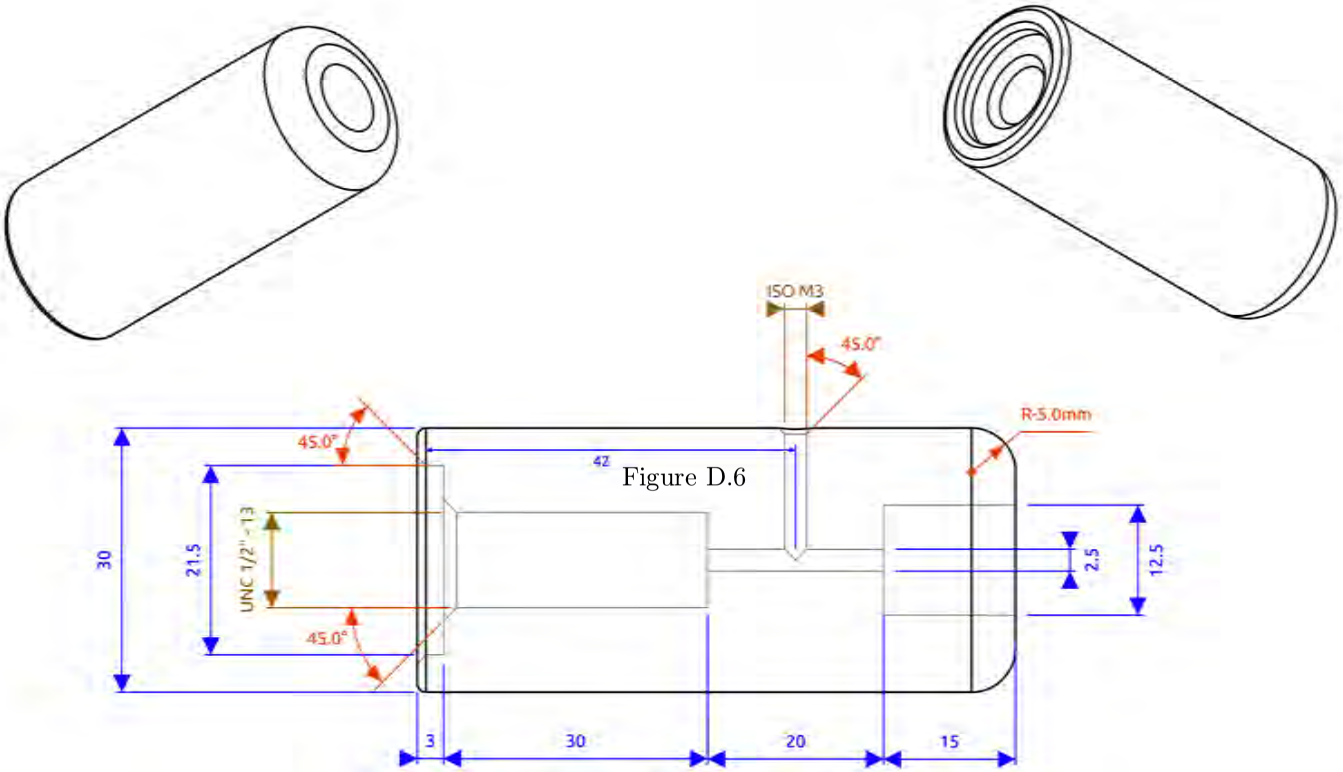

Figure D.6

Created by: Audric HUSSON	Title:	Size: A4	Sheet: 1 / 1	Scale:
Supplementary information: Connector Cable/Feedthrough Aluminum No sharp edge		Part number: PN Drawing no.: DN		
		Date: 05/08/2016		Revision:

Bouchon Haute Tension

GBAR - Décélérateur Antiprotons

Audric HUSSON
CSNSM/IN2P3/CNRS

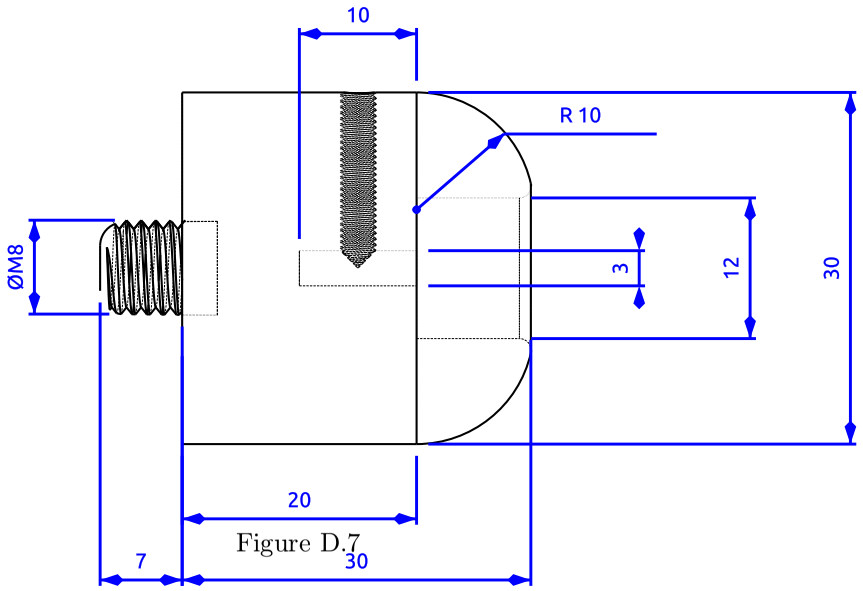

Figure D.7

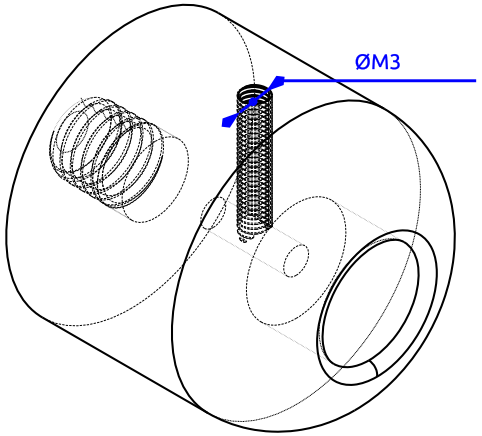

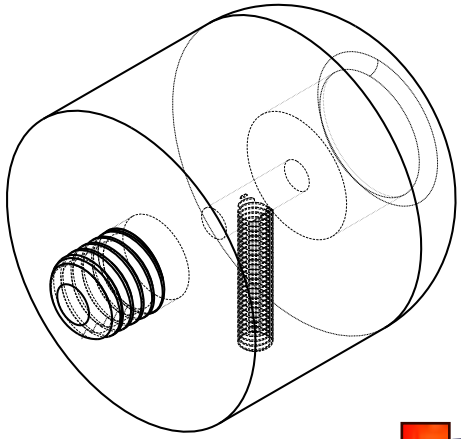

* Arrondissement des bords à vif

* Dimensions en mm

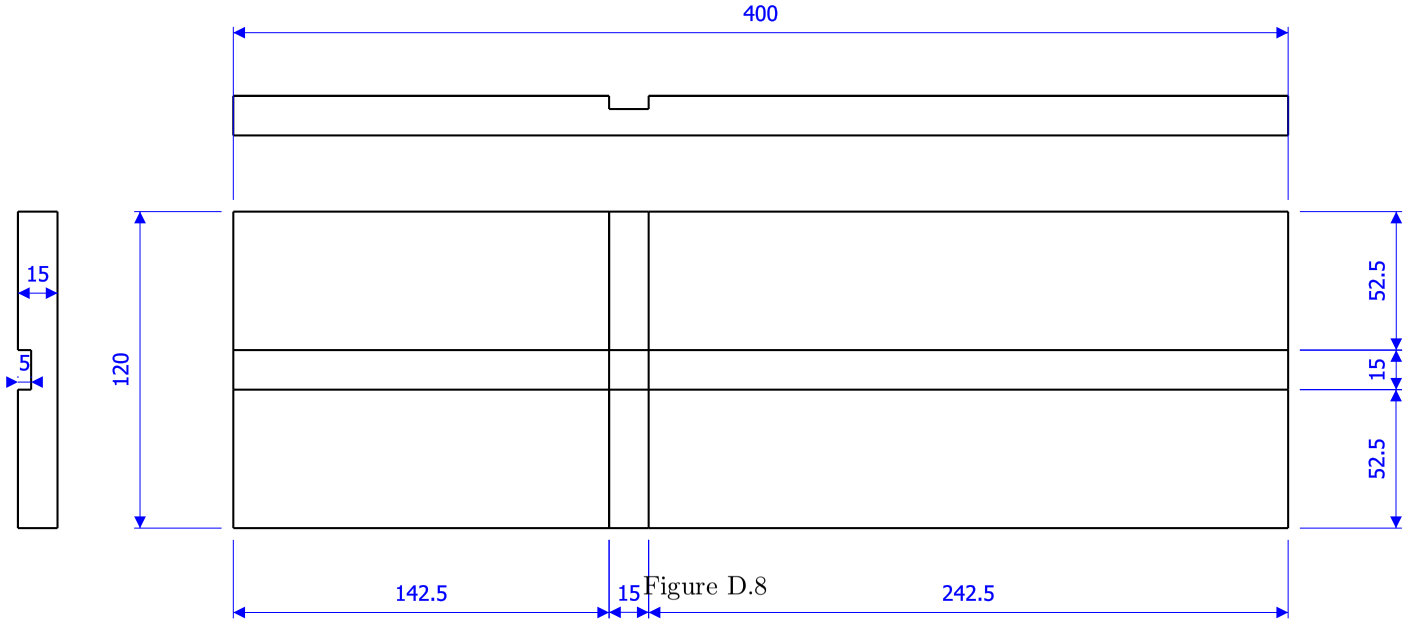

Figure D.8

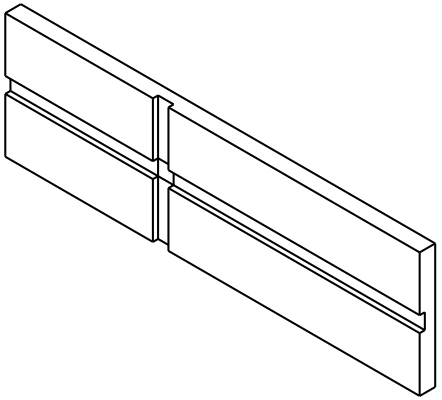

Matière : DELRIN

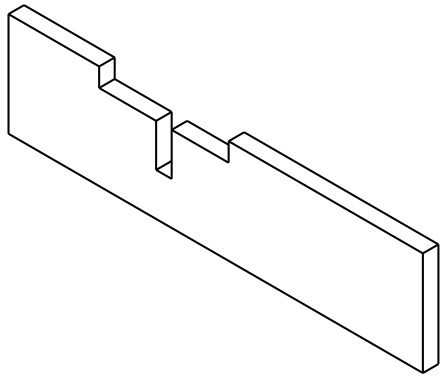

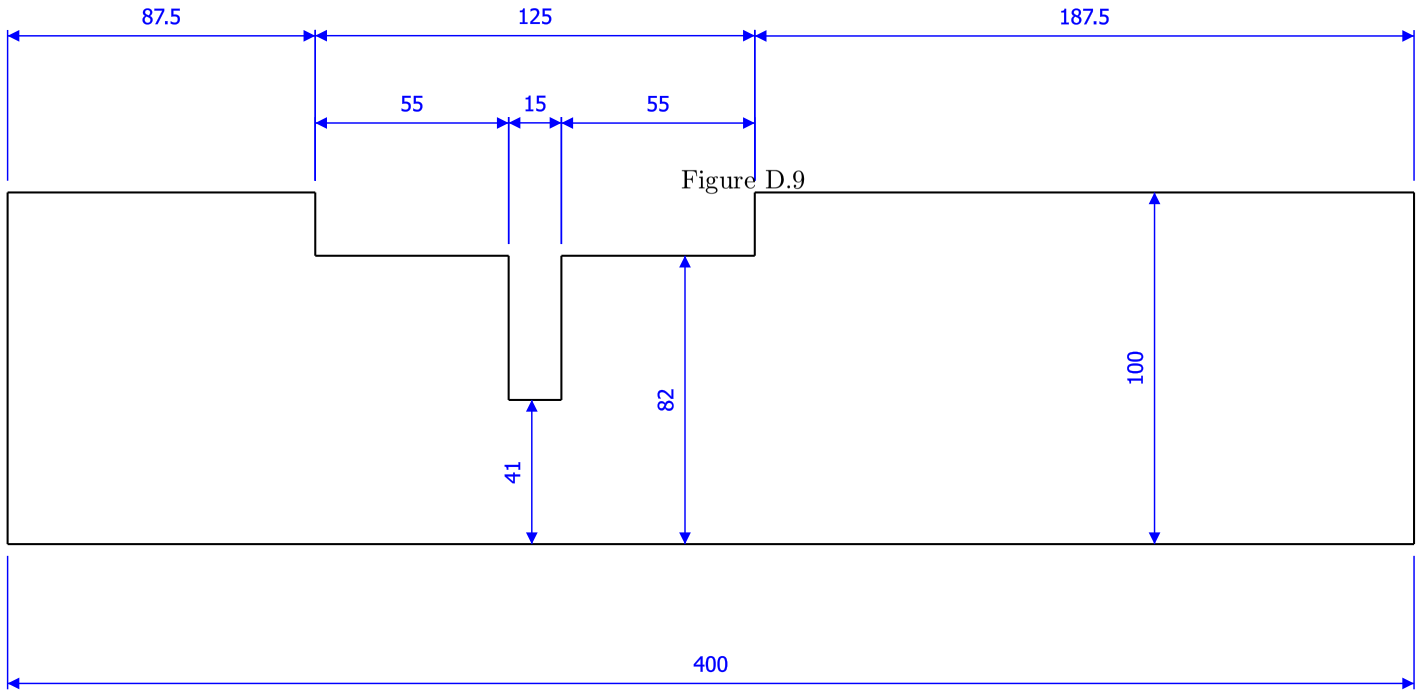

Figure D.9

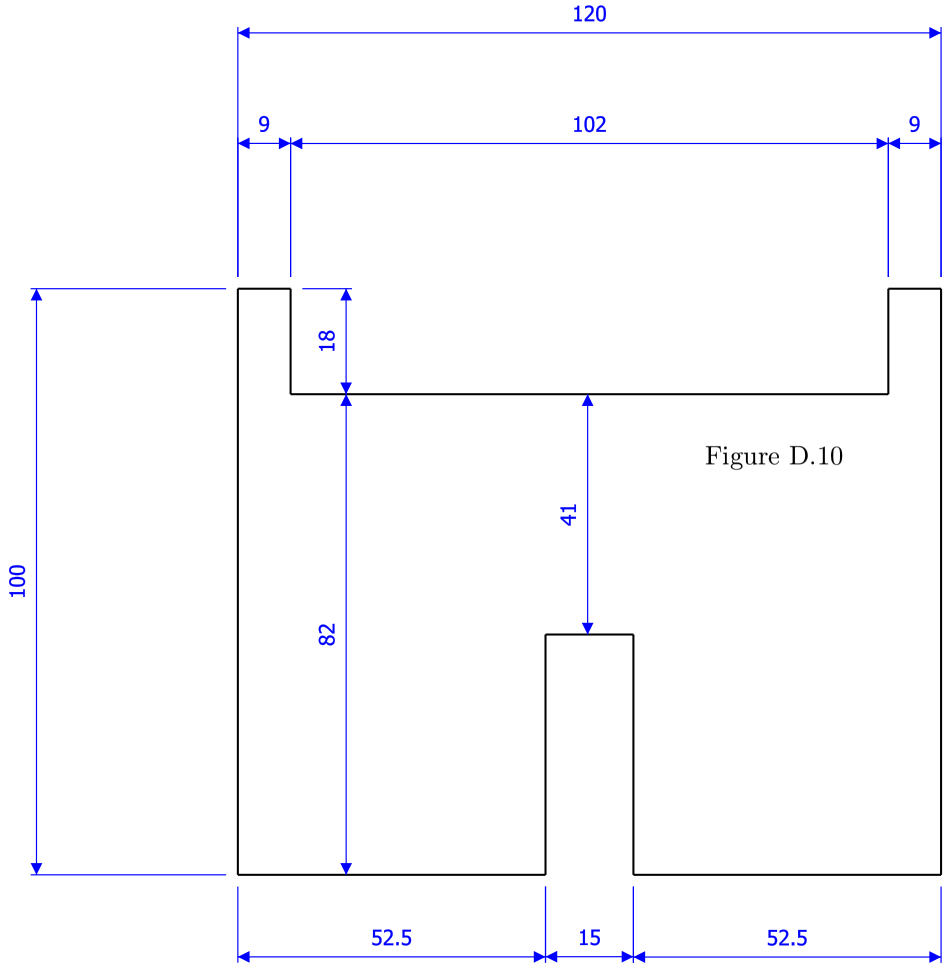

Figure D.10

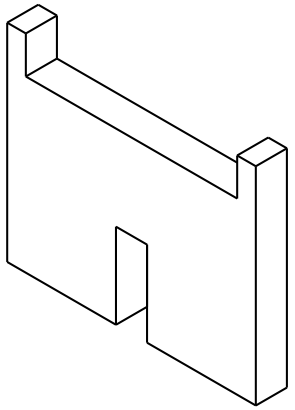

université PARIS-SACLAY | ÉCOLE DOCTORALE PHENIICS

Titre :Décélération d'antiprotons venant du synchrotron ELENA au CERN et transport de l'antimatière à travers l'expérience GBAR

Mots clés : antimatière, antihydrogène, décélération, optique électrostatique, algorithme génétique

Résumé : L'expérience GBAR vise à réaliser la première expérience de chute libre avec des atomes d'antihydrogène afin de tester le principe d'équivalence faible avec de l'antimatière. Dans un premier temps, des ions antihydrogène sont synthétisés à travers une double réaction d'échange de charges puis refroidis par laser pour atteindre des énergies suffisamment faibles pour observer les effets de la gravité. La synthèse d'anti-ions nécessite un très grand nombre d'antiprotons. Nous rapportons dans ce manuscript un nouvel instrument électrostatique permettant de décélérer des paquets d'antiprotons de $100\ keV$ à quelques keV. Cette nouvelle technique vise à éviter les pertes engendrées par l'utilisation de feuille de retardement. Des simulations basées sur un algorithme génétique ont permis d'établir les configurations électrostatiques les plus adaptées. Des tests préliminaires réalisés sur un prototype sont discutés. Les caractéristiques techniques du système de décélération notamment liées au vide, à la haute tension et à la protection des personnes sont décrites. Enfin, une ouverture sur des systèmes optiques secondaires tel qu'un aiguilleur/séparateur d'ions ou l'injection dans un piège de Penning sont étudiées.

Title : Deceleration of antiprotons from CERN's ELENA synchrotron and transport of antimatter beams through the GBAR experiment

Keywords : antimatter, antihydrogen, deceleration, electrostatic optics, genetic algorithm

Abstract : The GBAR experiment aims to perform the first free-fall experiment with antihydrogen atoms to test the weak equivalence principle with antimatter. In a first step, antihydrogen ions are synthesized through a double charge exchange reaction and then cooled by laser to reach sufficiently low energies to observe the effects of gravity. The synthesis of anti-ions requires a very large number of antiprotons. We report in this manuscript a new electrostatic instrument for decelerating antiproton bunches from $100\ keV$ to a few keV. This new technique aims to avoid losses caused by the use of degrader foils. Simulations based on a genetic algorithm made it possible to establish the most suitable electrostatic configurations. Preliminary tests carried out on a prototype are discussed. The technical characteristics of the deceleration system, particularly those related to UHV vacuum, high voltage and safety, are described. Finally, a secondary optical systems such as a switchyard or injection optics into a Penning trap are studied.